Supervisory Control and Power Management of an AC Microgrid

Submitted by Rashid Said Mohammed Al Badwawi to the University of Exeter

as a thesis for the degree of

Doctor of Philosophy in Renewable Energy,

May 2017

I certify that all material in this thesis which is not my own work has been identified and that no material has previously been submitted and approved for the award of a degree by this or any other University.

Signature: ……..

Abstract

The thesis examines the design and implementation of a supervisory controller for the energy management of an AC stand-alone microgrid. The microgrid under study consists of a photovoltaic (PV), battery energy storage system (BESS) and auxiliary (micro gas turbine) units connected to a common AC bus and supplies a local load. The BESS unit has to maintain the AC bus voltage and frequency and needs to balance the difference between the intermittent PV power and that consumed by the load. However, the BESS has limited energy capacity and power rating and therefore it is important to implement a supervisory controller that can curtail the PV power to prevent the battery from being overcharged and also to operate the auxiliary unit to prevent the battery from being over discharged. A Fuzzy Logic Controller (FLC) that can be implemented inside the BESS unit is proposed. It monitors the battery power and State of Charge (SOC) and varies the bus frequency accordingly. The variation in the bus frequency serves as a communication means to the PV and auxiliary units. If the frequency is increased above the nominal value, the PV unit starts to curtail its power and if the frequency is decreased, the auxiliary unit starts to generate power. Power curtailment and supplement are proportional to the frequency variation. In order to avoid any need for communication links between the units, the DC/AC inverters of all the units adopt the well-known wireless droop technique. The droop control of the auxiliary unit is implemented in such a way that the unit is floating on the bus and thus it generates power only if the bus frequency is decreased below its nominal value. The main merits of the proposed controller are simplicity and easiness of implementation inside the BESS unit. The effectiveness of the controller in protecting the battery from over-charging/over-discharging has been verified by simulations including a real-time simulation and experimentally.

Furthermore, the thesis investigates the effect of sudden shading of a PV and concentrated PV (CPV) on the bus frequency of an AC stand-alone microgrid. It is known that the CPV power can drop drastically, compared to traditional PV, when it is exposed to shading. A simulation model of the CPV in a microgrid has been built and the results are compared to those of the traditional PV. It is found that shading of the CPV has much more stronger effect on the bus frequency.

To my parents, my wife and children, and the rest of my family

Acknowledgments

Praise is due to Allah for everything. I'm sincerely grateful to Allah for blessing me with faith and health, and providing me with my lovely family who help me in completing my PhD work. It has been a real amazing journey for me to do my PhD at this stage of my life.

I would like to express my deep gratitude to my two supervisors; Professor Tapas Mallick and Dr. Mohammad Abusara, for their constructive advices, support and guidance during my PhD journey.

My sincere thanks go to Dr. Walid Issa for his support and advices especially for taking the lead in building the laboratory microgrid.

I am very grateful to Ministry of Higher Education, Sultanate of Oman, for providing the scholarship to do my PhD at the University of Exeter.

I am very obliged to Oman Electricity Transmission Company, Sultanate of Oman, for allowing me to do my PhD.

I would like to thank both UK and Indian parties of the EPSRC-DST funded project (Reliable and Efficient System for Community Energy Solutions (RESCUES - EP/K03619X/1)) for allowing me and my research to be part of the project.

I wish to thank all my friends and fellow students at the University of Exeter for their friendship that has made my PhD enjoyable.

I am indebted to all my friends in Cornwall who made my stay during my PhD pleasant.

Rashid Al Badwawi

Table of Contents

List of Figures

List of Tables

List of Publications

A list of the papers that have been published in journals and conferences is as follows. Copies of the papers can be found in Appendix.

Journals

[1] R. Al Badwawi, M. Abusara, T.K. Mallick, “Speed control of synchronous machine by changing duty cycle of DC/DC buck converter,” *AIMS Energy*, vol. 3, no. 4, pp. 728–739, 2015.

[2] R. AlBadwawi, M. Abusara, and T. Mallick, “A review of hybrid solar PV and wind energy system,” *Smart Sci.*, vol. 3, no. 3, pp. 127–138, 2015.

[3] R. Al Badwawi, W. Issa, T. Mallick, and M. Abusara, “Supervisory control for power management of islanded AC microgrid using frequency signalling-based fuzzy logic controller”, ready to be submitted to *IEEE Transactions on Sustainable Energy.*

Conferences

[1] R. Al Badwawi, M. Abusara, and T. Mallick, “Speed control of synchronous machine by changing duty cycle of DC/DC buck converter,” *in WEENTECH Proceedings in Energy: Proceedings of the Global Conference on Energy and Sustainable Development (GCESD2015)*, Coventry, UK, 2015, pp. 91–96.

[2] R. Al Badwawi, W. Issa, T. Mallick, and M. Abusara, “Power management of AC islanded microgrids using fuzzy logic,” *in 8th IET International Conference on Power Electronics, Machines and Drives (PEMD 2016)*, Glasgow, UK, 2016, pp. 1–6.

[3] R. Al Badwawi, W. Issa, T. Mallick, and M. Abusara, “DC microgrid power coordination based on fuzzy logic control,” *in 18th European Conference on Power Electronics and Applications (EPE'16 ECCE Europe)*, Karlsruhe, Germany, 2016, pp. 1–10.

Nomenclature

P_{pv}	PV power
P_{pv}^{*}	PV power demand or set-point
P_{aux}	Auxiliary power
P_{aux}^{*}	Auxiliary power demand or set-point
P_{bat}	Battery power
P_{ESS}^{*}	Energy storage system power demand or set-point
C_{bat}	Battery capacity
V_{bat}	Battery voltage
SOC	Sate of charge
SOC_{max}^{*}	Maximum state of charge
SOC_{min}^{*}	Minimum state of charge
$SOC_{min+10\%}^{*}$	Minimum state of charge plus 10%
P_{charge}	Charging power
$P_{charge\_max}^{*}$	Maximum charging power
$P_{discharge}$	Discharging power
$P_{discharge\_max}^{*}$	Maximum discharging power
ΔSOC_1	Change in SOC (first input to FLC top subsystem)
ΔP_{charge}	Change in P_{charge} (second input to FLC top subsystem)
ΔSOC_2	Change in SOC (first input to FLC bottom subsystem)
$\Delta P_{discharge}$	Change in $P_{discharge}$ (second input to FLC bottom subsystem)
m_{PV}	Active power/frequency droop coefficient for PV
m_{aux}	Active power/frequency droop coefficient for auxiliary unit
m_{ESS}	Active power/frequency droop coefficient for Energy Storage System
n_{PV}	Reactive power/voltage droop coefficient for PV
n_{aux}	Reactive power/voltage droop coefficient for auxiliary unit
n_{ESS}	Reactive power/voltage droop coefficient for Energy Storage System
P	Exported/measured active power

Q	Exported/measured reactive power
P^* or P_o	Active power demand or set-point
Q^* or Q_o	Reactive power demand or set-point
m or k_d	Frequency drooping coefficient
n or k_q	Voltage drooping coefficient
θ	Phase difference between each inverter output voltage and load voltage
V	Inverter output voltage
V_L	Load voltage
X	Load impedance
U_{ref}	Inverter reference signal
V_{ref}	Signal for duty cycle generation for the inverter
V_o	Nominal output voltage of inverter
$\omega_o = 2\pi f_o$	Nominal bus frequency
ω or G_f	Bus frequency
$\Delta\omega$ or $d\omega$	Bus frequency variation/deviation
$\Delta\omega_+$	Positive frequency shifting/deviation
$\Delta\omega_-$	Negative frequency shifting/deviation
$\Delta\omega_{max+}$	Maximum positive deviation in frequency
$\Delta\omega_{max-}$	Maximum negative deviation in frequency
ωt	Nominal phase angle
$G_{\omega t}$	Phase angle of the common bus
L_1	Inverter-side filter inductor
C	Filter capacitor
L_2	Grid-side filter inductor
C_{dc}	DC-link capacitor (converter output)
V_{dc}	Nominal DC-link voltage
V_{dc}^*	DC-link voltage set-point value
L_{line1}	Line1 inductor
L_{Line2}	Line2 inductor
f_{sw}	Switching frequency
f_s	Sampling frequency
L_{DC}	Converter inductor
V_{pv}	PV output voltage

k_{p_batc}	P-controller gain for battery current controller
k_{i_batc}	I-controller gain for battery current controller
k_{p_batv}	P-controller gain for battery voltage controller
k_{i_batv}	I-controller gain for battery voltage controller
k_{p_pvv}	P-controller gain for PV voltage controller
k_{i_pvv}	I-controller gain for PV voltage controller
k_{p_pvc}	P-controller gain for PV current controller
k_{i_pvc}	I-controller gain for PV current controller
k_v	Voltage controller gain for inverter voltage controller
k_c	Current controller gain for inverter voltage controller
L_v	Virtual inductor for inverter voltage controller
ω_c	Cut-off frequency for power measuring filter
k_{p-dc}	P-controller gain for PV DC voltage regulator
k_{i-dc}	I-controller gain for PV DC voltage regulator
s	Laplace operator
P_{PV_MPPT}	Maximum power tracking point of the PV power
R	Equivalent load resistor for converter
D	Steady state duty cycle
I_{LB}	Steady state BESS Inductor current
L_B or L_{dc}	BESS converter inductor
G_{iLB-d}	Transfer function for BESS boost converter (1)
$G_{vdc-iLB}$	Transfer function for BESS boost converter (2)
d	Averaged control input
$G_{PI-B1(s)}$	Current loop PI controller for BESS converter
$G_{PI-B2(s)}$	Voltage loop PI controller for BESS converter
L_{pv} or L_{dc}	PV converter inductor
i_{Lpv}	PV current
r_{pv}	PV Dynamic resistor
C_{pv}	PV Input capacitor
G_{iLpv-d}	Transfer function for boost PV converter (1)
$G_{vpv-iLpv}$	Transfer function for boost PV converter (2)
$G_{PI-pv1(s)}$	Current loop PI controller for PV converter
$G_{PI-pv2(s)}$	Voltage loop PI controller for PV converter

I_{sc}	PV short circuit current
V_{oc}	PV open circuit voltage
I_m	PV current at maximum power
V_m	PV voltage at maximum power
P_m	PV maximum power
FF	Fill factor (for PV)
P_T	PV theoretical non-obtainable maximum power
P_{out}	Output electrical power (for PV)
P_{in}	Input solar power (for PV)
η	Efficiency
I_{pv}	PV current
I_{ph}	Photocurrent generated by the current source
I_d	Diode current
I_{sh}	Shunt resistance current
I_0	Reverse saturation current
q	Electron charge
n	Ideality factor
R_s	Series resistance
R_{sh}	Shunt resistance
k	Boltzman constant
T_{pv} or T_c	Cell temperature
V_{pv}	PV voltage
I_{d1}	First diode current
I_{01}	Reverse saturation current for first diode
I_{d2}	Second diode current
I_{01}	Reverse saturation current for second diode
n_1	Ideality factor for first diode
n_2	Ideality factor for second diode
η_{PV}	PV cell efficiency
A_{PV}	Area of the PV cell
G_T	Total/global solar irradiation (direct + diffuse)
f	PV Correction coefficient for all factors except temperature
K_t	Correction coefficient factor for temperature
a	Normalized temperature for PV

$NOCT$	Normal operating cell temperature
T_a	Ambient temperature
P_{PVmod}	Ideal PV model electric power
$P_{PVmod,a}$	Actual PV model electric power
N_S	PV cell numbers in series
η_{PVmod}	PV module efficiency
η_{inv}	Inverter efficiency
P_{PVpar}	PV module parasitic current losses
G_{PVpar}	PV parasitic losses factor coefficient
C_g	Geometric concentration
A_a	Area of entry aperture of the optical element of the concentrator
A_b	Area of the exit aperture representing the active area of the solar cell
P_C	Electrical power of a single solar cell in a system that uses concentrator
$P_{C,a}$	Actual electrical power with concentrator
η_C	CPV cell efficiency
η_{opt}	Optical efficiency
A_C	Area of CPV cell
C	Concentration value
G_d	Direct solar irradiation
f_C	Non-ideal tracking correction factor in concentrated system
K_{tc}	Correction coefficient factor for temperature in concentrated system
$T_c(conc.)$	Cell temperature for concentrated system
a_C	Normalized temperature in concentrated module
P_{mod}	Ideal model electric power in concentrated system
$P_{mod,a}$	Actual model electric power in concentrated system
N_{SC}	CPV cell numbers in series
η_{mod}	CPV module efficiency
P_{par}	Module parasitic current losses in concentrated system
G_{par}	Parasitic losses factor coefficient in concentrated system

Abbreviations

AC	Alternating Current
BESS	Battery Energy Storage System
COG	Centre of Gravity
CPV	Concentrated Photovoltaic
DC	Direct Current
DG	Distributed Generator
ESS	Energy Storage System
FC	Fuel Cell
FLC	Fuzzy Logic Controller
H	High membership function
HAWT	Horizontal-Axis Wind Turbine
HCPV	High Concentrating Photovoltaic
IEA	International Energy Agency
IGBT	Insulated Gate Bipolar Transistor
I-V	Current-Voltage
L	Low membership function
LCPV	Low Concentrating Photovoltaic
LPSP	Loss of Power Supply Probability
M	Medium membership function
MCPV	Medium Concentrating Photovoltaic
MPP	Maximum Power Point
MPPT	Maximum Power Point Tracking
P	Proportional controller
PCC	Point of Common Coupling
PI	Proportional-Integral controller
PLL	Phase Looked Loop
PV	Photovoltaic
P-V	Power-Voltage
PWM	Pulse Width Modulation
RES	Renewable Energy Sources
SOC	State of Charge

STS	Static Transfer Switch
UPS	Uninterruptable Power Supply
VAWT	Vertical-Axis Wind Turbine
VSC	Voltage Source Converter
VSI	Voltage Source Inverter
WT	Wind Turbine
μGT	Micro Gas Turbine

CHAPTER 1: INTRODUCTION

1.1 Background

The reserves of fossil fuels such as gas, diesel and coal are depleting and the competition for obtaining those fuels is rising rapidly with the rapid increase in the world population and the high demand for electricity across the world [1]. Hence, there is more need to utilize alternative power sources. Renewable Energy Sources (RES), such as sun, wind, tides and geothermal heat are sustainable sources that are naturally replenished. Due to the sustainable nature and reduction in cost of those sources, they become a very attractive solution for power supply. Solar and wind energies are two of the most promising of these renewable energy technologies.

With more environmental awareness and a drop in the cost of RES, the global penetration of renewable energy in power systems is increasing rapidly especially for Photovoltaic (PV) and wind systems [2]. The largest ever annual increase in global renewable energy capacity has been seen in the year 2015 as per the 2016 renewables global status report with an estimated 147 gigawatts (GW) of additional renewable power capacity. Solar PV and wind contributed around 77% of the new added capacities in the power sector and hydropower represented most of the remainder. In other words, solar PV, wind and hydro power dominated the market. By the end of 2015, the available renewable capacity was sufficient to supply an estimated 23.7% of the global electricity demand with 16.6% coming from hydropower. Renewable energy deployment is expected to increase further. An analysis in the status report had a projection that there will be a five folds increase in the solar power capacity and three times increase in the wind power capacities over the next 15 years [3]. Table 1.1 provides a summary of some important selected indicators from the 2016 report and the previous years' reports showing the global rapid penetration of renewable energy.

Table 1.1: Important global indicators for renewable energy

		2010	2011	2012	2013	2014	2015
Renewable power installed capacity (with hydro)	GW	1,250	1,355	1,470	1,578	1,701	1,849
Renewable power installed capacity (without hydro)	GW	315	395	480	560	665	785
Solar PV installed capacity	GW	40	71	100	138	177	227
Wind power installed capacity	GW	198	238	283	319	370	433
Concentrating solar thermal power installed capacity	GW	1.1	1.6	2.5	3.4	4.3	4.8

Solar and wind power systems can be either grid-connected or stand-alone systems. Most of the current installations are grid-connected [3]. Higher penetration of these technologies could create high technical challenges especially in weak grids due to their intermittent and unpredictable nature. Intermittency in power generation, as a result of solar radiation and wind speed variations with time, can cause voltage fluctuation. The impact of such a disturbance is highly dependent on load type and size along with the strength of the connected electrical utility grid and its size. Frequency fluctuation in AC grids, due to sudden changes in active power drawn by a load, is another quality issue for systems with solar and wind power generation. Another quality issue is the existence of harmonics which are normally caused by power electronic devices and non-linear appliances.

A new trend has been developed to integrate RES in microgrids [4], which can work in both grid-connected and stand-alone modes. The driver for this trend is to have the RES as Distributed Generators (DG) as close as possible to the loads reducing losses and voltage drops in a power system. Therefore, power is generated and used locally by local loads without the need for expensive transmission and distribution networks. This clearly reduces procurement, installation, operation and maintenance costs. Another driver is the stringent

environmental requirements and legislation that are implied in attempts for utilization of more RES and reduction of CO_2 emissions by using less fossil fuel in power generation. On occasion, there is even subsidization and support from Governments for utilization of power from RES. In view of the above, microgrids become an attractive solution for power generation by integrating DG, including RES, and loads. There are many benefits for having microgrids such as better power quality, increased reliability and security for utility grid's operators and end users, more controllability and cost competitiveness.

As per the International Energy Agency (IEA) 2015 World Energy Outlook report, the global population in 2013 was around 7.1 billion and is expected to increase to 9 billion in 2040. There were around 1.2 billion people living without electricity in 2013. This represents about 17% of the global population. Sub-Saharan Africa and developing Asia have more than 95% of those living without access to electricity and they are primarily in rural areas [5]. Hence, a stand-alone renewable energy power system represents an excellent solution for those rural areas that are not connected to a utility grid. The stand-alone system provides an economical system to run in comparison to the extension of existing infrastructure facilities such as transmission lines and gas lines.

1.2 Microgrid

Microgrid is a small-scale power system or grid that consists of DG (conventional and/or renewable), storage (battery, fuel cell) and load with associated control (local and supervisory) and protection systems. It can be connected to a utility grid (grid-connected mode) or can work independently in a stand-alone (sometimes called island or autonomous) mode. A microgrid can be classified into two types either AC or DC. Whenever both types are connected together, they can be called hybrid AC-DC microgrids. The stand-alone AC microgrid is the focus of this thesis.

A general AC microgrid structure is shown in Figure 1.1 which consists of RES, ESS, loads and an auxiliary unit that are all connected in a common AC bus along with a supervisory controller and a Static Transfer Switch (STS). The auxiliary unit is shown as a micro gas turbine in this case, but it could be a fuel cell (FC), diesel generator or even another battery. PV and Battery ESS (BESS)

units are interfaced by two stages DC/DC and DC/AC power electronic converters. On the other hand, the wind turbine (WT) and micro gas turbine (μGT) units are interfaced by two-stage AC/DC and DC/AC power electronic converters. The AC outputs' voltages from individual DGs, through individual converters, are integrated and combined on a common AC bus to provide the power to the utility grid / loads even with only one source available. The output current and voltage from each source are controlled independently. However, low speed communication between the STS and the different DG units is still required to know the status of the STS. In order to isolate (or re-connect) the microgrid from (or to) the utility grid seamlessly, the STS is used at the Point of Common Coupling (PCC) which could be monitored and controlled by the supervisory controller of the microgrid. Local loads are connected to the microgrid side of the STS in order to ensure that they are always supplied whether the microgrid is operating in grid-connected mode or stand-alone mode i.e. regardless of the status of the STS [6].

In the grid-connected mode of operation, the RES units act as current sources and inject power directly into the AC bus. The utility grid is dictating the bus voltage and frequency and the individual RES units control the power flow. The battery system is interfaced by a bi-directional converter and can be charged or discharged depending on the situation of the generation, load and its state of charge. However, in the stand-alone mode, the RES act as current sources feeding directly the loads and the battery unit acts as a voltage source controlling the AC bus voltage by charging or discharging. The battery DC/AC converter regulates the magnitude and frequency of the bus voltage. The individual RES units operate in Maximum Power Point Tracking (MPPT) in the grid-connected mode. The same is applicable in the stand-alone mode provided that the generated power can be either consumed by the load or used to charge the battery [7]. In a stand-alone mode, the BESS is used as a grid forming unit regulating the AC bus, while the RES is used as a grid feeding unit injecting power into the AC bus [8].

Although the AC microgrids are more dominant in terms of research and existence compared to the DC microgrids, the DC microgrids have started receiving more attention and consideration with their higher efficiency, natural

interface of RES and other advantages. In addition, some of the issues that are faced in AC microgrids, like reactive power flow, power quality, and frequency control, do not exist in DC microgrids. This makes the corresponding primary control notably less complex than its equivalent AC version [9].

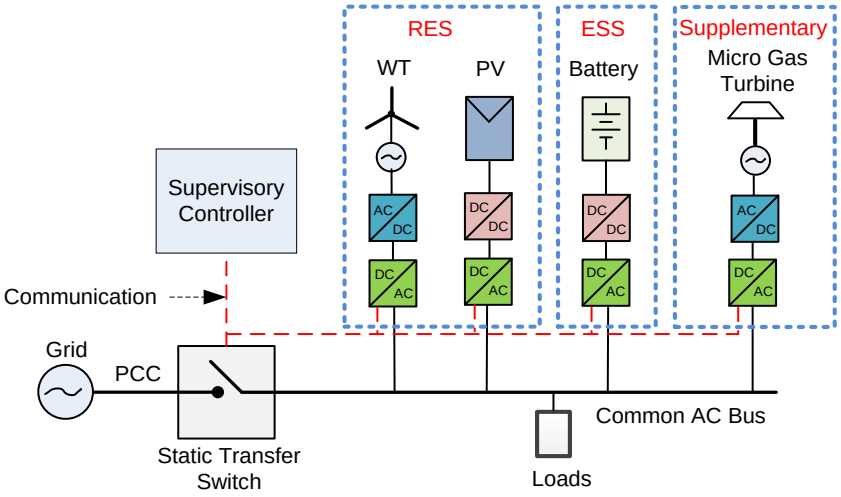

Figure 1.1: General AC microgrid structure

1.3 System under Study

The stand-alone AC microgrid under study consists of PV based RES, BESS, micro gas turbine auxiliary supplementary unit and load. The proposed stand-alone AC microgrid control topology is as shown in Figure 1.2 and it operates as follows:

1- PV unit which consists of a unidirectional DC/DC converter and a DC/AC inverter. The DC/DC converter controls the PV output voltage to achieve MPPT while the DC/AC inverter regulates the DC link voltage.
2- BESS unit which has a bidirectional DC/DC converter and a DC/AC inverter. The bidirectional DC/DC converter regulates the DC link voltage while the DC/AC inverter represents the master unit that maintains and controls the AC bus frequency and voltage of the microgrid.
3- Auxiliary supplementary unit (micro gas turbine in this case) consists of a unidirectional AC/DC converter and a DC/AC inverter. The unidirectional AC/DC converter regulates the DC link voltage while the DC/AC inverter controls the output power to the AC bus. The auxiliary supplementary unit operates during low battery SOC and/or low PV generation cases.

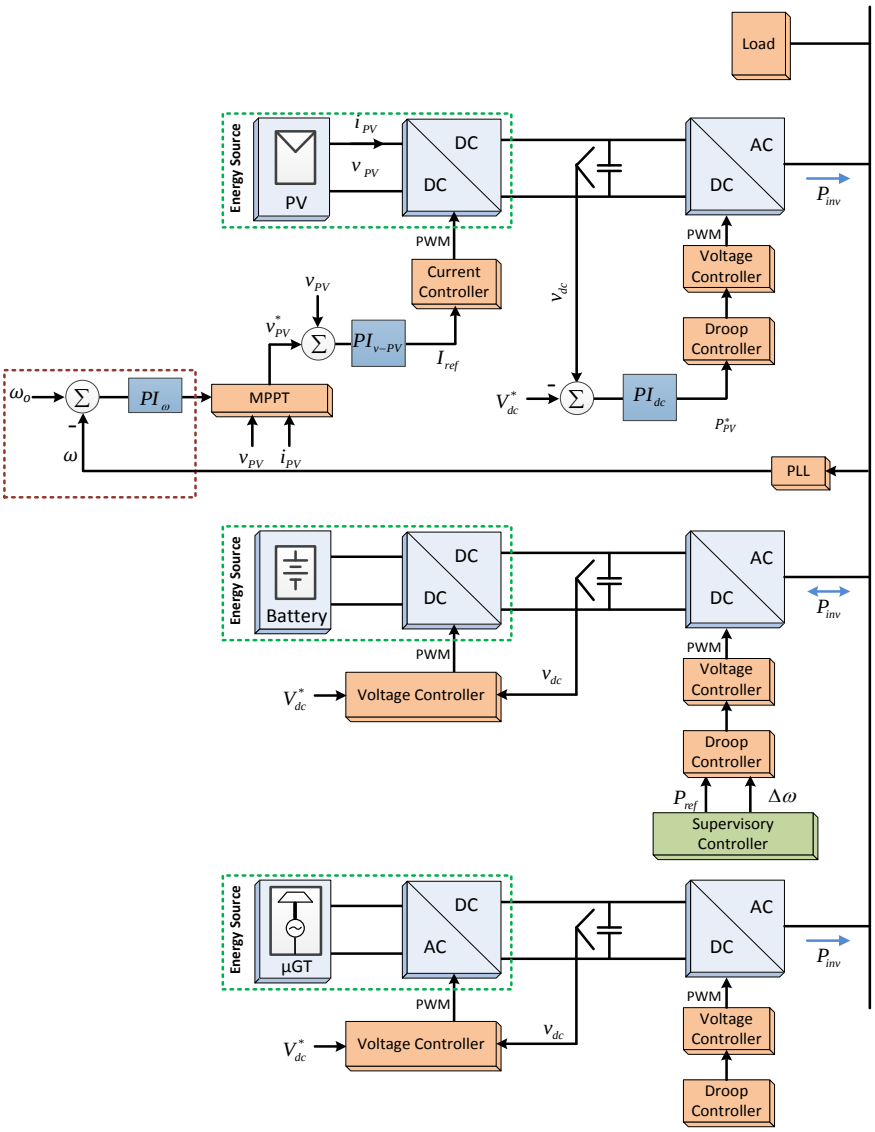

Figure 1.2: Proposed stand-alone AC microgrid control topology

1.4 Problem Statement

With its limited capacity and power rating, the BESS has to maintain the bus voltage and frequency in the AC stand-alone microgrid. The BESS needs to balance the difference between the intermittent RES power and that consumed by the load. At the same time, the battery's SOC and charging/discharging power need to be maintained within their allowable limits. The control needs to be wireless to increase reliability and no dump load is to be used. Therefore, the supervisory controller has to fulfil two main tasks; firstly, the SOC of the battery has to be maintained between the maximum and minimum limits and secondly,

the battery power needs to be kept within the maximum charging/discharging limits.

1.5 Aims and Objectives

The main aim of this thesis is to develop an energy management system for a stand-alone AC microgrid consisting of a RES, BESS, auxiliary unit and load. The thesis presents a wireless supervisory controller to limit the charging and discharging power of the BESS and the state of charge from exceeding their maximum limits by controlling the operation of the PV and auxiliary units. The objectives of the thesis are summarised as follows:

- To review different control techniques used for energy management of a standalone microgrid.
- To study the effect of intermittency and varying load on the operation of the battery.
- To design a Fuzzy Logic supervisory controller that can be implemented within the battery unit that varies the bus frequency of AC microgrid according to the battery unit power and state of charge.
- To design a local controller for the RES units that curtails the power according to the bus frequency of the AC microgrid.
- To build a laboratory scale AC microgrid consisting of a solar based RES, BESS, auxiliary unit, and load and implement the supervisory controller experimentally.
- To evaluate the effectiveness of the proposed controller using real solar radiation data and different load profiles.
- To investigate the effect of a sudden shading of a PV and concentrated PV (CPV) on the bus frequency.

1.6 Thesis Contribution

The main contributions of the thesis are as follows:

- Development of a novel energy management system for a standalone microgrid that is based on Fuzzy Logic. The supervisory controller can be implemented wirelessly using the bus frequency for the AC microgrids.

The local droop controller reacts to the change in bus frequency to curtail or supplement power.

- Investigation into using an auxiliary unit such as a micro gas turbine in a standalone microgrid to support the load in case the power from the RES is insufficient.
- Design of a droop controller which enables the auxiliary unit to respond automatically to the change in the bus frequency so it supplies power only when the frequency is reduced below its nominal value and the amount of deviation of the frequency determines the amount of power to be supplied by the auxiliary unit. The novelty of the work lies in making the micro gas turbine floating on the bus so it generates power only when commanded, wirelessly, by the Fuzzy Logic Controller.
- Experimental implementation of the controller using an AC microgrid that has different converter stages including the DC/DC converters.
- Investigation into the effect of sudden fluctuation of PV and CPV power, due to shading, on the AC bus frequency.

1.7 Thesis Outline

The outline of the thesis is as follows:

Chapter 2 presents a literature review of hybrid solar PV and wind power systems. It provides a review of the main research work reported in the literature with regard to optimal sizing design, power electronics topologies and control. It also presents a review of the state of the art of both grid-connected and stand-alone hybrid solar and wind power systems.

Chapter 3 is considers the power management of a stand-alone AC microgrid that consists of RES, ESS, auxiliary units and loads. FLC is proposed as the supervisory controller for the microgrid for overall power management. The chapter also gives an overview of a typical inverter-based AC microgrid and the method of operation in stand-alone and grid-connected modes. It shows different control strategies for the DC link voltage in a two-stage converter. The chapter also provides details about the droop control strategies for ESS and RES units by introducing the basic concept of the droop control and then shows different strategies for the relevant DC/AC inverters. The concept of a floating

auxiliary unit (micro gas turbine (μGT)) on the common bus is introduced and its droop control strategy is provided. The effectiveness of the proposed FLC is verified by simulation.

Chapter 4 shows a simplified model of the microgrid that is developed to speed up the simulation time in order to assess the performance of the FLC especially over long periods of time. The whole microgrid is simplified and each unit is represented only by its droop controller. The chapter provides short time and long real-time simulation results. In the short simulation, the FLC is compared with a Proportional (P) controller while the real-time simulation is conducted both with and without the FLC.

Chapter 5 presents the design and experimental set-up for a laboratory-scale microgrid. The effectiveness of the proposed FLC is verified experimentally.

Chapter 6 describes the modelling of PV and CPV including single-diode and two-diode models that are used for modelling a PV cell. The chapter shows the impact of changing solar irradiation or shading of PV and CPV on the microgrid AC bus frequency. Sample simulation results of $1m^2$ area of 135Wp PV, and 500 suns concentration (500X) CPV modules both with and without shading are shown to assess the impact on the frequency.

Chapter 7 provides a discussion of the findings and conclusion and makes suggestion for future work.

CHAPTER 2: LITERATURE REVIEW

2.1 Introduction

The literature is reviewed in this chapter to have an understanding of challenges and possible solutions/mitigations to hybrid solar PV and wind power systems. It provides a review of the main research work reported in the literature with regard to optimal sizing design, power electronics topologies and control including the supervisory control. It presents a review of the state of the art of both grid-connected and stand-alone hybrid solar and wind systems. This review should provide insights to aid the improvement of supervisory control of the hybrid power system including a fuzzy logic controller.

Energy management is very important for any power system to control the power flow between generators and loads. With the intermittent power from RES; it becomes more challenging to design a suitable energy management strategy or supervisory controller. One solution for the intermittency issue is to have a hybrid solar PV and wind power system together in a fully integrated power system along with sufficient storage facilities such as batteries. Another possible solution is to use fast-act energy sources such as a gas turbine as a back-up generating unit [10]. However, the use of a fossil unit needs to be controlled effectively to ensure reducing its usage to the minimum possible limit in order to reduce the CO_2 emissions which reduce the overall cost as well. Voltage and frequency fluctuation, and harmonics injection are also major power quality issues for renewable energy power systems.

2.2 Hybrid Solar PV-Wind Systems

A hybrid solar PV and wind power generation system is a very attractive solution for stand-alone applications that are not connected to an existing grid. Reliability could be increased by integrating solar and wind together compared to one individual system. In addition, their hybrid system becomes more economical to run since each system complements the other one. Furthermore, connecting hybrid solar and wind power systems with a grid can further help improving the overall economy and reliability of renewable power generation to

supply its load and exchange power with the grid whenever required. Similarly, the integration of hybrid solar and wind power in a stand-alone system can reduce the size of energy storage needed to supply continuous power to a connected load. Literature reviews for hybrid grid-connected and stand-alone solar PV and wind energies have been conducted worldwide by many researchers who have presented various challenges and proposed several possible solutions [11], [12].

2.2.1 Solar energy (PV/CPV)

Solar electricity generation systems could produce electricity from either Photovoltaics (PV) or concentrated solar power plants. In this thesis, the focus is on the PV type. The PV uses direct and diffused solar radiations to generate electrical power. Concentrated Photovoltaics (CPV) uses only direct solar radiation to provide electrical power where a large area of sunlight is focused on a solar cell using optics such as lenses. That is why CPV requires days with highly concentrated sunlight and continuous tracking of solar radiation (i.e. it cannot produce power with diffused solar radiation) [13]–[16].

PV modules produce outputs that are determined mainly by the level of incident radiation. As the light intensity increases, photocurrent will be increased and the open-circuit voltage will be reduced [17]. For provided external conditions, the PV modules are characterized by I-V curves, like the ones shown in Figure 2.1. The power depends on the operating point and the Maximum Power Point (MPP) is the point near the knee of the I-V curve, which provides the maximum power. The photovoltaic voltage of the MPP is generally bounded by 70% to 82% of the open circuit voltage, which helps in providing suitable MPP tracking unlike the current of the MPP that dramatically varies with radiation. In addition, the voltage signal measurement is better in quality, cheaper and easier in implementation in comparison to current detection [18]. An appropriate tracking of the MPP provides better efficiency of the PV system. Furthermore, the efficiency of any PV cell decreases with increasing temperature which is non-uniformly distributed across the cell [19].

The CPV technology generates electricity by utilizing optics, such as lenses or mirrors, in order to concentrate a large amount of sunlight onto a small area of

solar photovoltaic materials. This increases the efficiency, reduces the cost of manufacturing in particular photovoltaic materials cost since the area becomes small and it is more environmentally friendly due to the fact that CPV requires less area for installation in comparison to the normal flat PV [14]. The CPV can be classified into three types: low concentrating PV (LCPV) with concentration factors below 10 suns; medium concentrating PV (MCPV) with concentration factors between 10 and 300 suns and high concentrating PV (HCPV) with concentration factors above 300 suns. The medium concentration CPV systems with concentration factors between 10 and 300 suns have disappeared from the market since these systems require two-axes solar tracking and cooling, which makes them quite complicated [20]. Solar radiation, ambient temperature and atmospheric conditions are the main factors affecting the performance of the CPV. However, other factors such as solar cell efficiency, optics efficiency, solar cell temperature do have an impact as well.

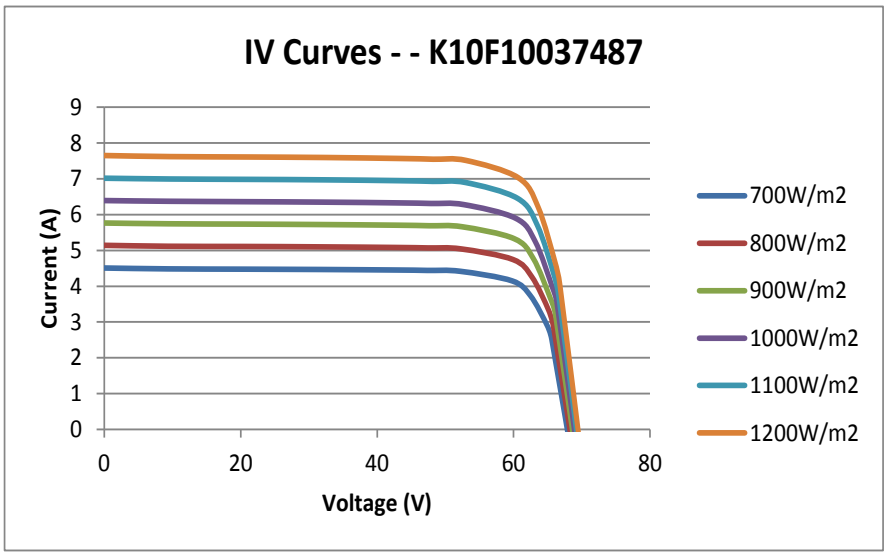

Figure 2.1: I-V curves

2.2.2 Wind energy

A wind turbine (WT) converts kinetic energy from the wind into mechanical energy and that energy can then be converted to electrical energy using a wind generator [21]. Detailed descriptions of the wind energy can be found in references [16] and [22]. WTs are classified into two types: 1) Horizontal-Axis WT (HAWT) which has the main rotor shaft and electrical generator at the top of a tower and 2) Vertical-Axis WT (VAWT) which has the main rotor shaft

arranged vertically. The highest achievable extraction of power by a WT is 59% of the total theoretical wind power [22]. Table 2.1 provides a brief summary of the main advantages and disadvantages of each type of wind turbine [23].

Table 2.1: Brief summary of main advantages and disadvantages of wind turbines

Type of WT	Advantages	Disadvantages
VAWT	– Does not require to be placed in a particular direction since it can catch wind from any direction, which provides a great flexibility in terms of installation and operation. It is a great advantage for sites with highly variable wind direction. – It works with relatively low wind speed compared to HAWT type. – It can be installed at a low height with no high tower. This means low costs of transportation, installation, construction and maintenance.	– Produce less electricity in comparison to HAWT type since it has relatively low rotational speed because it is normally installed at a low height. – Stay wires might be required for its stability and support. – Since it is installed near the ground, it has relatively high vibration because the air flow near the ground creates turbulent flow. This causes less power generation compared to HAWT type.
HAWT	– It is normally more efficient in producing power since it is installed on a high tower in high places with blades which move perpendicular to the wind. – It can catch high winds since it is installed on a high tower. – It is more stable in comparison to VAWT type	– It must be pointed to the wind to be able to work. – It has high installation, construction and maintenance cost. – It is heavy in comparison to VAWT type.

Type of WT	Advantages	Disadvantages
	with no stay wire for support since the blades are installed to the side of the turbine's centre of gravity.	

2.2.3 Grid-connected System

Integrating hybrid solar PV or CPV and wind power systems with a utility grid can help in reducing the overall cost and improving the reliability of the renewable power generation to supply its load. Surplus renewable power is provided to the grid and the grid supplies power to the loads connected to the RES when required. Grid-connected systems with solar PV and wind hybrid systems could be either connected to a common AC or DC bus. In a grid-connected system or mode, the utility grid dictates the voltage and frequency. The grid provides a stiff and robust regulation of the frequency and the microgrid buys or supplies power from/to the grid during transient with little variation in the frequency. In addition, the Automatic Generation Control provides the required balance during steady state [24]. Individual PV and/or wind power systems normally operate in MPPT mode in a grid-connected system.

Solar PV and wind systems generate electricity only during sunny and windy days. The connection of their power systems with a utility grid can improve the overall energy output. Various optimization techniques [25]–[27] have been developed and reported in the literature to achieve techno-economically optimum hybrid renewable energy systems. A suitable optimization is required to ensure having the optimal number and size of a PV and WT. The traditional sizing method for hybrid solar PV and wind systems is based on availability of long-term weather data, such as solar radiation and wind speed [28]. Since long-term weather data is not always available, artificial intelligence techniques such as fuzzy logic [2], genetic algorithms and artificial neural network are used. Furthermore, optimization performance indicators such as Net Present Value [29], Energy Index Reliability and Energy Expected Not Supplied [30] and Cost of Energy [31] have been used and reported to decide on implementation of a particular project or not.

Sun tracking systems can provide marked improvements in the performance of a hybrid system in general or PV/CPV systems in particular since they track the sun's position in the sky, which maximize solar power generation. The number and orientation of the tracker's axes defines the types of trackers whether single-axis or two-axis. Single-axis trackers have only one axis of movement and it is normally aligned with North-South. On the other hand, two-axis trackers have more freedom to move since they have two axes of movement and are aligned with North-South and East-West. Tina and Gagliano [30] found that a two-axis tracking system of a PV/WT power system has a better performance in terms of monthly power generation in comparison with single-axis tracker which reached a maximum of 7% in particular in summer. Essalaimeh et al. [32] conducted a feasibility study using payback period for a hybrid PV-wind system and pointed out that clean PV panels could produce extra power, with 31% to 35% on the maximum solar intensity, compared to panels with dust.

A grid-connected solar PV and wind hybrid system can be either connected to a common AC or DC bus. Ahmed et al. [33] presented a utility hybrid PV/wind/FC power system where the DC bus line output voltage from each converter is fixed and controlled independently. The controllers of wind and PV systems carry out MPPT while the controller of the FC is responsible for supporting the system when the load power fluctuates. The voltage converters play an important role in controlling the amount and the type of voltage whether AC or DC and the duty cycle of those converters can be used to improve the quality of power.

Intermittency in power generation, as a result of solar radiation and wind speed variations with time, is a major problem for solar and wind sources since it can cause voltage fluctuation. The impact of such a disturbance is highly dependent on load type and size along with the strength of the connected electrical grid and its size. Active power filters such as dynamic voltage regulators can be used to resolve voltage fluctuation. In addition to the voltage fluctuations as a result of the intermittency in renewable power generation, a common problem in grids is the consumption of reactive power by induction generators. The higher the generated active power by the induction generators, the greater the amount of reactive power required. The voltage at PCC fluctuates as a result of the

fluctuations in the active and reactive powers. Therefore, power compensators, with high energy density and shorter charging time, such as fixed or switched capacitor (for step changes in capacitor size) can be used to resolve reactive power issue. It is achieved by installing those compensators as close as possible to the loads to support the voltage, which in turn can reduce the power losses and minimize the impact of voltage fluctuations/dips. In addition, accurate statistical forecasting and regression analyses and algorithms that are used to forecast weather pattern, solar radiation and wind speed can reduce the impact from such quality issues [34]–[37].

Smaller RES units scattered in wide geographical areas could reduce the impact of intermittency in comparison to the installation of big units at the same site [38]. Frequency fluctuation in AC grids, due to sudden changes in active power drawn by a load, is another quality issue for hybrid solar and wind power systems. Hence, it is important to design control loops for power and frequency control to mitigate quality issues [39]. Another quality issue is the existence of harmonics which are normally caused by power electronics devices and non-linear appliances. Harmonics can be mitigated by appropriate filters and a Pulse Width Modulation (PWM) switching converter [40], [41].

2.2.4 Stand-alone System

The design of a stand-alone power system is normally more challenging in comparison to the design of a grid-connected power system due to the fact that the grid-connected system does benefit from the grid which is normally a strong system that can support the microgrid system, which is connected to it with very stable voltage and frequency most of the times. Unlike a grid-connected hybrid solar PV and wind power system, its stand-alone version does face more challenges since it needs to depend on itself without any support from other systems. A stand-alone system needs to rely on its internal backup system such as a battery or a FC to provide required power to the connected loads during a shortage of power in particular from the RES. A stand-alone microgrid should satisfy the voltage and frequency management, supply and demand balancing, and power quality [42]. Having said so, the stand-alone power system or microgrid still represents an excellent solution for remote areas that are not connected to a grid. The stand-alone system provides an economical system to

run in comparison to the extension of existing infrastructure facilities such as transmission lines, gas lines and others.

If a storage system is combined with a hybrid solar PV and WT in a stand-alone power system, the reliability of the overall system is improved [43]. A storage system is a very essential part of a stand-alone power system to ensure continuous power supply to connected loads. However, the storage cost is still high and represents major economic issue for stand-alone power systems. Integrating both PV solar and wind powers together could reduce the storage requirements, which will ultimately reduce the cost of the overall system [44]. Balancing the number of PV panels, high capacity of WT and number of batteries should be taken into accounts when design is carried out since batteries are much more expensive with a shorter lifespan compared to the life time of a PV or WT. However, for high reliability systems, too few batteries cannot meet the reliability requirements, which will incur more cost since too many PV modules or too large WTs will be required [45]. Individual PV and/or wind output power might need to be curtailed in stand-alone systems if the battery is fully charged and the available power from the PV and/or wind is higher than that required by the load. This is required to prevent the ESS from over-charging. Integration of renewable energy generations with battery storage and diesel generator back-up systems is a promising cost-effective solution for a better utilization of the RES. [46], [47].

Several optimization techniques have been reported in the literature for stand-alone hybrid renewable energy systems [48]–[52]. A combination of solar PV and wind sources improves the overall energy output. However, an energy storage system is required to have a continuous power supply and to cover any deficiency in the power generation from the renewable energy sources. The storage system can be a battery or FC with a stronger focus here on the battery. Artificial intelligence techniques such as fuzzy logic, genetic algorithms [53] and artificial neural network [23] are used for sizing stand-alone hybrid solar PV and wind systems since it is not always possible to have long-term weather data, such as solar radiation and wind speed.

Habib et al. [54] achieved a minimum capital cost with an optimal solar/wind ratio of 70% in terms of the size of a hybrid PV/wind energy system for a constant load in Dhahran area, Saudi Arabia. For a Loss of Power Supply Probability (LPSP) of 0, Diaf et al. [55] found that in order to obtain a total renewable contribution of an autonomous hybrid PV/wind system, more than 30% of the energy production was unused unless the battery capacity was very large.

Kaldellis et al. [56] developed a methodology for a stand-alone PV-battery configuration with minimum life-cycle energy requirements. They highlighted that the contribution of the battery component exceeded 27% of the system life-cycle energy requirements in all cases examined. In hybrid PV/wind energy systems for remote locations, Notton et al. [57] found that more than 40% of the total production is provided by the WT in windy sites, whereas the WT contribution represents only 20% of total production energy for non-windy regions. Smaller RES units when connected together in a system could reduce the intermittency level and provide a higher efficiency when compared to one single equivalent unit. Huang et al. [58] highlighted that when a single 400W WT of a hybrid solar PV-wind power system is replaced by 8 smaller WTs with a capacity of 50W each at three different locations in China, the power output of the overall system increased by 18.69% (at Shenyang), 31.24% (at Shanghai) and 53.79% at Guangzhou) due to the fact that small wind turbines can capture wind at a lower speed in comparison to larger ones.

Similar to grid-connected systems, the two topologies for stand-alone solar PV and wind hybrid systems are AC and DC common buses. The form of a pure AC bus system is widely used worldwide with many advantages, such as simple operation, plug and play scenario, low cost and easy extension according to the load's requirement. On the other hand, controlling AC voltage and frequency, and energy management are some of the challenges for this type of topology. Unlike the AC common bus, one of the main advantages of the DC common bus is to include a DC interface bus for coupling different generation sources, which do not have to operate at a constant frequency and in synchronism [26]. In the conventional method for controlling the complete hybrid system, power electronics converters are used for maximum energy extraction from solar and

wind energy resources. In addition, advanced controlling techniques can remove the power fluctuations caused by the variability of the renewable energy sources [59], [60].

A droop control is normally applied to generators for a frequency control and sometimes a voltage control in order to have a load sharing of parallel generators and for avoiding circulating currents or powers between different power units. It can also be used to perform an appropriate current sharing in a microgrid. With a droop control, a decentralized control for each interfacing converter is achieved. At the same time, no communication or only low bandwidth communication, such as power line communication, can be used in AC systems [61]. A line interactive Uninterruptable Power Supply (UPS) and its control system were presented by Abusara et al. [6]. A power flow is controlled using a frequency and voltage drooping technique in order to ensure seamless transfer between grid-connected and stand-alone parallel modes of operation.

Intermittent energies from solar and wind has a huge impact on loads security since those loads have no connection with a utility grid. So, any shortfall in the power generation from those sources may leave the connected loads without a power supply. Voltage fluctuation, frequency fluctuation and harmonics injection are major power quality issues. The voltage fluctuation as a result of radiation changes could make the PV system unstable, which will have an impact on the overall reliability of the hybrid stand-alone solar PV and wind system. The same thing is applicable with respects to the variations in the wind speed, which affects the performance of the wind system and ultimately the overall hybrid system. Accurate forecasting and scheduling systems can minimize the impacts. The frequency stability of a generator should be taken into account based on load requirements and whether the generator is connected to AC loads with critical power frequency requirements or not. High frequency fluctuations can be suppressed by using storage devices such as electrolytic double layer capacitor [62].

2.3 Energy Management in Stand-alone Microgrid

One of the most crucial challenges in hybrid renewable energy systems is to have a suitable power management for intermittent generation units and how to

distribute the power to the variable loads without exceeding the design limits of different equipment and units in the system. This intermittency can sometimes lead to instability or can affect the quality of the overall power system. The energy management needs to be carried out at the different levels of power systems or microgrids whether at a high level for an overall control or at a low level for each generating unit. A primary control is responsible for each generating unit whereas a supervisory control is responsible for the overall control and management of power from generations to loads. Although there are many studies and works for individual solar PV or wind power systems, there are relatively few studies in the literature for the power management of hybrid stand-alone power systems [63], [64]. Most of those studies use conventional power management methods such as Proportional (P) or Proportional-Integral (PI) controllers [23].

An energy management system is a very complicated system with multi-objective functions that needs to deal with various technical, commercial and environmental issues such as voltage/frequency/power regulation, load power sharing/distribution, market/tariff, weather fluctuations (solar radiation, wind speed), etc. A hierarchical control scheme capable of handling such issues that defines the responsibilities of each control's level has been proposed and widely used as an acceptable standard solution for a suitable and efficient microgrid management [65],[66]. Three main hierarchical control levels are normally used for controlling microgrids or hybrid renewable energy systems where bandwidths of the different control levels are normally separated by at least an order of magnitude [42],[65],[66]:

- **Primary control:** It is the local control for each power unit which performs the control of a local power, voltage and control in accordance with instructions from the higher level controllers. It can be achieved by a droop control to share loads between separate converters. A typical response is within 1 to 10ms.
- **Secondary control:** It is used to remove any steady-state errors caused by the primary control/droop control. So, it is on top of the primary control dealing with voltage/frequency restoration, voltage unbalance and others. A typical response can be 100ms to 1s.

- **Tertiary control:** It is the highest level of control providing supervisory and global control function that decides the management of the overall system. A typical response can vary between seconds to hours.

The supervisory control / energy management system architectures in microgrids or hybrid renewable energy systems can be either a centralized, decentralized/distributed or even a hybrid centralized and decentralized/distributed system. Table 2.2 provides a brief summary of the advantages and disadvantages of each type [65]–[67]:

Table 2.2: Summary of supervisory control / energy management system architectures in microgrid or hybrid renewable energy system

Controller architectures	Advantages	Disadvantages	Remarks
Centralized controller	- Best for multi-objective power management hybrid system, which allows a global optimization based on available information	- High computational cost and complexity - High communication cost - Less flexibility/ expandability - Single point failure with one master controller	- More suitable for small scale microgrids. - Master control works as a supervisory controller and decides on the overall power management and optimization based on measured signals by slave/ local controllers and pre-determined objectives and constrains.

Controller architectures	Advantages	Disadvantages	Remarks
Decentralized (distributed) controller	- Low computational cost and complexity - Low communication cost - More flexibility/ expandability - Less single-point failure issue - Easy realization of plug and play functionality - Best solved with artificial intelligence algorithms	- Requires good synchronization between different units. - Complexity in communication is within local controllers	- More suitable for large scale microgrids or wide spread power systems. - Local controller receives measurements' signals from its generation unit and then that controller communicates with other local controller for other generation unit for global optimization.
Hybrid centralized and decentralized/ distributed controller	- No single-point failure issue - Optimization is divided between centralized controller and decentralized controller with less burden on each type.	- Could be a bit expensive	- Suitable for all types of microgrids/ power systems. - Central controller is applied for optimization and power management within each group of renewable energy sources. Decentralized controller is applied between

Controller architectures	Advantages	Disadvantages	Remarks
			different groups within larger power systems for overall power management and global optimization.

As per the literature, in order to have a suitable continuous energy management at higher levels between different generation units and connected loads, such management can be achieved by a centralized control system with communication between the different units [68]–[70]. In this case, all generation and load units or even nodes must have suitable power measurement and communication modules to provide required data to the power management system in order to give the right decision for the power balance between generations and loads. This is definitely not practical in most conventional power systems especially with the increase of the power system size [71]. Failure in communication can cause unbalance between the generation units and loads. The communication does definitely add extra cost and complexity for the overall power system in particular when the system becomes large with many DG units and loads scattered in wide geographical areas making the communication system less attractive and/or less reliable. Furthermore, the communication link which is used for control increases the control complexity and affects the expandability of the power system [72]. The design of an effective coordination strategy becomes a challenging task if communication between different units is not used simply because there will be neither a central energy management system nor a direct interaction between the different units. On the other hand, decentralized control strategies for managing PV and battery units in droop controlled microgrids are not thoroughly explored in the literature [24].

Traditionally, the classical energy management system for a stand-alone system or microgrid relies on batteries or ESS in general to absorb surplus power from RES once tracking their maximum power points (MPPs) independently. In other

words, the RES work as current sources with MPPT while the ESS is used as a voltage source to control the voltage and frequency. However, if excess energy is not used, it can cause over-charging to batteries and ultimately can damage the batteries. A review about excess energy utilization is carried out in [73]. The review shows that considerable amounts of excess energy can be left unutilized as a result of running hybrid renewable energy systems. Many studies as per that review suggest the usage of dumped loads for excess energy, while others propose utilizing this excess energy by other means. For grid-connected systems, it is straight forward that any excess energy can be directly injected to the grid. However, for standalone systems, one costly recommendation is to use excess energy for producing hydrogen by electrolyzers, which in turn can be stored in hydrogen tanks in order to be used by FCs. This can work as an energy storage system capable of providing power in case of power shortage from RES. Another possible solution is to design an energy management system that uses the surplus energy to provide power supply to other loads, such as water heating with storage tanks, surrounding heating/air-conditioning, and pumping water [74] or use dump load for protecting battery from over-charging where the output powers from the RES are normally equal to the maximum power available [75].

A different approach was taken in [71] where a power management strategy was proposed to operate a PV/battery hybrid unit, in an islanded microgrid, as a voltage source that employs an adaptive droop control to share loads with other generation sources while charging the battery. At the same time, the MPPT can still be tracked and supplied by the PV/battery unit provided that there is sufficient load. In this case, there is no external communication between the PV and battery since they represent a single hybrid unit.

In an islanded AC microgrid with a wind turbine, battery bank and load in [76], the terminal voltage of the battery bank is maintained and controlled within the maximum allowable limit. The control of the terminal voltage represents an indirect control of the SOC. It is achieved by utilizing the frequency bus-signalling technique in order to limit the generated power whenever needed. A frequency bus-signalling technique of ESS is also used in [8] to provide a power management for a stand-alone AC microgrid with a PV, ESS and load. This is

achieved by mapping AC bus frequency with estimated SOC. A primary frequency signalling is also used in [77] along with a droop control method in order to change modes of operations of a stand-alone AC microgrid with a RES, ESS and loads in different operation scenarios (i.e. decides whether the RES or ESS is working in power control mode or voltage control mode).

While many authors in the literature have implemented energy management systems for hybrid renewable energy systems with single battery, the frequency-based energy-management strategy in [78] has been developed for multiple batteries without communication cables between distributed inverters. The power is transferred from the fully charged or discharged battery to the one with less charging or discharging power without the limitation of RES power. A PV generation is reduced when the frequency is high to provide protection for over-charging or high charging current. On the contrary, noncritical loads are regulated/disconnected or the system stops when the frequency is low. This provides protection against over-discharging or high discharging current.

The aforementioned references in particular references for power management strategies with frequency bus-signalling technique use conventional controllers such as Proportional-Integral (PI) controller for power management. No intelligent or artificial methods have been used with frequency bus-signalling technique. Furthermore, only RES units are used as DG units without the use of other conventional DG units such as micro gas turbines or diesel generators.

To the best knowledge of the author, the supervisory control or power management for conventional energy sources along with RES including controller based on Fuzzy Logic is not yet fully resolved and research into obtaining optimal operational modes continues to increase. Although controller is an essential part of any hybrid system, it did not have enough attention in the areas of study as per the literature. Novel controllers for effective power management, battery SOC management and dump power control represent only 6% of the total studies conducted in the field while 4% studies only considered modelling of batteries for analysing its statues [79]. Therefore, more research work is required on the supervisory control/energy management of hybrid RES. Non-conventional type of control such as Fuzzy Logic Control

could be an excellent candidate for this and it is discussed in terms of brief literature review as follows in section 2.3.1.

2.3.1 Fuzzy Logic Control

In the last couple of years, the interest on designing rule-based microgrid' supervisory controllers increased to provide a suitable power management of different power generation units, including RES. In line with this direction, researchers worldwide adopted FLC for energy management in both stand-alone and grid-connected hybrid renewable energy systems [80].

A FLC provides rules for power management based on human knowledge and experience that can deal with unpredictable variables or uncertainties such as intermittency behaviour of RES even when they are connected to each other in a hybrid power system. Unlike other intelligent or artificial controllers, there is no need for training and availability of historical data in order to use FLC. This makes the FLC a well-adapted tool for energy management of RES and other relevant control tasks for RES [74], [80], [81]. FLC has been used for both AC and DC microgrids (grid-connected and stand-alone mode of operations) in the literature for several purposes due to its good performance and simplicity. FLC has been used for Maximum Power Point Tracking (MPPT) of solar PV [82]–[84], frequency regulation [85], [86], controlling batteries' output charger current [87] and improvement in wind power prediction accuracy [88]. A FLC has been also used in [89] to provide powers' split between solar PV and BESS based on operator's experience through a pre-defined rules in order to supply DC load. The PV power, SOC of the battery and power required by the load are the inputs to the FLC. The output of the FLC decides the operation of the different switches to have one of the possible connections; PV-battery, battery-load and PV-load.

A FLC was used to manage the SOC of a Li-ion battery in a DC microgrid with a solar PV, wind and fuel cell system [4]. There were two inputs to the FLC: power difference between generation and load, and difference between measured SOC and required SOC. The output of the FLC was the charging/discharging current demand for the battery.

In a grid-connected mode, a FLC was proposed in [90] to minimize energy storage range of the battery and power variation range exchanged between the grid and the microgrid. A smart FLC was also proposed in [91] in order to minimize the number of times required to switch between stand-alone and grid-connected modes. This in turn maximized the usage of renewable energy and reduced the dependency on the main grid. The SOC of a BESS in a hybrid microgrid was controlled by a FLC in [92] to improve the performance of the hybrid generation system with a smaller energy capacity of the BESS. A decentralized fuzzy logic gain-scheduling controller was proposed in [93] to balance the stored energy between different battery systems in a DC microgrid by adjusting the droop coefficients of the primary controllers.

In view of the above, integrating artificial intelligence techniques such as FLC to work as supervisory controller with a conventional controller such as droop control to work as primary controller, will add an extra great benefit for power managements.

2.4 Summary

Many of the issues and challenges for hybrid solar PV and wind systems are the same for both grid-connected and stand-alone systems. Table 2.3 summarizes the main challenges for grid-connected hybrid solar PV and wind systems with possible solutions or mitigations. Similarly, the main challenges and solutions/mitigations for stand-alone systems are summarized in Table 2.4. The main challenge for grid-connected systems as well as the stand-alone systems is the intermittent nature of solar PV and wind sources. By integrating the two resources into an optimum combination, the impact of the variable nature of solar and wind resources can be partially resolved and the overall system becomes more reliable and economical to run. The issue of intermittency in the stand-alone generation becomes more serious and continuous power supply will not be guaranteed without sufficient energy storage system.

Voltage and frequency fluctuation, and harmonics injection are major power quality issues for both grid-connected and stand-alone systems with greater impact in case of a weak grid. An overview of the research related to optimal

sizing design, power electronics topologies and control for grid-connected and stand-alone hybrid solar PV and wind systems has been provided. Solar PV and wind hybrid system can be connected in a common DC or AC bus whether they are working in a grid-connected mode or a stand-alone mode.

To the best knowledge of the author, the supervisory control and power management for conventional energy sources along with RES including controller based on Fuzzy Logic are not yet fully resolved and research into obtaining optimal operational modes continues to increase. Therefore, more research work is required on the supervisory control/energy management of hybrid RES along with non-conventional types of control. Hence, the aim of the work in this thesis is to fill the gap and provide an appropriate supervisory controller based on Fuzzy Logic that provides power management of an islanded microgrid which consists of a PV, battery, load and auxiliary unit (a micro gas turbine in this case, but it can be a FC or another battery). The supervisory controller will be implemented wirelessly using the bus frequency for the AC microgrids without any external communications and without any dump load. A local droop controller will be designed to react to the change in bus frequency to curtail or supplement power.

Table 2.3: Main challenges and possible solutions for grid-connected systems

No.	Challenges	Solutions	References
1	Voltage fluctuation due to variations in wind speed and irregular solar radiation	Active power filters such as dynamic voltage regulators Power compensators such as fixed/switched capacitor or static compensator.	[34], [40] [34], [41]
2	Frequency fluctuation for sudden changes in active power by loads	Design control loops for power and frequency control to mitigate quality issues	[39]
3	Harmonics by power electronics devices and non-linear	PWM switching converter and appropriate filters.	[40], [41]

No.	Challenges	Solutions	References
	appliances.		
4	Intermittent energy's impacts on network security	Accurate statistical forecasting and scheduling systems. Regression analysis approaches and algorithms for forecasting weather pattern, solar radiation and wind speed. Increase or decrease dispatchable generation by system operator to deal with any deficit/surplus in renewable power generation. Advanced fast response control facilities such as Automatic Generation Control and Flexible AC Transmission System.	[34]–[37]

Table 2.4: Main challenges and possible solutions for stand-alone systems

No.	Challenges	Solutions	References
1	High storage cost	Combining both PV solar and wind powers will minimize the storage requirements and ultimately the overall cost of the system.	[25], [44]
2	Less usable energy during the year.	Integration of renewable energy generation with battery storage and diesel generator back-up systems.	[46]–[48]
3	Intermittent energy/ power quality	Integration of renewable energy generation with battery storage or fuel cell and in some cases with diesel generator back-up systems.	[43], [46]–[48] & [59], [62]

CHAPTER 3: CONTROL OF A HYBRID POWER SYSTEM WITH FUZZY LOGIC SUPERVISORY CONTROLLER

3.1 Introduction

This chapter examined the power management of a stand-alone AC microgrid that consists of RES, ESS, auxiliary units and loads. Power management is performed by a supervisory controller which interacts with the local controllers of the generating units. A Fuzzy Logic Controller (FLC) is proposed and implemented within the ESS unit. It interacts with the local droop controllers by changing the bus frequency. In an AC stand-alone microgrid, the battery unit forms the AC bus and has to supply or absorb the difference between varying RES and load powers. However, the power rating and energy capacity of the battery are limited and therefore, power management of the microgrid is required to ensure both battery power and energy do not exceed their maximum limits.

The chapter starts by giving an overview of a typical inverter-based AC microgrid and the method of operation in stand-alone and grid-connected modes. It then shows different control strategies for the DC-link voltage in a two-stage converter. The chapter also provides details about the droop control strategies for ESS and RES units by introducing the basic concept of droop control and then shows different strategies for the relevant DC/AC inverters. The concept of a floating auxiliary unit (micro gas turbine (μGT)) on the common bus is introduced and its droop control strategy is provided. The main merits of the proposed controller are simplicity and easiness of implementation without the need for any communication links between the parallel units and any dump load. The proposed controller uses the AC bus frequency as a communication signal to curtail RES power or increase/decrease the auxiliary unit power. The design of the FLC for energy management of the microgrid is discussed in detail. Matlab/Simulink simulations show that the proposed controller can maintain the SOC and the charging/discharging power of the battery within their design limits irrespective of changes in generation from RES or changes in the load.

3.2 System Overview

A typical AC microgrid structure that can work in both stand-alone and grid-connected modes is shown in Figure 3.1. It consists of RES, ESS, auxiliary unit and loads that are all connected to a common AC bus which can be connected to or isolated from the grid by a Static Transfer Switch (STS) controlled by a supervisory control unit. The auxiliary unit is shown as a micro gas turbine, but it could be a fuel cell, diesel generator or even another battery. PV and BESS units are interfaced by two-stage DC/DC and DC/AC power electronic converters. On the other hand, the wind turbine (WT) and micro gas turbine units are interfaced by two-stage AC/DC and DC/AC power electronic converters. The AC output voltages from individual units are connected to a common AC bus to provide the power to the utility grid or local loads. The output voltage from each source is controlled independently. However, low speed communication between the STS and the different Distributed Generator (DG) units is still required to detect the status of the STS. In order to isolate (or re-connect) the microgrid from (or to) the utility grid seamlessly, STS is used at the Point of Common Coupling (PCC), which could be monitored and controlled by the supervisory controller of the microgrid. In order to ensure that the local loads are always supplied with power, they are connected to the microgrid side of the STS [6].

In grid-connected mode of operation, the utility grid dictates the bus voltage and frequency. Hence, all units act as current sources controlling the amount of power injected into the grid. The RES, among other DG units, act as current sources and inject power directly into the AC bus according to their Maximum Power Point Tracking (MPPT) algorithms. Power can be imported when the electricity import tariff is low to be stored and used later by the load during the high tariff period. Power can also be exported to the utility grid when there is surplus power from PV. The battery is interfaced by a bidirectional converter and can be charged or discharged depending on its SOC. However, in stand-alone mode, the bus needs to be maintained by the microgrid itself. This thesis is concerned with a stand-alone microgrid.

The paralleled units can all work as voltage sources and by using droop control will share the power equitably [94], [95]. In this case, the amount of power drawn by each unit depends on the local load and therefore, the power generated from RES is not maximised. It is desirable to maximise the power generated by the RES using MPPT. Thus the RES need to be controlled as current sources with the output power proportional to the available renewable sources at the time of using MPPT. At any moment in time, generated power needs to equal load power to achieve the power flow balance and maintain the AC bus stability. Therefore, a balancing mechanism is required. ESS is a natural choice for this as it can supply and absorb/store power (i.e. to balance the difference between the power generated by RES and that consumed by the load). In order to achieve the above, the ESS has to be controlled as a voltage source in parallel with RES that operates as a current source as shown in Figure 3.2. The load is represented as a current source also. So, in a stand-alone AC microgrid, the RES units act as current sources feeding the loads directly while the ESS acts as a voltage source controlling the AC bus voltage and frequency [7].

The parallel inverters should control the AC bus voltage of the stand-alone microgrid. In other words, in a stand-alone AC microgrid with ESS and RES, the ESS is used as a grid forming unit regulating the AC bus, while the RES is used as a grid feeding unit injecting the power to the power system [8]. The ESS has limited energy capacity and therefore if it is full, the RES power must be curtailed and if it is exhausted, the load must be shed. An additional problem is that the ESS has limited power capability and charging and discharging power levels must not exceed the maximum limits. Shedding the load is not a desirable solution and a better alternative is to use a supplementary unit that supplies power only when needed. In view of the above, a supervisory controller is required, which needs to monitor the SOC and power of the battery and to instruct the RES and auxiliary units. Communication-based control can be used, but system frequency is proposed in this thesis as a communication mean.

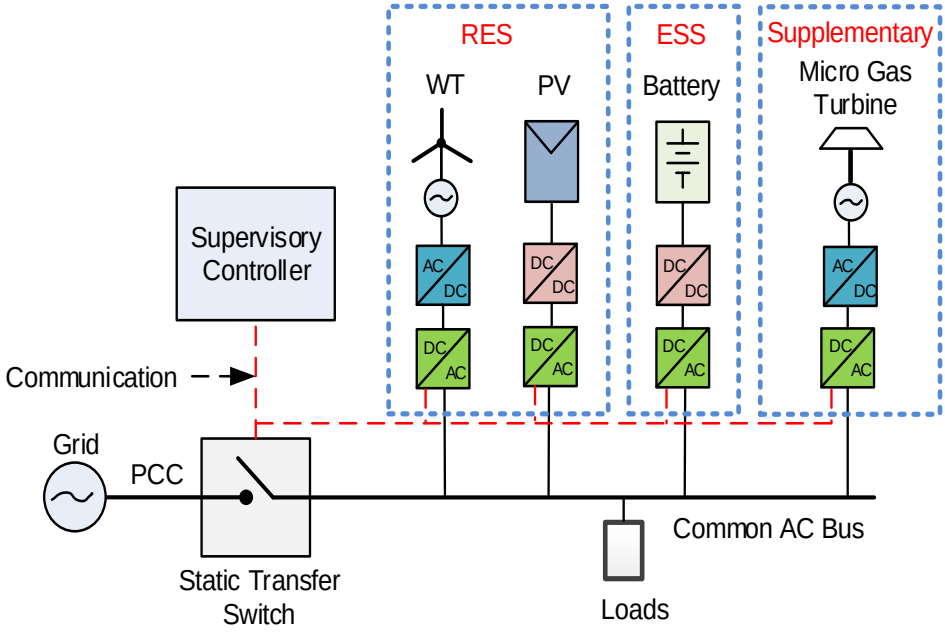

Figure 3.1: Typical AC microgrid structure

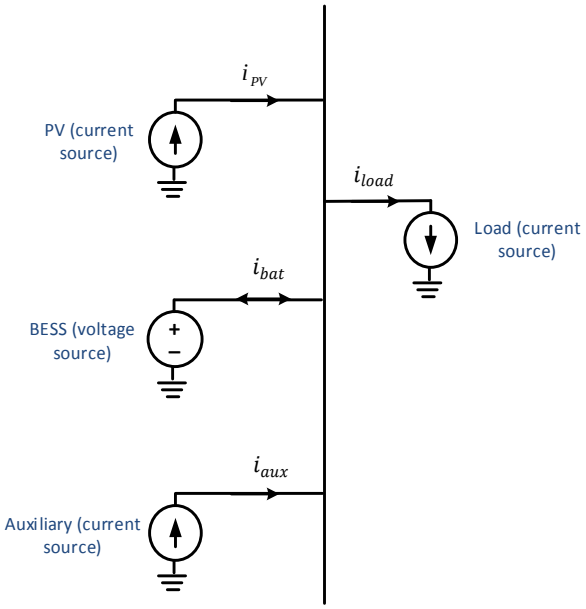

Figure 3.2: ESS as a voltage source and RES, auxiliary and load as current sources

3.3 Control Strategies

There are two options for controlling the two-stage converters for each generation unit in Figure 3.1 as follows:

1. Stage 1 converter (DC/DC for PV and ESS and AC/DC for wind and μGT) regulates power flow between the energy source and the DC-link

capacitor (acting as current source), while stage 2 converter (DC/AC) regulates the DC-link voltage, i.e., acting as a voltage source across the capacitor. This option is shown in Figure 3.3(a) assuming DC energy source. The DC/AC converter has three control loops: an outer DC-link voltage regulator loop that sets the power demand to the middle power control loop which in turn sets the voltage demand to the inner AC voltage control loop.

2. Stage 1 converter (DC/DC for PV and ESS and AC/DC for wind and μGT) acts as a voltage source that regulates the DC-link voltage. On the other hand, the DC/AC converter acts as a current source that regulates the power flow from/to the grid. The scheme of this option is shown in Figure 3.3(b) assuming DC energy source. The DC/AC converter has two control loops: an outer power loop, based on droop control that sets the voltage demand to an inner voltage control loop.

Selecting from the two options above depends entirely on how the specific unit is required to operate. For the PV-based RES unit, the PV output voltage should be controlled in order to achieve MPPT and this can be achieved by the unidirectional DC/DC converter which senses the PV output voltage directly. On the other hand, the DC/AC inverter regulates the DC-link voltage in order to regulate the power flow from/to the AC bus. Therefore, option 1 is selected for the PV-based RES unit. The battery unit should work as the grid former that maintains and controls the AC bus frequency and voltage of the stand-alone microgrid. In addition, it should be capable of switching seamlessly between a stand-alone mode (AC bus frequency and voltage regulations) and a grid-connected mode (power flow regulation) in the case that the microgrid is required to connect to a utility grid. Hence, option 2 is selected for the battery unit. Therefore, the bidirectional DC/DC converter regulates the DC-link voltage while the DC/AC converter regulates the AC bus.

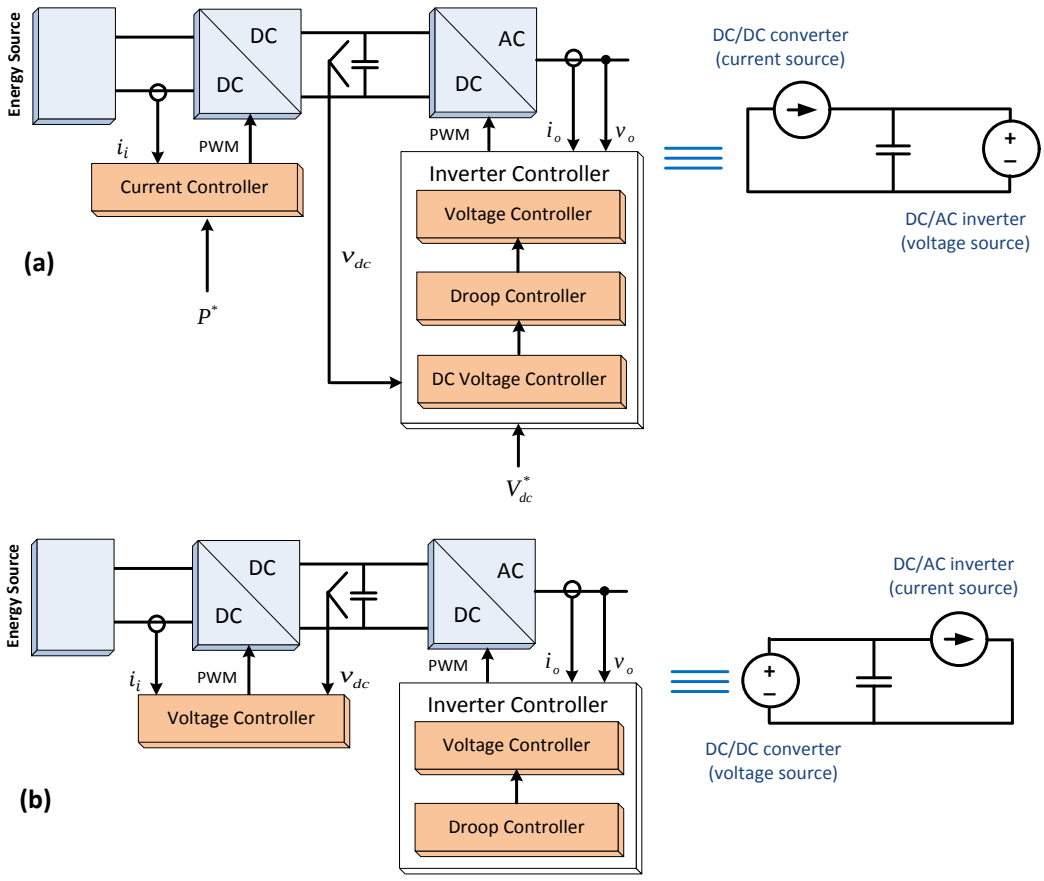

Figure 3.3: Energy sources control scheme as (a) current-controlled source (b) voltage-controlled source

The stand-alone AC microgrid control topology including the proposed FLC as the supervisory controller is shown in Figure 3.4. The microgrid consists of a PV, BESS and auxiliary (micro gas turbine) units connected to a common AC bus and supplies a local load. For the PV unit, the DC/DC converter controls the PV output voltage to achieve MPPT while the DC/AC inverter regulates the DC-link voltage. The BESS unit forms the AC bus by controlling the voltage and frequency. Hence, for the BESS, the DC/DC converter regulates the DC-link voltage and the DC/AC inverter maintains and controls the AC bus frequency and voltage of the microgrid. The BESS absorbs surplus power from the PV unit if it exceeds the load demand and it supplies power when the PV power is less than that absorbed by the load.

The auxiliary supplementary unit (micro gas turbine in this case) in Figure 3.4 is interfaced by a unidirectional AC/DC converter (equivalent to a passive rectifier along with a DC/DC converter) and a DC/AC inverter. The unidirectional DC/DC

converter regulates the DC-link voltage while the DC/AC inverter controls the output power according to the AC bus frequency altered by the BESS based on FLC command [96]. The main role of the auxiliary supplementary unit is to support the battery unit when the SOC of the battery is low and/or the PV power cannot meet the load requirement.

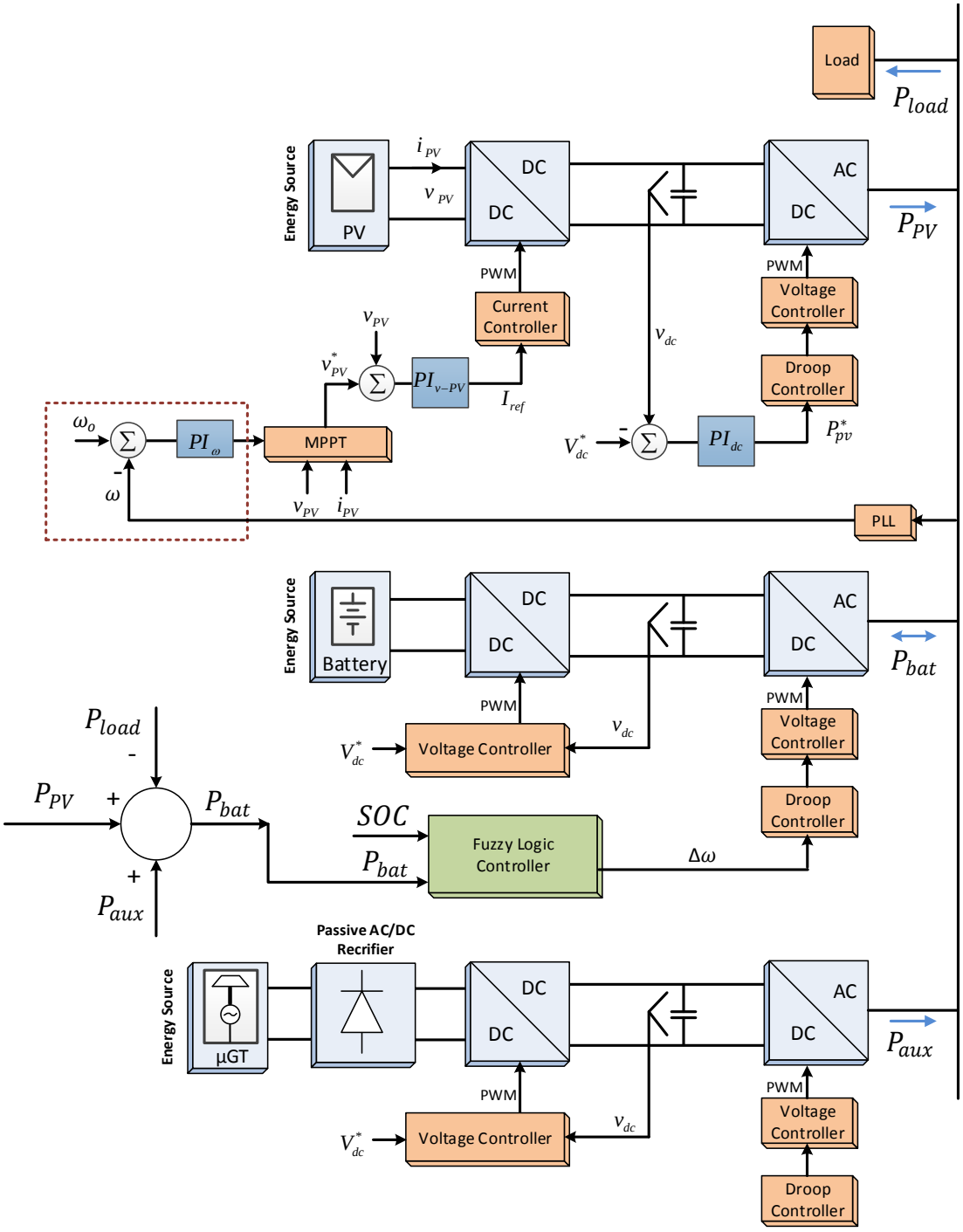

Figure 3.4: The stand-alone AC microgrid control topology with proposed FLC

The power of the battery P_{bat} is the power difference between the generation ($P_{PV} + P_{aux}$) and the load P_{load} as shown in Figure 3.4. If the PV power is higher than the load, the battery absorbs the excess power. However, if the SOC of the battery is very high, the PV power should be curtailed to prevent over-charging the battery. To achieve this, a PV power shifter is implemented. The MPPT controller measures the bus frequency using a Phase Looked Loop (PLL). Normally, the MPPT controller regulates the voltage across the PV to supply the maximum power. When a curtailment is needed, the power shifter shifts the PV voltage to deviate it from the maximum power point to a lower point (see Figure 3.8 if required). The changes in the battery SOC and power are the two inputs of the FLC while the change in the bus frequency is the output which serves as a communication means to the PV and auxiliary units. If the frequency is increased above the nominal value, the PV unit curtails its power. On the other hand, if the frequency is decreased, the auxiliary unit generates power. The power curtailment and supplement are proportional to the frequency variations. In order to avoid any need for communication links between the units, the DC/AC inverters of all the units adopt the well-documented wireless droop technique. The droop control of the auxiliary unit is implemented such that the unit is floating on the bus and thus it generates power only when required if the bus frequency is decreased below its nominal value.

The FLC is proposed to protect the battery and hence to prevent its SOC and charging/discharging power from exceeding their maximum limits regardless of the variations in the load and RES intermittent power. Based on the decision from the FLC, the power management system acts as per the following strategy:

1- The PV power system is the primary source of the power to the load.
2- The BESS is the secondary power source to the load. If the power generated by the PV unit is more than the load, the battery unit absorbs the surplus power (charging mode). Similarly, if the PV power is less than the load, the battery supplies the shortage (discharging mode). The battery power is assumed to be negative in the charging mode and positive in the discharging mode.

3- The micro gas turbine works only during low battery SOC and/or low PV generation scenarios.

Details of the droop control strategies and FLC will be discussed in the following sections below.

3.3.1 Droop Control Strategies for ESS and RES

Two methods of control can be implemented in order to enable a power sharing between the different units in a microgrid; communication-based control (such as master-slave) and non-communication-based control (wireless based on droop control). In this thesis, wireless droop control is used as a primary controller for the generating units in order to stay in parallel and avoid circulating currents between them [65], [94]. Parallel structure in a wireless-based control system depends on the capability of the inverter units to regulate the output voltage and frequency while sharing the active and reactive power demands between the units. To illustrate the droop control principle, Figure 3.5 is used to show two parallel inverters supplying a common load. Each inverter is connected to the load bus through an inductive output impedance. The primary controller mimics the behaviour of the synchronous generator in terms of decreasing the frequency when the active power is increased and vice versa. The exported active and reactive powers for each inverter, assuming pure inductive output load impedance, are given by

$$P = \frac{V_L V sin(\theta)}{X} \tag{3.1}$$

$$Q = \frac{V(V - V_L)\cos(\theta)}{X} \tag{3.2}$$

If θ becomes very small, these two equations can be approximated as given by (3.3) and (3.4), respectively [97]:

$$P \approx \frac{V_L V \theta}{X} \tag{3.3}$$

$$Q \approx \frac{V(V - V_L)}{X} \tag{3.4}$$

where P and Q are the exported active and reactive powers, respectively. X is the load impedance. The active power depends on the phase difference (θ) between each inverter output voltage (V) and the load voltage (V_L). Hence, the active power is controlled by the phase angle. On the other hand, the reactive power depends on the difference in magnitudes between the inverter output voltage and load voltage $(V - V_L)$. Therefore, the reactive power is controlled by the voltage difference. Basic P- ω and Q- V droop curves are as shown in Figure 3.6(a) and Figure 3.6(b), respectively. The higher the generated active power, the greater the drop in frequency from its nominal value. Similarly, the higher the supplied reactive power, the greater the voltage drop.

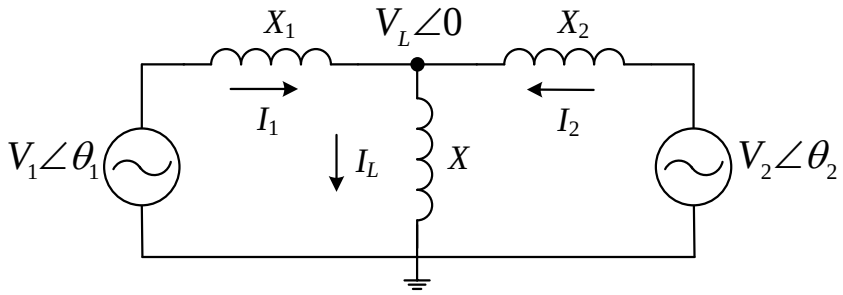

Figure 3.5: Equivalent circuit of two parallel inverters connected to a common load

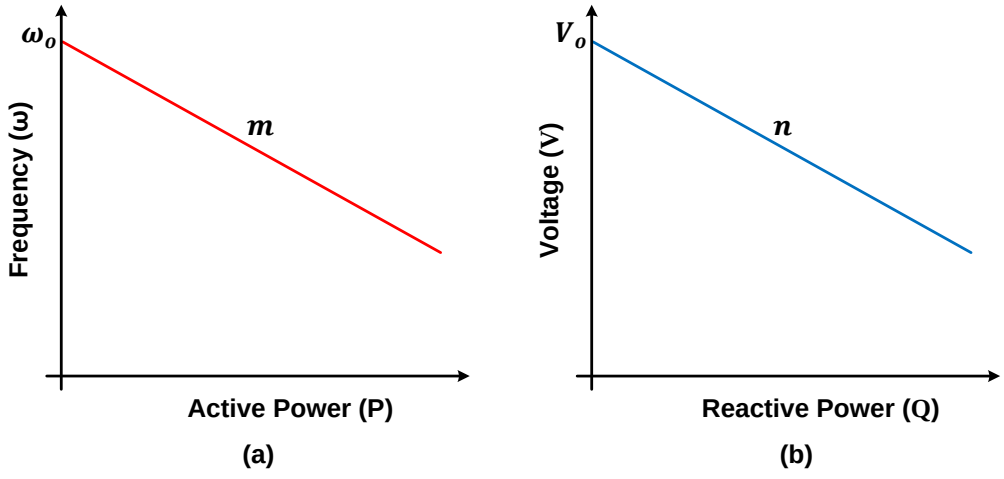

Figure 3.6: Basic P- ω and Q- V droop curves

In traditional droop control, the output frequency ω and voltage amplitude V of any DC/AC inverter are given by (3.5) and (3.6), respectively.

$$\omega = \omega_o - m(P - P^*) \tag{3.5}$$

$$V = V_o - n(Q - Q^*) \tag{3.6}$$

where ω_o, V_o, m, and n are the nominal frequency, nominal voltage, frequency drooping coefficient, and voltage drooping coefficient, respectively. P and Q are the measured active and reactive powers. $P^*$and Q^* are the active and reactive power demands or set-points, respectively. The coefficient m and the set-point P^* depend on whether the microgrid is in grid-connected mode or in stand-alone mode.

The three DC/AC inverters in Figure 3.4 have the same droop equations for voltage/reactive power [98] as in (3.6). However, for active power, each unit has a different droop coefficient and power demand depending on its role. The battery unit is required to be a voltage source that forms the AC bus in the stand-alone microgrid. The AC bus is dictated by the BESS unit and has to control the output voltage and frequency. The power delivered/absorbed by the battery depends on the PV power and load. To achieve this functionality, the droop coefficient of the battery unit m needs to be set to zero. In addition, in order to be able to curtail the PV power or to supplement power from the auxiliary unit, the bus frequency is varied by $\Delta\omega$ which is the output from the FLC as shown in Figure 3.4. Thus, the output frequency of the battery unit is given by

$$\omega = \omega_o + \Delta\omega \tag{3.7}$$

The DC/AC inverter of the PV unit controls the DC-link voltage by injecting more or less power into the AC bus. The droop control of the PV unit is given by

$$\omega = \omega_o - m_{pv}(P - P_{pv}^*) \tag{3.8}$$

where the power demand P_{pv}^{*} is the output of the proportional-integral (PI) controller that regulates the DC-link voltage (see Figure 3.4). In the steady state, the power demand P_{pv}^{*} equals the power generated by the DC/DC converter according to its MPPT algorithm. The PV unit acts as a current or power source injecting maximum power available from PV to the AC bus.

For the PV unit in the proposed stand-alone microgrid, the P_{pv}^{*} is given by

$$P_{pv}^{*} = (k_{p-dc} + \frac{k_{i-dc}}{s})(V_{dc} - V_{dc}^{*}) \tag{3.9}$$

where V_{dc} and V_{dc}^{*} are the DC-link voltage and its set-point value, k_{p-dc} and k_{i-dc} are the proportional and integral controller gains of the PI controller that regulates the DC-link voltage in Figure 3.4, respectively, and '*s* ' is the Laplace operator.

It is important to note that even if this stand-alone microgrid is connected to a utility grid, m_{pv} and P_{pv}^{*} are still the same.

3.3.2 Variable AC Bus Frequency and Proposed Floating μGT

The proposed controller is to use the AC bus frequency as a communication signal to curtail RES power or increase/decrease the auxiliary unit (micro gas turbine (μGT)) power. The frequency is kept at its nominal value during normal operation. If the SOC or charging power is higher than their maximum limits, the bus frequency is increased so the local controller of the RES curtails the power. Conversely, the frequency is lowered to instruct the μGT to supplement more power. The greater the frequency deviation from its nominal value, the higher the power supplied by the μGT. The auxiliary unit provides power only when needed according to the bus frequency and its droop control is calculated by

$$\omega = \omega_o - m_{aux}(P - P_{aux}^{*}) \tag{3.10}$$

The power set-point P_{aux}^{*} is set to zero in this stand-alone microgrid in order to make the auxiliary unit floating on the AC bus to supplement power automatically in response to variation in the bus frequency. However, if at all, a

decision is made to connect this microgrid to the utility grid, P^*_{aux} is set to the required power level. Whether the mode of operation is grid-connected mode or stand-alone mode, the active power/frequency droop coefficient for the auxiliary unit m_{aux} does not change.

Table 3.1 below summarises m and P^* for the three units for the proposed stand-alone microgrid. It provides a summary for grid-connected types as well to ensure a full understanding of the two modes of operation.

Table 3.1: Droop control and power set-points

	m		P^*	
	Grid-connected	Stand-alone	Grid-connected	Stand-alone
PV	m_{pv}	m_{pv}	P^*_{pv} (See (3.9))	P^*_{pv} (See (3.9))
ESS	m_{ESS}	0	P^*_{ESS}	0
Auxiliary	m_{aux}	m_{aux}	P^*_{aux}	0

The droop strategy is illustrated in Figure 3.7 which shows the frequency/power droop control for the three units based on (3.7), (3.8) and (3.10). This droop strategy means that the μGT unit is floating on the bus and it will automatically generate power only if the frequency is reduced below its nominal value. The zero droop coefficient of the battery unit makes it the grid former and hence it dictates the AC bus frequency. The bus frequency can be shifted up to curtail PV power or shifted down to produce power from the auxiliary unit. For the PV unit, the output power P equals the demanded power P^*_{pv} when the bus frequency ω equals the nominal frequency ω_o. If the bus frequency is shifted down, the DC/AC inverter of the PV unit delivers more power than that produced by the DC/DC converter which causes the DC-link voltage to drop. This drop causes the PI controller of the DC-link voltage to reduce the power demand P^*_{pv} so that the DC/AC inverter delivers the same power produced by the DC/DC converter. However, if the bus frequency is shifted up, this acts as a message to the MPPT controller that the PV power needs to be curtailed. The MPPT controller measures the bus frequency using a Phase Looked Loop (PLL) (see Figure 3.4) and it shifts the maximum power point to a lower value

by increasing the PV output voltage as illustrated in Figure 3.8. The higher the rise in the frequency, the greater the curtailment in the PV power. Shifting the voltage from the voltage at the maximum power to a higher value (to the right of the MPP towards the open circuit voltage V_{oc}) mimics the insertion of a low load while shifting it to a lower value (to the left of the MPP) requires the converter to absorb more current that is not preferable. In addition, the right of the MPP represents a higher efficiency of the PV in comparison to the left of the MPP due to high voltage values which means less losses. Furthermore, the gradient of the P-V curve for the power change to the voltage change ($\frac{\Delta P}{\Delta v}$) in the right of the MPP is relatively bigger in comparison to the left of the MPP, which makes the PV system more robust with a better voltage stability.

When the bus frequency is equal to or higher than the nominal frequency ω_o, the auxiliary unit produces no power according to (3.10) and as illustrated in Figure 3.7. If the bus frequency is shifted down, however, the auxiliary unit starts producing power and the higher the drop in the frequency, the greater the power produced. This way, power curtailment and supplement are controlled wirelessly through the bus frequency without any extra communication. The limit for the frequency deviation is set as ± 1% of the nominal value (50Hz). This provides a variation in the frequency between 49.5Hz and 50.5Hz. The range of the frequency variation can be changed based on requirement, but the principles of the power management and control will remain the same.

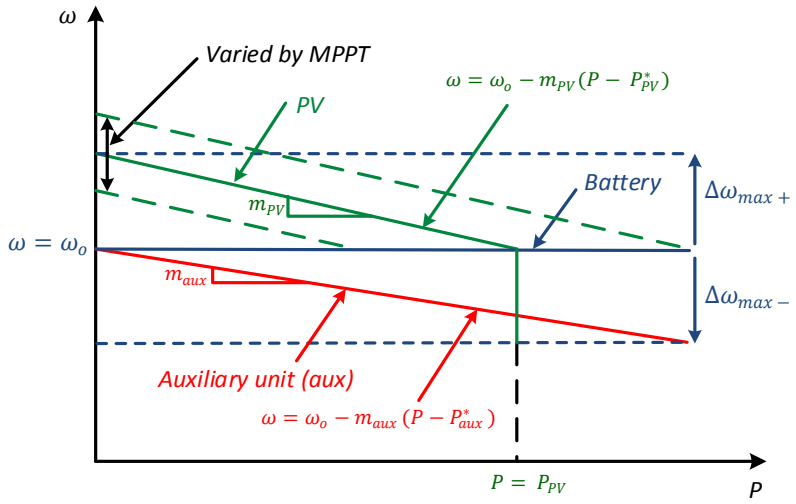

Figure 3.7: Power – frequency droop control curves

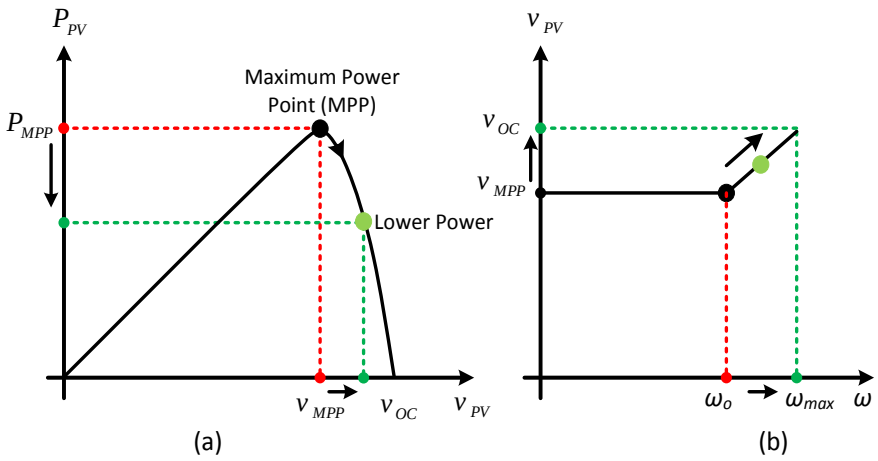

Figure 3.8: PV MPP shifting operation: (a) PV power versus output voltage (b) output voltage versus frequency

3.4 Proposed Fuzzy Logic Controller

3.4.1 Introduction to Fuzzy Logic

The bulk of information that is used on a daily basis is fuzzy at least from the perspective of human beings. However, that is not the case with respect to most of the actions or decisions taken to deal with this information which are crisp in nature. The crisp value is either true (1) or false (0). In 1965, the idea of fuzzy logic was introduced for the first time by Lotfi Zadeh of the University of California (Department of Electrical Engineering and Electronics Research Laboratory), Berkeley, California, USA [99]. He observed that conventional controllers lack the capability of manipulating subjective or vague data not like human thinking or reasoning. In 1973, he introduced the concept of "linguistic variables" which is equal to a variable defined as a fuzzy set [100]. The first application of the fuzzy logic in the industry was introduced in 1975 when a cement kiln built and came into operation in Denmark in an attempt to control a steam engine and boiler combination [101].

Unlike traditional binary logic (where variables can be either true (1) or false (0)), fuzzy logic variables may have a value between 0 and 1. So, contrary to conventional binary logic, fuzzy logic can give different solutions which are not necessarily true or false, black or white. It can be partially true or partially false. This is where the word “fuzzy” comes from. In addition, fuzzy logic can

complement conventional controllers and simplify their implementation rather than replacing them. A controller that is based on fuzzy logic is a form of an estimate or approximation that is designed with rules based on human knowledge and experience to give different possible solutions to a problem with different variables. Those solutions are then combined together to give a single crisp value as a final solution to the problem. Fuzzy logic is an intelligent technique that can be used to solve or control complicated problems or systems without the knowledge of their mathematical models. However, good understanding of the system's behaviour is required which comes from experience and can be translated to several IF and THEN rules or conditions, which makes the whole design process easy to understand since simple natural language is used. Common sense and linguistic descriptions between process's inputs and outputs are converted into a computer controlled system that is capable of providing a reliable and convenient solution [102]. It makes a fuzzy logic controller a powerful tool in solving imprecise and uncertain decision making problems. This leads to other useful features of fuzzy logic which are flexibility and the ability to model non-linear systems. It means that someone can add rules to existing ones without the need to start from the beginning. Furthermore, one complex or vague rule can be simplified or divided into more than one rule to give a better solution to a problem [103].

In view of the above, a controller based on fuzzy logic can be very useful in renewable energy managements and the following represent some of the areas that can be used or developed based on the advantages or features of the FLC:

- Since a FLC can control complicated systems without the knowledge of their mathematical models, it can be used to control power converters and tune conventional controllers to improve their performance.
- Due to the fact that a FLC can solve non-linear problems with imprecise and uncertain behaviours, the effect of the intermittency nature of the RES can be minimized especially with the available energy storage system. This is very helpful with complex systems like microgrids with different types of imprecise inputs and unpredictable variables and disturbances in particular if they are connected or supplied through RES and the power is consumed by varying and unpredictable loads.

- Because there is no need for training and availability of historical data in order to use FLC, it can be easily used for energy management of RES.
- The relationship between the PV power and voltage is non-linear as shown in Figure 3.8(a), which is affected by the solar irradiance and temperature. A FLC can deal with this non-linear relationship and it is possible to be used for maximizing the power delivery by extracting the maximum power point of the PV or other types of RES.
- Minimizing the cost of the overall control system since a controller based on fuzzy logic can be implemented using very cheap sensors making the control process easier and cheaper than a conventional controller.
- Since IF and THEN rules form an essential part of a FLC process, the FLC can be used as an assessment/evaluation tool for the selection of the RES sites based on their costs and benefits.
- Frequency regulation can be implemented using a FLC as a means of communication due to the simplicity of the FLC design.
- Due to the fact that fuzzy logic is based on several IF and THEN rules or conditions, a FLC can be used to improve the RES power prediction accuracy.
- Because a fuzzy logic controller is designed with rules based on human knowledge and experience, an experienced operator can design the rules to provide very reliable outputs in terms of power management taking into account the given constrains. This will minimize the impact of the intermittency nature of the RES and the variations in the loads.

The fuzzy logic control system consists of the following components and its architecture is as shown in Figure 3.9 below.

1- Fuzzification: Converts the crisp inputs to linguistic variables (fuzzy inputs) using membership functions stored in the rule base. Therefore, the input variables are assigned degrees of membership in various categories.
2- Inference Engine: Evaluates all rules and determines their truth values (fuzzy outputs). There are two types of inference engines; Mamdani and Sugeno. Mamdani type is the most commonly used where the output membership functions consist of fuzzy sets. It was proposed by Ebrahim

Mamdani in 1975 [101]. On the other hand, Sugeno type is used only when the output membership functions are expected to be either linear or constant. For the work conducted in this thesis, the Mamdani type of inference engine is used.

3- Defuzzification: Converts the fuzzy outputs obtained by the rules evaluation into crisp outputs which can be used as inputs to control a plant or system. There are many defuzzification methods such as centroid method, weighted average method and mean-max [104]. The centroid method is the most commonly used defuzzification method and is the one used in this thesis. It is often called centre of area or centre of gravity (COG) method. The centroid method finds the centre point of the targeted fuzzy region by calculating the weighted mean of the output fuzzy region as shown in (3.11).

$$Centroid = COG = \frac{\int_a^b \mu_A(x)\, x\, dx}{\int_a^b \mu_A(x)\, dx} = \frac{\sum_{i=1}^{n} A_i x_i}{\sum_{i=1}^{n} A_i} \qquad (3.11)$$

where $\mu_A(x)$ is the degree of a membership function A of a vector x on the interval between a and b and A_i is the area.

4- Rule Base: Contains knowledge in a set of rules to control the system. The rules are based on IF and THEN conditions where operators such as OR (for minimum values) or AND (for maximum values) can be added in the middle of the rule between IF and THEN.

The process for designing an FLC is as follows:

1- Identify available input(s) and possible output(s).
2- Define fuzzy sets and membership functions.
3- Classify linguistic variables using membership functions.
4- Form the rules by using fuzzy sets and linguistic variables.
5- Determine defuzzification method.
6- Check the performance of the system and modify accordingly.

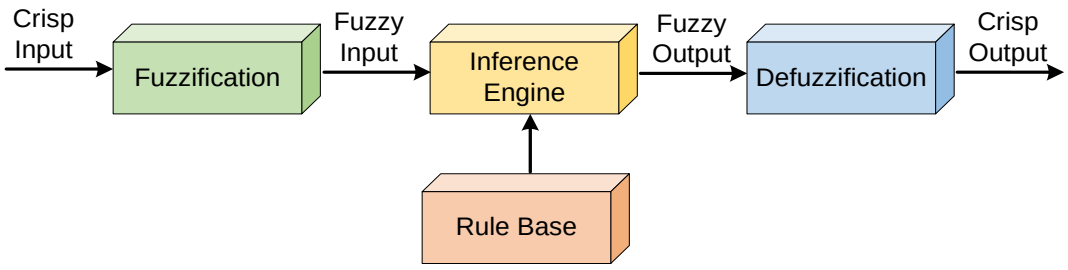

Figure 3.9: Fuzzy logic control architecture

Input and output variables in a fuzzy logic control system are mapped by sets of membership functions defined in the universe of discourse. Those sets are called "fuzzy sets" and their membership functions provide the degree of membership of any element in the universe of discourse. The degree of membership is between 0 (does not belong to the set) and 1 (entirely belongs to the set). A degree value between 0 and 1 means that the element belongs to the set [105]. There are many types of membership functions such as triangular, trapezoidal, Gaussian and bell. However, the degree of membership should be always between 0 and 1 for any type of membership function [106]. The types that have been used in this thesis are the most commonly used membership functions which are triangular and trapezoidal due to their simplicity.

3.4.2 Design of FLC for Energy Management of Microgrid

The FLC is proposed to protect the battery and prevent its SOC and charging/discharging power from exceeding their maximum and minimum limits regardless of the variation in the load and RES intermittent power. The FLC, which is implemented inside the BESS unit, alters the AC bus frequency which is used by the local controllers of the parallel units to curtail the power generated by the PV or to supplement power from the auxiliary unit as was explained earlier in section 3.3.2.

The proposed FLC is responsible for varying the bus frequency and is shown in Figure 3.10. To simplify the design, the FLC is divided into two subsystems: top and bottom. The top subsystem is responsible for preventing the battery from over-charging (i.e. keeping the SOC below its maximum limit) and the battery

charging power from exceeding its limit. The inputs for this subsystem are ΔSOC_1 and ΔP_{charge} which are given by (3.12) and (3.13), respectively.

$$\Delta SOC_1 = \frac{SOC^*_{max} - SOC}{SOC^*_{max} - SOC^*_{min}} \tag{3.12}$$

$$\Delta P_{charge} = \frac{P^*_{charge\_max} - P_{charge}}{P^*_{charge\_max}} \tag{3.13}$$

where SOC is the current state of charge and SOC^*_{max} is its maximum value. P_{charge} is the charging power and $P^*_{charge\_max}$ is the maximum charging power value. The output of the top FLC subsystem causes a positive shift in the frequency $\Delta\omega_+$. As this controller is implemented in the BESS, the bus frequency is deviated and as a consequence, the PV power is curtailed.

On the other hand, the bottom FLC subsystem is responsible for preventing the battery from over-discharging (i.e. keeping the SOC above its minimum limit) and the battery discharging power from exceeding its limit. The inputs for this subsystem are ΔSOC_2 and $\Delta P_{discharge}$ which are given by (3.14) and (3.15), respectively.

$$\Delta SOC_2 = \frac{SOC - SOC^*_{min}}{SOC^*_{min+10\%} - SOC^*_{min}} \tag{3.14}$$

$$\Delta P_{discharge} = \frac{P^*_{discharge\_max} - P_{discharge}}{P^*_{discharge\_max}} \tag{3.15}$$

where SOC^*_{min} is the SOC minimum value and $SOC^*_{min+10\%}$ is the SOC minimum value plus 10%. $P_{discharge}$ is the discharging power and $P^*_{discharge\_max}$ is its maximum discharging power value. The output of this subsystem is a negative shift in the bus frequency $\Delta\omega_-$ which causes the auxiliary unit to supplement power.

The two FLC subsystems work simultaneously. Therefore, the shift of frequency $\Delta\omega$ is the result of $\Delta\omega_+$ and $\Delta\omega_-$ as given by

$$\Delta\omega = \Delta\omega_{+} - \Delta\omega_{-} \quad (3.16)$$

To further clarify how the two subsystems work simultaneously; suppose that the battery power is P. If P is positive then the battery is discharging and if it is negative then the battery is charging. If $P > 0$, it means $P_{discharge} = |P|$ and $P_{charge} = 0$. This means that $\Delta P_{charge} = 1$ according to (3.13), which provides the second input to the top FLC subsystem while the first input value (for example X) will be the SOC. According to the Fuzzy rules, 1 AND X = X. Therefore, the top FLC subsystem output ($\Delta\omega_{+}$) is determined by SOC during discharging mode. Similarly, if $P < 0$, it means $P_{charge} = |P|$ and $P_{discharge} = 0$. This means $\Delta P_{discharge} = 1$ according to (3.15) that provides the second input to the bottom FLC subsystem whereas the SOC is the first input value (for example Y). By applying the operator AND in the fuzzy rules, 1 AND Y = Y. Hence, $\Delta\omega_{-}$ as the bottom FLC subsystem output is determined by SOC during charging mode. In view of the above, during charging mode $\Delta\omega_{+}$ is determined by ΔSOC_1 and ΔP_{charge} while $\Delta\omega_{-}$ is determined by ΔSOC_2 only. On the other hand, during discharging mode $\Delta\omega_{-}$ is determined by ΔSOC_2 and $\Delta P_{discharge}$ while $\Delta\omega_{+}$ is determined by ΔSOC_1 only. The change in the frequency occurs automatically based on the results from the two FLC subsystems. From the above, the SOC is plays a bigger role in determining the change in the frequency.

It is important to note that the PV curtailment by the command from the top FLC subsystem will not occur if the auxiliary unit is generating power as commanded by the bottom FLC subsystem. Hence, there is no clash between the two FLC subsystems since each one deals with different ranges in terms of inputs. The top FLC subsystem is responsible for protecting the battery from over-charging and it will curtail the PV power when the SOC is high or the charging power is higher than the maximum limit. The action is to increase the bus frequency. On the other hand, the bottom FLC subsystem is responsible for protecting the battery from over-discharging and it operates if the SOC is low in order to supply power by the auxiliary unit to support the battery. The action is to reduce the bus frequency. The change in frequency $\Delta\omega$ is a combination cause of both positive shift $\Delta\omega_{+}$ and negative shift $\Delta\omega_{-}$. Sometimes, neither PV curtailment

nor power supply by the auxiliary unit should be done. However, the battery can be in any mode or status. That is the reason for adding the outputs of the top and bottom FLC subsystems together, which provides the change in the frequency Δω. The maximum frequency deviation for the top and bottom FLC subsystems (see Figure 3.10) are $\Delta\omega_{max+}$ and $\Delta\omega_{max-}$, respectively. This allows the change in the PV power from 0% to 100% in such a way that when $\Delta\omega_{+} = 0$, no PV curtailment occurs, while when $\Delta\omega_{+} = \Delta\omega_{max+}$, the PV power is curtailed to zero. Similarly, when $\Delta\omega_{-} = 0$, no power is generated from the auxiliary unit, while when $\Delta\omega_{-} = \Delta\omega_{max-}$, the maximum power from the auxiliary unit is generated.

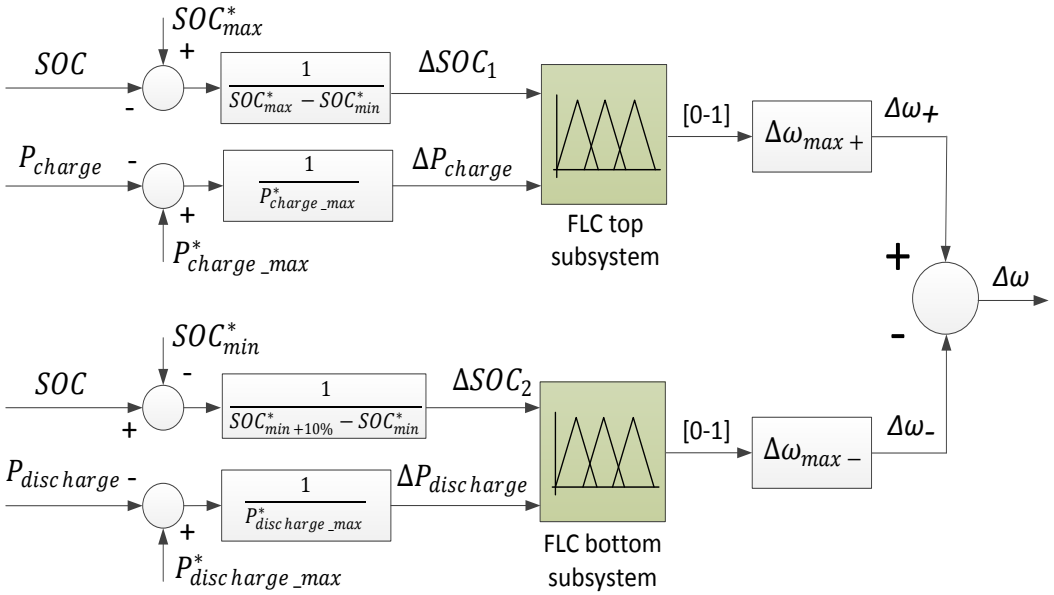

Figure 3.10: Proposed fuzzy logic controller

The membership functions of the top and bottom FLC are as shown in Figure 3.11 and Figure 3.12, respectively. The two types that have been used in this thesis are the most commonly used membership functions which are triangular and trapezoidal due to their simplicity. The membership functions are tuned several times during the design stage to assess and improve the performance of the supervisory controller in managing the stand-alone microgrid and the values in Table 3.2 represent the final ones that give the required performance. The two FLC subsystems have different shapes or combinations because they should deal with different ranges of values in terms of controlling. The range of

SOC in the top FLC subsystem is 55% which represents the difference between SOC maximum value SOC^*_{max} (95%) and SOC minimum value SOC^*_{min} (40%). The ΔSOC_1 value is normalized by dividing it by 55%. The curtailment of the PV power does not start until SOC value is more than 91%. In other words, ΔSOC_1 is considered high for a wide range to ensure that the battery is charged at a high rate whenever PV power is available and curtailment only occurs when the battery SOC is higher than 91%. This is the reason why the High fuzzy set is concentrated between 0 and 0.1 at the x-axis of Figure 3.11(a). Low (L) and High (H) sets in Figure 3.11(b) are only at the edges because the set H denotes that the charging power ΔP_{charge} is much less than the maximum charging power $P^*_{charge\_max}$, so curtailment is not necessary. However, the set L denotes that ΔP_{charge} is close to $P^*_{charge\_max}$, so there is a need to curtail the PV power to prevent the battery charging power from exceeding its limit. Therefore, L set is at the edge because curtailment is required just when it is very close to the maximum charging power and not before that. Otherwise, some PV power will be wasted if curtailment occurs at a prior point. In any case, the two inputs for the top FLC subsystem work together to provide the required output in terms of PV curtailment. On the other hand, the range of SOC in the bottom FLC subsystem is 10% which represents the difference between SOC minimum value plus 10% ($SOC^*_{min+10\%}$) and SOC minimum value (SOC^*_{min} (40%)). This allows the bottom FLC subsystem to work up to 10% more than SOC^*_{min}. Hence, ΔSOC_2 is normalized by dividing its value by 10% and therefore the bottom FLC subsystem should not work for a value higher than $SOC^*_{min+10\%}$. The two inputs for the bottom FLC subsystem work simultaneously to provide the required output in terms of power from the auxiliary unit.

Both ΔP_{charge} and $\Delta P_{discharge}$ are normalized by dividing their values by the maximum allowable limit for charging ($P^*_{charge\_max}$) and discharging ($P^*_{discharge\_max}$), respectively. Both inputs and outputs of both FLC subsystems are limited between 0 and 1. The degree of membership (y-axis of the membership function) should be always between 0 and 1 for any type of membership function while the x-axis of the membership function has no limitation as far as it is adjusted with the rest of the system to provide the required output.

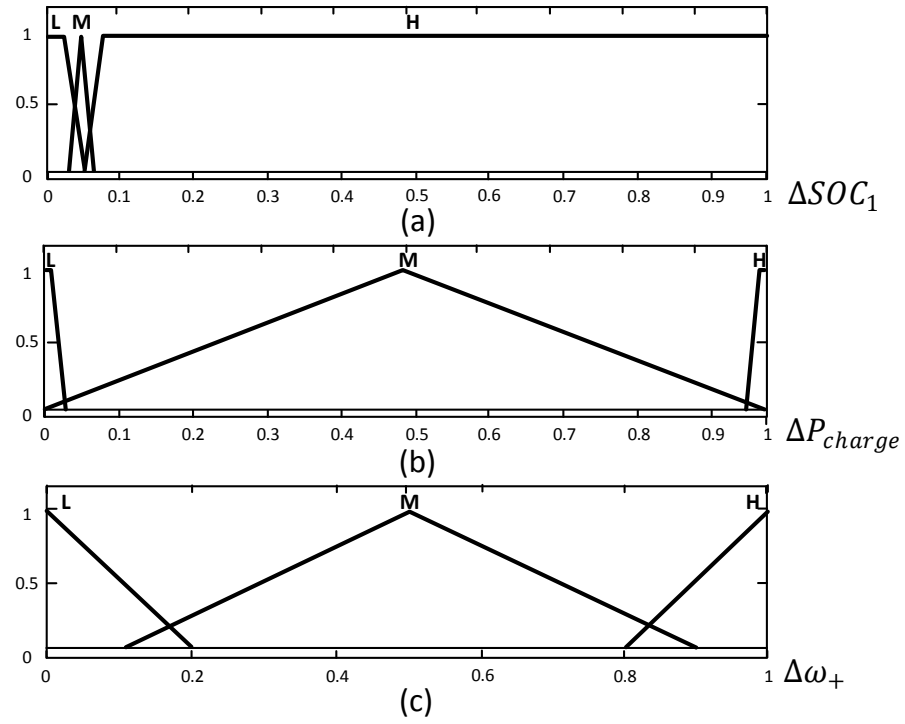

Figure 3.11: Membership functions of top FLC: (a) Input ΔSOC_1 (b) Input ΔP_{charge} (c) Output $\Delta\omega_+$

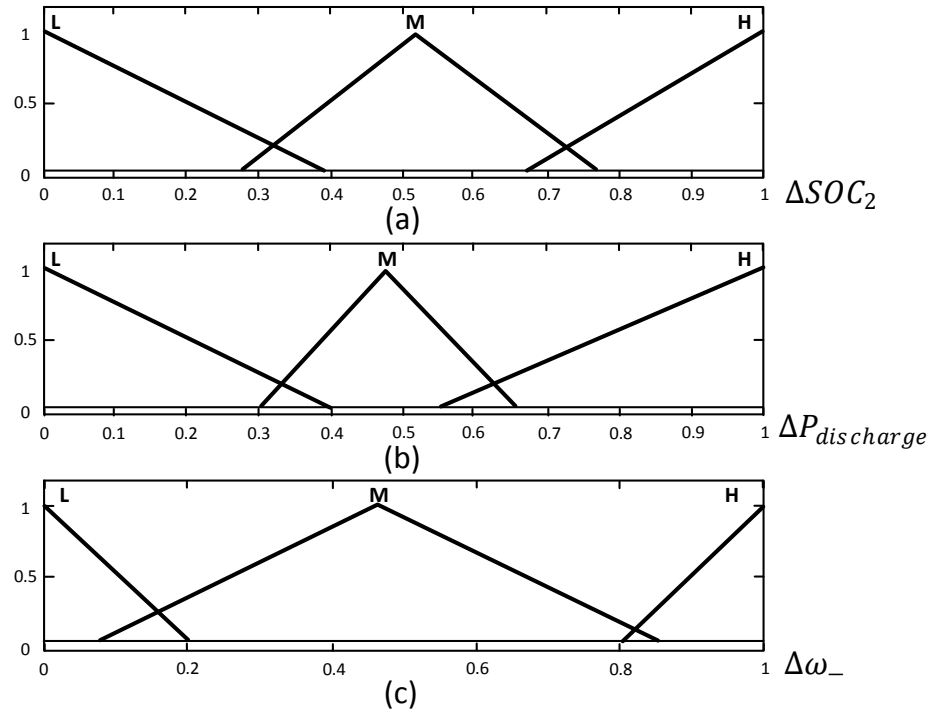

Figure 3.12: Membership functions of top FLC: (a) Input ΔSOC_2 (b) Input $\Delta P_{discharge}$ (c) Output $\Delta\omega_-$

The following shows an illustration of how different shape values are defined. It is for the two types of membership functions used. The shape values for the membership functions that are designed and used in the thesis are as shown in Table 3.2.

1- Triangular membership function:

The degree of a triangular membership function, for example $\mu_A(x)$, of a vector x in a fuzzy set, for example A, is defined as a function of 'x' that depends on provided parameters a, b and c, where $a < b < c$. The parameters a and c locate the feet of the triangle while b locates the peak as follows [104], [106]:

$$\mu_A(x) = \begin{cases} \dfrac{x-a}{b-a} & a \le x \le b \\ \dfrac{c-x}{c-b} & b \le x \le c \\ 0 & otherwise \end{cases} \tag{3.17}$$

It can also be written as follows:

$$\mu_A(x) = max\left(min\left(\frac{x-a}{b-a}, \frac{c-x}{c-b}\right), 0\right) \tag{3.18}$$

In this example, Figure 3.13 shows a triangular membership function with $a = 0$, $b = 0.2$, $c = 0.4$ at the x-axis.

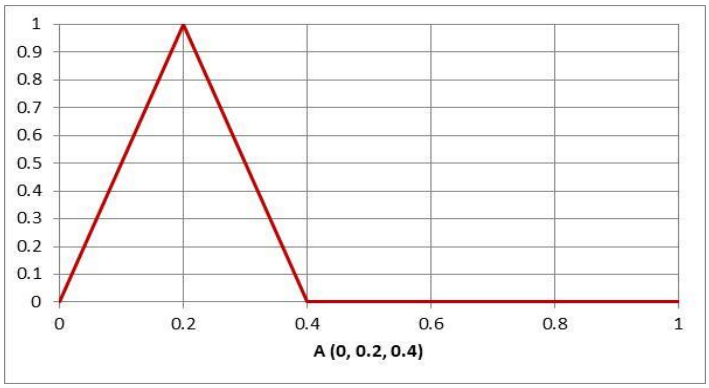

Figure 3.13: Triangular membership function

2- Trapezoidal membership function:

The degree of a trapezoidal membership function $\mu_A(x)$ of a vector x in a fuzzy set, for example A, is defined as a function of 'x' that depends on provided parameters a, b, c and d, where $a < b < c < d$. The parameters a and d locate the feet of the trapezoid while b and c locate the shoulders as follows [104], [106]:

$$\mu_A(x) = \begin{cases} \dfrac{x-a}{b-a} & a \le x \le b \quad (Left - \text{side trapezoid}) \\ 1 & b \le x \le c \\ \dfrac{d-x}{d-c} & c \le x \le d \quad (\text{Right} - \text{side trapezoid}) \\ 0 & otherwise \end{cases} \tag{3.19}$$

It can also be written as follows:

$$\mu_A(x) = max\left(min\left(\frac{x-a}{b-a}, 1, \frac{d-x}{d-c}\right), 0\right) \tag{3.20}$$

In this example, Figure 3.14 shows a trapezoidal membership function with $a = 0.2$, $b = 0.4$, $c = 0.6$, $d = 0.8$ at the x-axis.

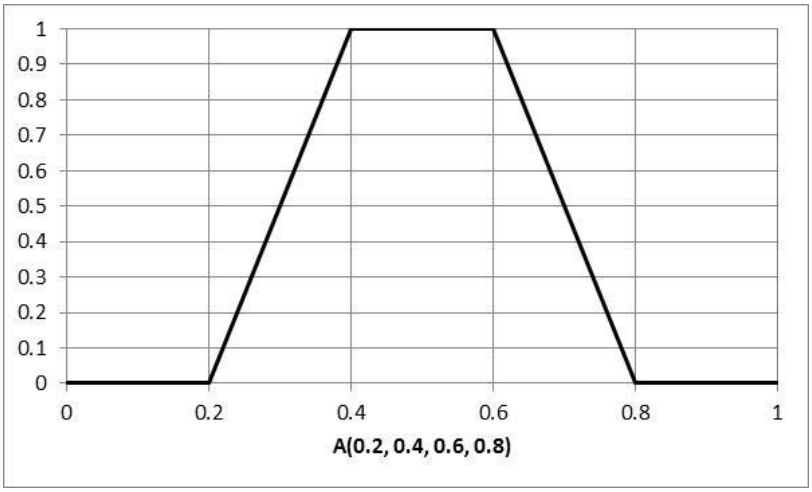

Figure 3.14: Trapezoidal membership function

Table 3.2: Membership functions details

FLC subsystem	Input / Output of FLC	Membership function	Type of membership function	Shape values
Top	ΔSOC_1 (1st input)	Low	trapezoidal	a=0, b=0, c=0.025, d=0.05
		Medium	triangular	a=0.025, b=0.045, c=0.065
		High	trapezoidal	a=0.05, b=0.075, c=1, d=1
	ΔP_{charge} (2nd input)	Low	trapezoidal	a=-0.02, b=0, c=0.01, d=0.02
		Medium	triangular	a=-0.00661, b=0.5, c=1
		High	trapezoidal	a=0.98, b=0.99, c=1, d=1
	$\Delta\omega_+$ (output)	Low	triangular	a=-0.2, b=0, c=0.2
		Medium	triangular	a=0.1, b=0.5, c=0.9
		High	triangular	a=0.8, b=1, c=1.2
Bottom	ΔSOC_2 (1st input)	Low	trapezoidal	a=-0.206, b=-0.206, c=0, d=0.39
		Medium	triangular	a=0.271, b=0.5093, c=0.777
		High	trapezoidal	a=0.668, b=1, c=1.31, d=1.31
	$\Delta P_{discharge}$ (2nd input)	Low	trapezoidal	a=-0.505, b=-0.505, c=-0.00505, d= 0.39
		Medium	triangular	a=0.298, b=0.477, c=0.6468
		High	trapezoidal	a=0.56, b=1.01, c=1.51, d=1.51
	$\Delta\omega_-$ (output)	Low	triangular	a=-0.2, b=0, c=0.2
		Medium	triangular	a=0.06923, b=0.4462, c=0.85
		High	triangular	a=0.8, b=1, c=1.2

Table 3.3 and Table 3.4 show the rules for the FLC top subsystem and bottom subsystem, respectively. The terms L, M and H denote Low, Medium and High membership functions, respectively. The rules are designed based on experience and observations. The number of possible rules is determined by knowing the number of inputs and how many linguistic values for each input. Therefore, the maximum possible number of the rules of each FLC subsystem in this case is $3^2 = 9$ rules since there are 2 FLC inputs and 3 linguistic values for each input. The rules are changed along with the changes in the membership functions during the design stage to assess the performance of the stand-alone microgrid and modifications are carried out as per the requirement. The method in [107] and [108] for developing the fuzzy rules from numerical data is used in this thesis and can be summarized as follows:

1- Divide the input and output spaces of the given numerical data into fuzzy regions or partitions either by using available information from experts or by normalization process. Select a type of membership function and assign one fuzzy set to each range. Normalization has been used in this thesis, so each universe of discourse is divided into three partitions.
2- Create a set of preliminary possible linguistics fuzzy rules using inputs and output along with linguistics operators (AND, OR, NOT). This set should cover the different possibilities.
3- Provide an importance degree to each preliminary rule in the developed set. All the preliminary rules with the same antecedent (IF-part of the rule) are grouped together irrespective of the consequent part of the rules (THEN-part), which can lead to conflicts between the rules. To resolve such conflicts, the rule with the maximum degree is selected among the conflicting rules making final rules in the group and the other conflicting rules are deleted.
4- Generate final Rule Base similar to the ones in Table 3.3 and Table 3.4 using the final rules obtained from point 3 above.

Table 3.3: Rules of top FLC

$\Delta\omega_+$		ΔP_{charge}		
		L	M	H
ΔSOC_1	L	H	H	L
	M	M	M	M
	H	H	L	L

Table 3.4: Rules of bottom FLC

$\Delta\omega_-$		$\Delta P_{discharge}$		
		L	M	H
ΔSOC_2	L	H	H	H
	M	H	M	M
	H	H	M	L

Illustrations with sample results of how the membership functions are used as part of the overall fuzzy logic control process is shown in Figure 3.15 and Figure 3.16. For Figure 3.15, the SOC value is 95%. It needs to be subtracted from SOC^*_{max} which is 95% in this case. Hence, ΔSOC_1 = 0 before normalization. It is then normalized by dividing it by 55 (difference between SOC^*_{max} and SOC^*_{min}) which gives 0. Therefore, Input-ΔSOC_1 = 0 which is a crisp value used as input 1 to the top FLC. For this crisp input value, the degree of the membership in the Low set (fuzzy input) is 1 while the degree of the membership in the Medium and High sets (fuzzy inputs) is 0 since 0 does not belong to the Medium and High sets. Similarly, the P_{charge} is 100W. It needs to be subtracted from $P^*_{charge\_max}$ which is 1000W in this case. Therefore, ΔP_{charge} = 900W before normalization. It is then normalized by dividing it by $P^*_{charge\_max}$ (1000W) which gives 0.9. Hence, Input-ΔP_{charge} = 0.9 which is a crisp value used as input 2 to the top FLC. For this crisp input value, the degree of the membership in the Medium set (fuzzy input) is 0.25 while the degree of the membership in the Low and High sets (fuzzy inputs) is 0 since 0.25 does not belong to the Low and High sets. Now by referring to Table 3.3, rule 2 is read as follows; "IF ΔSOC_1 is

Low AND ΔP_{charge} is Medium, THEN $\Delta\omega_+$ is High". From rule 2, the degree of the membership for the first input ΔSOC_1 in Low is 1 and the second input ΔP_{charge} in Medium is 0.25. Therefore, the result of applying the operator (AND) in rule 2 gives 1 AND 0.25 where AND gives the lowest value. Hence, the lowest value (0.25) is taken for applying on the set High in output $\Delta\omega_+$ in the next step. Therefore, when it is applied on the set High of Figure 3.15(c), the set is attenuated by 0.25 and it is used as an output for changing the frequency $\Delta\omega$ in a positive shift $\Delta\omega_+$ to curtail the PV power.

Similarly in Figure 3.16, the SOC value is 42%. The value should be subtracted from SOC^*_{min} which is 40% in this case. Hence, ΔSOC_2 = 2 before normalization. After that, it is normalized by dividing it by 10 which is the difference between SOC minimum value plus 10% ($SOC^*_{min+10\%}$) and SOC minimum value (SOC^*_{min}). The answer is 0.2 and hence input-ΔSOC_2 = 0.2 which is used as input 1 to the bottom FLC. For this crisp input value, the degree of the membership in the Low set (fuzzy input) is 0.48 while the degree of the membership in the Medium and High sets (fuzzy inputs) is 0 since 0.2 does not cross the Medium and High sets. In the same way, the $P_{discharge}$ is 720W. When it is subtracted from $P^*_{discharge\_max}$ which is 1000W in this case, $\Delta P_{discharge}$ = 280W before normalization. It is then normalized by dividing it by $P^*_{discharge\_max}$ (1000W). Therefore, Input-$\Delta P_{discharge}$ = 0.28 which is a crisp value used as input 2 to the bottom FLC. For this value, the degree of the membership in the Low set (fuzzy input) is 0.28 while the degree of the membership in the Medium and High sets (fuzzy inputs) is 0 since 0.28 does not belong to the Medium and High sets. From Table 3.4, rule 1 is read as follows; "IF ΔSOC_2 is Low AND $\Delta P_{discharge}$ is Low, THEN $\Delta\omega_-$ is High". From rule 1, the degree of the membership for the first input ΔSOC_2 in Low is 0.48 and second input $\Delta P_{discharge}$ in Low is 0.28. Therefore, the result of applying the operator (AND) in rule 1 gives 0.48 AND 0.28. Hence, 0.28 is taken for applying on the set High in output $\Delta\omega_-$ in the next step since it is the lowest value amongst the two values. Consequently, when it is applied on the set High of Figure 3.16(c), the set is attenuated by 0.28 and it is used as an output for changing the frequency $\Delta\omega$ in a negative shift $\Delta\omega_-$ to cause the auxiliary unit to supplement power.

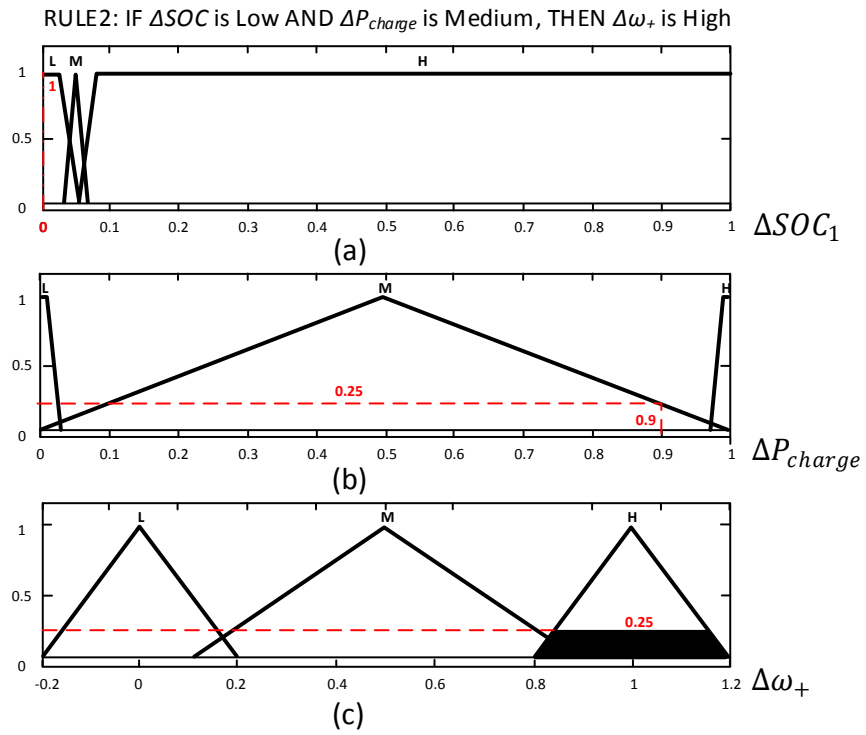

Figure 3.15: Example for top FLC membership functions: (a) Input-ΔSOC_1 (b) Input-ΔP_{charge} (c) Output-$\Delta\omega_+$

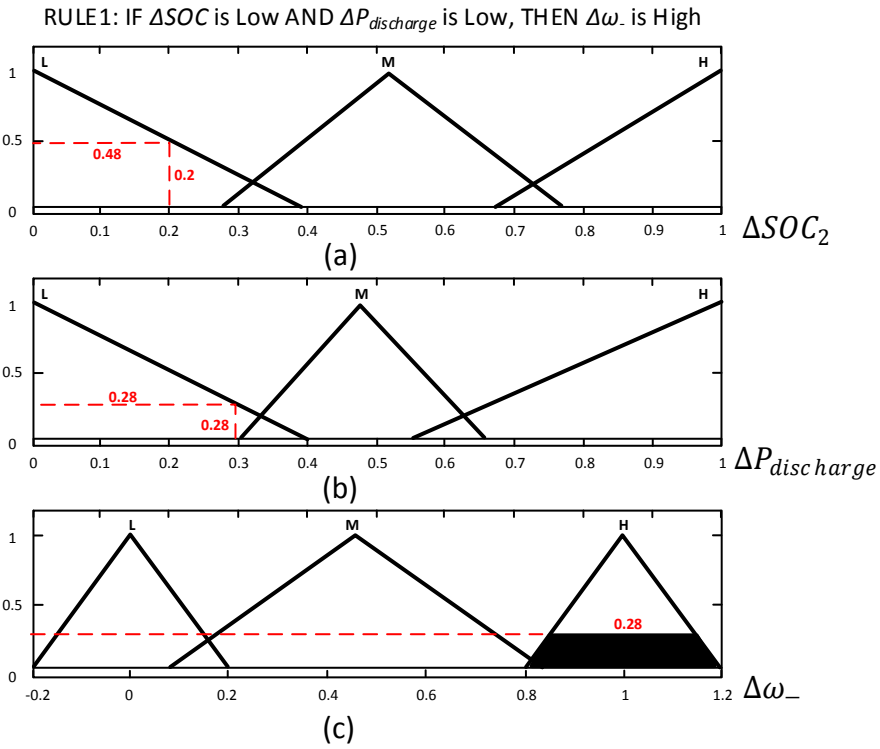

Figure 3.16: Example for bottom FLC membership functions: (a) Input-ΔSOC_2 (b) Input-$\Delta P_{discharge}$ (c) Output-$\Delta\omega_-$

The two FLC subsystems work simultaneously and $\Delta\omega$ is given by (3.16) where the top FLC subsystem is responsible for protection from over-charging while the bottom FLC subsystem is responsible for protection from over-discharging. In other words, the change in frequency $\Delta\omega$ will be a combination of a positive shifting $\Delta\omega_+$ and a negative shifting $\Delta\omega_-$ together.

3.5 Matlab/Simulink Simulation

3.5.1 Simulation Model

A 3-phase AC microgrid that consists of three power generation units (i.e., solar PV, battery and auxiliary), loads and proposed controllers has been built in Matlab/Simulink with SimPowerSystem and Fuzzy Logic tool boxes. The system in Figure 3.4 is modelled and simplified as follows:

1- The PV, MPPT controller and the DC/DC converter have been modelled as an ideal current source.
2- The 3-phase converter with the LC filter has been modelled as an average model ideal converter which is a block provided by Matlab/Simulink.

Figure 3.17 shows block diagrams of the generation units, loads and their relevant circuit breakers. The PV, battery and auxiliary units' models are as shown in Figure 3.18, Figure 3.19 and Figure 3.20, respectively.

The PV unit is modelled as a controlled current source as shown in Figure 3.18. The reference power for the current source decides how much power is required to be generated by the PV (the controlled current source). The reference power represents the available power from the PV unit. The MPPT controller measures the bus frequency using a Phase Looked Loop (PLL) (see Figure 3.4). If the bus frequency is shifted up, this acts as a message to the MPPT controller that the PV power needs to be curtailed and it shifts the maximum power point to a lower value by increasing the PV output voltage as illustrated in Figure 3.8. A generic battery block used in the battery's model that is simplified as shown in Figure 3.19 where Lead-Acid type is selected. The battery is required to be a voltage source and the droop coefficient of the

battery unit m is set to zero. The auxiliary unit is modelled as a DC voltage source as it represents a rectified voltage from the micro gas turbine with 750V amplitude as shown in Figure 3.20.

The Universal Bridge block which is shown in Figure 3.18, Figure 3.19 and Figure 3.20 implements a universal three-phase power converter that consists of six power switches connected in a bridge configuration. An averaged-model based voltage source converter (VSC) has been used for modelling the DC/AC inverters to represent the power-electronic switches. Parallel to the VSC, there is a capacitor (C_{dc}) that represents the DC-link. The DC-link controller will control the DC-link voltage by injecting more or less power into the microgrid. It uses the reference signals that represents the average voltages generated at the ABC terminals of the bridge. The reference value of the output voltage (V_o^*) is used to generate the duty cycle for the inverter. The inverters control the voltage of the DC-link. The ABC terminals of the bridge are connected to 3-phase series RL branch which represents the output impedance of the DC/AC inverter. The output from the PV and auxiliary (μGT) units are connected to individual breaker in order to connect or isolate them from the common bus as shown in Figure 3.17.

Figure 3.21 shows the droop control of the PV unit which is given by (3.8) while Figure 3.22 shows the battery droop control block with $\Delta\omega$ as given by (3.7). The auxiliary unit droop control block is shown in Figure 3.23 based on (3.10). The power set point P^* of the auxiliary unit is set to zero in order to supplement power in response to variation in the bus frequency. Instantaneous active and reactive powers used by the droop controllers are measured using the 3-phase voltage V_{abc} and current I_{abc} and filtered using a Low Pass Filter (LPF) as shown in Figure 3.17. The power calculations block for all the power units is the same as shown in Figure 3.24 based on the power calculation method used in [109] where a product of the output voltage and current of the inverters along with LPF are used. Detailed Matlab/Simulink files are shown in Appendix. The system parameters used in the simulation are shown in Table 3.5.

Table 3.5: System parameters

Parameter	Symbol	Value
Maximum state of charge	SOC^*_{max}	95%
Minimum state of charge	SOC^*_{min}	40%
Minimum state of charge plus 10%	$SOC^*_{min+10\%}$	50%
Maximum charging power	$P^*_{Charge\_max}$	1000W
Maximum discharging power	$P^*_{Discharge\_max}$	1000W
Nominal bus frequency	$\omega_o = 2\pi f_o$	$2\pi(50)$=314rad/s
Nominal bus voltage	V_o	220V
Battery nominal voltage	V^*_{DC}	750V
PV DC voltage P-controller gain	k_{p-dc}	20
PV DC voltage I-controller gain	k_{i-dc}	60
DC-link capacitor	C_{dc}	1200μF
Active power droop coefficients for PV and auxiliary units	m_{PV}, m_{aux}	0.9e-4 rad/s/W
Active power droop coefficients for battery unit	m_{bat}	0
Reactive power droop coefficients	n	0.9e-4 V/Var
PV current P-controller gain	k_{p_pvc}	0.003
PV current I-controller gain	k_{i_pvc}	0.01
PV voltage P-controller gain	k_{p_pvv}	10
PV voltage I-controller gain	k_{i_pvv}	250
Frequency - gain	PI_ω	30000
VSC-output resistance	R	0.08Ω
VSC-output inductance	L	1mH
Voltage amplitude of micro gas turbine	V_{aux}	750V

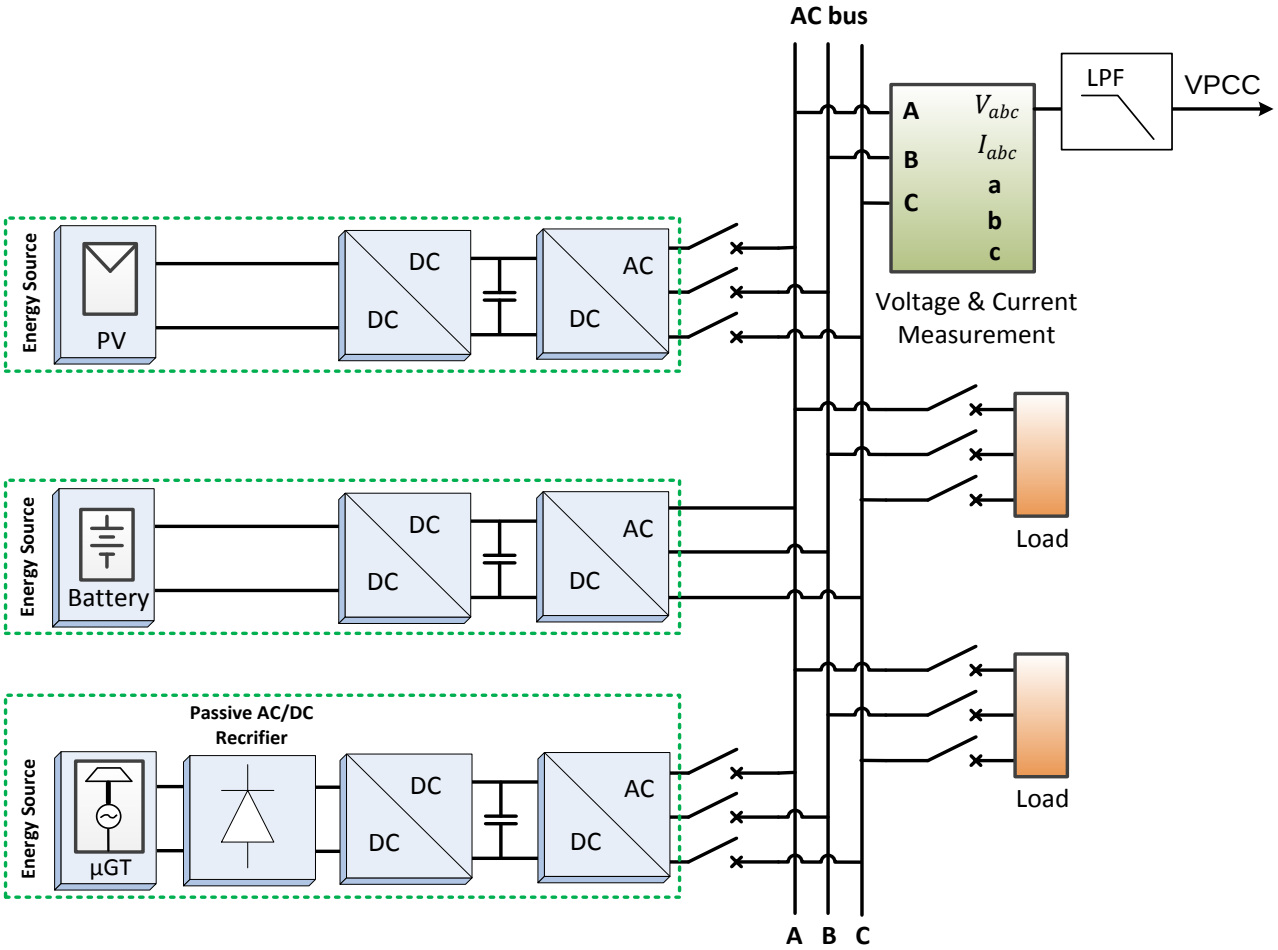

Figure 3.17: Block diagrams model of the microgrid

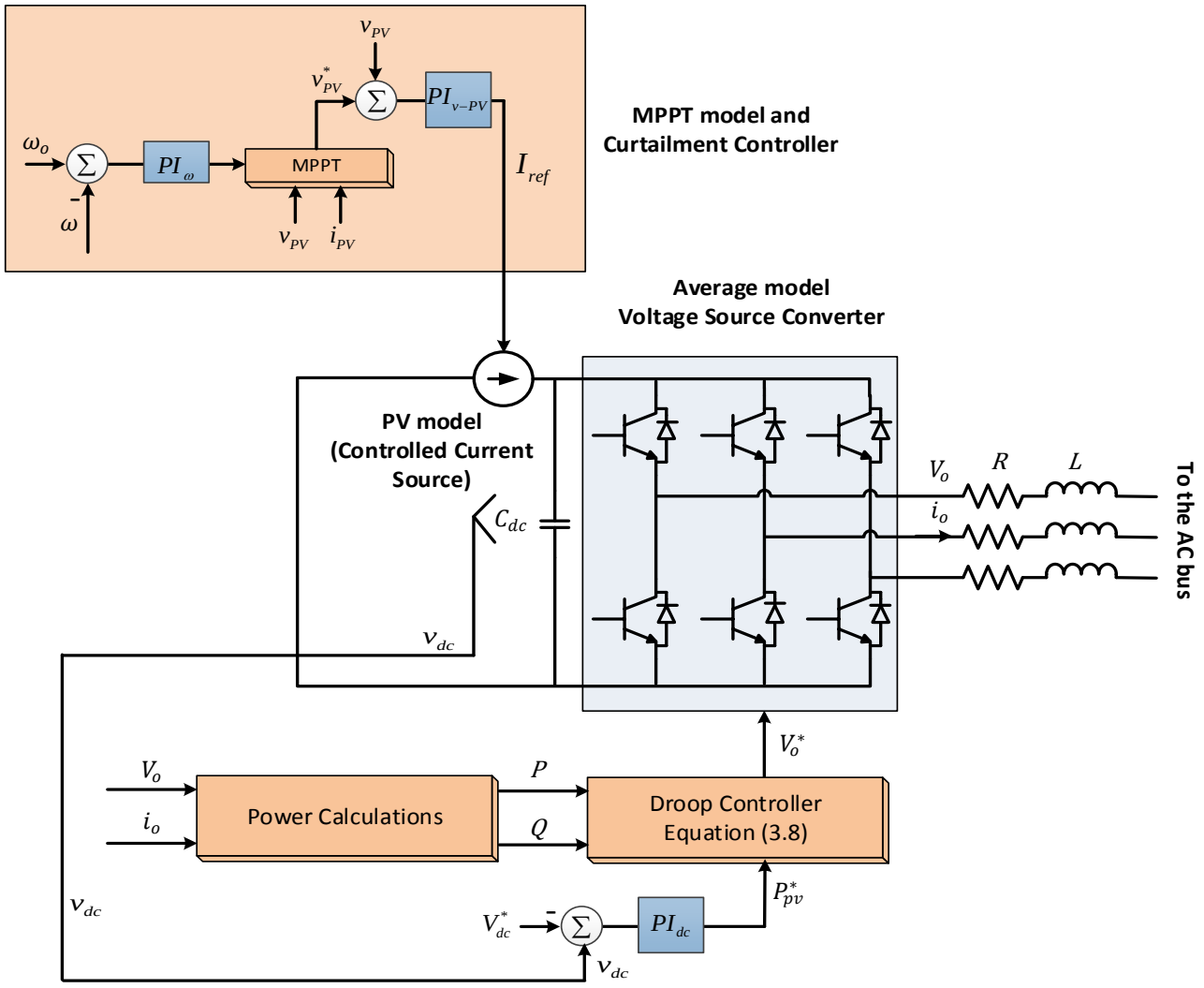

Figure 3.18: PV unit model

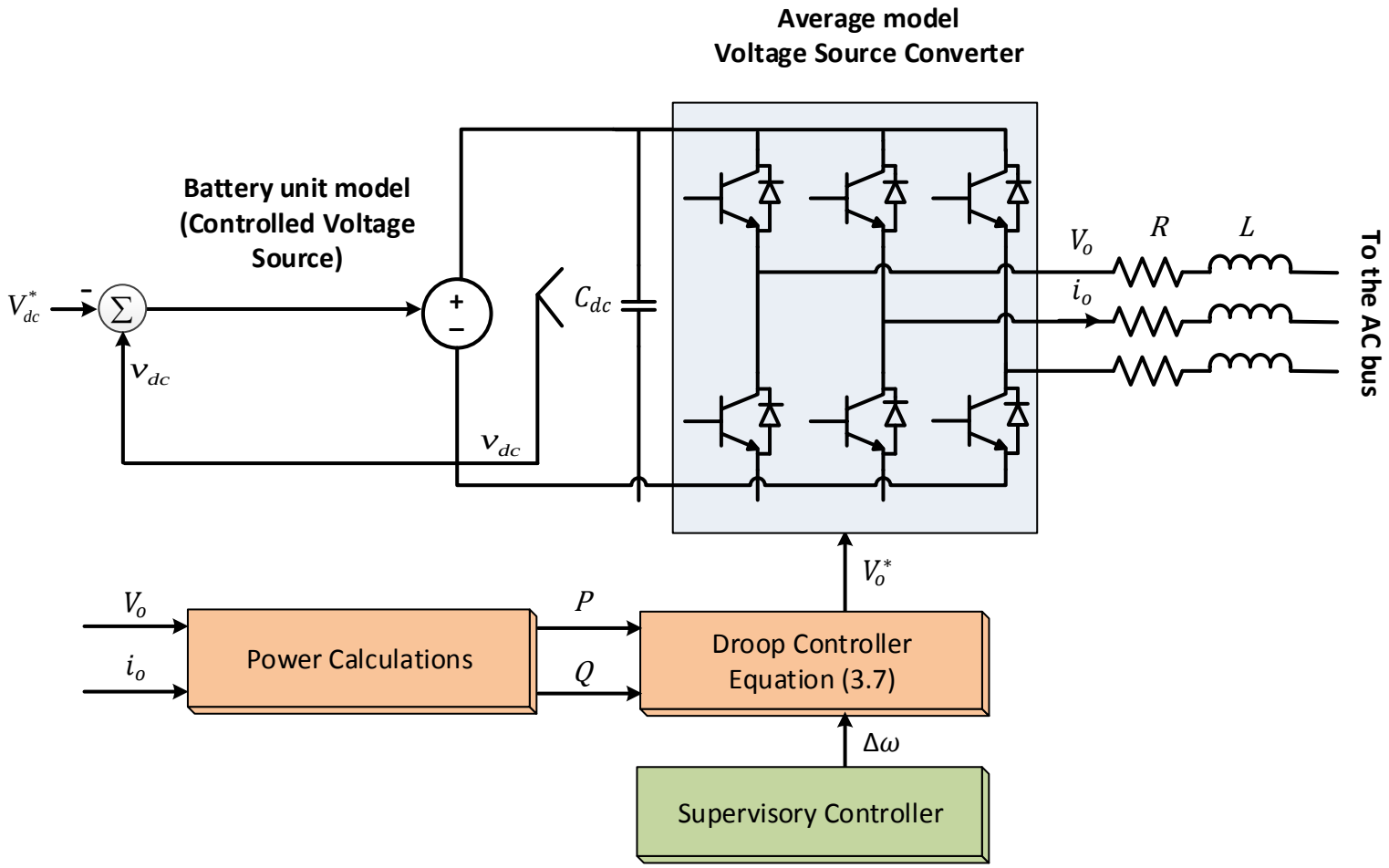

Figure 3.19: Battery unit model

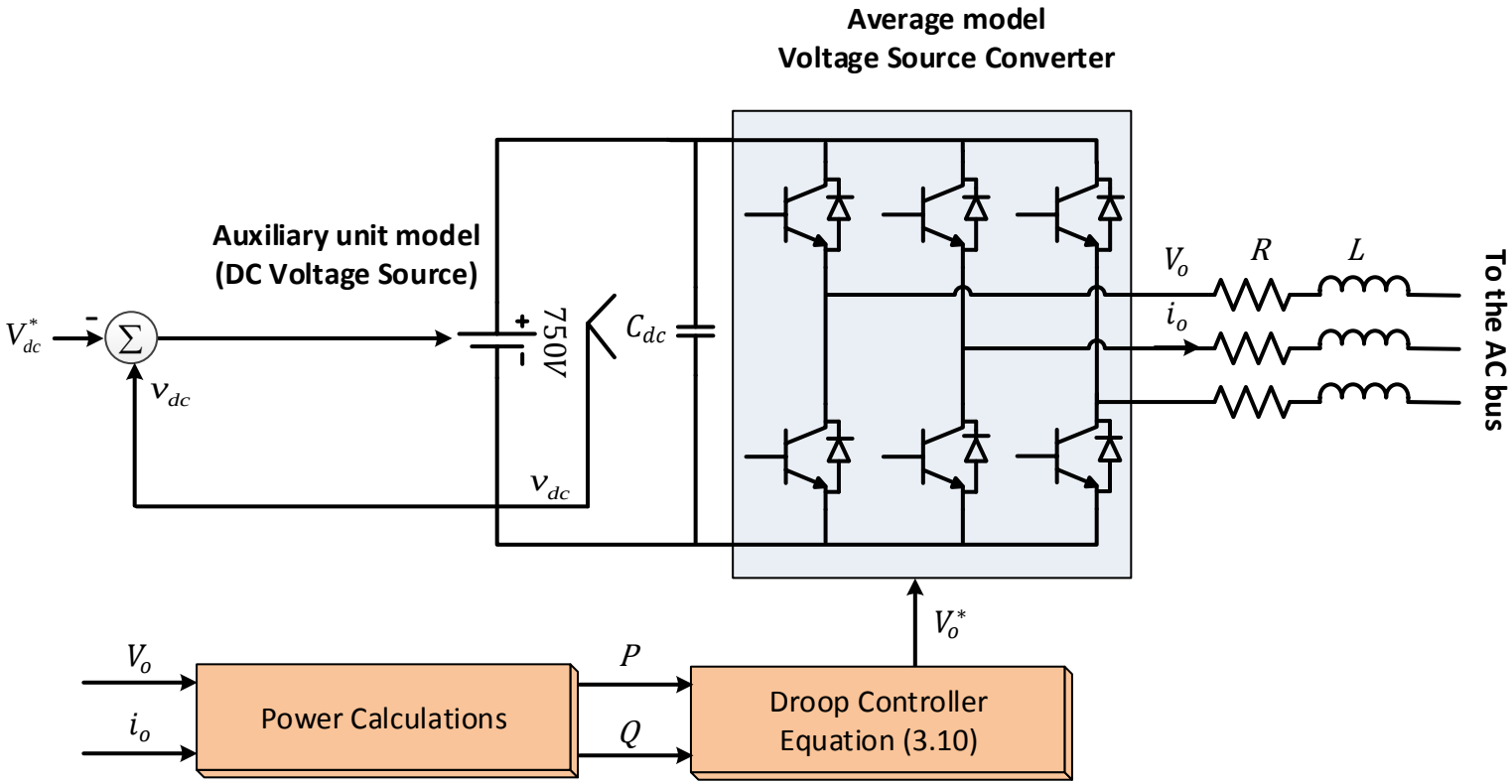

Figure 3.20: Auxiliary unit model

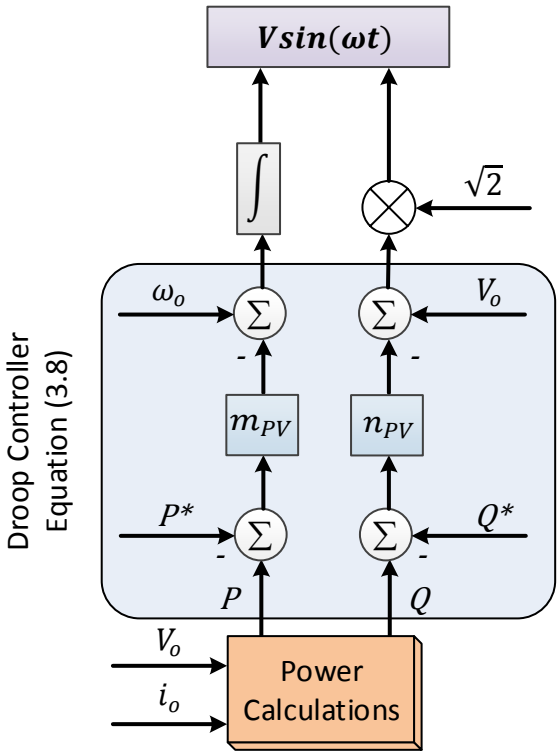

Figure 3.21: PV droop control

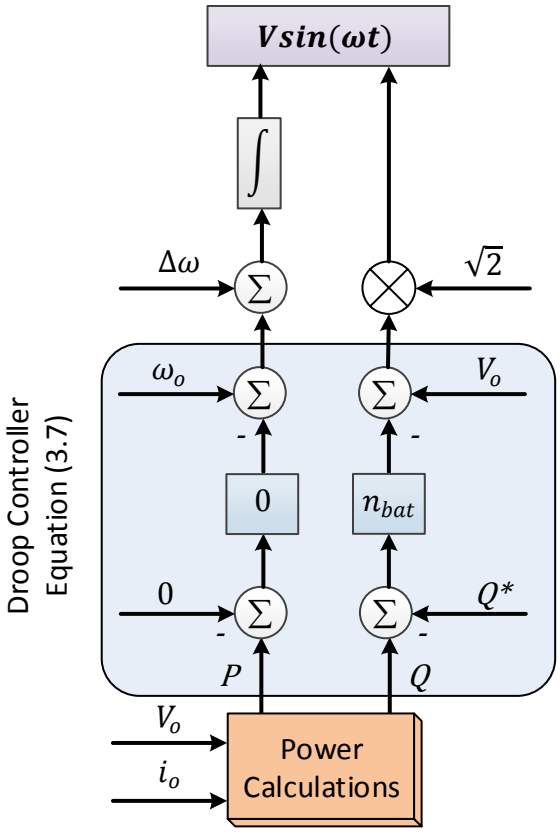

Figure 3.22: Battery droop control

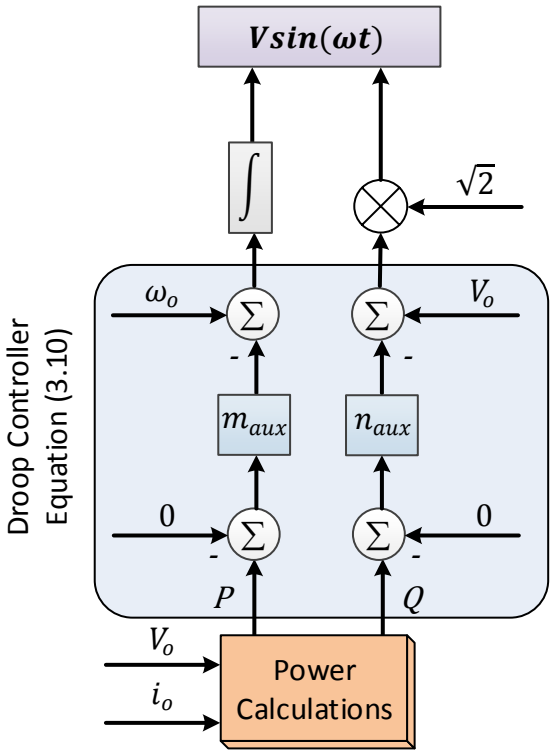

Figure 3.23: Auxiliary unit droop control

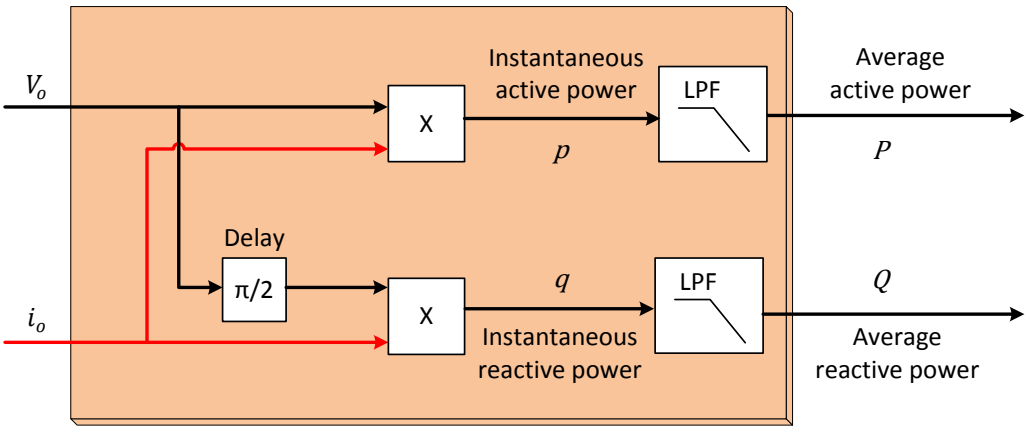

Figure 3.24: Power calculations block for power units

3.5.2 Simulation Results

Figure 3.25 shows the power output of the PV, battery and auxiliary units along with the load power. The initial value of the SOC is approaching the maximum limit of 95%. Before t=3s, the FLC is deactivated. The available power from the PV is 1000W and the load is 500W. Therefore, the battery is charging at 500W rate. If the battery is kept charging at this rate, the SOC will exceed the 95% as can be noticed from the slope of the SOC between t=2.5s and t=3s. The

auxiliary unit is not running due to the high SOC. At t = 3s, the FLC is activated and the AC bus frequency starts to increase. The Local controller of the PV unit curtails the power to 500W and consequently the SOC stops increasing. At t = 5s, the load changes suddenly from 500W to 1000W and the generation from the PV unit is increased proportional to the reduction in the frequency commanded by the FLC until the PV has restored its full generation. The SOC is prevented from increasing beyond the maximum limit by curtailing the PV power. However, when the load increases, the curtailment stops in order to make use of full PV power.

Figure 3.26 shows the power output of the PV, battery and auxiliary units and load where the initial value of the SOC is approaching its minimum limit of 40%. The FLC is deactivated before t = 3s. The battery is discharging and providing 600W power since the load is 1600W while the PV power is only 1000W. Hence, the SOC is declining (under-charging). The auxiliary unit is not providing any power. However, at t = 3s, the FLC is activated and the bus frequency starts to decrease, so the auxiliary unit reacts by generating 600W. The generated power is proportional to the frequency drop. The SOC has stopped declining; hence that battery is protected from under-charging. At t = 5s, the load changes suddenly from 1600W to 100W. Therefore, the available generation to be absorbed by the battery is now 1500W which exceeds the maximum charging power of 1000W. Thanks to the FLC, the auxiliary unit stopped generating and the PV power supplied the load and charged the battery by the surplus power to heal the low SOC. As a result of that, the charging power was limited to 900W instead of 1500W (if the auxiliary unit had been left to generate). The bus frequency was increased according to the FLC command in order to stop the auxiliary unit from supplying power. The SOC started to increase by using the available surplus power.

From the results, it is very clear that the FLC provides suitable power management to the generation units regardless of the changes in the PV and load powers. Consequently, the battery's SOC and power are prevented from exceeding their limits. During transient, however, the battery power exceeded the 1000W limit, but only for a very short period of time of 1 second. This will be eliminated later on in the coming simulations by tuning and optimizing the

membership functions of the FLC (refer to Chapter 4). The developed model has achieved the required objectives, but it produces errors when running for a long period of time. This might be due to the fact that it requires a high memory for storing data while running for a long period. Therefore, there is a need to simplify it to be able to use the designed fuzzy logic controller for longer periods rather than short ones only. This helps in testing the controller with large fluctuations of both generations and loads. The new simplified model will be discussed in Chapter 4.

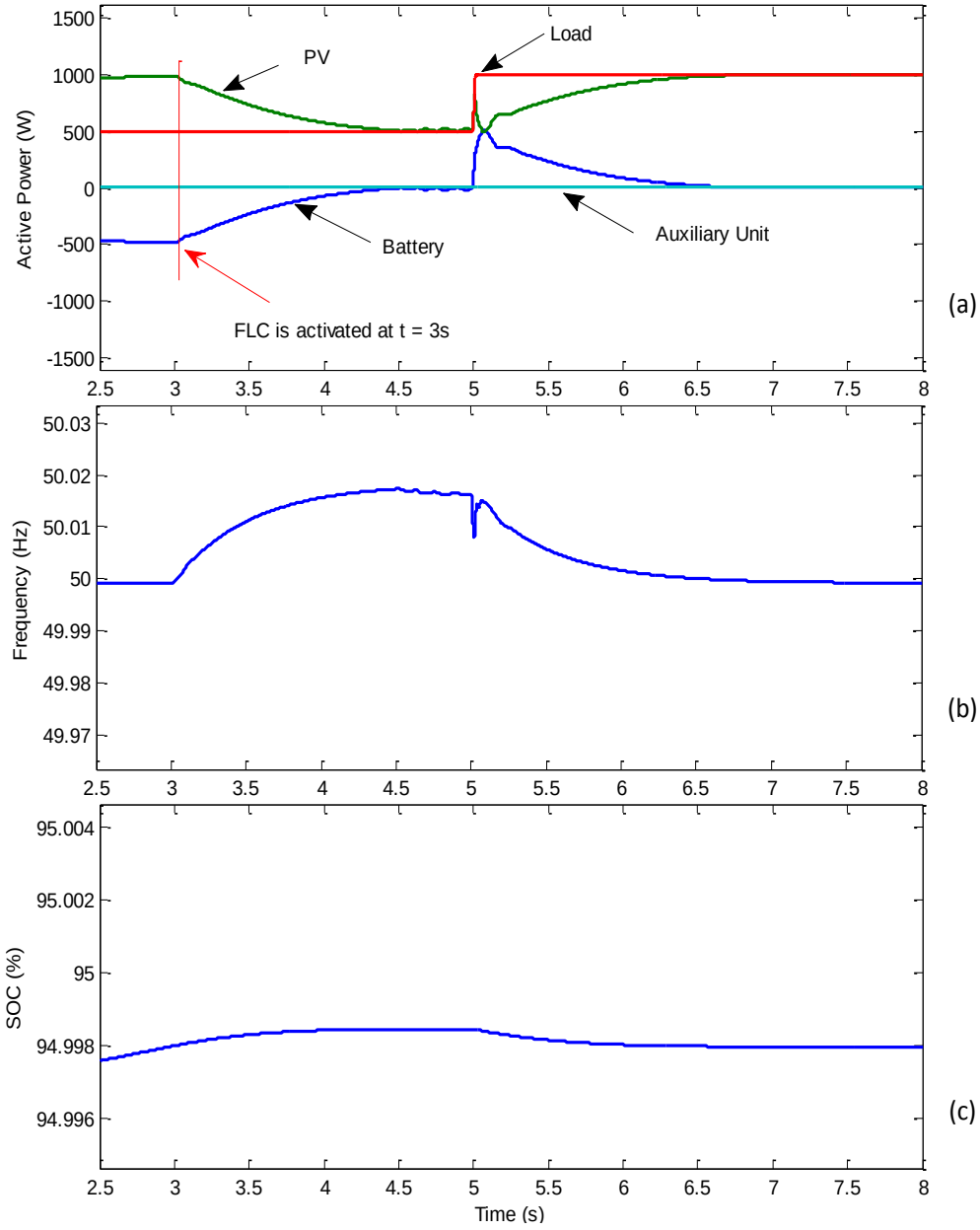

Figure 3.25: Output response for 95% SOC case: (a) output power (b) frequency (c) SOC

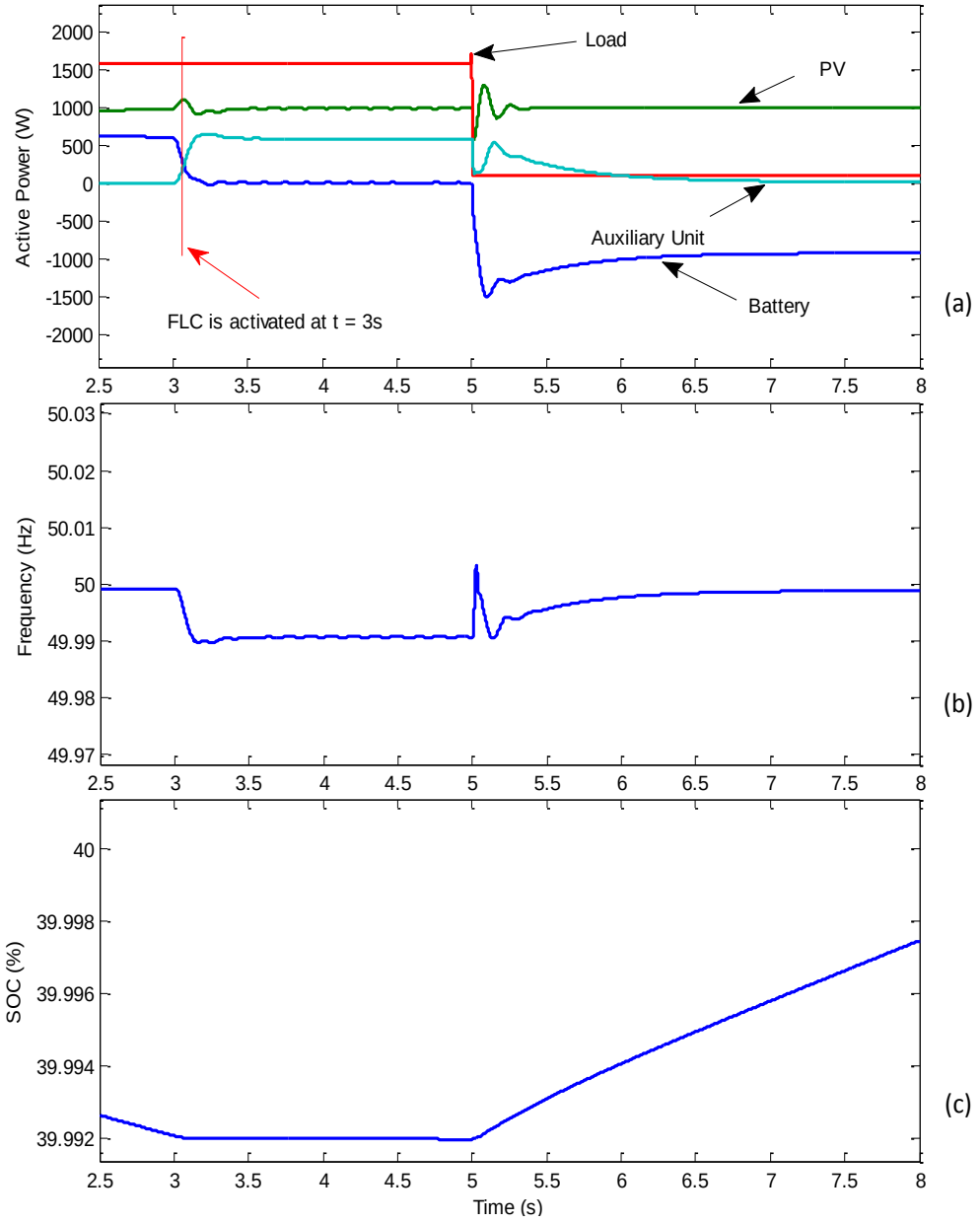

Figure 3.26: Output response for 40% SOC case: (a) output power (b) Frequency (c) SOC

3.6 Summary

This chapter has examined the power management of a stand-alone AC microgrid that consists of a RES, ESS, auxiliary unit and loads. The chapter proposed a droop control for each power unit and a Fuzzy Logic Controller was proposed as the supervisory controller for the microgrid for overall control of power from generations to loads. The chapter has given an overview of a typical AC inverter based microgrid and the method of operation in stand-alone and

grid-connected modes. It presented the control strategies by providing the two possible options for controlling the two-stage converters and provided details about the droop control strategies for the ESS and RES where the battery unit was the master controller for the AC bus frequency. The proposed floating auxiliary unit (micro gas turbine (μGT)) on the common bus was introduced and its droop control strategy is provided.

By varying the AC bus frequency which was used by the local droop controllers, a supervisory controller based on fuzzy logic was proposed and implemented for energy management without the need for any communication links between the microgrid units. The supervisory controller was designed to decide whether to curtail the power generated by the PV or to supplement power from the auxiliary unit. The chapter covered a Matlab/Simulink simulation model and provides some results. It is concluded that the proposed FLC managed to maintain the SOC and the charging/discharging power of the battery within their design limits irrespective of changes in generation from the RES or changes in the load.

CHAPTER 4: SIMULATION RESULTS & DISCUSSION OF A SIMPLIFIED MICROGRID MODEL

4.1 Introduction

This chapter presents the simulation results of a simplified microgrid model. This model has been developed to speed up the simulation time in order to assess the performance of the Fuzzy Logic Controller (FLC) especially over long periods of time and to avoid any difficulties that may arise when running the model presented in Chapter 3 as was discussed in section 3.5.2. Two types of simulation models have been considered:

1- Matlab/Simulink simulation (short-term simulation)
2- Real-time simulation by RT-LAB with Matlab/Simulink (long-term simulation)

A short-term simulation has been carried out to compare the FLC performance against a proportional controller. Due to the fact that the PV power fluctuates and the load changes, the need of a potent power controller is crucial to manage the PV, battery and auxiliary units. The amount of power required to supply the load or to charge the battery is not fixed and it keeps changing to achieve the AC bus balance. Hence, a proportional change between the frequency and power is required as fast as possible. Therefore, a proportional (P) controller is more suitable for dealing with such frequent changes, with no fixed set point, in comparison to an integral (I) or a proportional-integral (PI) controller. The integral component slows the controller's response. A proportional-integral-derivative (PID) controller can generally enhance the dynamic transient responses in terms of damping the overshoots. However, the supervisory controller is slow and targeting the steady state response more. Therefore, the proportional controller is selected for the comparison with the FLC. The real-time simulation is conducted both with and without the FLC. The two simulations are required to assess the performance and robustness of the designed FLC in preventing the battery SOC and charging/discharging power

from exceeding their limits regardless of the variations in load and intermittent power of renewable sources.

The results of the real-time simulation show that the proposed FLC provides a suitable control of the microgrid in full compliance with the designed limits of the SOC and charging/discharging power of the battery.

4.2 Simplified Model

The model presented in Chapter 3 section 3.5.1 was based on ideal voltage and current sources and it included all the required control loops. The model considered in this section only considers the droop control level and the battery model. The PV unit will produce maximum possible power according to its MPPT as long as the bus frequency ω equals or is less than the nominal frequency ω_o. However, if the bus frequency is increased above the nominal frequency, then the power is curtailed as was explained in section 3.3.2. Therefore, the PV power, P_{PV} is given by

$$P_{PV} = P_{PV\_MPPT}\left(1 - \frac{\Delta\omega}{\Delta\omega_{max+}}\right), \qquad 0 \leq \Delta\omega \leq \Delta\omega_{max+} \tag{4.1}$$

where P_{PV_MPPT} is the maximum power tracking point of the PV power. $\Delta\omega$ and $\Delta\omega_{max+}$ are the bus frequency deviation/variation and its maximum positive deviation value, respectively.

The auxiliary unit will only produce power if the bus frequency drops below the nominal frequency. Therefore, the power from the auxiliary unit P_{aux} is given by

$$P_{aux} = \frac{\Delta\omega}{m_{aux}}, \qquad \Delta\omega_{max-} \leq \Delta\omega < 0 \tag{4.2}$$

For the standalone microgrid where the battery is the AC bus former, the power of the battery P_{bat} is given by

$$P_{bat} = P_{PV} + P_{aux} - P_{load} \tag{4.3}$$

Equations (4.1) to (4.3) represent the simplified model which is shown in Figure 4.1. The FLC takes SOC and P_{bat} as the inputs and determines the required shift in the bus frequency as the output.

The method in [71] is used for the SOC calculation which is based on the coulomb counting principle as shown in Figure 4.2. C_{bat} is the battery capacity in amp hour (Ah) while V_{bat} is the battery voltage. Because there are 3600 seconds in an hour, one Ah equals 3600 coulombs and that is reason for using this value. $SOC_{initial}$ is the initial SOC value. The whole SOC calculation block is just like a low pass filter where "s" is the Laplace operator. This low pass filter (LPF) with a small time constant is simply required because the change in the SOC is slow while the current is changing quickly. Hence, the LPF will slow the battery's current to make it suitable and in line with the slow response of the SOC.

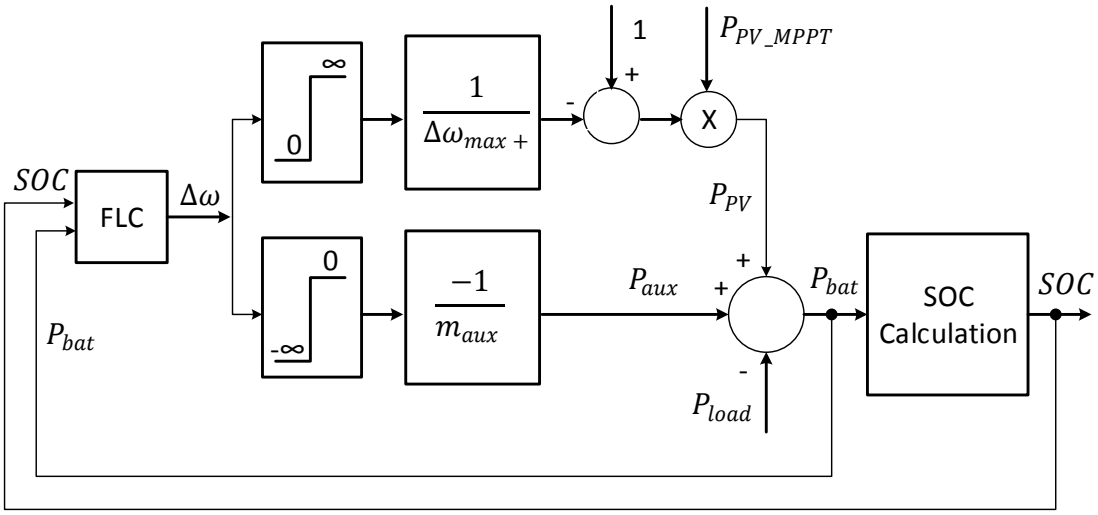

Figure 4.1: Simplified model

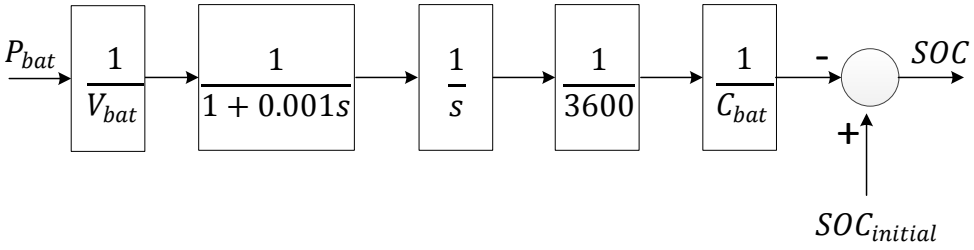

Figure 4.2: SOC calculation

In order to assess the performance of the FLC against that of a conventional proportional controller, a proportional controller is designed and proposed for comparison with the FLC. The proposed controller is shown in Figure 4.3 where P_1, P_2, P_3 and P_4 are the proportional controller's gains. The simplified model with the proportional controller is shown in Figure 4.4.

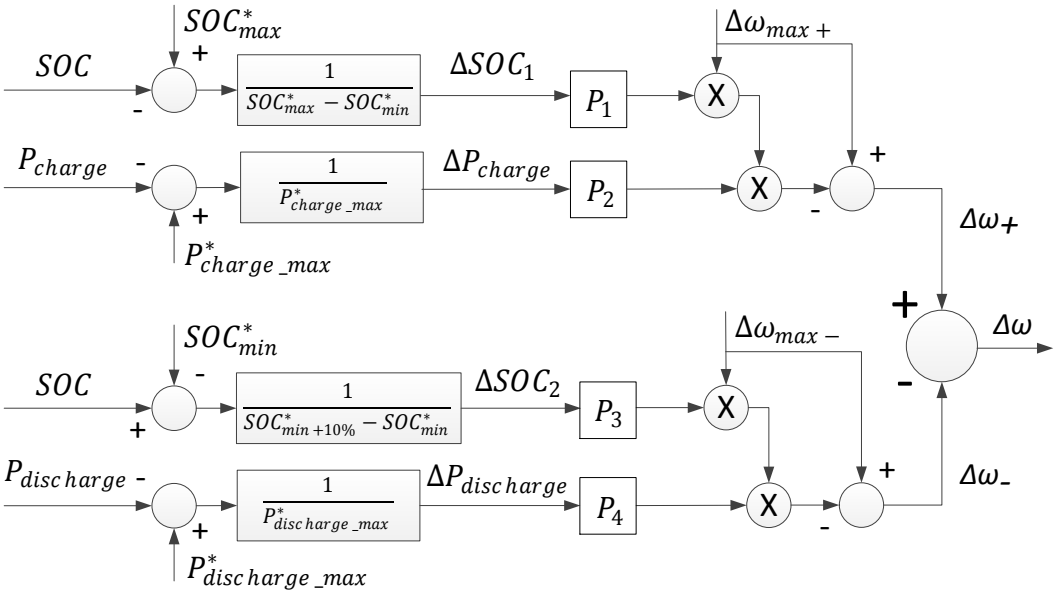

Figure 4.3: Proposed proportional controller

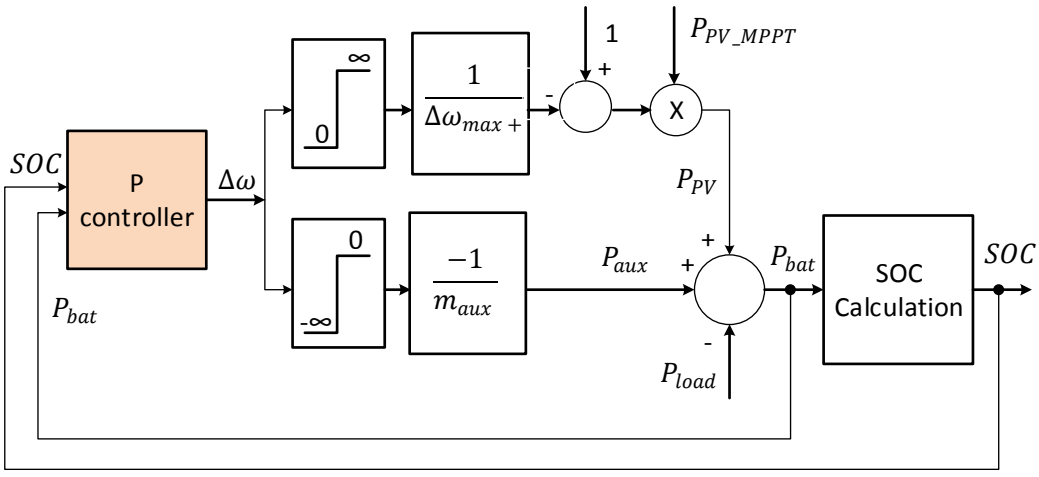

Figure 4.4: Simplified model with proportional controller

4.3 Short-term Matlab/Simulink Simulation Results

The purpose of this simulation is to assess the performance of the FLC in keeping the battery power and SOC within their limits. To test the FLC's performance, its performance is compared with the performance of the conventional proportional controller where quick step changes in the load profile are applied for various scenarios with different values of maximum PV power and SOC. The available PV power used in the simulation represents the maximum power. The aim is to design the proportional controller and then through simulations prove that the performance of the FLC is superior to that of the proportional controller in achieving the required results within the given constraints.

Simulation case 1 and 2 are carried out as part of the design of the proportional controller. To test the FLC controller at different input values and to make the designed controller working universally rather than limited to a particular value only, the minimum SOC limit SOC_{min}^{*} is used as 30% in short-term simulation instead of 40%. However, this does not affect the results' dynamics in terms of the behaviour or decision of the FLC. The minimum SOC limit is a controller input parameter that can be changed by the user. The controller's performance should show that the SOC can be limited to this new value. The system parameters used in the simulation are shown in Table 4.1. The simulation results of different cases with the FLC and proportional controller are presented below.

Table 4.1: Simulated System parameters

Parameter	Symbol	Value
Maximum state of charge	SOC^*_{max}	95%
Minimum state of charge	SOC^*_{min}	30% in short-term simulation (40% in long-term simulation)
Minimum state of charge plus 10%	$SOC^*_{min+10\%}$	40% in short simulation (50% in long simulation)
Maximum charging power	$P^*_{Charge\_max}$	1000 W
Maximum discharging power	$P^*_{Discharge\_max}$	1000 W
Nominal bus frequency	$\omega_o = 2\pi f_o$	$2\pi(50)$=314.16 rad/s
Maximum positive frequency deviation	$\Delta\omega_{max+}$	0.5 Hz
Maximum negative frequency deviation	$\Delta\omega_{max-}$	-0.5 Hz
Proportional controller gains	P_1, P_2, P_3, P_4	10
Battery capacity	C_{bat}	100Ah
Battery voltage	V_{bat}	120V
Active power droop coefficients	m_{PV}, m_{aux}	0.75e-4 rad/s/W
Reactive power droop coefficients	n	0.75e-4 V/Var

Case1: 1500W PV power & 50% SOC:

Figure 4.5 shows the power output of the PV, battery and auxiliary units along with the load, SOC and frequency with an initial value of the battery SOC equals to 50%. The FLC is deactivated before t=2s and the available PV power (dotted line of P_{pv}) and the load are 1500W and 1700W, respectively. Therefore, the battery is in discharging mode and provides 200W power (P_{bat}). The auxiliary unit is not providing any power (P_{aux} = 0). At t=2s, the FLC is activated and there is no requirement for any change, so everything remains the same. From t=3s to t=5s, responses are almost the same without changes although there are several drops in the load from 1700W at t=3s to 1000W at t=4. The battery is still in charging mode during this period, but the amount of charging power increases with the reduction in the load. At t=5s, the charging power reaches the maximum allowable value (i.e. 1000W). Hence, the PV power generation is curtailed in steps until it reaches around 980W (solid line of P_{pv}) at t=8s since the load becomes zero at this time. The SOC increases with the time during the second half of the simulation period. Discharging power is maintained below the maximum limit. Frequency is altered and maintained within its limits as per the FLC command.

Similar responses are obtained when using the proportional controller as can be seen from Figure 4.6 which is activated at t=2s. This scenario/case is used for designing the proportional controller and it shows that the proportional controller provides similar responses like the FLC.

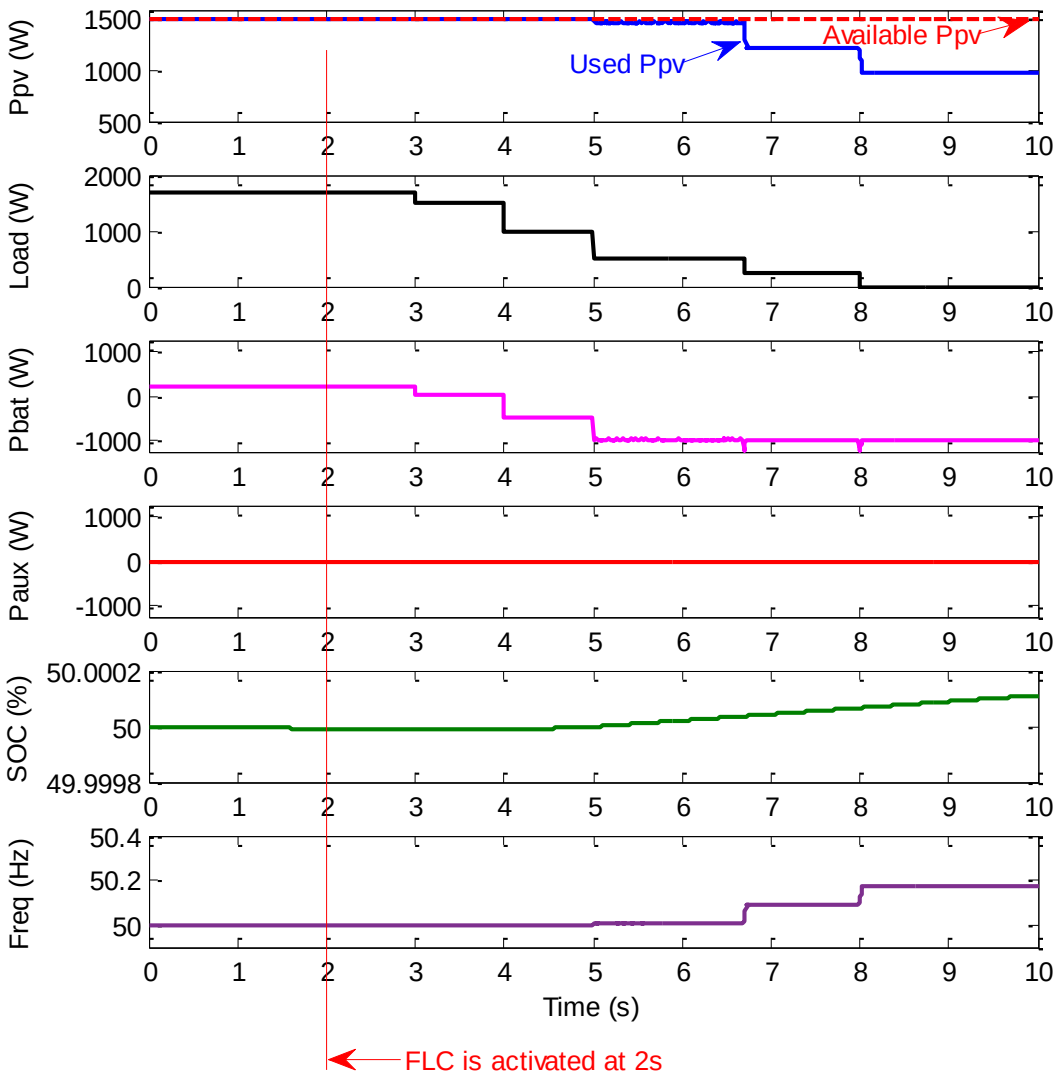

Figure 4.5: Output responses for 1500W PV power & 50% SOC - FLC case

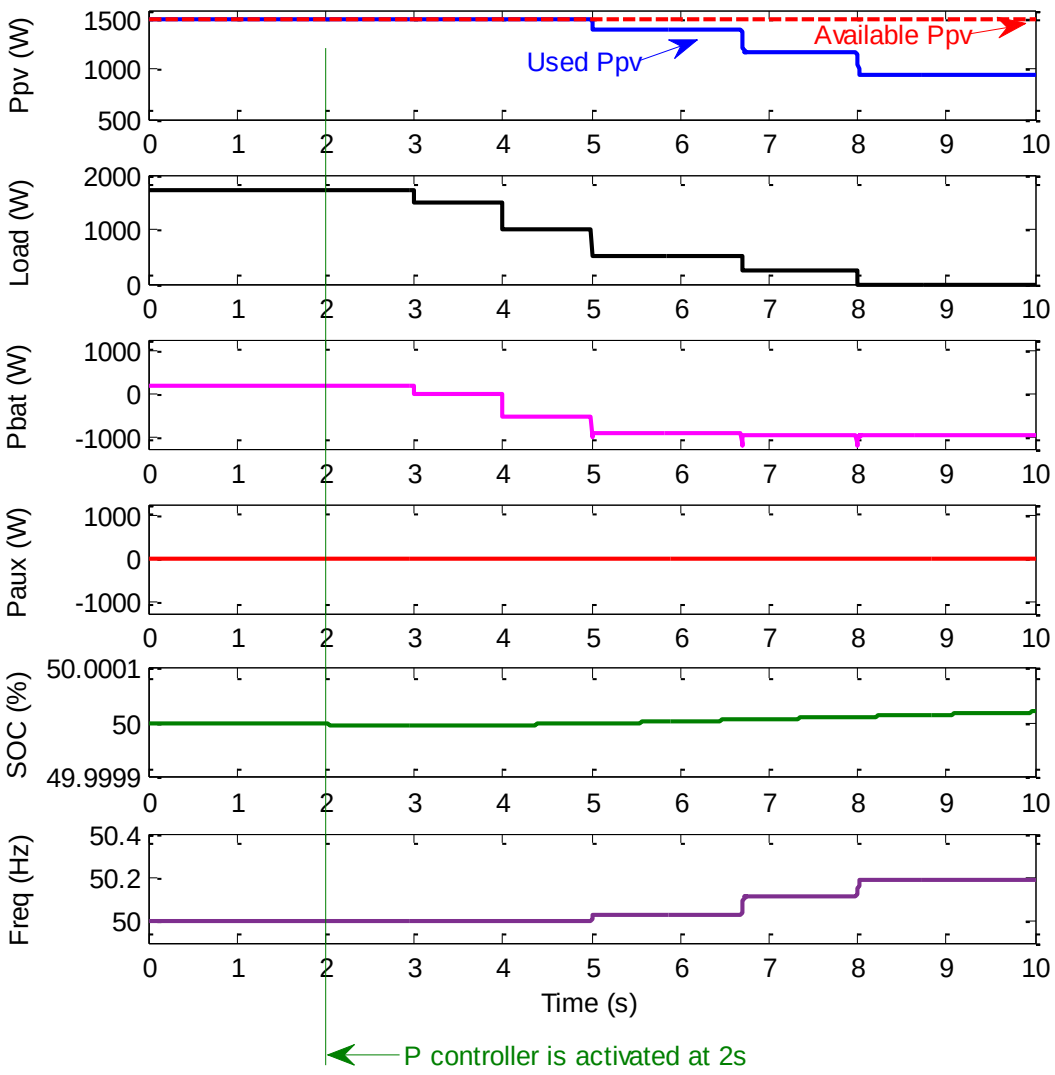

Figure 4.6: Output responses for 1500W PV power & 50% SOC - proportional controller

Case2: 500W PV power & 30% SOC case:

Another design case for the proportional controller is this one where the proportional controller provides similar responses like the FLC. The simulation result is shown in Figure 4.7 for the FLC and Figure 4.8 for the proportional controller where similar responses are obtained with an available PV power equals to 500W and an initial SOC value of 30%. Before the activation of the FLC or proportional controller, the maximum discharging power limit is exceeded since the load is much higher than the PV generation and the remaining power is supplied by the battery. The auxiliary unit is not used. Once the FLC (Figure 4.7) or proportional controller (Figure 4.8) is activated at t=2s, the auxiliary unit is used immediately since the PV power is less than the load

and the SOC is very low. The SOC is stopped from declining, kept constant and hence protected from under-charging before it starts increasing until the end of the simulation. The SOC in the case of the FLC is increasing at a higher rate compared to the case with the proportional controller. Again the frequency is changing as per the FLC or proportional controller command, but the PV power is not curtailed this time since the SOC value is very low and the available PV power is not high in comparison to the load.

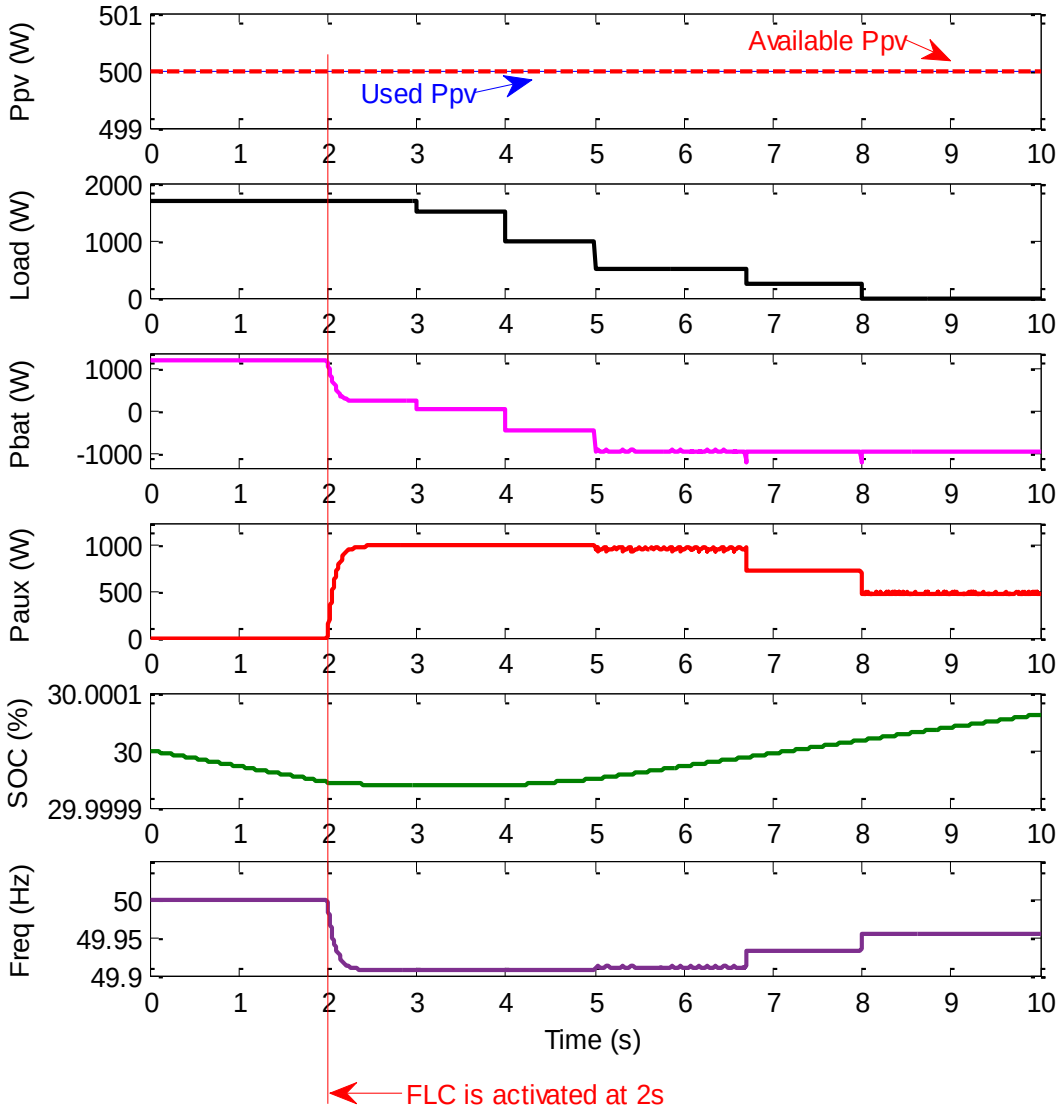

Figure 4.7: Output responses for 500W PV power & 30% SOC - FLC case

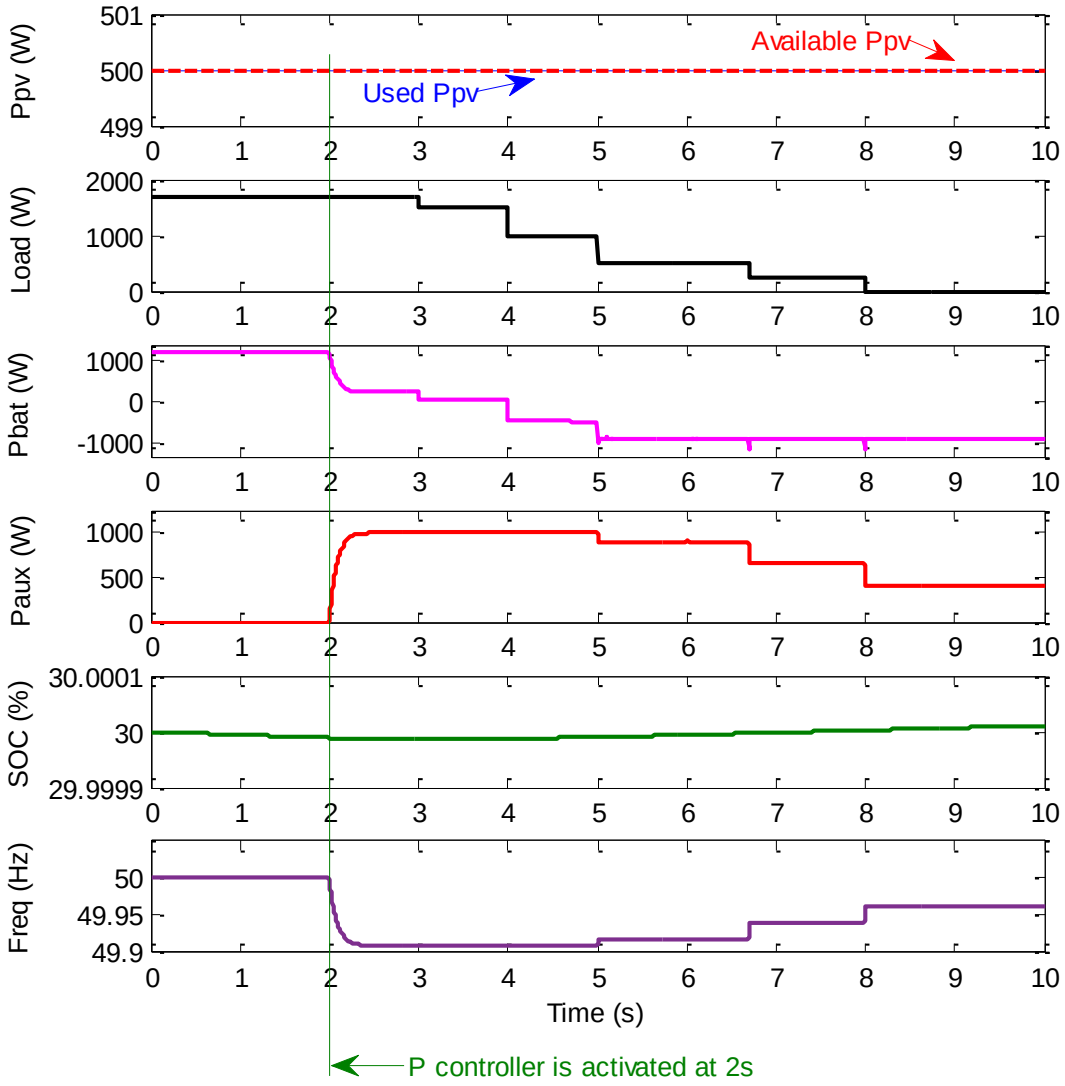

Figure 4.8: Output responses for 500W PV power & 30% SOC - proportional controller

Case3: 1500W PV power & 95% SOC case:

Figure 4.9 shows the response when the initial SOC value equals to 95%. The FLC is deactivated before t=2s. The available PV power is 1500W and the battery provides 200W power since the load is 1700W. Therefore, the battery is in discharging mode and the auxiliary unit is not providing any power. At t=2s, the FLC is activated and there is no requirement for any change. However, at t=4s, the load becomes 1000W and the SOC is still equal to 95%. Hence, the PV power generation is curtailed until it becomes very close to zero towards the end of the simulation and the SOC is maintained at the maximum allowable limit (95%). The frequency is maintained within its limit. Results with the proportional controller in Figure 4.10 show that the PV power is curtailed to 285W

immediately after the controller activation at t=2s, which causes the maximum discharging power to exceed its maximum limit between t=2s and t=4s. There is no power from the auxiliary unit. It is very clear from this case that the performance of the FLC is better than that of the proportional controller.

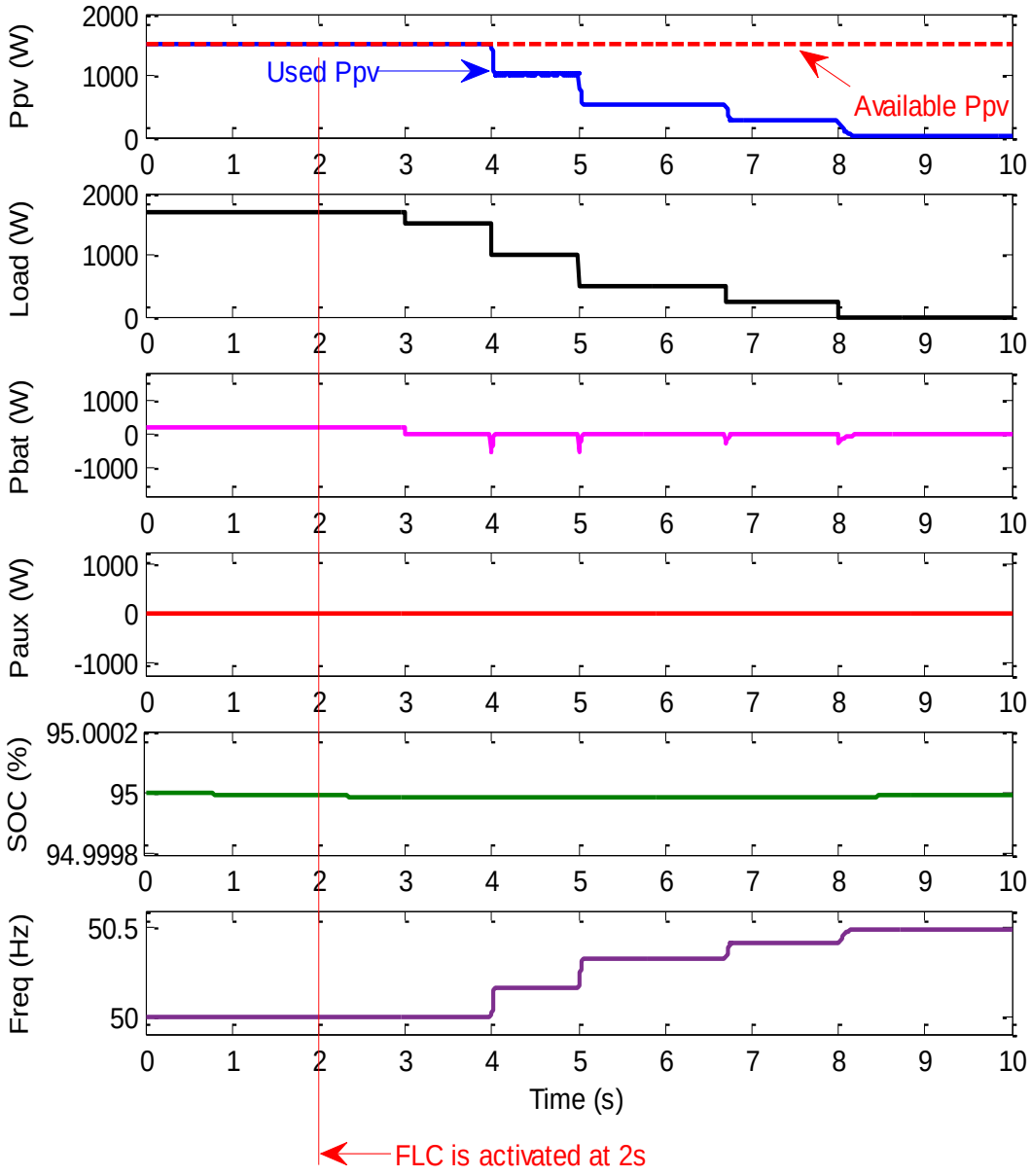

Figure 4.9: Output responses for 1500W PV power & 95% SOC - FLC case

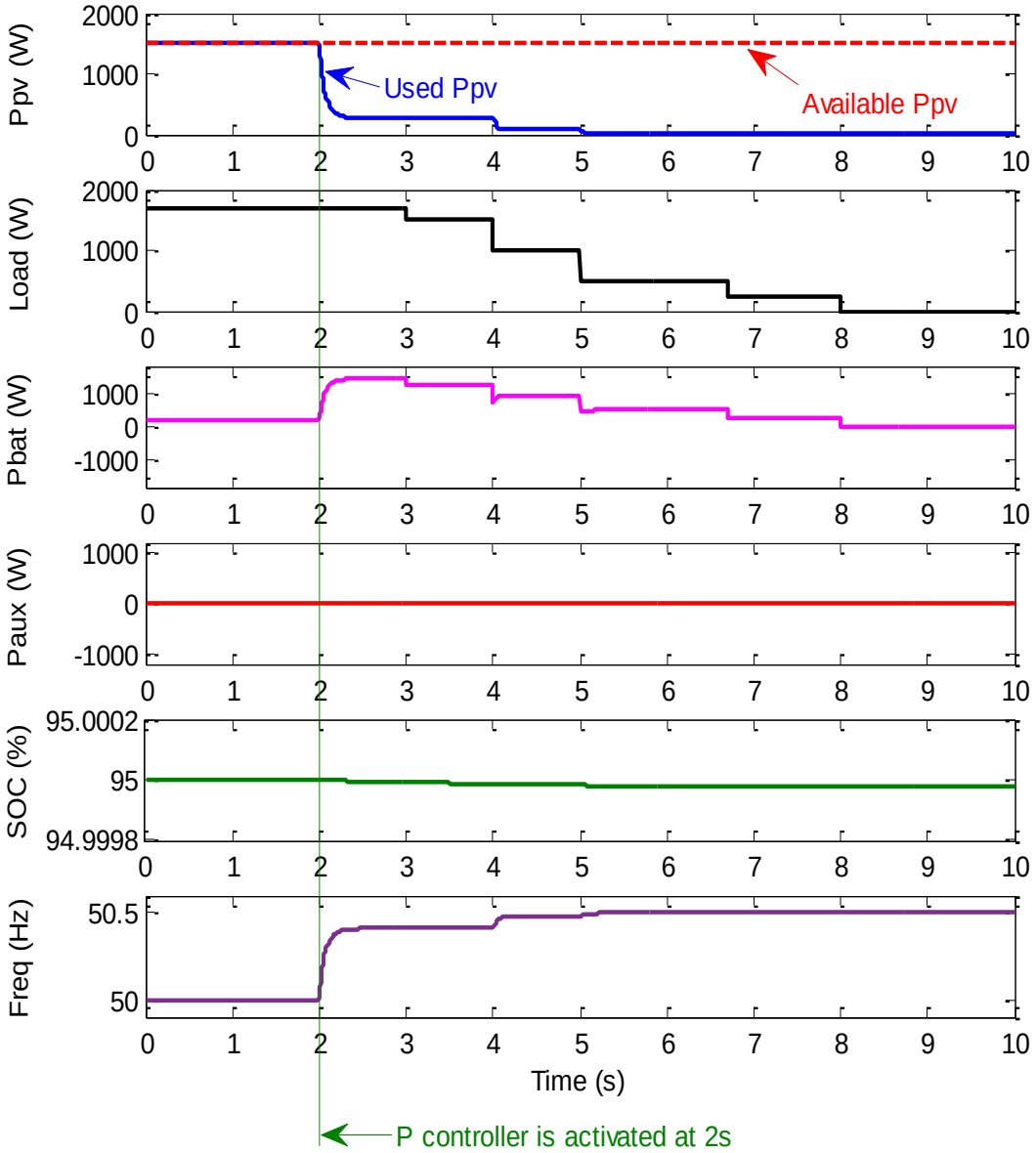

Figure 4.10: Output responses for 1500W PV power & 95% SOC - proportional controller

Case4: 2000W PV power & 30% SOC case:

Another comparison is carried out between the FLC in Figure 4.11 and the proportional controller in Figure 4.12. The available PV power is 2000W and the load is 1700W. The initial SOC value is 30% and the battery is always in charging mode. In this case, the auxiliary unit is used immediately after the activation of the FLC (Figure 4.11) or proportional controller (Figure 4.12) at t=2s until t=4s where the PV power is curtailed. The SOC and charging power are maintained within their allowable limits for both controllers. However, the SOC in the case of the FLC is increasing at a higher rate compared to the case

with the proportional controller. The frequency is changed as per the FLC or proportional controller command and maintained within the limits.

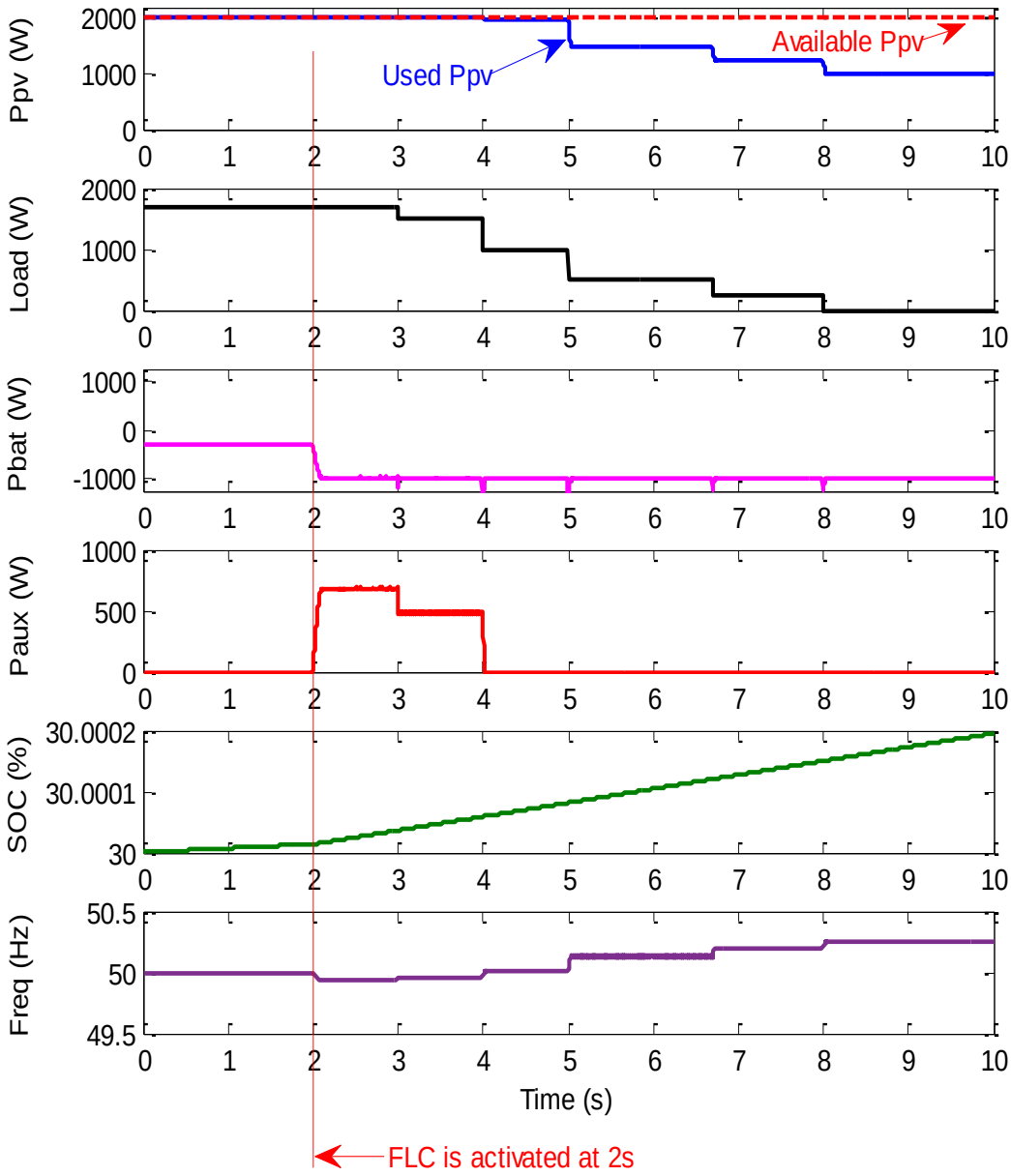

Figure 4.11: Output responses for 2000W PV power & 30% SOC - FLC case

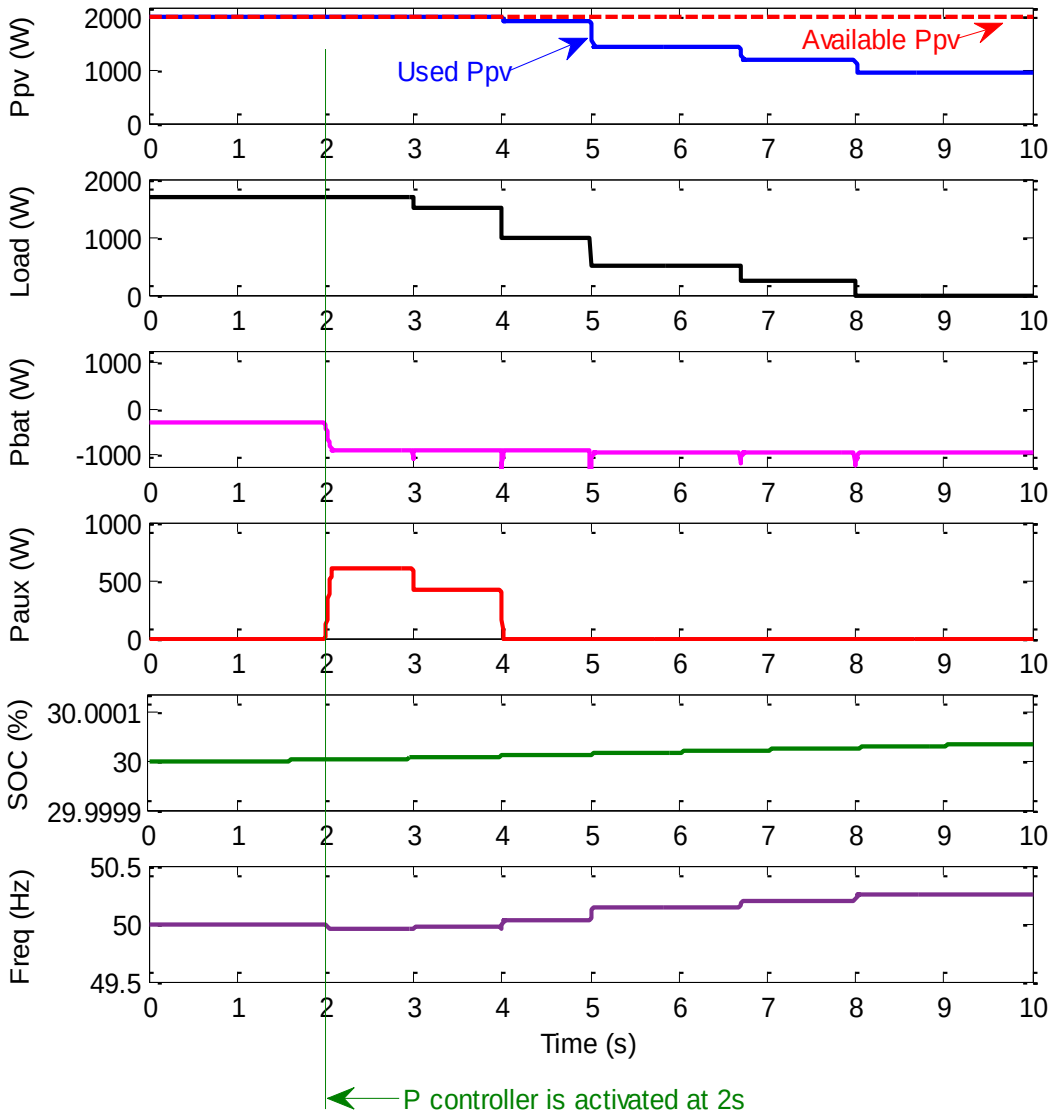

Figure 4.12: Output responses for 2000W PV power & 30% SOC - proportional controller

Case5: 100W PV power & 95% SOC case:

Figure 4.13 shows the case when the PV power equals 100W only and the initial value of the SOC is 95%. Before the activation of the FLC, the maximum discharging power limit is exceeded since the load is much higher than the PV generation and the auxiliary unit is not used. Thus, the remaining power is supplied by the battery. Immediately after the FLC is activated at t=2s, the auxiliary unit provides the required shortage in the power and relieved the battery. The battery still remains in discharging mode, but with less contribution after t=2s. The PV power is curtailed at t=8s when the load becomes zero. The SOC, the discharging power of the battery and the frequency are all maintained

within their limits. Results with the proportional controller are shown in Figure 4.14. The PV power is curtailed immediately after the activation of the proportional controller in comparison to the PV curtailment at t=8s for the FLC case as shown in Figure 4.13. Therefore, more power is taken from the battery rather than utilizing the available PV power. This causes the discharging power to exceed its maximum limit. The auxiliary unit is not providing any power. So, from this case, it is again very clear that the performance of the FLC is better than the proportional controller.

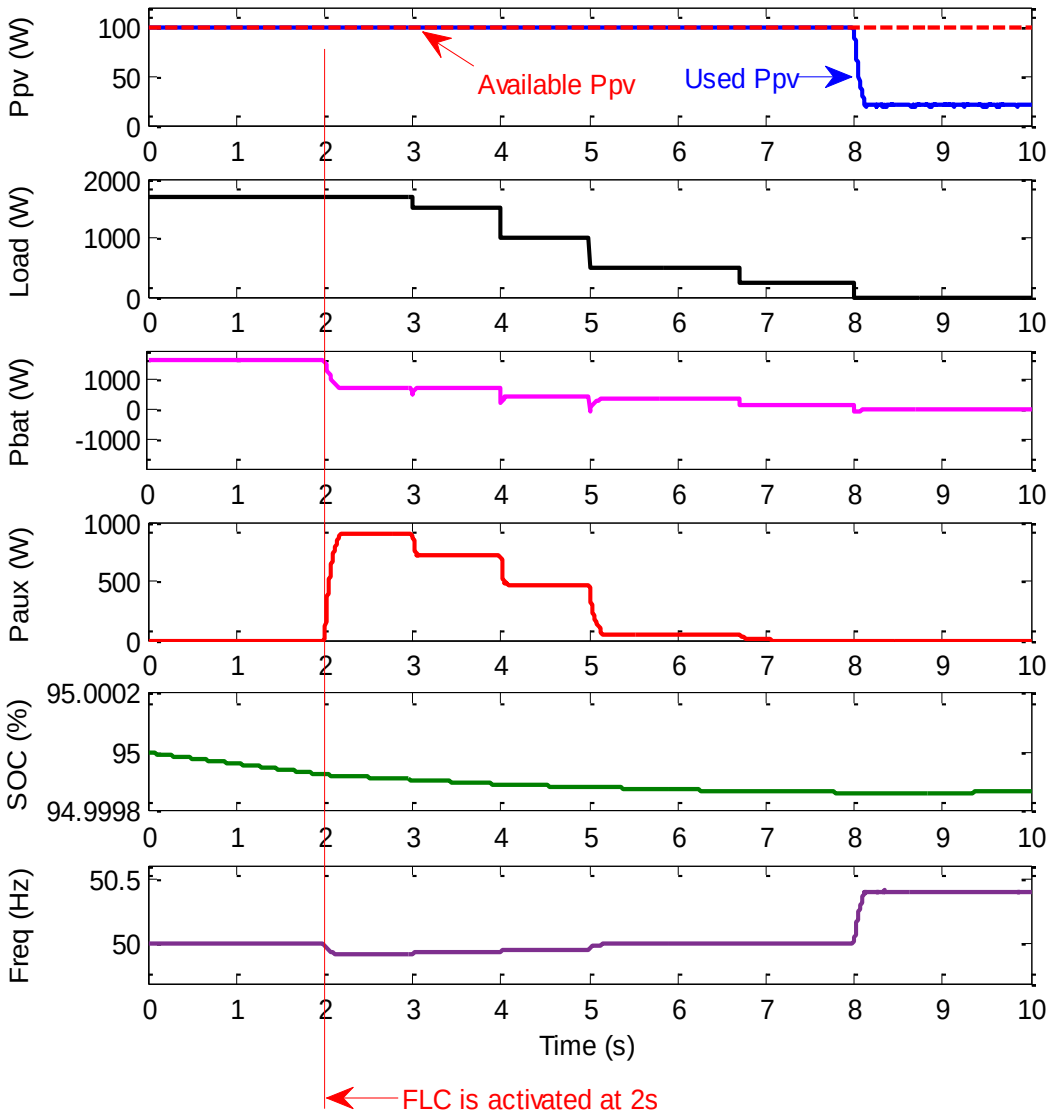

Figure 4.13: Output responses for 100W PV power & 95% SOC - FLC case

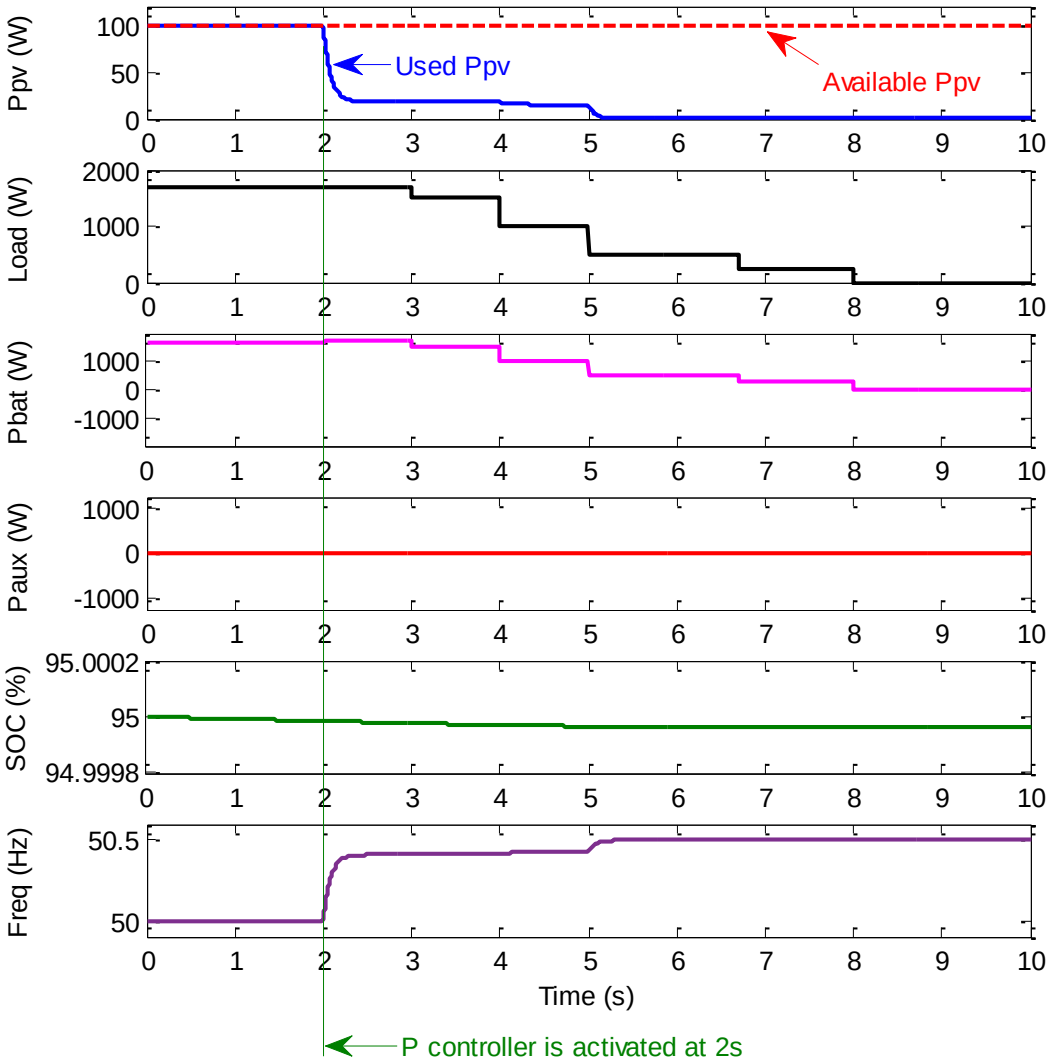

Figure 4.14: Output responses for 100W PV power & 95% SOC - proportional controller

According to the above results, the FLC uses the available full PV power when required and curtails it to prevent the battery from over-charging only when needed. In addition, it activates the auxiliary unit to support the battery and to protect it from under-charging. This is achieved by changing the frequency in such a way that the PV unit produces maximum possible power according to its MPPT as long as the bus frequency equals or less than the nominal frequency. On the other hand, the auxiliary unit produces power only if the bus frequency dropped below the nominal frequency. The SOC and frequency are maintained within their acceptable limits. The FLC shows better results when compared to the proportional controller. Therefore, real-time simulation will be conducted with the FLC only.

4.4 Real-Time Simulation Results

A real-time simulation allows a particular designed system to run with the same rate or speed of the physical system. The rationale behind using a real-time simulation is mainly speed as well as being able to supply real input data in a real-time. Nowadays, a real-time simulator can be used to emulate the actual performance of a system or controller. Hence, the system or controller can be modelled either completely by a real-time simulator without hardware or partially (where some parts of the system can be built in hardware). This does avoid the need for building the whole actual system at full capacity [110], [111]. The OPAL real-time simulator, which is used in the work of this thesis, does have high speed and powerful CPU with a larger memory which are great advantages in comparison with normal simulation using standard computers. This will decrease the time required for the simulation.

The simplified model shown in Figure 4.1, including the three power units with the load and the proposed controllers, has been developed and built in Matlab/Simulink, but this time using the OPAL RT-LAB (real-time simulator) to assess the performance of the proposed FLC in the real-time environment and for a long period of time. The SOC calculation is as shown in Figure 4.2. The minimum SOC limit SOC_{min}^{*} for this simulation type is 40% which is the base case. However, this can be changed to any other value as decided by the user. The rest of the system parameters are the same as those shown in Table 4.1. The real-time simulation (long-term simulation) does not require the comparison with the proportional controller since the first type of the simulation concludes that the FLC is superior in in achieving the required results within the given constraints compared to the proportional controller.

Solar radiation is recorded on the roof of the Environment and Sustainability Institute (ESI) in Penryn Campus at Penryn, UK. Figure 4.15 shows 12 hours of actual solar radiation data recorded on 25th October 2015 from 07:00 a.m. to 07:00 p.m. which is used for each case of the real-time simulations. However, the simulation assumes a larger PV area since the available solar PV panels that are installed as part of the microgrid have a total capacity of 1034W (3 x 345W of X21 Sunpower panels) only as will be seen in Chapter 5. The following

simulation cases have been conducted to demonstrate the performance of the FLC.

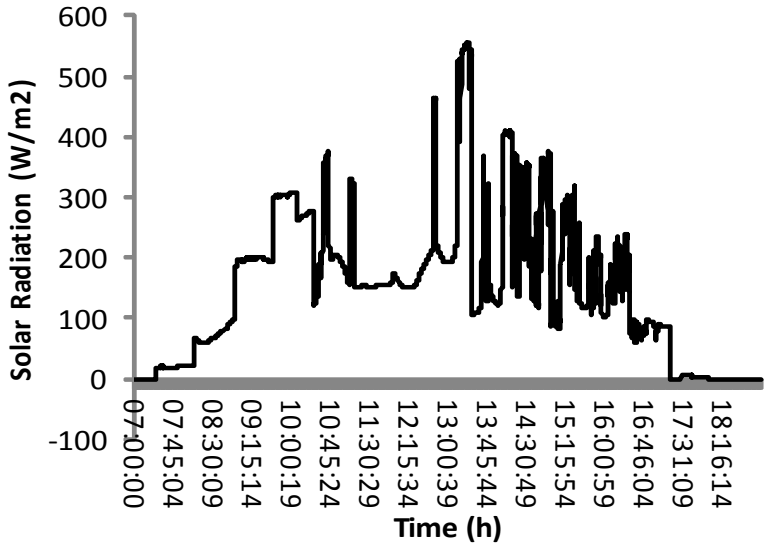

Figure 4.15: Actual solar radiation

Case 1: High SOC:

In this case, the battery has a high SOC value of 95%. The power output of the PV, battery and auxiliary units along with the load power are shown in Figure 4.16(a). The load demand profile is lower than the available PV power and therefore, there will be a surplus PV power that might exceed the battery charging requirement. The FLC is not activated in this case to observe the response of the system without the FLC. Because no PV power curtailment occurs (i.e. the available and used PV powers are the same) and the load power is quite low, the battery has to absorb most of the PV power which is shown by the negative sign of the battery power (charging mode). This caused the battery to over-charge and the SOC to increase beyond the limit of 95% as shown in Figure 4.16(b). In addition, the maximum charging power limit (i.e. 1000W) is exceeded several times due to continuous utilization of full PV power. Figure 4.16(c) shows a constant bus frequency as the FLC is disabled.

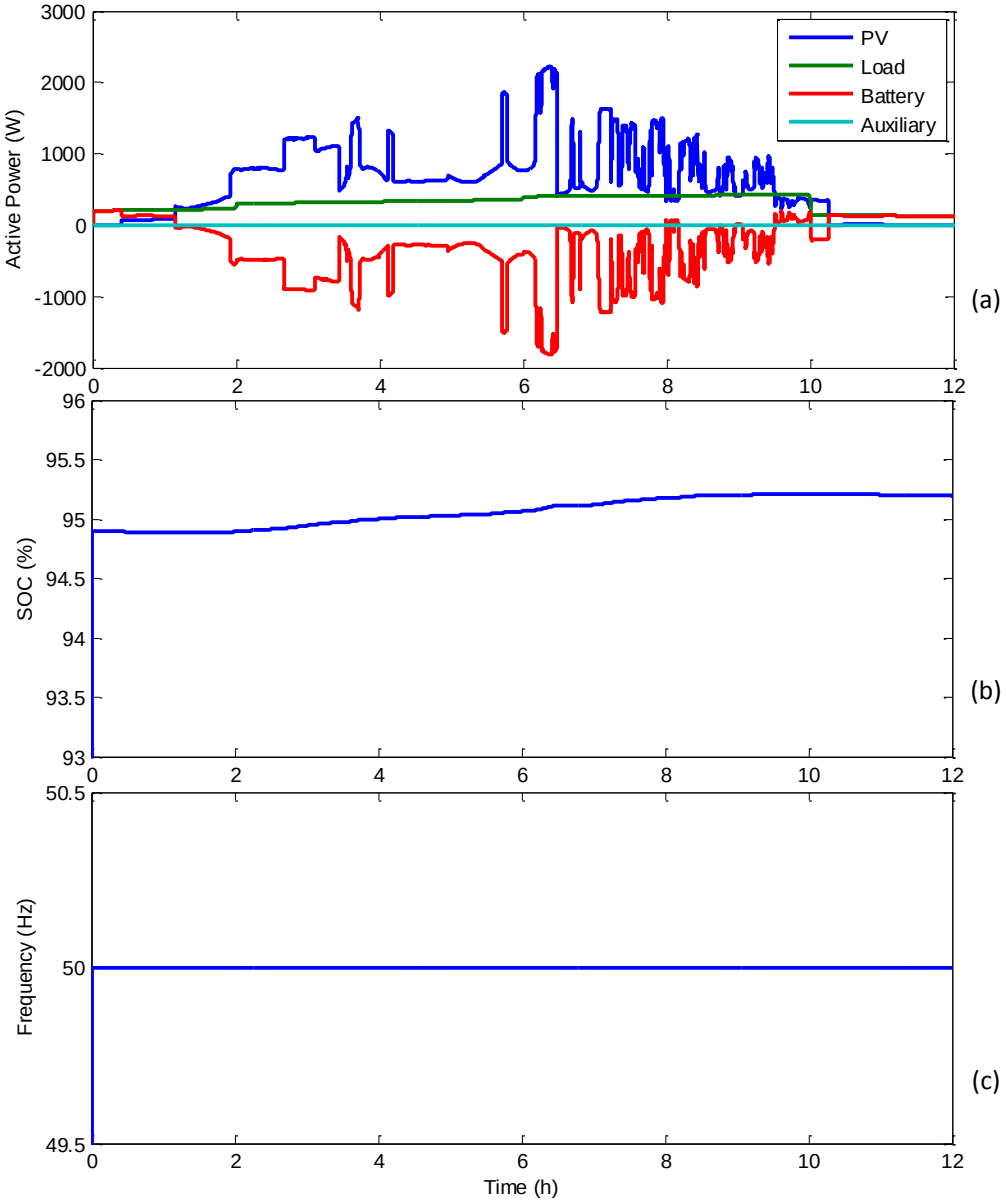

Figure 4.16: Output response for 94.9% SOC case without FLC: (a) power (b) SOC (c) frequency

Figure 4.17 shows the simulation results of the same case, but the FLC is activated. The expectation is that the PV power should be used to supply the load and any excess power will be curtailed. Initially, there is no power generated by the PV since the solar radiation is almost zero during the first 30min. The load is fully supplied by the battery (starting from 200W) and the auxiliary unit is not supplying any power as the battery SOC is high. After the PV starts generating more power, the contribution from the battery is reduced.

At t=1h, the PV generation is almost following the load's profile and the extra power is curtailed.

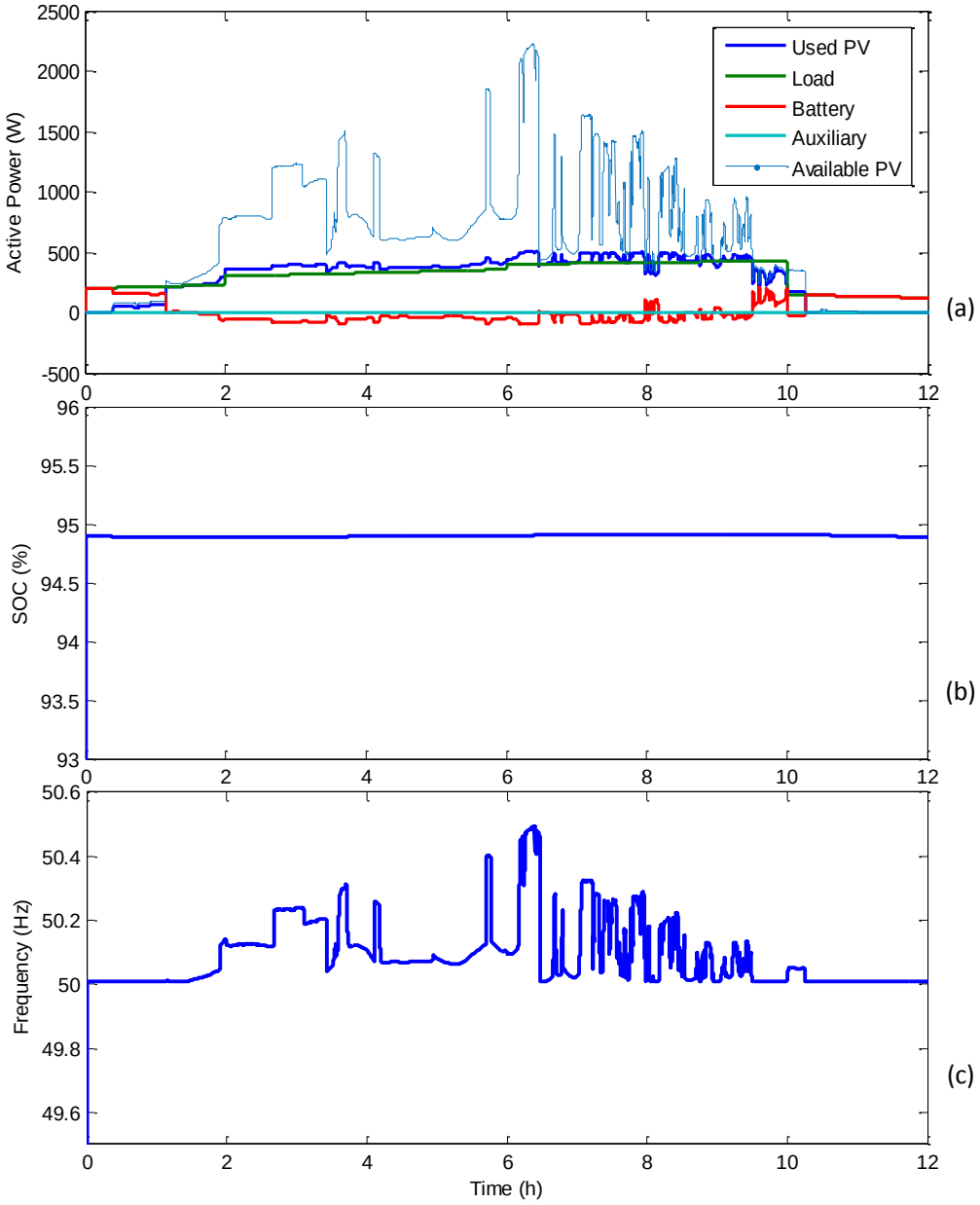

Figure 4.17: Output response for 94.9% SOC case with FLC: (a) power (b) SOC (c) frequency

Most of the time, the used PV is a little bit higher than the load as shown in Figure 4.17(a) and the battery is not really used much as per the FLC command since the priority is given for full utilization of the PV power and the SOC is high. However, whenever there is a need for extra power to meet the load, the battery is supplying that extra power and this can be easily observed from t=9.5h

onwards. The auxiliary unit is not used at all throughout the simulation in this case since the PV and the SOC of the battery are sufficient to cope with the load. The charging/discharging power is maintained within its limit. Figure 4.17(b) shows that the SOC remains almost constant and it is prevented from exceeding its maximum limit. If the battery had been charged with the surplus available PV power and the FLC didn't give the command for the PV curtailment whenever required, the SOC would definitely exceed the 95% (maximum limit) and the maximum charging power of the battery would be exceeded as well. Figure 4.17(c) shows the frequency curve where the frequency is maintained within its limits (± 1%) irrespective of the changes in the load or the PV generation.

Case 2: Low SOC:

Figure 4.18(a) shows the power output along with the load power for a low SOC value equals to the minimum limit which is 40%, but the FLC is not activated this time. Initially, there is no power generated by the PV in the first half an hour since the solar radiation is almost zero. The battery is completely supplying the load. At t=1h, the PV starts generating power and the contribution from the battery is reduced. The charging power of the battery exceeds 1000W as can be seen in Figure 4.18(a) due to the continuous utilization of PV full power which is much higher than the load most of the time. The available PV power equals the used PV power (no PV power curtailment). Furthermore, Figure 4.18(b) shows that the SOC is gradually rising. Figure 4.18(c) shows a constant frequency as the FLC is disabled.

Figure 4.19(a) shows the same case, but with FLC activated. Since the SOC value is low, the auxiliary unit is commanded to operate to avoid the SOC from declining below the minimum limit. The auxiliary unit is floating throughout the simulation period where priority is given to full utilization of the PV power and then the auxiliary unit is used if required. It is obvious that the maximum charging power of the battery is well maintained to the maximum allowable limit which is 1000W throughout the full period of the simulation irrespective of the change in the generation and the load. Figure 4.19(b) shows the SOC curve where SOC is increasing all the time in a higher rate compared to Figure 4.18(b) since the generation is more than the load due to the full utilization of

the PV power most of times and the use of the auxiliary unit whenever required to support the battery because the SOC value is still within the range of the bottom FLC subsystem (40% to 50%) which is responsible for operating the auxiliary unit. This is required because the SOC process is slow and charging takes time. Hence, the battery is always in charging mode to avoid the SOC from declining below its minimum limit. Figure 4.19(c) shows that the frequency is maintained within its limits.

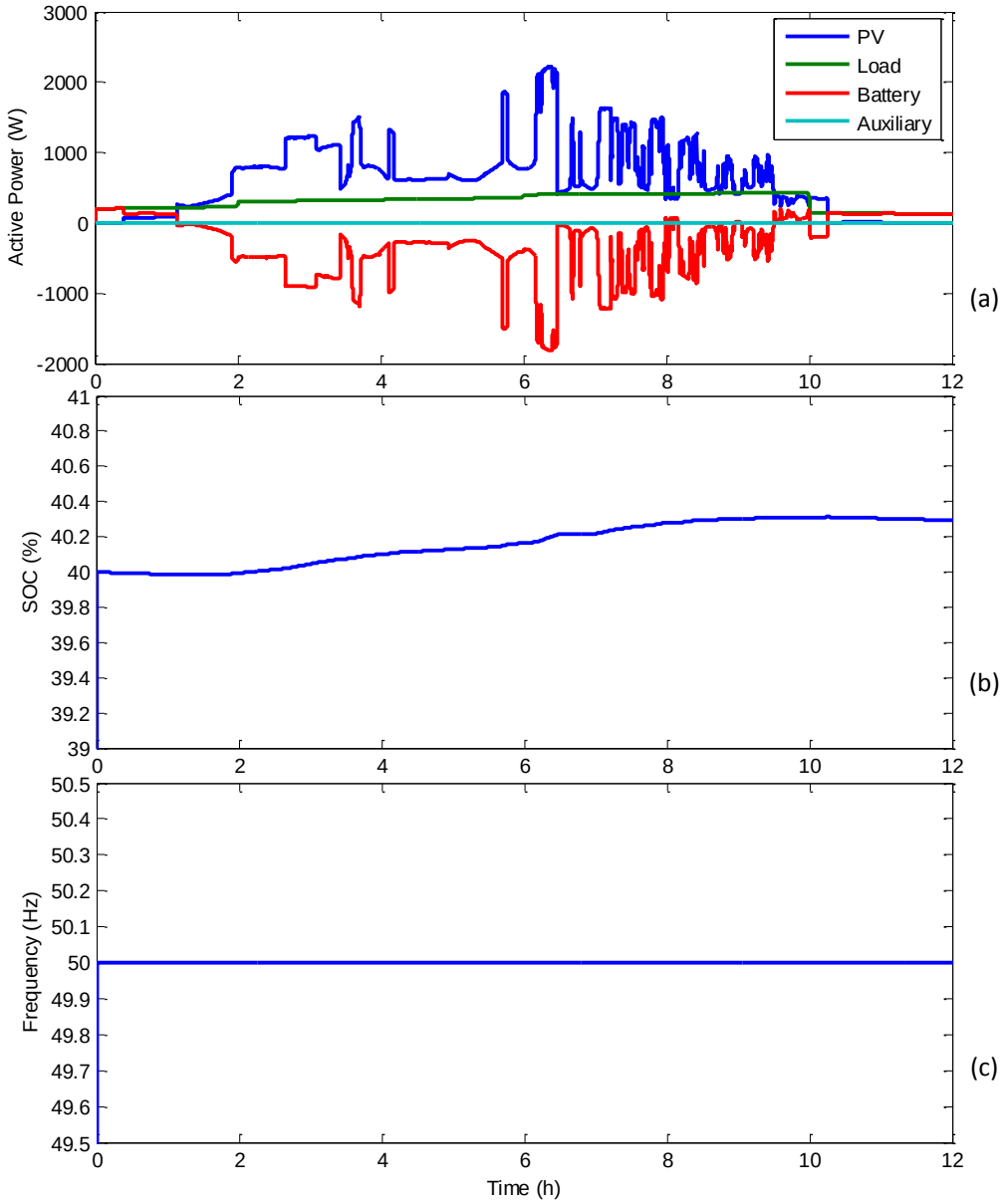

Figure 4.18: Output responses for 40% SOC case without FLC: (a) power (b) SOC (c) frequency

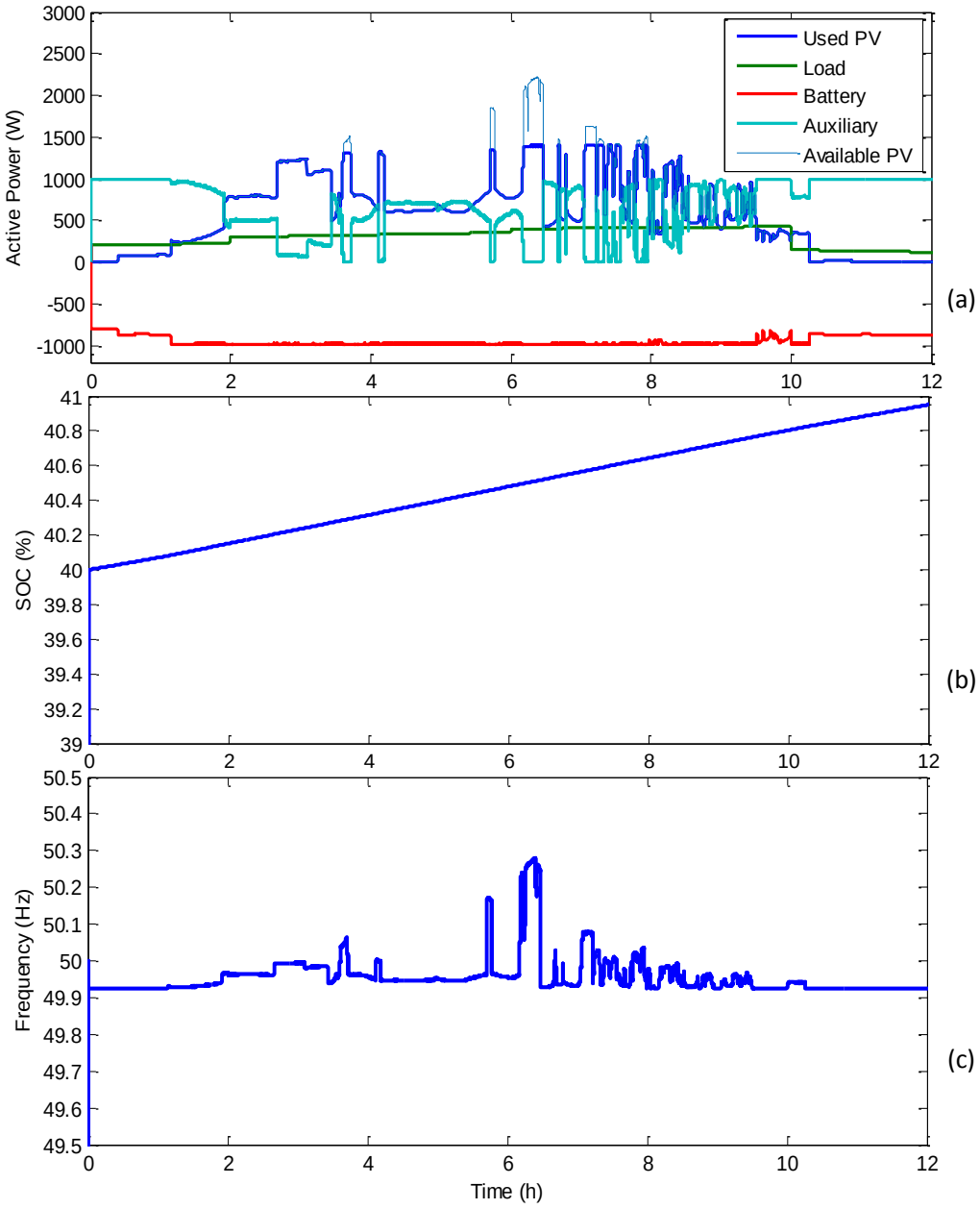

Figure 4.19: Output responses for 40% SOC case with FLC: (a) power (b) SOC (c) Frequency

Case 3: Low SOC with high load:

In this case, the load profile is high which is 4 times of the load considered in cases 1 and 2. The idea is to have higher load values for simulation with similar trend while the rest remains the same. This helps in having a wider range of the load to examine the performance of the FLC. In this scenario, most of the time, the available PV power is lower than the load profile which means there is more

need for support from the battery and auxiliary unit. No PV power curtailment is carried out. Hence, the used PV power equals the available PV power.

Figure 4.20(a) shows the power output along with the load power in the case where SOC is 40%, but the FLC is not activated. Initially, there is no power generated by the PV since the solar radiation is almost zero. The battery is completely supplying the load. After around 30min, the PV starts generating power and the contribution from the battery is reduced. The maximum discharging power of the battery (i.e. 1000W) is exceeded as can be seen in Figure 4.20(a) since the PV generation is lower than the load most of the time and the auxiliary unit is not used. Furthermore, Figure 4.20(b) shows that the SOC is declining and it reaches values lower than the acceptable minimum limit (40%). A constant bus frequency is shown in Figure 4.20(c) since the FLC is not activated.

Figure 4.21(a) shows the power output along with the load power for 40% initial SOC case and high load. The FLC is activated in this case. After the first half an hour, the PV starts generating power. Since the SOC value is low, the auxiliary unit starts providing power immediately to avoid possible decline of the SOC value below the minimum allowable limit (40%). The auxiliary unit is floating throughout the simulation period and providing required power as per the FLC command since the available PV power is lower than the load profile most of the time and the SOC is low. It is obvious that the maximum charging/discharging power of the battery is well preserved within the maximum allowable limit (1000W) throughout the full period of the simulation. Figure 4.21(b) shows the SOC curve where SOC is increasing most of the time since overall generation is generally more than the load and the battery is mostly in charging mode opposite to the case in Figure 4.20(b) where FLC is disabled. Figure 4.21(c) shows that the frequency is maintained within its limits.

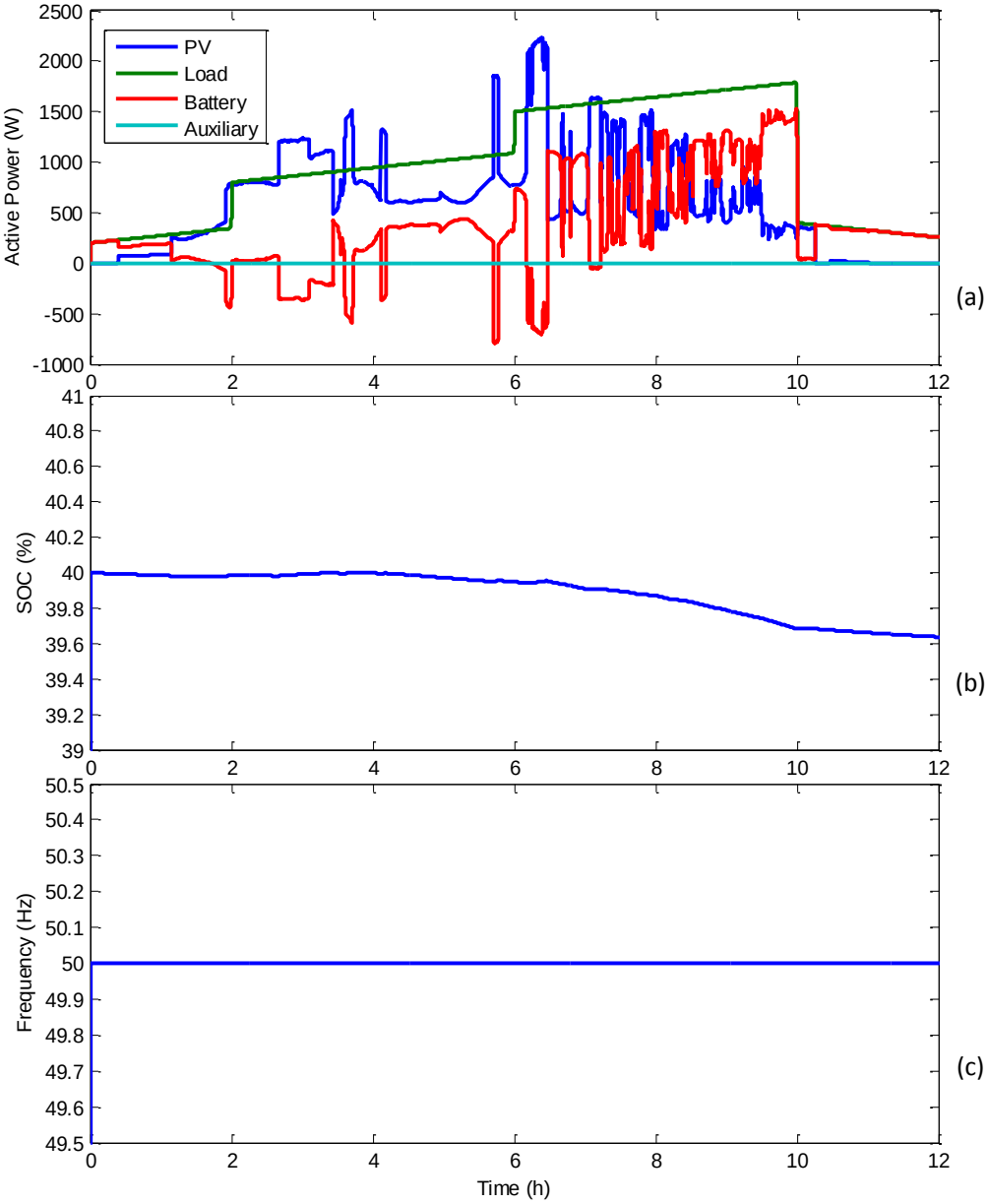

Figure 4.20: Output responses for 40% SOC case without FLC and high load: (a) power (b) SOC (c) frequency

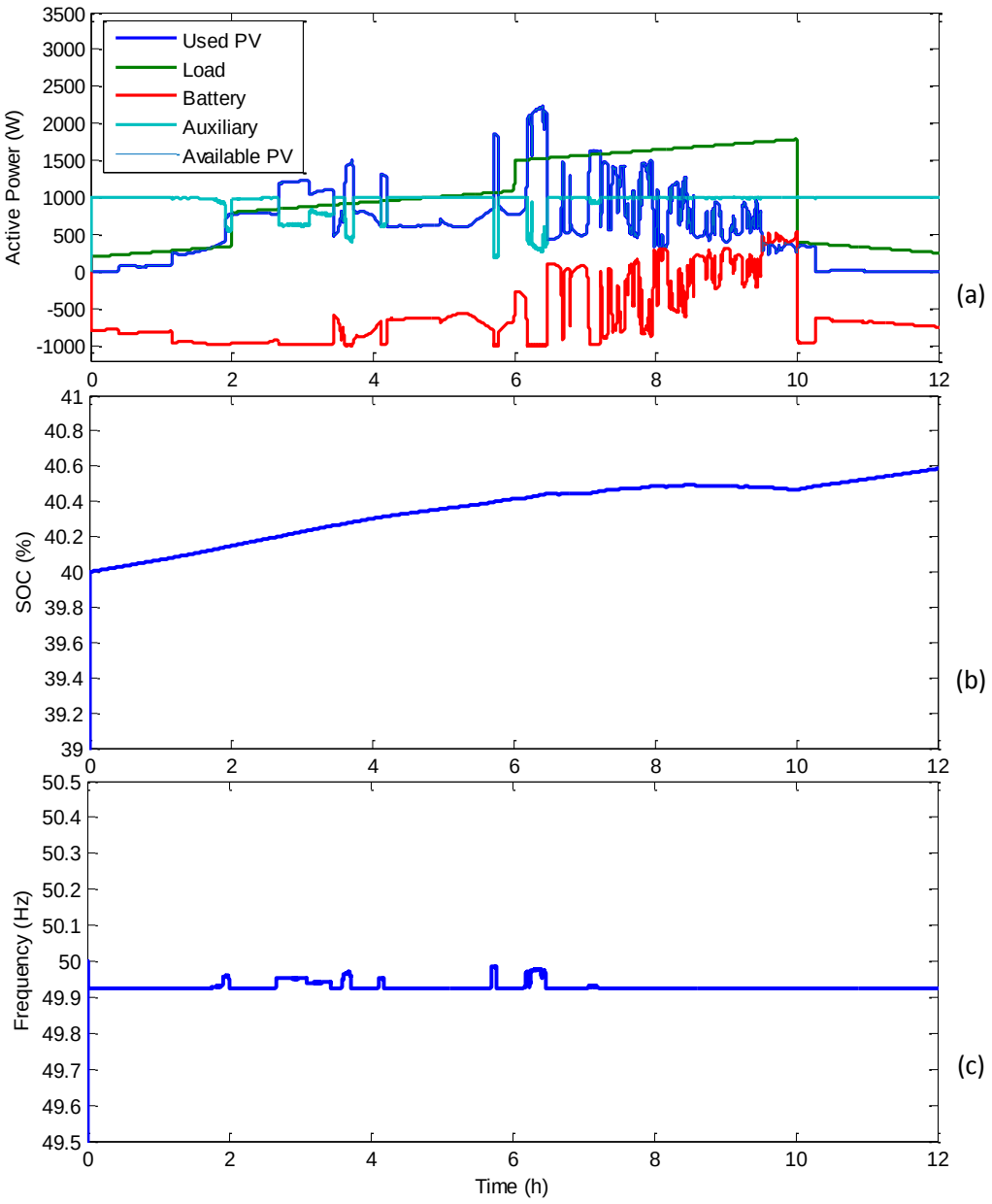

Figure 4.21: Output responses for 40% SOC case with FLC and high load: (a) power (b) SOC (c) frequency

Case 4: Very low SOC:

To further assess the performance of the FLC, simulation is carried out with a starting value of the SOC equals to only 20%. This value is the SOC value before starting the simulation and not a result of the simulation. Hence, there is a real need for charging since the starting value is lower than the minimum limit of the SOC. Therefore, the auxiliary unit is expected to support the battery since the SOC value is very low and the charging process is slow. The SOC value is

within the range of the bottom FLC subsystem (40% to 50%) which is responsible for operating the auxiliary unit. However, the FLC is still expected to maintain the maximum charging to 1000W irrespective of that lower SOC input to the FLC. Figure 4.22(a) shows the power output and as expected the FLC maintains the maximum charging limit and the SOC continues to increase throughout the full simulation period as can be seen in Figure 4.22(b). At the same time, the frequency is maintained within its limit as shown in Figure 4.22(c).

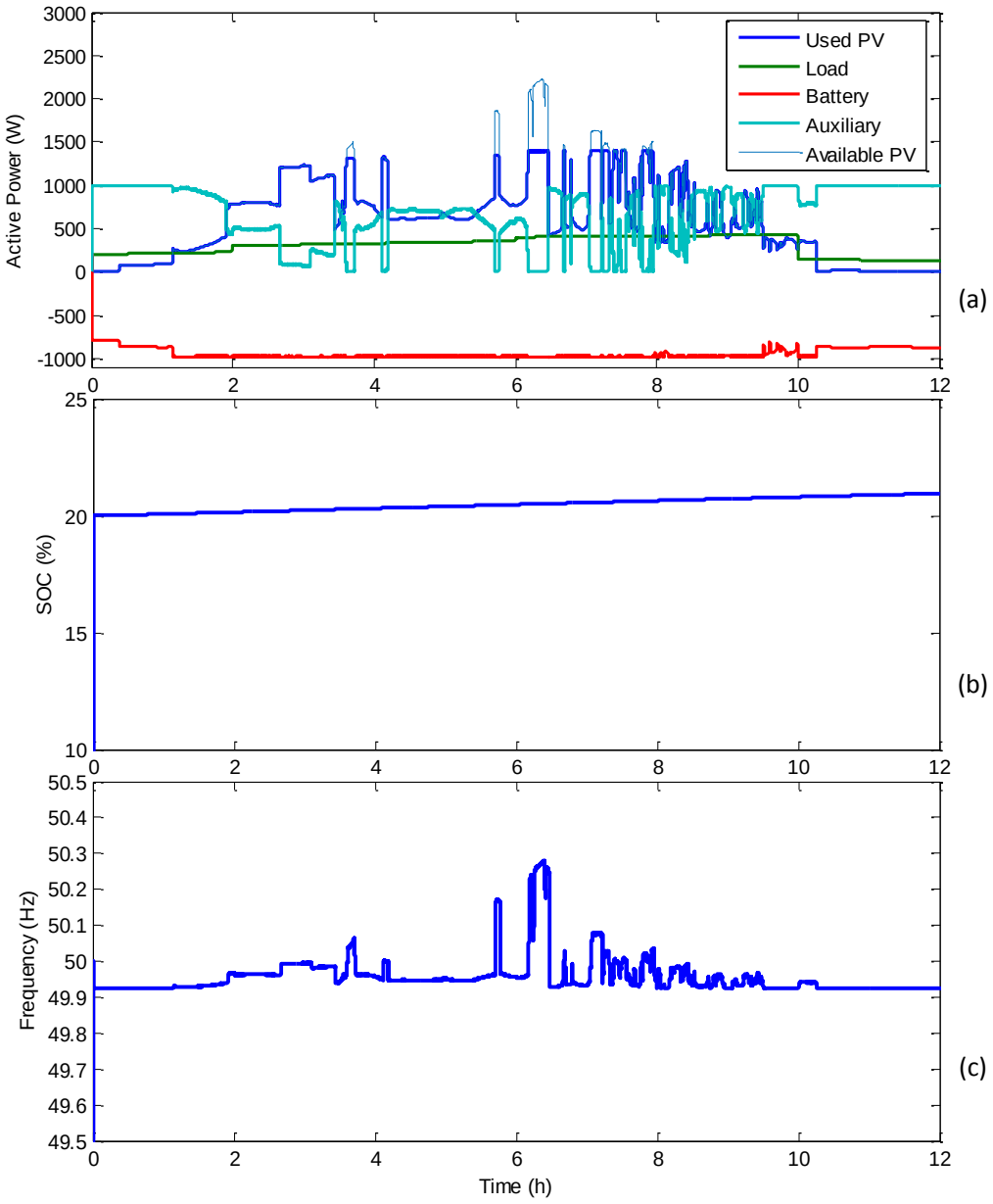

Figure 4.22: Output responses for 20% SOC case with FLC: (a) power (b) SOC (c) frequency

From the results of the real-time simulation, the FLC uses the full available PV power whenever required and curtails it to prevent the battery from over-charging. In addition, it activates the auxiliary unit to support the battery and to protect it from over-discharging. At the same time, the SOC and frequency are maintained within its allowable limits. The results show that if the FLC is not activated or used, the SOC and charging/discharging power may not be maintained within their maximum allowable limits.

4.5 Summary

Short-term Matlab/Simulink simulations and long-term real-time simulations have been conducted for different cases. Results from both simulations have been presented to validate the functionality and performance of the proposed controller. Both simulations show that the proposed FLC uses the full available PV power whenever required and curtails it to prevent the battery from over-charging only when needed. In addition, it activates the auxiliary unit to support the battery and protect it from over-discharging. At the same time, the SOC and frequency are maintained within their allowable limits. The FLC has been compared with a proportional controller and the results show that the FLC performs better than the proportional controller in achieving the required results within the given constraints. As a result, a similar comparison in the real-time simulation has not been conducted. Real-time simulation has been conducted both with and without FLC to demonstrate the effectiveness of the controller. The FLC has managed to provide suitable power management of the microgrid in full compliance with design limits of SOC and charging/discharging power of the battery.

CHAPTER 5: EXPERIMENTAL IMPLEMENTATION OF AN AC MICROGRID WITH FLC

5.1 Introduction

This chapter covers the design and implementation of an AC microgrid prototype including the DC/AC inverters and DC/DC converters where the proposed FLC is verified experimentally. The rated power of the generation units are lower than those presented in Chapter 4 due to the limitations of the laboratory facilities.

5.2 System Overview

A single phase microgrid prototype that consists of PV simulator/PV panels, lead-acid battery bank, and AC source (as auxiliary unit representing micro gas turbine (μGT) with an AC/DC rectifier) has been built at the Solar Laboratory in the ESI building at the University of Exeter (Penryn Campus). The schematic diagram of the microgrid setup is as shown in Figure 5.1. The microgrid has three of 345W X21 Sunpower PV panels that are configurable to be connected either in series or parallel. They are installed on the roof of the ESI as shown in Figure 5.2 and used when the PV simulator is not used. The programmable PV simulator LAB-SMS 31000, shown in Figure 5.3, is rated at 3kW, 0-1000V and 0-3A. The battery bank, shown in Figure 5.4, consists of 10 units of Victron Energy AGM 12-110 type that are connected in series. Each unit is rated at 12V and 110AH. An autotransformer (variac) is used to set the voltage of the μGT unit. Two DC/DC converters and three identical DC/AC inverters with low pass LCL filters are built. One of the DC/DC converters is configured as a unidirectional boost converter with MPPT controller to interface the PV panels/PV simulator while the other one is configured as a bidirectional converter to interface the battery bank. The DC/AC inverters are used for the generation units (i.e. the PV simulator/PV panels, the battery bank and the auxiliary unit). The control algorithms of the converters, inverters and the supervisory control have been realized by OPAL-RT real-time simulator.

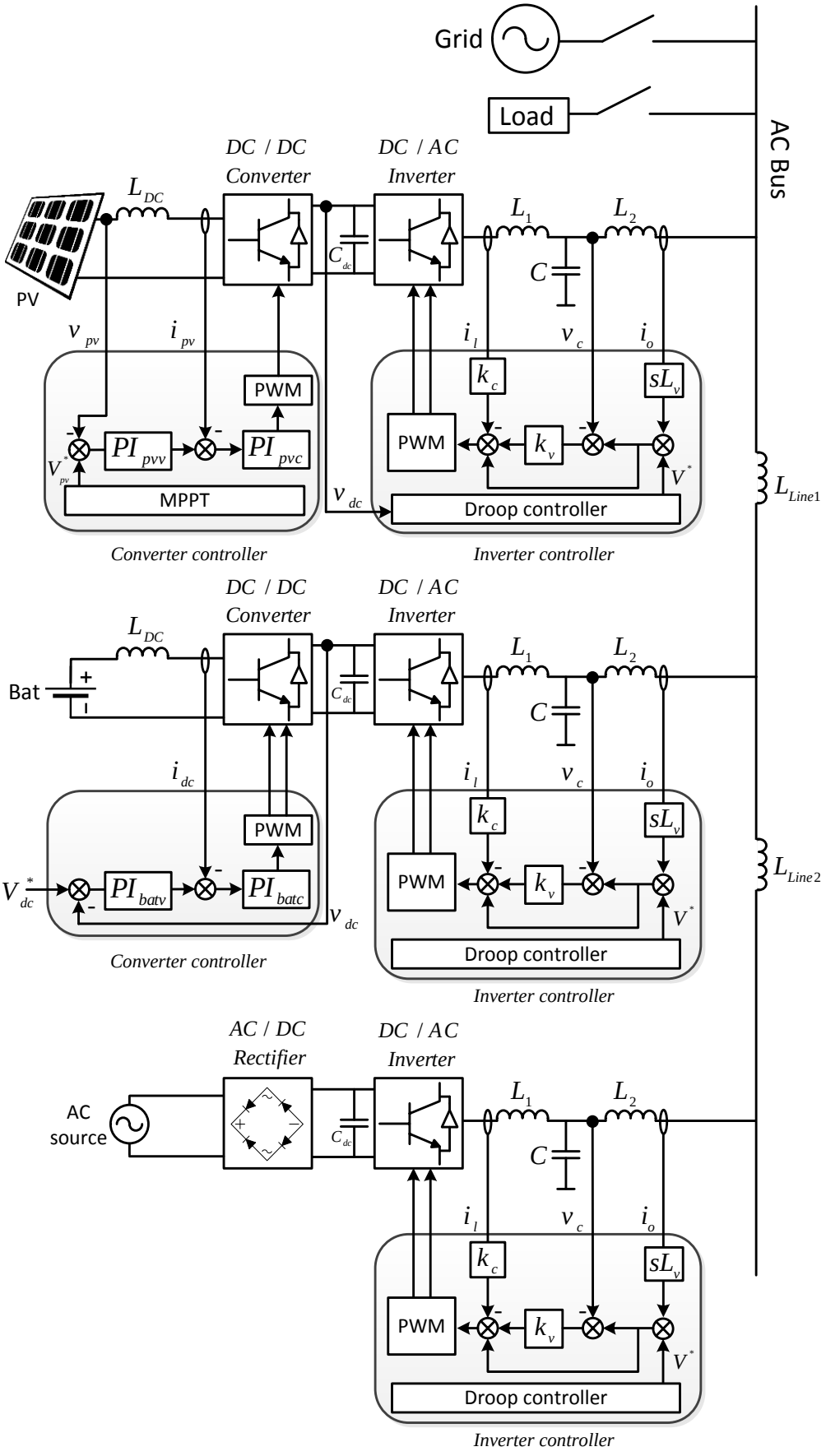

Figure 5.1: Schematic diagram of the microgrid prototype setup

Figure 5.2: Sunpower X21 solar panels (3 x 345W)

Figure 5.3: Programmable PV simulator LAB-SMS 31000

Figure 5.4: Battery bank

The product SEMITEACH from Semikron is used to realize the switching elements for the converters and inverters. The SEMITEACH and its schematic diagram are shown in Figure 5.5 and Figure 5.6, respectively [112]. Three identical SEMITEACH units are used as part of the microgrid. The SEMITEACH has three-phase diode-rectifier, Insulated Gate Bipolar Transistor (IGBT) modules and 1100μF/800V DC bus equivalent filtering capacitor. The maximum allowable AC voltage for the rectifier is 440V. The rectifier is designed for a three-phase configuration. However, it is used here for a single-phase configuration by leaving one branch of the rectifier disconnected. The IGBTs are designed to be forced closed by 15V signal and forced open by –15V between the gate and the associated emitter. Each IGBT module represents an inverter leg that consists of 2 IGBTs with an anti-parallel diode, connected in series. The maximum rated voltage of the SEMITEACH equals 1200V which represents the IGBT breakdown voltage. The maximum allowed current is 30A. The SEMITEACH is designed for three-phase systems, but it is configured to work as a single-phase inverter since only two phases are used. The first two legs of the SEMITEACH are configured for the DC/AC inverter and the third leg is for the DC/DC converter. Further details about the SEMITEACH can be found in reference [112].

For each inverter, the control feedback measurements are V_o (AC voltage across the filter capacitor), I_o (output current), I_L (inductor current), I_c (capacitor current), and V_{dc} (DC-link voltage) signals. LEM sensors are used for the measurements of voltage and current signals that are fed-back to the controller's Analog/Digital (A/D). One current signal from each inverter can be used either the inductor current or the capacitor current. In our case, the inductor current is used. The Digital/Analog (D/A) output signals from the OPAL-RT are the duty cycles for the converters and inverters. These signals are taken to PWM generation boxes which generate PWM for the converters and inverters. Different circuit breakers are used for connection/disconnection of the PV panels and battery bank. Isolation transformers are used to provide power supplies to the PV simulator and programmable load. A picture of the practical setup is shown in Figure 5.7.

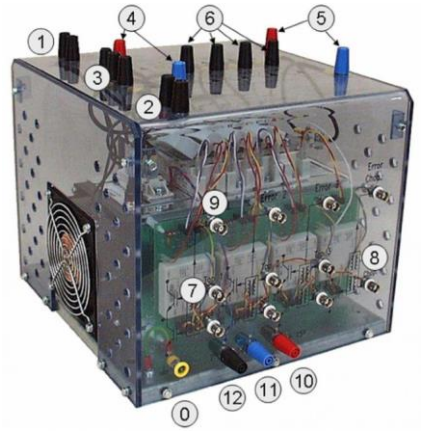

0 Earth connection
1 Fan power supply
2 Thermal trip
3 Rectifier input
4 DC rectifier outputs
5 DC IGBT inverter inputs
6 AC IGBT inverter + chopper outputs
7 PWM input of inverter
8 PWM input of brake chopper
9 Error output
10 15V driver power supply
11 0V driver power supply
12 Temperature sensor

Figure 5.5: SEMITEACH from Semikron [112]

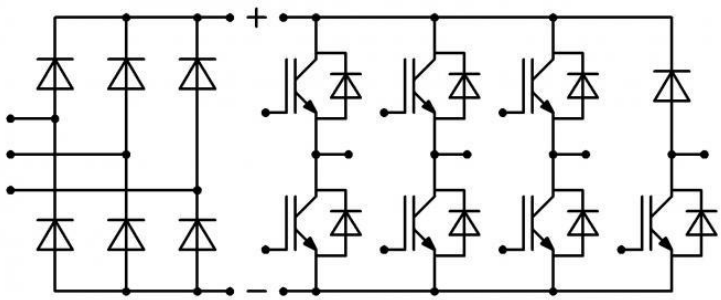

Figure 5.6: Schematic diagram of SEMITEACH [112]

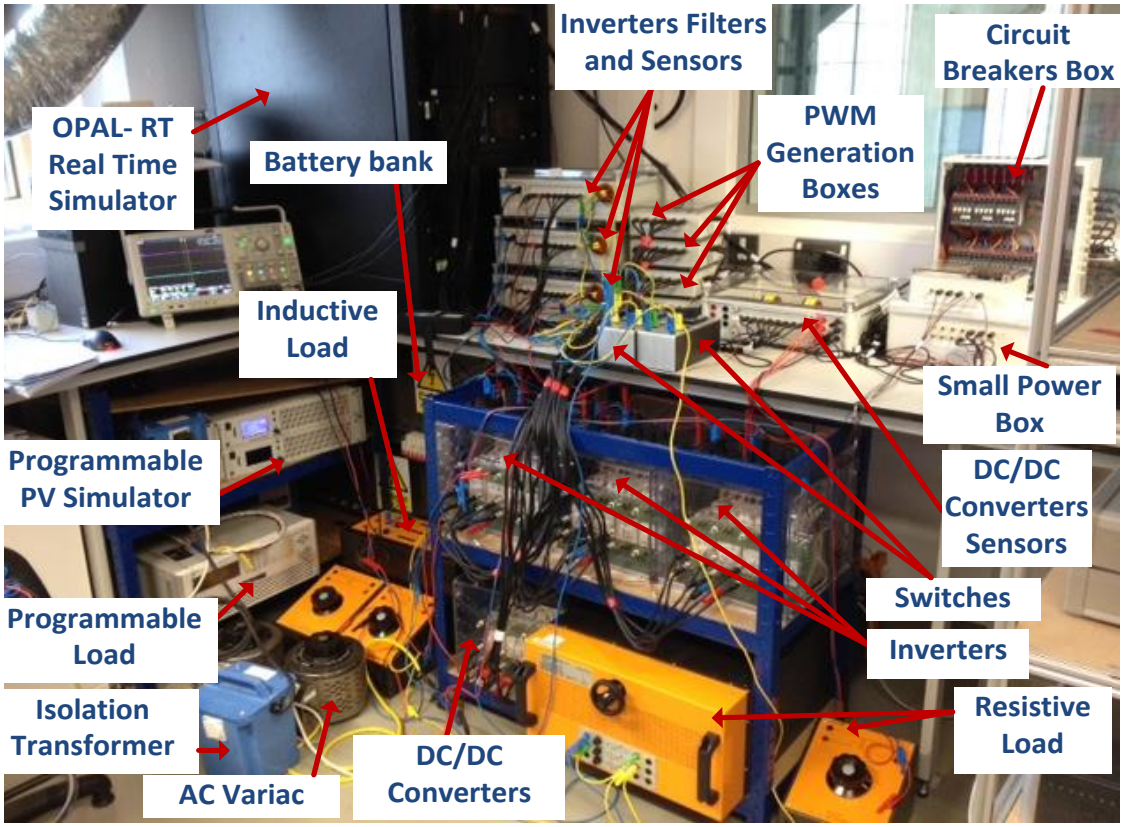

Figure 5.7: The microgrid prototype experimental setup

5.3 DC/AC Inverter

Figure 5.8 shows a schematic diagram of the inverter and its controller. The output of the inverter is connected to a low pass LCL filter. The controller consists of an inner and outer feedback loops. The inner feedback loop of either the inductor current or capacitor current can be used to provide active damping of the resonance created by the LCL filter. The outer feedback loop is implemented using the capacitor voltage. In addition, a feedforward loop of the reference voltage is also used in order to minimize the steady state error [113]. The parameters of the controllers will be shown in Table 5.3 below.

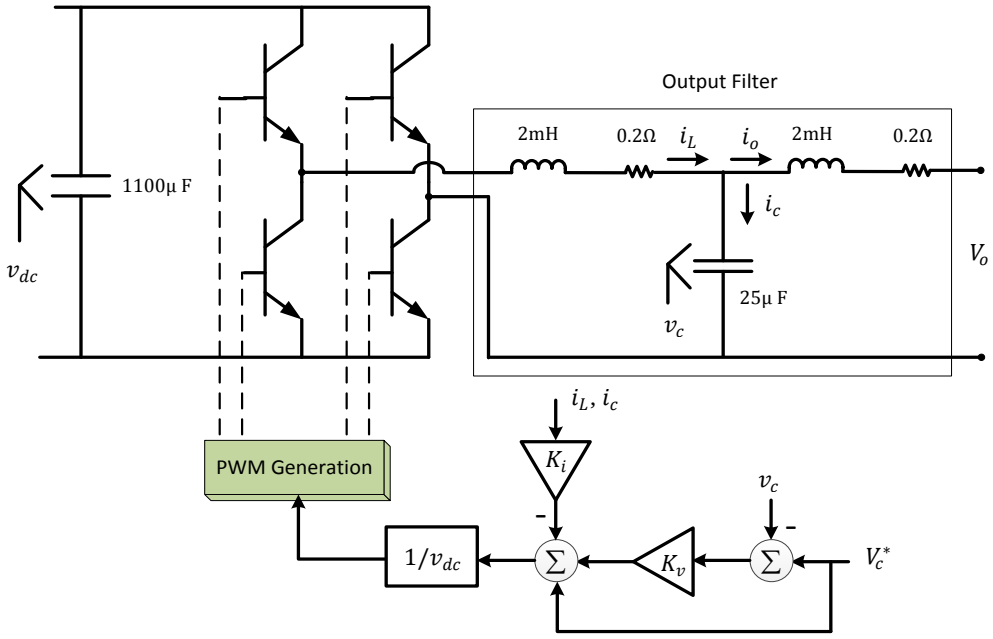

Figure 5.8: Block diagram of inverter and its controller

5.4 DC/DC Converter for BESS

Figure 5.9 shows a schematic diagram of the BESS converter and its controller. The controller consists of an inner and outer feedback loops. The inner feedback loop of the inductor current is used. The outer feedback loop is implemented using the DC voltage.

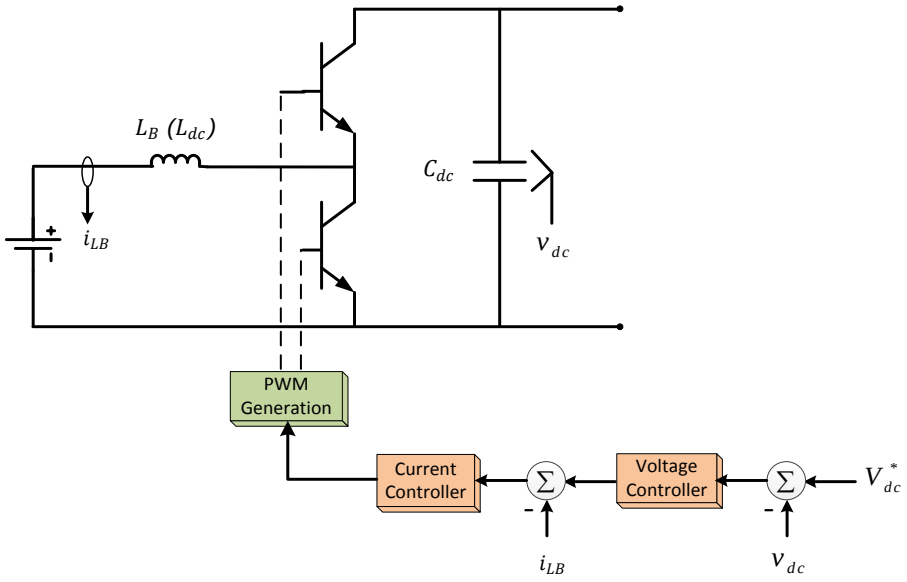

Figure 5.9: Block diagram of BESS converter and its controllers

Converters are nonlinear devices and all states of the system are discontinuous because of the switching. The linearized model is derived in the vicinity of some operating points to aid with the controller design and analyse the stability of the controls' loops for different gains [9]. The linearized averaged state-space model for the bidirectional boost BESS DC/DC converter is defined by (5.1) and (5.2). The states of the system are the inductor current i_{LB} and output voltage v_{dc}. The duty cycle D and inductor current I_{LB} are the steady state operating points of the linearized system while d is the averaged control input representing the small signal variations around the steady state duty cycle D. The output signals of the system are the inductor current and output voltage that are used to be fed back to implement the double feedback control system. Furthermore, the linearized model is used to calculate the transfer functions G_{iLB-d} and $G_{vdc-iLB}$ given in (5.3) and (5.4), respectively as derived in [114], [115].

$$\begin{bmatrix} \dot{i_{LB}} \\ \dot{v_{dc}} \end{bmatrix} = \begin{bmatrix} 0 & \frac{-(1-D)}{L_B} \\ \frac{1-D}{C_{dc}} & \frac{-1}{RC_{dc}} \end{bmatrix} \begin{bmatrix} i_{LB} \\ v_{dc} \end{bmatrix} + \begin{bmatrix} \frac{V_{dc}}{L_B} \\ \frac{-I_{LB}}{C_{dc}} \end{bmatrix} d \tag{5.1}$$

$$\text{y}=\begin{bmatrix} 1 & 0 \\ 0 & 1 \end{bmatrix} \begin{bmatrix} i_{LB} \\ v_{dc} \end{bmatrix} \tag{5.2}$$

$$G_{iLB-d} = \frac{i_{LB}(s)}{d(s)} = \frac{RC_{dc}V_{dc}s + [(1-D)RI_{LB} + V_{dc}]}{RC_{dc}L_Bs^2 + L_Bs + R(1-D)^2} \tag{5.3}$$

$$G_{vdc-iLB} = \frac{v_{dc}(s)}{i_{LB}(s)} = \frac{-I_{LB}RL_Bs + V_{dc}R(1-D)}{V_{dc}RC_{dc}s + [V_{dc} + (1-D)I_{LB}R]} \tag{5.4}$$

where L_B, V_{dc}, C_{dc} and R are the converter inductor, nominal DC-link voltage, DC-link capacitor and equivalent load resistor, respectively.

The parameters and operating points of the BESS bidirectional boost converter including their controllers are shown in Table 5.1 and Table 5.3 .

Table 5.1: Key system parameters and operating points for BESS bidirectional DC/DC converter

Parameter / operating point	Symbol	Value
Load resistance	R	440Ω
DC output capacitor	C_{dc}	1100μF
Nominal DC-link voltage	V_{dc}	200V
Steady state duty cycle	D	0.25
Steady state inductor current	I_{LB}	0.7A
BESS converter inductor	L_B *or* L_{dc}	0.8mH

The control system structure for the battery bidirectional boost converter is as shown in Figure 5.10.

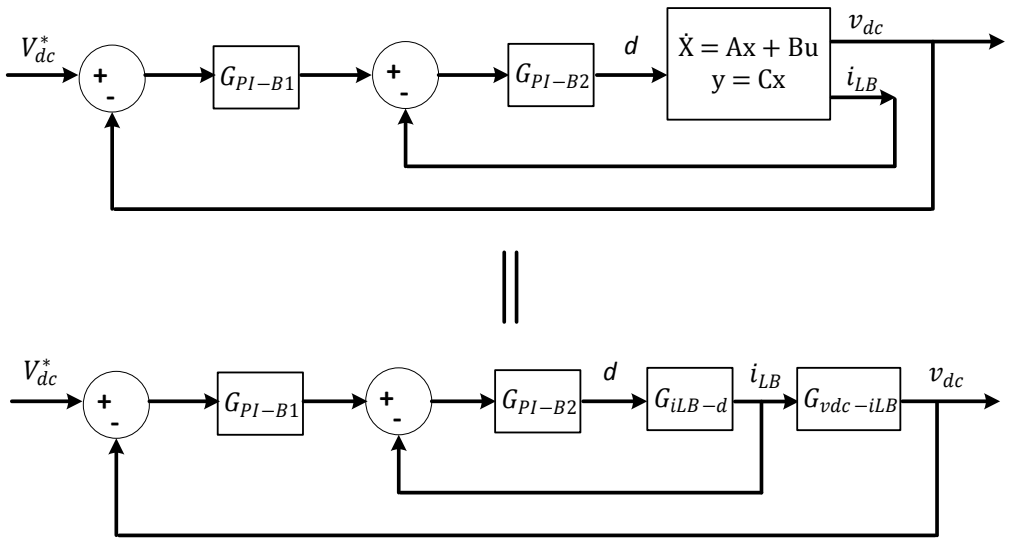

Figure 5.10: Control system structure for the bidirectional BESS boost DC/DC converter

The current loop and voltage loop PI controllers, have been addressed in the literature as in [115], [116], and are given by (5.5) and (5.6) respectively.

$$G_{PI-B1(s)} = \frac{0.005s + 1}{s} \tag{5.5}$$

$$G_{PI-B2(s)} = \frac{1.5s + 50}{s} \tag{5.6}$$

The gains' values of the controllers have been selected in line with the values that have been found in the literature. They have been tested for the system stability using bode diagram. The open-loop and closed-loop bode diagram for the bidirectional boost DC/DC converter is as shown in Figure 5.11 where the controller has a gain margin of 46.6 dB and a phase margin of 69.4 deg [116]. The bandwidth of the control loop is 1580 rad/s. See Appendix for Matlab program for plotting the bode diagram.

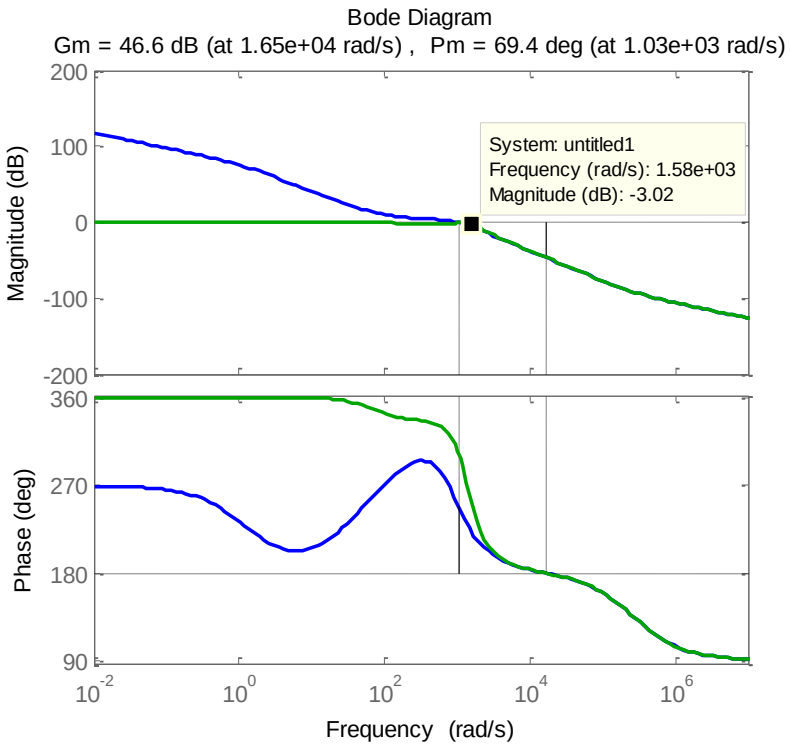

Figure 5.11: Open-loop and closed-loop bode diagram for the bidirectional BESS boost DC/DC converter

5.5 DC/DC Converter for PV

Figure 5.12 shows a schematic diagram of the PV converter and its controller. The controller consists of an inner and outer feedback loops. The inner feedback loop of the PV's current is used. The outer feedback loop is implemented using the PV's voltage. The DC/DC converter controls the PV output voltage to achieve MPPT. It is important to note that the MPPT has many

techniques [83]. However, the fractional open circuit voltage is used because of its simplicity. It states that the MPP is approximately at $V_{pv} = 0.8\, V_{oc}$.

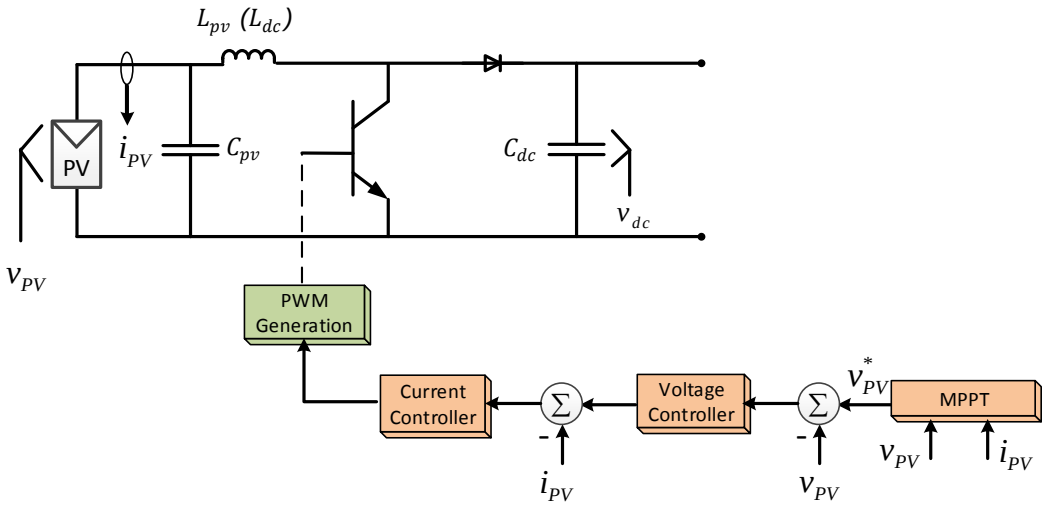

Figure 5.12: Block diagram of PV's converter and its controllers

The linearized averaged state-space model for the unidirectional boost PV DC/DC converter is defined by (5.7) and (5.8). The PV current i_{Lpv} and PV voltage v_{pv} are the states of the system. The duty cycle D is the steady state operating point of the linearized system while d is the averaged control input representing the small signal variations around the steady state duty cycle D. The output signals of the system are the PV current and voltage that are used to be fed back to implement the double feedback control system. The linearized model are used to calculate the transfer functions G_{iLpv-d} and $G_{vpv-iLpv}$ given in (5.9) and (5.10), respectively [18], [114], [115].

$$\begin{bmatrix} \dot{i_{Lpv}} \\ \dot{v_{pv}} \end{bmatrix} = \begin{bmatrix} 0 & \frac{1}{L_{PV}} \\ \frac{-1}{C_{pv}} & \frac{1}{r_{pv}C_{pv}} \end{bmatrix} \begin{bmatrix} i_{Lpv} \\ v_{pv} \end{bmatrix} + \begin{bmatrix} \frac{V_{dc}}{L_{PV}} \\ 0 \end{bmatrix} d \tag{5.7}$$

$$\mathrm{y} = \begin{bmatrix} 1 & 0 \\ 0 & 1 \end{bmatrix} \begin{bmatrix} i_{Lpv} \\ v_{pv} \end{bmatrix} \tag{5.8}$$

$$G_{iLpv-d} = \frac{i_{Lpv}(s)}{d(s)} = \frac{(C_{pv}r_{pv}s - 1)V_{dc}}{L_{pv}C_{pv}r_{pv}s^2 - L_{pv}s + r_{pv}} \tag{5.9}$$

$$G_{vpv-iLpv} = \frac{v_{pv}(s)}{i_{Lpv}(s)} = \frac{-r_{pv}}{C_{pv} r_{pv} s - 1} \tag{5.10}$$

where L_{pv}, V_{dc}, C_{pv} and r_{pv} are the converter inductor, nominal DC-link voltage, PV input capacitor and dynamic resistor of the PV around operating point, respectively.

The dynamic output resistance (r_{pv}) of the PV changes over the full range of the P-V or I-V curve of the PV [71]. It can be defined as the ratio between the change in voltage to the change in current. It can be approximated and represented by a straight line in the P-V curve of the PV cell as shown in Figure 5.13 where the slope of the line equals $-r_{pv}$. The r_{pv} is positive on the left of the maximum power point (MPP) and negative on the right of the MPP.

The parameters and operating points of the PV unidirectional DC/DC converter including their controllers are listed in Table 5.2 and Table 5.3.

Table 5.2: Key system parameters and operating points for PV unidirectional DC/DC converter

Parameter / operating point	Symbol	Value
Load resistance	R	440Ω
DC output capacitor	C_{dc}	1100μF
Nominal DC-link voltage	V_{dc}	200V
Steady state duty cycle	D	0.25
PV converter inductor	L_{pv} *or* L_{dc}	0.8mH
PV Dynamic resistor	r_{pv}	-6Ω
PV Input capacitor	C_{pv}	1100μF

The control system structure for the PV unidirectional converter is shown in Figure 5.14.

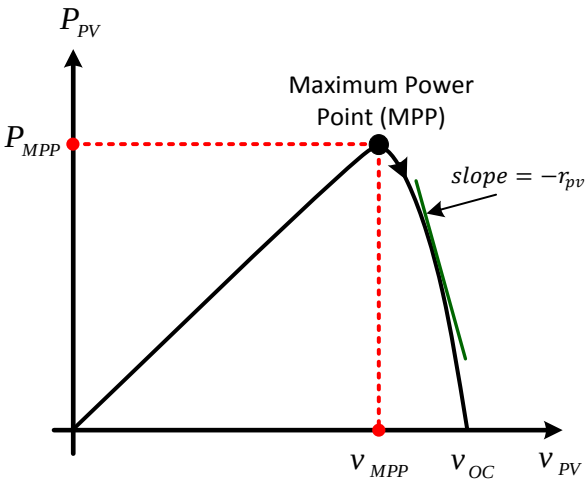

Figure 5.13: Approximation of dynamic resistor (r_{pv}) of the PV from P-V curve

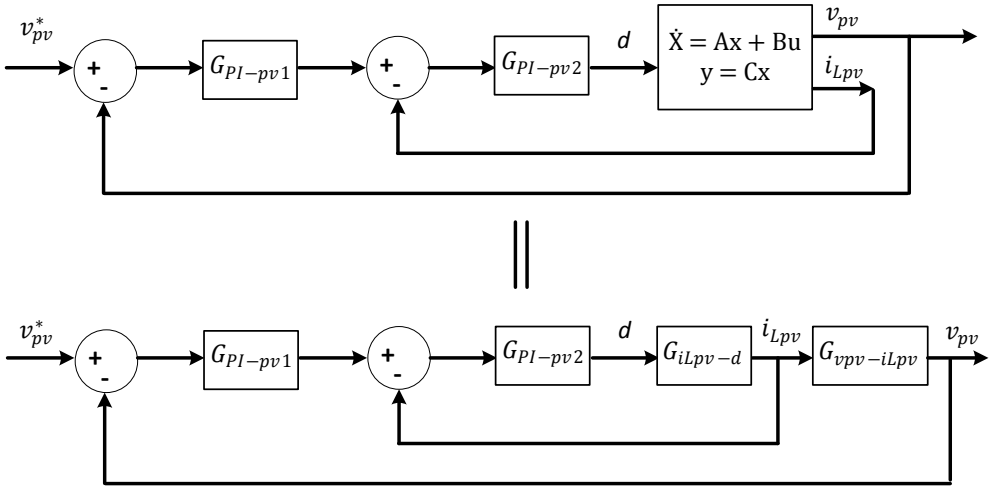

Figure 5.14: Control system structure for the unidirectional boost PV DC/DC converter

The current loop and voltage loop PI controllers, have been addressed in the literature as in [115], [116], and are given by (5.11) and (5.12), respectively.

$$G_{PI-pv1(s)} = \frac{10s + 250}{s} \tag{5.11}$$

$$G_{PI-pv2(s)} = \frac{0.05s + 1}{s} \tag{5.12}$$

Bode diagram has been used to assess the system stability for the selected gains' values of the controllers that have been selected in line with the values in the literature. The open-loop and closed-loop bode diagram for the unidirectional boost PV DC/DC converter is as shown in Figure 5.15 where the controller has a very high gain margin and a phase margin of 66.6 deg [116]. The bandwidth of the control loop is 745 rad/s (See Appendix for Matlab program for plotting the bode diagram).

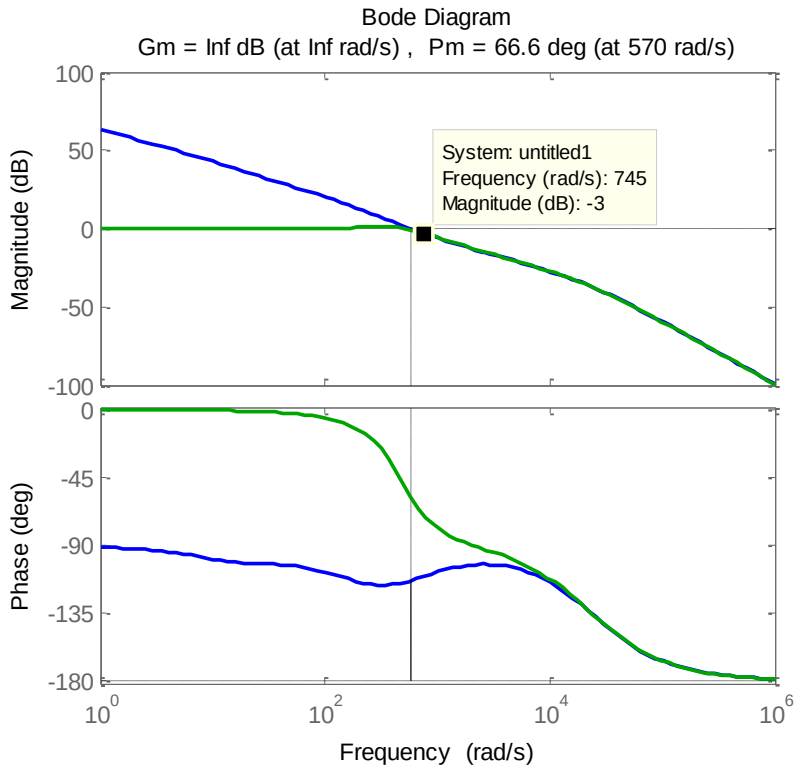

Figure 5.15: Open-loop and closed-loop bode diagram for the unidirectional boost PV DC/DC converter

5.6 PV Power shifter

If the power generation from the PV is higher than the load, the battery absorbs the excess power. However, if the SOC of the BESS is very high, the PV power should be curtailed to prevent over-charging the battery. For the latter objective, a PV power shifter is implemented. Normally, the MPPT controller regulates the voltage across the PV to supply the maximum power. When a curtailment is needed, the power shifter shifts the PV voltage to deviate it from the maximum

power point to a lower point as illustrated in the PV MPP shifting operation shown in Figure 3.8 of Chapter 3 [96], [116].

5.7 Microgrid Controllers Integration

The proposed control system in Chapter 3 is divided into two levels separated by a control bandwidth. The primary level of each generating unit contains the voltage and current controllers for the DC/DC converters and DC/AC inverters as shown in Figure 5.1. They are designed to have a fast disturbance rejection with a high bandwidth control loop to track commanded references' values. The parameters of the system and controllers are shown in Table 5.3 below. The secondary level is represented by the FLC which is designed to have a lower bandwidth in order to preserve system stability like any other nested control loops. The FLC maintains the power management in the microgrid according to pre-defined rules. Its output manipulates the voltage/current references values of the primary control [116]. The FLC has been realized by OPAL-RT with the aid of Matlab/Simulink fuzzy logic block where the FLC rules and membership functions as per the design shown in Chapter 3. The FLC is 10 times less than the bandwidth of the inner loop. RT-LAB enables Simulink models for real-world interaction with hardware-in-the-loop engineering simulators and rapid prototyping controllers. The RT-LAB links the Simulink codes to highly-optimized runtime libraries that allows a model time step as low as 10 microseconds. More details for interfaces with the OPAL-RT can be found in reference [117].

Table 5.3: Experimental setup parameters

Inverters parameters			PV current controller		
Inverter-side filter inductor	L_1	4mH	P-controller gain	k_{p_pvc}	0.05
Filter capacitor	C	25μF	I-controller gain	k_{i_pvc}	1
Grid-side filter inductor	L_2	2mH	Inverter voltage controller		
Nominal output voltage	V_o	120V	Voltage controller gain	k_v	0.01
Nominal frequency	$\omega_o = 2\pi f_o$	$2\pi(50) = 314.16$rad/s	Current controller gain	k_c	3
DC-link capacitor	C_{dc}	1100μF	Virtual inductor	L_v	8mH
Line1 inductor	L_{line1}	1mH	Droop controller		
Line2 inductor	L_{Line2}	2mH	Frequency drooping coefficient	m	1×10^{-3} rad/s/W
Sampling/ Switching frequency	f_s, f_{sw}	10kHz	Voltage drooping coefficient	n	0.05 V/Var
DC/DC Converters			Power measuring filter		
Converter inductor	L_{DC}	0.8mH	Cut-off frequency	ω_c	2rad/s
Battery voltage	V_{bat}	125V	PV DC voltage regulator		
PV output voltage	V_{pv}	110V	P-controller gain	k_{p-dc}	20
Battery current controller			I-controller gain	k_{i-dc}	2
P-controller gain	k_{p_batc}	5×10^{-3}	Nominal DC-link voltage	V_{dc}	200V
I-controller gain	k_{i_batc}	1	State of charge limits		
Battery voltage controller			Max. SOC	SOC^*_{max}	95%
P-controller gain	k_{p_batv}	1.5	Min. SOC	SOC^*_{min}	40%
I-controller gain	k_{i_batv}	50	Max. charging/ discharging power		
PV voltage controller			Max. charging power	$P^*_{Charge\_max}$	70W
P-controller gain	k_{p_pvv}	10	Max. discharging power	$\mathrm{P}^*_{\mathrm{Discharge\_max}}$	150W
I-controller gain	k_{i_pvv}	250			

5.8 Experimental Results

Different case scenarios are tested and the results are obtained from the internal memory of the OPAL system using Matlab. The below cases show the responses of the microgrid to various disturbances in the system. Similar cases are shown with the FLC and proportional (P) controller in order to have a comparison between the two controllers.

Figure 5.16 shows a snapshot of the oscilloscope. The battery voltage input is 120V while the DC voltage output of the DC/DC converter for the battery is boosted to 150V and then 300V.

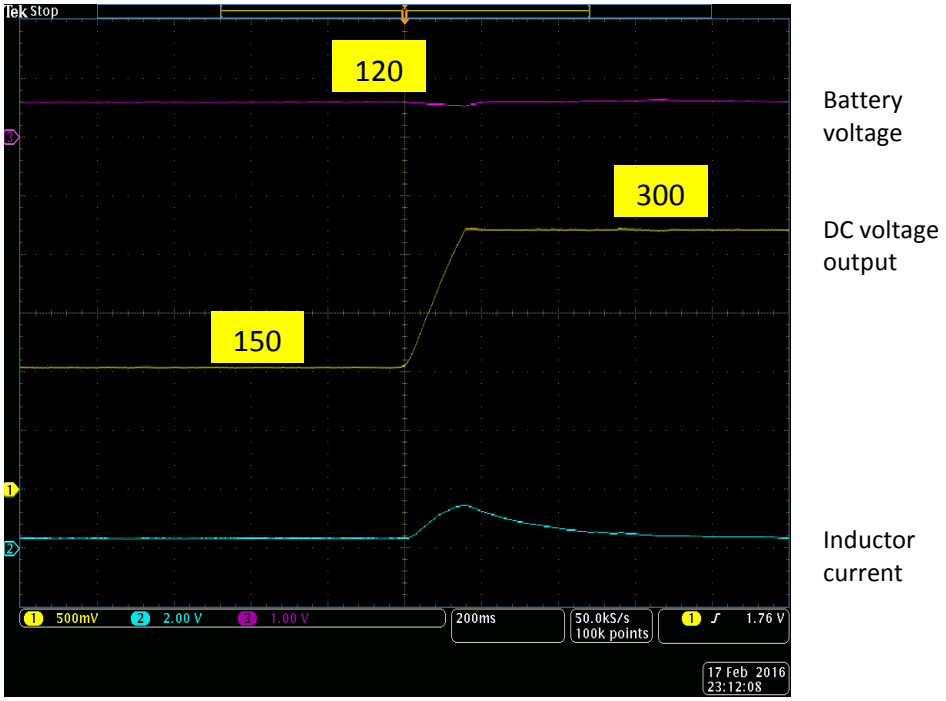

Figure 5.16: DC/DC converter for battery

Figure 5.17 shows a screenshot of the oscilloscope with the outputs' voltages of the three DC/AC inverters after the synchronization of the three power units.

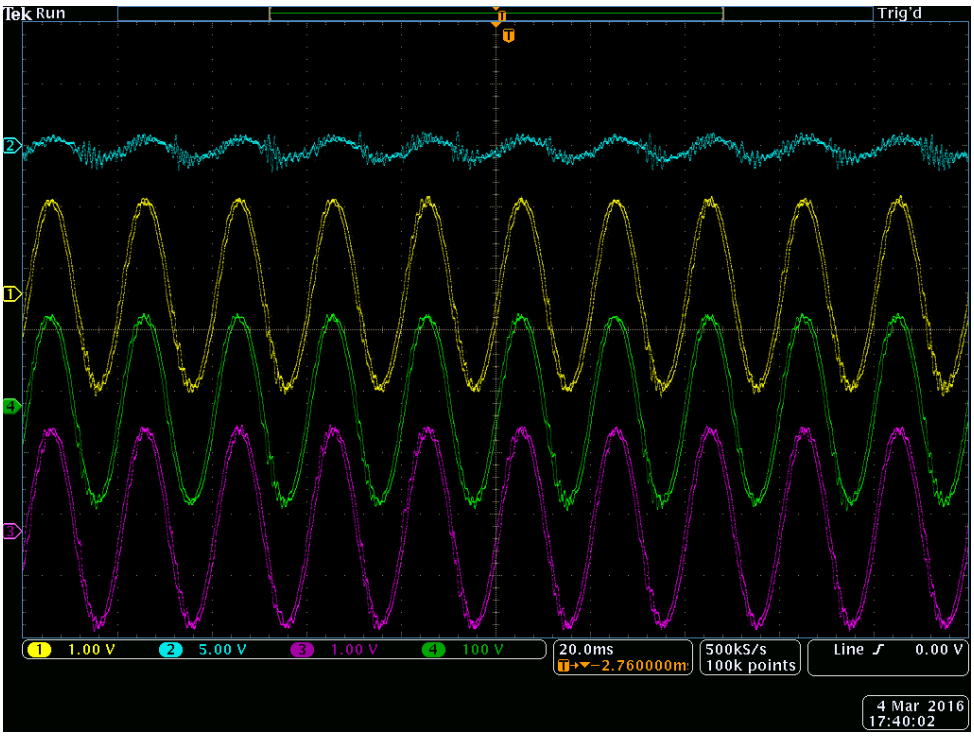

Figure 5.17: DC/AC inverters outputs

Case 1: 40% to 95% SOC with FLC:

Figure 5.18 shows the case when a fixed PV power is available over the full time of the experiment. The initial SOC value is 40%. Figure 5.18(a) shows the experimental output power responses of the PV, battery and auxiliary units while the load power is shown in Figure 5.18(b). The PV generation is just slightly higher than the load, but the SOC value is low. Hence, the auxiliary unit is used to charge the battery at its maximum charging power of 70W. Once the SOC becomes around 47.58% at about 165s in Figure 5.18(c), the power from the auxiliary unit becomes around zero as per the FLC command since the PV can supply the whole load and the SOC level is not critical. This saves the cost of running the auxiliary unit while still satisfying the system needs. A battery charging current multiplier of 100k to 500k is used to speed up the increase in the SOC in order to decrease the time required for the experiment, but this does not affect the results' dynamics in terms of the behaviour or decision of the FLC. At around 378s, the load is dropped to zero and the PV power is curtailed to keep the charging power within the limit of 70W. When the SOC becomes around 91.97%, the PV power starts to curtail even more to maintain the SOC below its maximum limit of 95%.

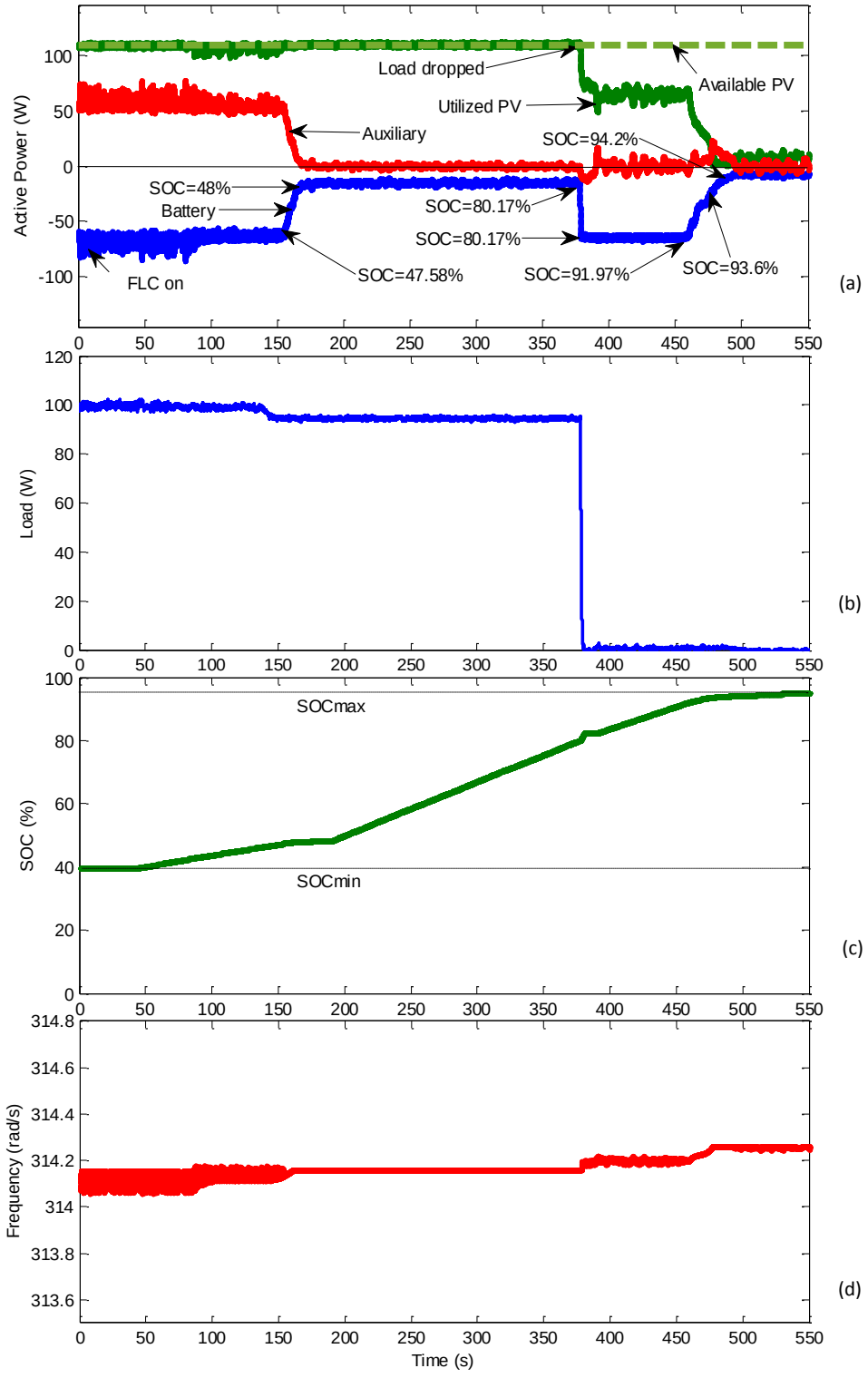

Figure 5.18: Experimental output responses for 40% to 95% SOC with FLC case: (a) power (b) load (c) SOC (d) Frequency

Thanks to the FLC, the SOC is maintained between the minimum (40%) and maximum (95%) allowable limits as can be seen in Figure 5.18(c). The frequency response is shown in Figure 5.18(d). As discussed in section 3.3.2,

the MPPT controller measures the bus frequency using a Phase Looked Loop (PLL) (see Figure 3.4) and the PV output voltage is increased to shift the MPP to a lower value when required as illustrated in Figure 3.8. On occasions, the PV output voltage signal, used by the PLL, is not a pure sinewave since it has some distortions/harmonics. Therefore, the high frequency variations in the power and frequency responses represent noise which comes from the measurements of the bus frequency. This could be treated by an appropriate filter in non-laboratory installations if the auxiliary unit cannot cope with high frequency actuations. The high frequency variations do not have any implication on the controller's performance within the microgrid, since the control loops of the microgrid are slow in comparison to the noise and such noise probably will not appear if units with larger capacities are used. This scenario validates the capability of the FLC in keeping the SOC and charging power within their desired limits by adjusting the frequency.

Case 2: 40% to 95% SOC with proportional controller:

In order to compare the performance of the FLC with the P controller, similar scenario of case 1 has been carried out, but with the P controller and the results are as shown in Figure 5.19. Figure 5.19(a) shows the experimental output responses in terms of the power output of the different generation units while the load power is shown in Figure 5.19(b). The initial SOC value is 40% and the PV generation is slightly higher than the load. Therefore, the auxiliary unit is used to charge the battery. At the beginning of the experiment, when the P controller is activated as can be seen from Figure 5.19(a), the maximum charging limit (70W) is slightly exceeded during transient unlike in the case with the FLC in Figure 5.18(a). At around 31s when the SOC becomes about 41.05%, the auxiliary unit power is reduced in response to the P controller decision until it becomes zero at around 42s since the PV can supply the whole load although the SOC level is not very high in comparison to the situation at the beginning of the experiment. Similar to the case with the FLC, a battery charging current multiplier is used to speed up the increase in the value of the SOC, which reduces the time required for the experience.

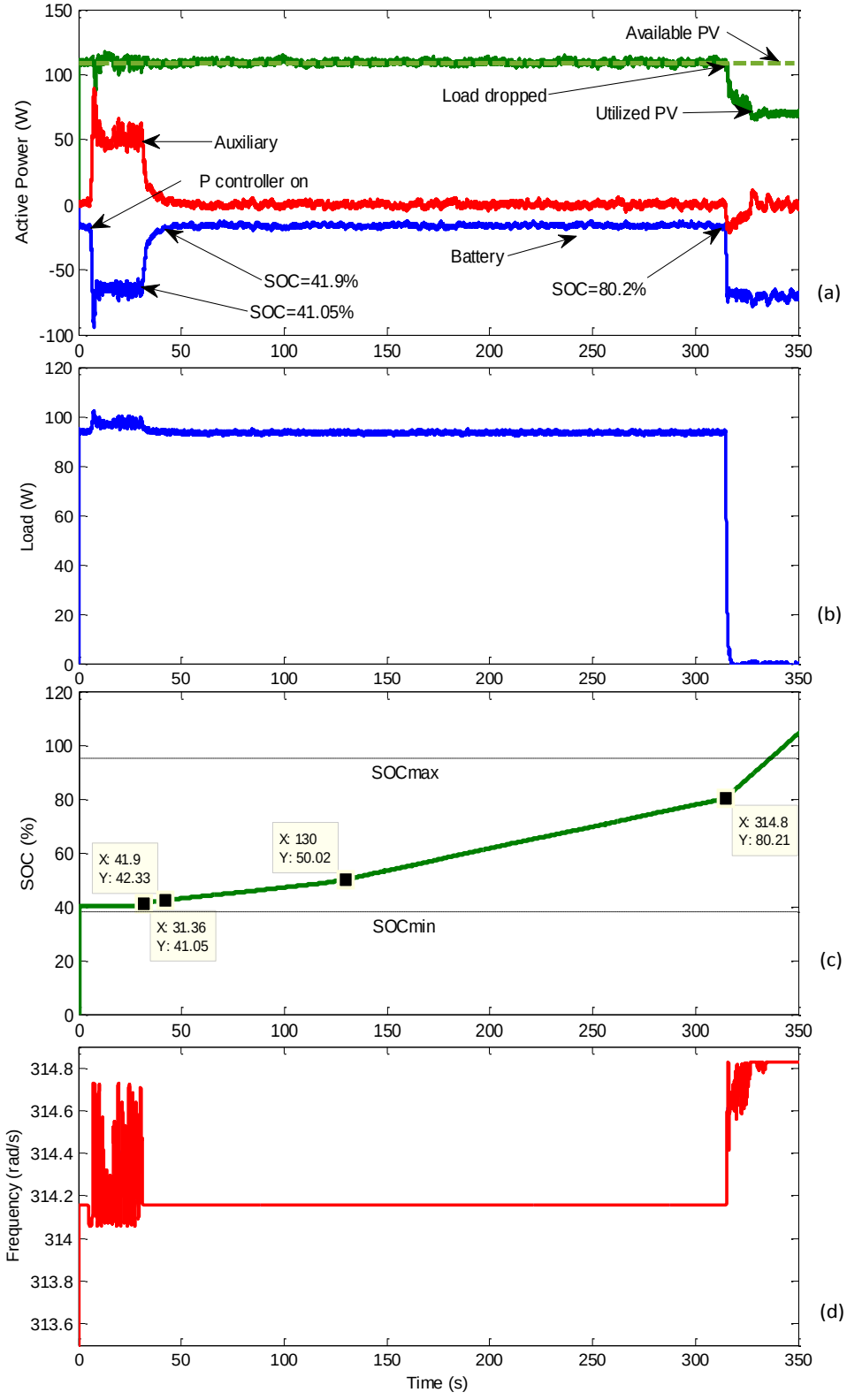

Figure 5.19: Experimental output responses for 40% to 95% SOC with proportional controller case: (a) power (b) load (c) SOC (d) Frequency

At around 315s, the load is dropped to zero and the PV power is curtailed to keep the charging power within the limit which is 70W. The SOC has exceeded

the maximum allowable limit (95%) towards the end of the experiment as can be seen in Figure 5.19(c) unlike the case with the FLC in Figure 5.18(c) where the SOC is limited to the 95% limit. The frequency is maintained within its limits as can be seen from Figure 5.19(d), but with more oscillations in comparison with the case of the FLC shown in Figure 5.18(d). Although the P controller provides similar responses like the FLC, however, it is very clear from this case that the FLC is performing better than the P controller in terms of maintaining the limits required.

Case 3: 51% SOC with FLC:

Figure 5.20 shows a discharging scenario for the battery with an initial SOC value of 51%. Figure 5.20(a) shows the experimental output power responses of the PV, battery and auxiliary units along with the load power in Figure 5.20(b). The FLC is initially not activated and no load is connected to the system. The PV generation is around 30W which is absorbed completely to charge the battery. The load is then applied and the battery starts supplying the power demand shortage as the PV power is not enough. After t=50s, the FLC is activated and the auxiliary unit starts providing power according to the drop in bus frequency shown in Figure 5.20(d). At around t=100s when the SOC drops to 47.19%, the battery contribution is gradually reduced to about 35W while the auxiliary unit contribution is gradually increased. At around t=250s, the SOC reaches a critical value of 42.98% and consequently the battery stops discharging while the auxiliary unit provides about 150W which is the difference between the PV and load powers. This way, the minimum SOC limit is preserved. At t=370s, the load is fully disconnected and consequently the power output of the auxiliary unit is reduced by the FLC to around 30W only as it is enough for the PV power to charge the battery at its maximum limit. At t= 440s, the PV power is increased, but it is curtailed to keep the charging limited. In addition, the auxiliary unit is stopped by the FLC as the PV power is sufficient. At t= 470s, the load is re-connected and the FLC stops the curtailment to utilize more PV power for the new load without running the auxiliary unit. The charging power is maintained within the maximum limit of 70W. The SOC is maintained above the minimum allowable limit of 40% and the frequency is maintained within its limits as well.

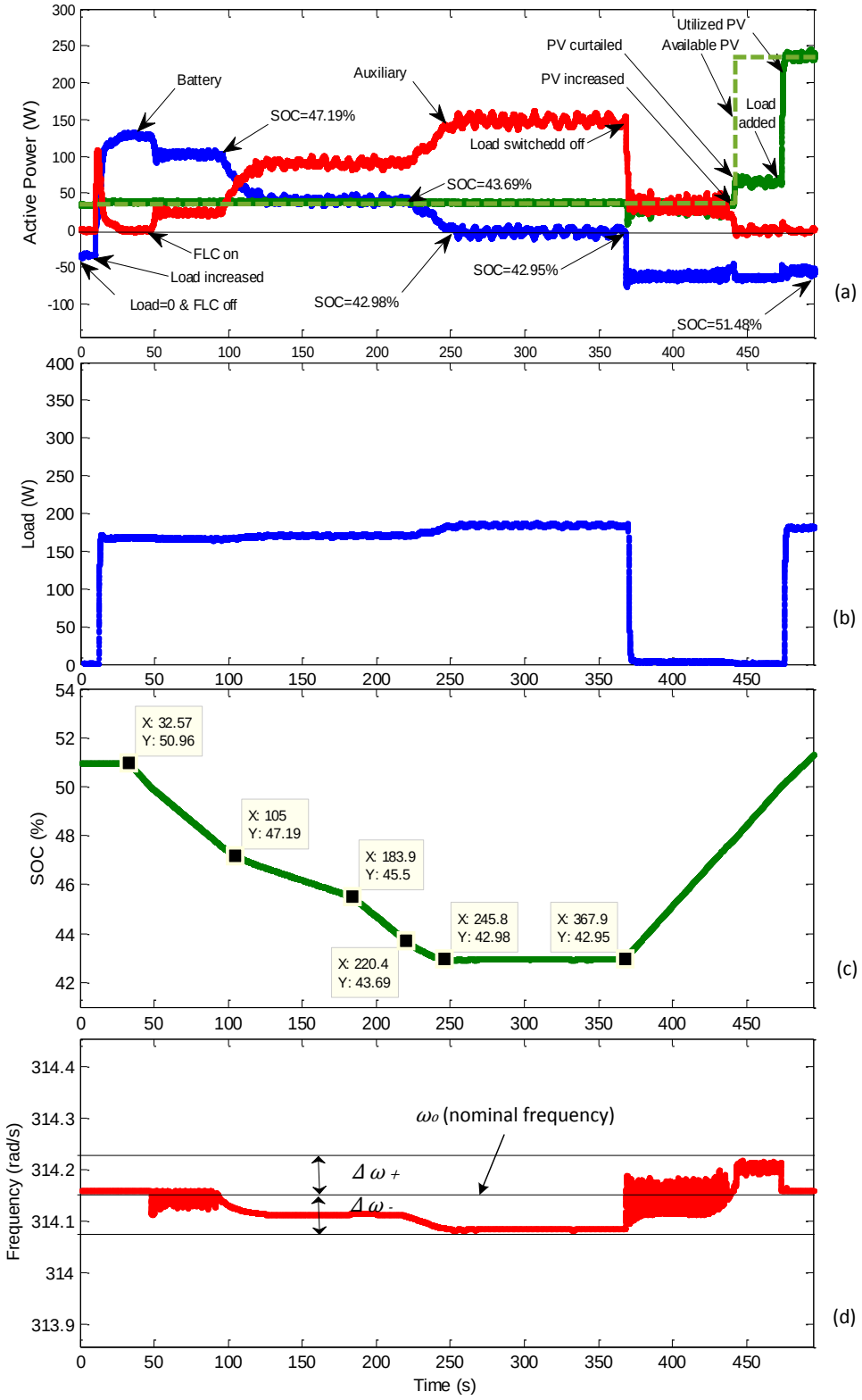

Figure 5.20: Experimental output responses for 51% SOC with FLC case: (a) power (b) load (c) SOC (d) Frequency

Case 4: 52% SOC with proportional controller:

Similar to Case 3, Figure 5.21(a) shows the experimental output responses with the P controller and an initial SOC value of 52%. The P controller is activated at around 65s. At 168s, the load is dropped to zero. The PV power is increased at around 184s and the P controller couldn't carry out the required curtailment of the PV power completely. Consequently, the maximum charging limit (70W) is exceeded unlike the case with the FLC in Figure 5.20(a). It becomes even worse at the end of the experiment when the PV is further increased and the P controller couldn't cope at all with that and the charging power becomes around 3.4 times the allowable maximum charging limit. Hence, the experiment has been stopped. The load profile, SOC curve and frequency curve are as shown in Figure 5.21 (b), (c) and (d), respectively. The SOC is maintained above the minimum allowable limit (40%) and the frequency is maintained within its limits as well with more oscillations in comparison with the case of the FLC in Figure 5.20(d). Unlike the FLC case, it is very obvious that the P controller in this case could not cope with the disturbance in the system and could not be able to maintain the maximum battery charging limit.

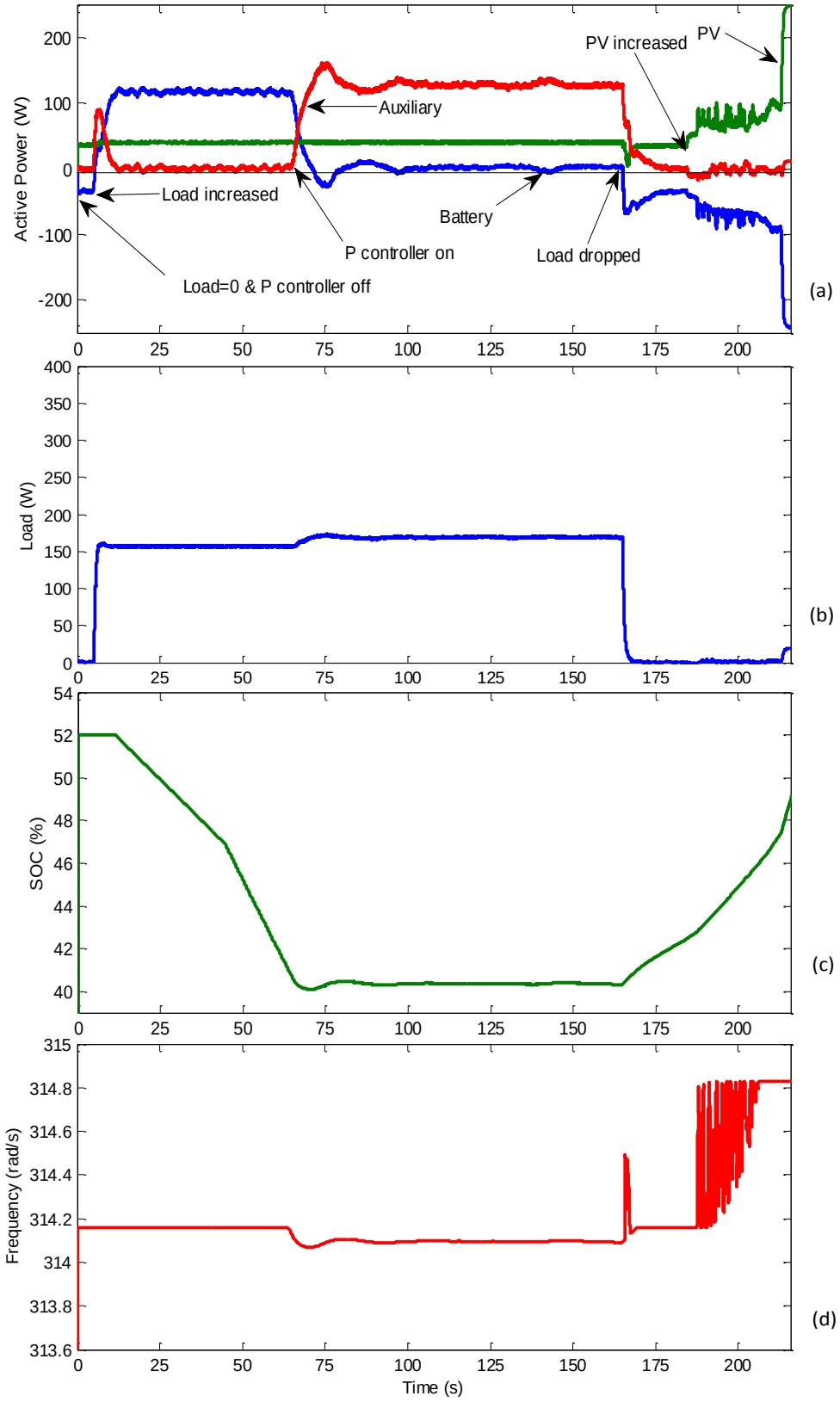

Figure 5.21: Experimental output responses for 52% SOC with P controller case: (a) power, (b) load, (c) SOC, (d) Frequency

5.9 Summary

This chapter has covered the design and practical implementation of the prototype AC microgrid including the DC/AC inverters and DC/DC converters. It presented the design of the different controller loops for the DC/DC converters using linearized method. It covered practical realisation of the controller using OPAL real-time controller. The proposed FLC / power management strategy has been verified experimentally with the laboratory-scale microgrid prototype. Experimental results of the developed microgrid have been presented where the FLC is compared with a proportional controller. The results show that the FLC is far superior in achieving the required goals and the proportional controller was not always able to maintain the SOC and charging/discharging power within their design limits.

CHAPTER 6: MODELLING OF PHOTOVOLTAIC AND CONCENTRATED PHOTOVOLTAIC

6.1 Introduction

Photovoltaic (PV) is characterized by a Current-Voltage (I-V) curve. This chapter provides details on the I-V curve and how to obtain important parameters from it. PV uses direct and diffused solar radiations to generate electrical power. On the other hand, Concentrated PV (CPV) uses only direct solar radiation to provide electrical power where a large area of sunlight is focused on a solar cell using optics such as lenses. This chapter covers PV and CPV modelling including single-diode and two-diode models that are used for modelling a PV cell. The chapter shows the impact of changing solar irradiation or shading of PV and CPV on the microgrid AC bus frequency. Sample simulation results of around $1m^2$ area of 135Wp PV, and 500 suns concentration (500X) CPV modules both with and without shading are shown to assess the impact on the frequency. Standard Test Conditions are $1000W/m^2$ solar irradiance, 25^oC temperature and AM1.5 air mass.

6.2 Modelling of Photovoltaic/Concentrated Photovoltaic

Modelling is carried out for the following types of PV and CPV cells and modules:

a) 13.6cm x 13.6cm PV cell
b) $1m^2$ area of 135Wp PV module that consists of 49 of 13.6cm x 13.6cm PV cells
c) 1cm x 1cm CPV cell
d) $1m^2$ area of 500 suns concentration (500X) CPV module that consists of 25 of 1cm x 1cm CPV cells where “X” is the intensity of concentration

Parameters for PV’s cell and module will be shown later in Table 6.1 while Table 6.2 will show the parameters used in the CPV’s cell and module.

6.2.1 I-V Curve of Solar Photovoltaic

PV modules produce outputs that are determined mainly by the level of incident radiation. For given external conditions, the PV modules are characterized by Current-Voltage (I-V) curve as shown in Figure 6.1.

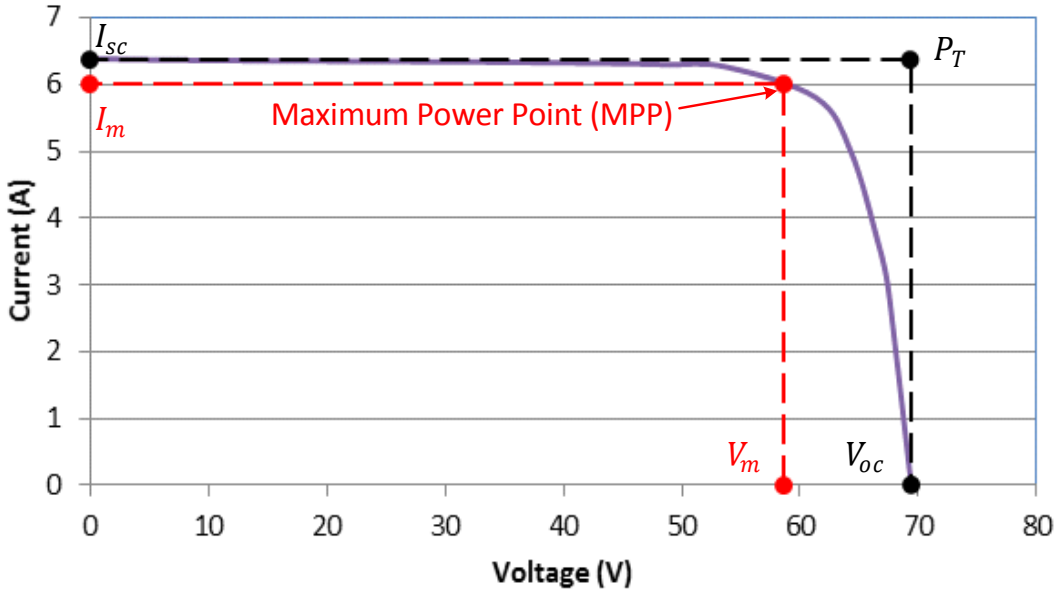

Figure 6.1: I-V curve of a solar panel connected to a variable resistive load

Important parameters such as I_{sc}, V_{oc}, I_m, V_m, P_m and FF could be determined from the I-V curve. Those parameters are normally provided by the PV's manufacturer. They can be defined as follows [118]:

$$P_m = I_m V_m \tag{6.1}$$

$$P_T = I_{sc} V_{oc} \tag{6.2}$$

$$FF = \frac{P_m}{P_T} = \frac{I_m V_m}{I_{sc} V_{oc}} \tag{6.3}$$

$$\eta = \frac{P_{out}}{P_{in}} = \frac{P_m}{P_{in}} = \frac{FF\ I_{sc} V_{oc}}{P_{in}} \tag{6.4}$$

where

- I_{sc} is short circuit current. It is defined as the maximum current of a solar cell/panel under sunlight at zero voltage when it is connected to a low load with output terminals shorted.
- V_{oc} is open circuit voltage. It is the maximum voltage of a solar cell/panel under sunlight at zero current with no load is connected.
- P_m is maximum power. It is the actual rated highest power that can be generated by the solar cell/panel. It can be obtained by multiplying the current at the maximum power *(I_m)* by the voltage at maximum power *(V_m)* as shown in (6.1). The power of the PV panel depends on the operating point and the Maximum Power Point (MPP) is the point near the knee of the I-V curve, which provides the maximum efficiency.
- FF is fill factor. It can be defined as the ratio of the actual maximum power *(P_m)* and the theoretical non-obtainable maximum power *(P_T)* where P_T and FF can be calculated by (6.2) and (6.3), respectively. The fill factor provides a quick measurement of the quality and performance of a solar cell or panel. The closer FF is to one, the better quality of the PV cell or panel. A good typical value of the FF is 0.7 and above.
- η is efficiency. It is the ratio of the output electrical power *(P_{out})* to the input solar power *(P_{in})* as shown in (6.4) where P_{out} can be taken as P_m while P_{in} can be calculated by multiplying the irradiance of the incident light in W/m^2 by the surface area of the solar cell in m^2.

6.2.2 Solar Cell Model

One of the most commonly used method to model a solar cell is to use the single-diode model [119]–[121] which is shown in Figure 6.2. The solar cell, which is made of silicon, consists of a current source, a parallel diode, a shunt resistor and a series resistor. The current source generates the photocurrent when the sunlight hits the solar cell and it is directly proportional to the solar radiation while the diode represents the p-n junction of a solar cell. The shunt resistor represents the shunt leakage through the p–n junction whereas the series resistor represents the ohmic losses. This model can be used to calculate PV output power (P_{pv}) as follows:

$$I_{pv} = I_{ph} - I_d - I_{sh} \tag{6.5}$$

$$I_{pv} = I_{ph} - I_0(e^{\frac{q(V_{pv}+I_{pv}R_s)}{nkT_{pv}}} - 1) - (\frac{V_{pv} + I_{pv}R_s}{R_{sh}}) \tag{6.6}$$

$$P_{pv} = I_{pv}\, V_{pv} \tag{6.7}$$

where

I_{pv}: PV current (A)

I_{ph}: photocurrent generated by the current source (A)

I_d: diode current (A)

I_{sh}: shunt resistance current (A)

I_0: reverse saturation current (A)

q: electron charge (1.602 x 10^{-19} C)

n: ideality factor (between 1 and 2)

R_s: series resistance (Ω)

R_{sh}: shunt resistance (Ω)

k: Boltzman constant (1.381 x 10^{-23} J/°K)

T_{pv}: cell temperature (°K)

V_{pv}: PV voltage (V)

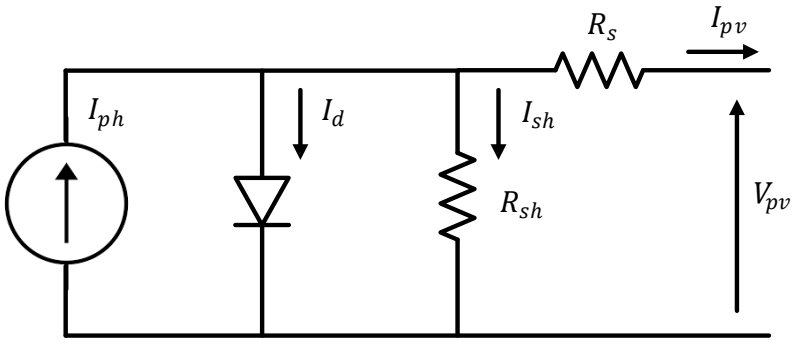

Figure 6.2: PV single-diode model

The two-diode model is used sometimes to model PV cells which is similar to the single-diode model, but with two parallel diodes instead of a single one, as shown in Figure 6.3. The two-diode model provides an improved accuracy in

comparison to the single-diode model and it is mainly for polycrystalline silicon solar cells [122]. The PV output current can be calculated as follows:

$$I_{pv} = I_{ph} - I_{d1} - I_{d2} - I_{sh} \tag{6.8}$$

$$I_{pv} = I_{ph} - I_{01}(e^{\frac{q(V_{pv}+I_{pv}R_s)}{n_1 kT_{pv}}} - 1) - I_{02}(e^{\frac{q(V_{pv}+I_{pv}R_s)}{n_2 kT_{pv}}} - 1) - (\frac{V_{pv}+I_{pv}R_s}{R_{sh}}) \tag{6.9}$$

where

I_{d1}: first diode current (A)

I_{01}: reverse saturation current for first diode (A)

I_{d2}: second diode current (A)

I_{01}: reverse saturation current for second diode (A)

n_1: ideality factor for first diode

n_2: ideality factor for second diode

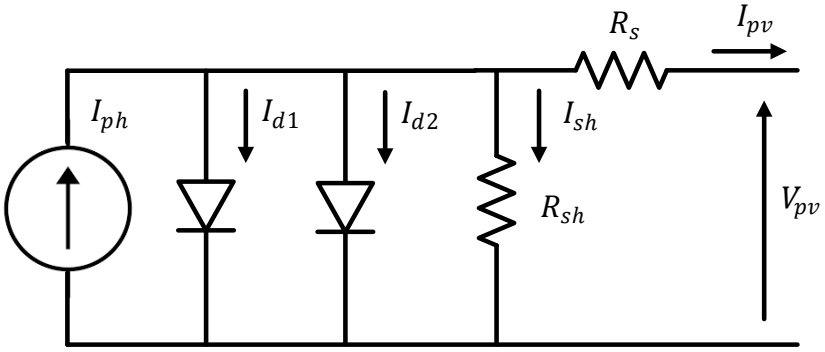

Figure 6.3: PV two-diode model

6.2.3 Modelling of PV's Cell and Module

Solar irradiance and PV temperature has a great impact on the performance of the PV cell or module. The electrical power of a single solar cell in a flat-plate module, without concentrator, P_{PV} can be calculated as in (6.10) while the actual electrical power ($P_{PV,a}$) is given by (6.11) [123], [124].

$$P_{PV} = \eta_{PV} A_{PV} G_T f \tag{6.10}$$

$$P_{PV,a} = K_t P_{PV} = K_t(\eta_{PV} A_{PV} G_T f) \tag{6.11}$$

$$K_t = 1 + a(T_c - 25) \tag{6.12}$$

where

η_{PV} is PV cell efficiency

A_{PV} is area of the PV cell in m^2

G_T is total/global solar irradiation (direct + diffuse) in W/m^2

f is correction coefficient for all factors except temperature

K_t is correction coefficient factor for temperature given by (6.12) when standard or cell reference temperature is 25 ^{o}C.

a is normalized temperature that depends on the cell type and manufacturer

T_c is cell temperature in ^{o}C that is affected by irradiance and ambient temperature and can be expressed by

$$T_c = T_a + \left(\frac{NOCT - 20}{800}\right) G_T \tag{6.13}$$

where normal operating cell temperature (NOCT) is defined as the cell temperature when a PV panel operates under 800W/m^2 of solar irradiation and 20 ^{o}C of ambient temperature. NOCT is usually between 42 ^{o}C and 46 ^{o}C [46].

The ideal PV module electric power (P_{PVmod}) is calculated by (6.14) where the cells are connected in series and the cell can operate at an efficiency lower than the nominal one. Hence, the actual PV module electric power ($P_{PVmod,a}$) is given by (6.15), taking into account the parasitic current losses generated in the module [123], [124]. Table 6.1 shows the parameters used in the flat-plate PV module which is shown in Figure 6.4. Equations (6.10) to (6.16) are used for developing Matlab model for the PV module as shown in Figure 6.5.

$$P_{PVmod} = P_{PV,a} N_S \eta_{PVmod} \tag{6.14}$$

$$P_{PVmod,a} = (P_{PVmod} - P_{PVpar})\eta_{inv} \tag{6.15}$$

$$P_{PVpar} = G_{PVpar} G_T A_{PV} N_c \tag{6.16}$$

where

N_S is PV cell numbers in series

η_{PVmod} is PV module efficiency

η_{inv} is inverter efficiency

P_{PVpar} is module parasitic current losses given by (6.16)

G_{PVpar} is parasitic losses factor coefficient that depends on radiation

Table 6.1: Parameters in the flat-plate PV module

Parameter	Symbol	Value
PV cell efficiency	η_{PV}	0.17
Area of the PV cell (15.6cm X 15.6cm)	A_{PV}	243.36 cm^2
Correction coefficient for all factors except temperature	f	1
Normalized temperature coefficient (for single-crystalline Si (c-Si) module)	a	-0.16%/ ^oC
Cell/Module temperature	T_c	45^oC
PV cell numbers in series	N_S	49
PV Module efficiency	η_{PVmod}	0.9
Inverter efficiency	η_{inv}	0.9
Parasitic losses factor coefficient	G_{PVpar}	0.023

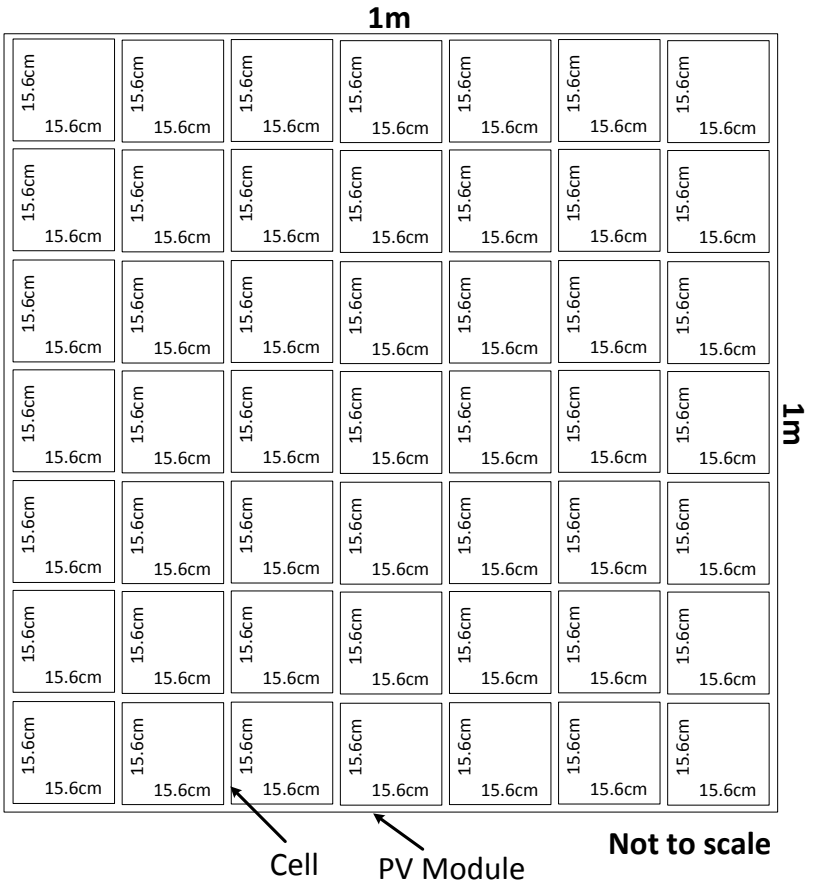

Figure 6.4: 1m^2 PV module

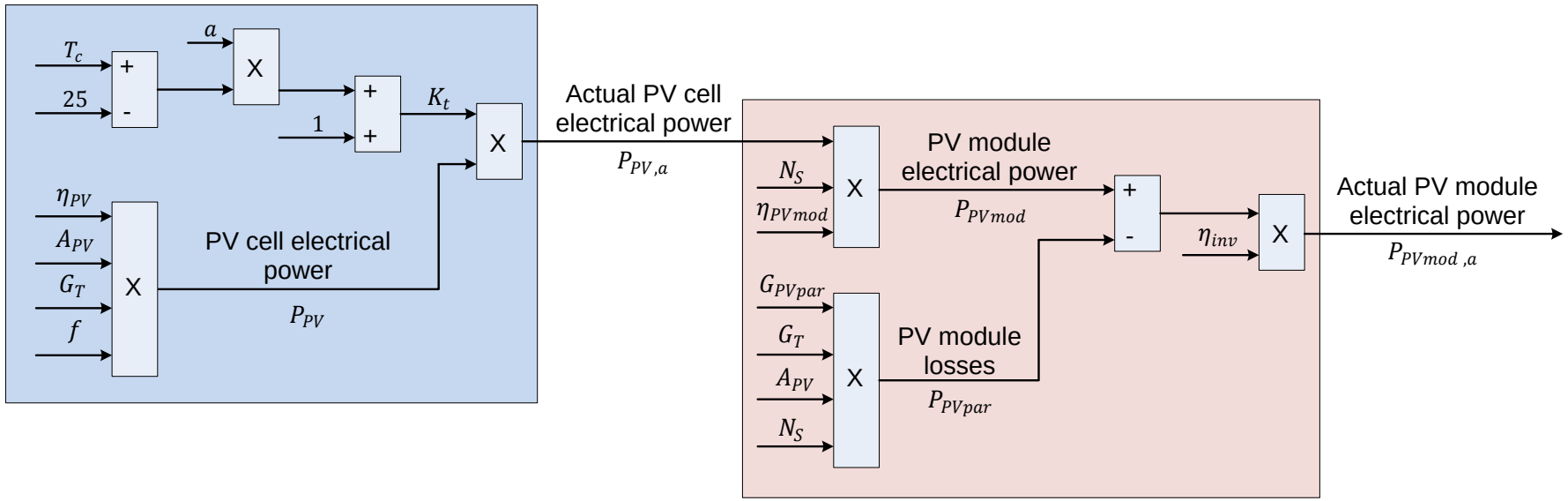

Figure 6.5: Model of PV module

6.2.4 Maximum Power Point of the Photovoltaic Cell and Module

The maximum power point (MPP) provides the maximum efficiency of the PV module. Therefore, it is very important to track this point in order to utilize the PV power efficiently. There are many different ways for Maximum Power Point Tracking (MPPT) of PV power as detailed in [83] where the majority of the reported techniques respond to variations in both irradiance and temperature. However, some of them are more suitable when the temperature is almost constant. Description of the different types of MPPT is not covered as part of the scope of this thesis. The MPP is normally working around 70% to 82% of the open circuit voltage. Hence, when the voltage regulation is applied, the MPP tracker can decide quickly on the initial point according to that percentage within a known tracking range [18]. This is an adequate and very cheap solution for tracking without any complications in executions. Therefore, fractional open circuit voltage (V_{oc} = 80% in this thesis), as one type of the available MPPT, is used in the PV MPP shifting operation (refer to Figure 3.8 of Chapter 3) for MPPT. However, other types of MPPT can be used if required.

6.2.5 Modelling of CPV's Cells and Module

Concentrated Photovoltaic (CPV) technology generates electricity by utilizing optics, such as lenses or mirrors, in order to concentrate a large amount of sunlight onto a small area of solar photovoltaic materials (concentrated solar cell). CPV uses tracker to track the sunlight and sometimes a cooling system to further increase its efficiency. Using less PV materials reduces the cost of the materials and overall product's cost. At the same time, the amount of generated power is increased. However, CPV technology suffers from the non-uniformity of the incident flux, which tends to create hot spots as well as current mismatch [125]. This has a negative impact on the overall efficiency. The CPV is classified based on their concentration ability which is related to the term called geometric concentration ratio (C_g). This term is given by (6.17) and defined as the ratio of the area of entry aperture of the optical element of the concentrator (A_a) to the area of the exit aperture representing the active area of the solar cell (A_b).

$$C_g = \frac{A_a}{A_b} \tag{6.17}$$

Furthermore, the intensity of concentration or “suns” is another means for measuring concentration which is denoted by the letter “X” and defined as the ratio of the average light intensity on a particular solar cell in W/m^2 to the standard radiation (1000W/m^2) [118].

The electrical power of a single solar cell in a system that uses concentrator P_C can be calculated as in (6.18) while the actual electrical power ($P_{C,a}$) is given by (6.19) [123], [124].

$$P_C = \eta_C \eta_{opt} A_C C G_d f_C \tag{6.18}$$

$$P_{C,a} = K_{tc} P_C = K_{tc}(\eta_C \eta_{opt} A_C C G_d f_C) \tag{6.19}$$

$$K_{tc} = 1 + a_C(T_C(conc.) - 25) \tag{6.20}$$

where

η_C is CPV cell efficiency

η_{opt} is optical efficiency

A_C is area of the CPV cell in m^2

C is concentration value in suns

G_d is direct solar irradiation in W/m^2

f_c is non-ideal tracking correction factor determined mainly by optical loss

K_{tc} is correction coefficient factor for temperature in concentrated module given by (6.20) when standard temperature is 25 ^{o}C.

a_C is normalized temperature in concentrated module that depends on the cell type and manufacturer

$T_C(conc.)$ is cell temperature for concentrated module in ^{o}C

The ideal module electric power (P_{mod}) can be calculated as shown in (6.21) while the actual module electric power ($P_{mod,a}$) is given by (6.22), taking into account losses [123], [124]. Table 6.2 shows the parameters used in the concentrated PV module which is shown in Figure 6.6. Figure 6.7 shows a Matlab model for the CPV module.

$$P_{mod} = P_{C,a} N_{SC} \eta_{mod} \tag{6.21}$$

$$P_{mod,a} = (P_{mod} - P_{par}) \eta_{inv} \tag{6.22}$$

$$P_{par} = G_{par} G_d A_C C N_{SC} \tag{6.23}$$

where

N_{SC} is CPV cell numbers in series

η_{mod} is CPV module efficiency

η_{inv} is inverter efficiency

P_{par} is module parasitic current losses given by (6.23)

G_{par} is parasitic losses factor coefficient that depends on radiation

Table 6.2: Parameters in the concentrated PV (CPV) module

Parameter	Symbol	Value
CPV cell efficiency	η_C	0.38
Optical efficiency (parabolic concentrator)	η_{opt}	0.85
Area of the CPV cell (1cm X 1cm)	A_C	1 cm^2
Concentration value	C	500:1 (500X)
non-ideal tracking system correction factor	f_C	0.9
Normalized temperature coefficient	a_C	-0.4%/ ^oC
Cell/Module temperature	$T_c(conc.)$	70^oC
CPV cell numbers in series	N_{SC}	25
CPV module efficiency	η_{mod}	0.9
Inverter efficiency	η_{inv}	0.9
Parasitic losses factor coefficient	G_{par}	0.023

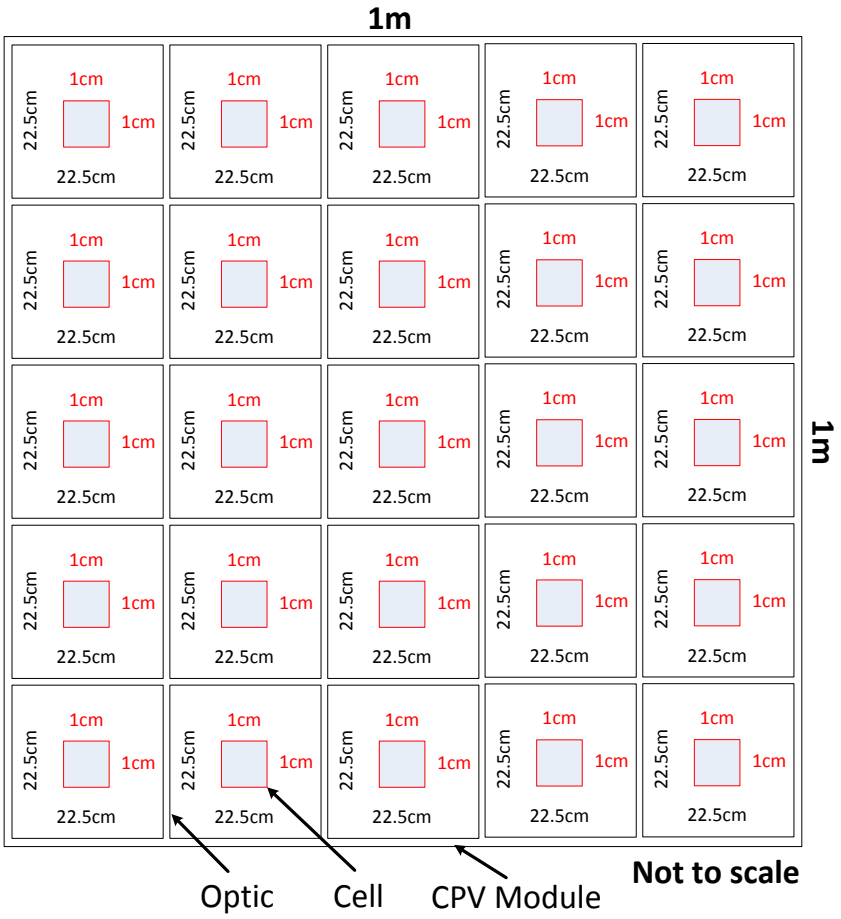

Figure 6.6: 1m^2 CPV module

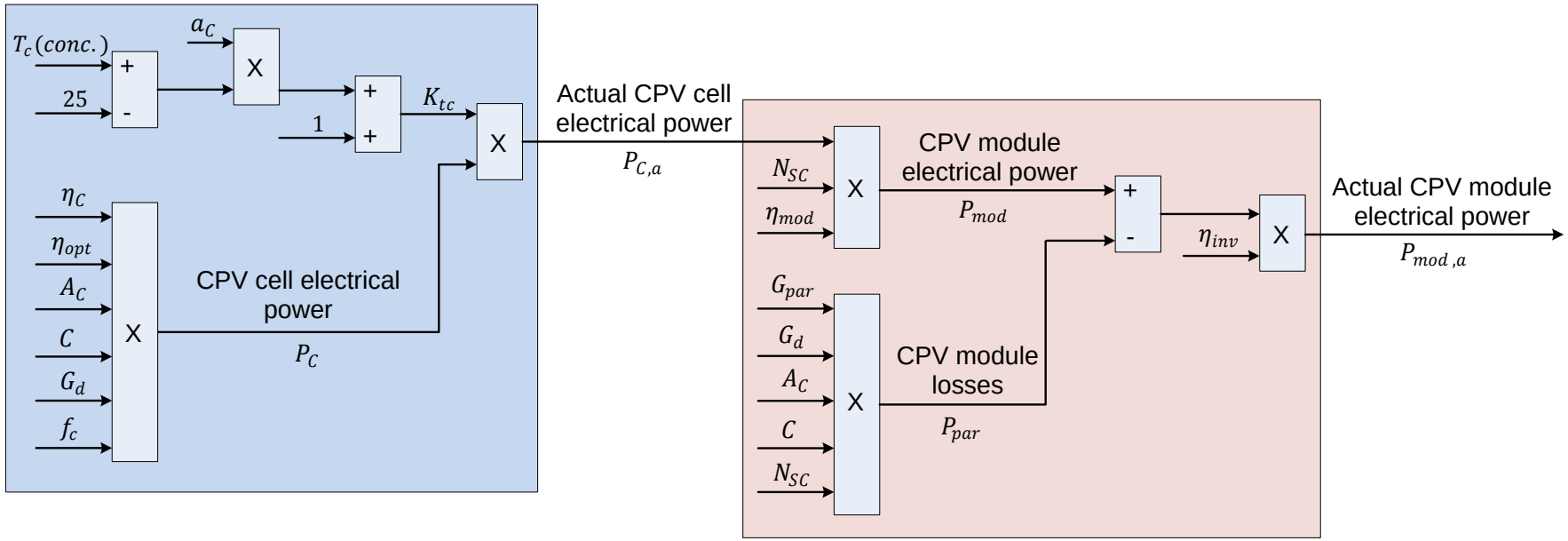

Figure 6.7: Model of CPV module

6.2.6 Impact of Shading on Frequency

The developed PV and CPV models in Figure 6.5 and Figure 6.7, respectively are connected to a simplified AC microgrid model, which consists of a PV/CPV, battery, auxiliary unit and load connected to a common AC bus. The whole idea is to check and compare the impact of shading or changing irradiation on the frequency for around $1m^2$ area of 135Wp PV (Figure 6.4) and 500X CPV (Figure 6.6) where the supervisory control is carried out by a Fuzzy Logic Controller (FLC). The simplified model of the microgrid that is developed in Chapter 4 along with the FLC designed in Chapter 3 are shown in Figure 6.8. They are used together for checking the impact of shading on the frequency by having either a PV or CPV as a technology for solar energy. The change in frequency $\Delta\omega$ is a combination of a positive shifting $\Delta\omega_+$ to curtail PV or CPV power when required and a negative shifting $\Delta\omega_-$ for providing power by the auxiliary unit whenever needed. Refer to Chapter 3 and Chapter 4 for further details on the design of FLC and simplified model if needed. Several simulations have been carried out for the PV and CPV to check the impact of a sudden change of solar irradiation on the frequency. Some sample results for 48% initial State of Charge (SOC) cases for the PV and CPV both with and without shading are shown as follows. The parameters in Table 6.1 and Table 6.2 are used for the flat-plate PV module and the concentrated PV module, respectively. Table 6.3 shows the parameters of the simplified model of the AC microgrid.

Table 6.3: Parameters in simplified model of AC microgrid along with FLC

Parameter	Symbol	Value
Maximum state of charge	SOC^*_{max}	95%
Minimum state of charge	SOC^*_{min}	40%
Minimum state of charge plus 10%	$SOC^*_{min+10\%}$	50%
Maximum charging power	$P^*_{Charge\_max}$	1000W
Maximum discharging power	$P^*_{Discharge\_max}$	1000W
Nominal bus frequency	$\omega_o = 2\pi f_o$	$2\pi(50)$=314.16rad/s
Maximum positive frequency deviation	$\Delta\omega_{max+}$	0.5Hz
Maximum negative frequency deviation	$\Delta\omega_{max-}$	-0.5Hz
Battery capacity	C_{bat}	100AH
Battery voltage	V_{bat}	120V
Active power droop coefficient for auxiliary unit	m_{aux}	0.75e-4 rad/s/W

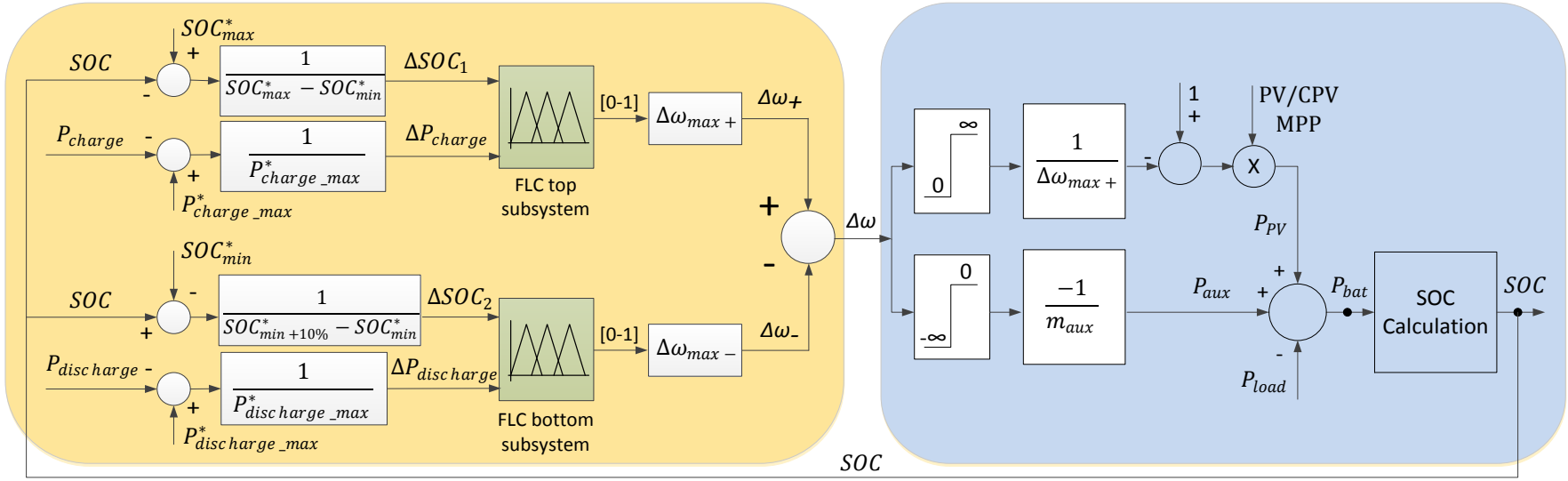

Figure 6.8: Simplified model of AC microgrid along with FLC

Case 1: Simulation results when PV is working without shading:

Figure 6.9 shows that PV generation starts at t=5h and stops at t=20h due to the change in global solar irradiation shown in Figure 6.9(a) which has a maximum value of around 1340W/m^2. Figure 6.9(b) shows power from individual PV cell, module power and module losses that all follow the shape of irradiation. The maximum power of individual PV cell is around 5W while the maximum actual electrical power from the PV module is around 180W. The peak losses from the whole module are around 36W. Frequency is shown in Figure 6.9(c) while both frequency deviations are shown in Figure 6.9(d). The two deviations' values are added together which ultimately decide on the frequency deviation from the nominal frequency. The negative deviation in this case prevails and the frequency is lowered by the negative deviation amount as can be easily noticed from the shape of the frequency after t=5h.

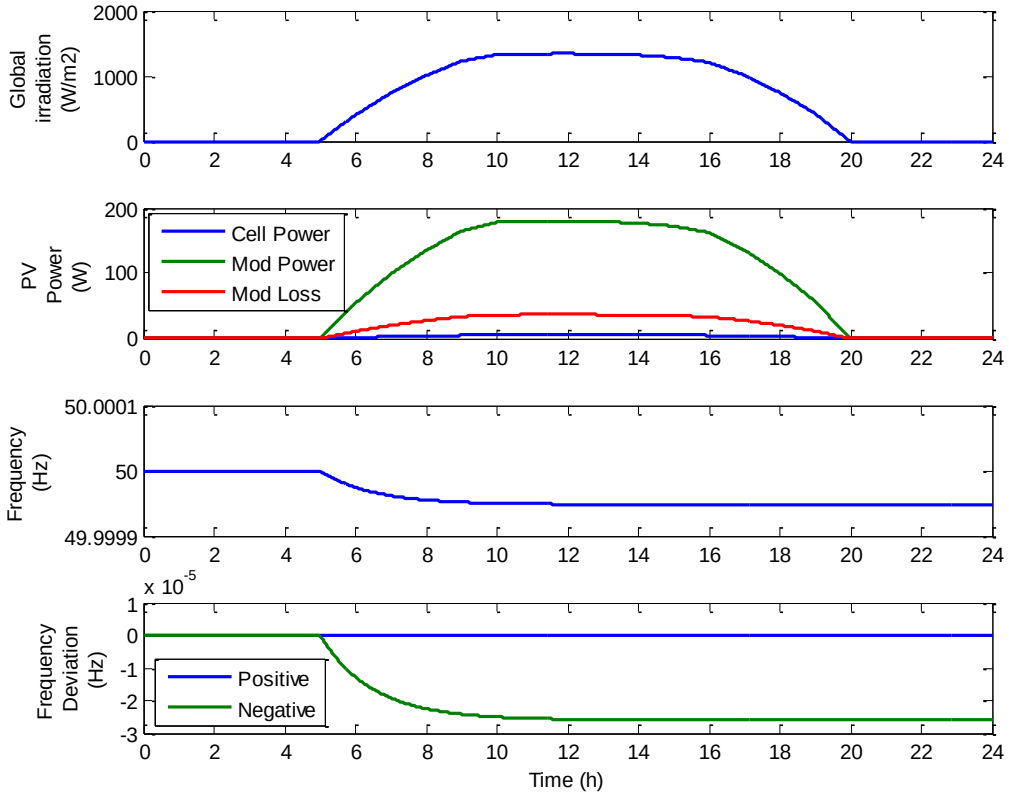

Figure 6.9: PV without shading-Part1: (a) global irradiation (b) PV power (c) frequency (d) frequency deviation

Figure 6.10(a) shows the PV power (P_{pv}) with a fixed load of 200W as shown in Figure 6.10(b). The battery provides the additional power (P_{bat}) required to meet

the load's demand that cannot be provided by the PV as shown in Figure 6.10(c). The battery is always in discharging mode since the PV generation is lower than the load. For the periods from t=0 to t=5h, there is no PV generation since the solar irradiation is equal to zero and the whole power for supplying the load is coming from the battery. After that, the PV generates power until t=20h where the solar irradiation goes back to zero and the battery provides the whole power again. The battery power shape takes the opposite shape of the PV power, so any increase in the PV power has a decrease in the battery power. The auxiliary power (P_{aux}) is very little power, which starts from t=5h to the end of simulation with a maximum production of around 0.3W only as shown in Figure 6.10(d) while SOC is declining from the 48% initial value as shown in Figure 6.10(e). The contribution from the auxiliary unit could be more if a higher capacity of the PV module is used.

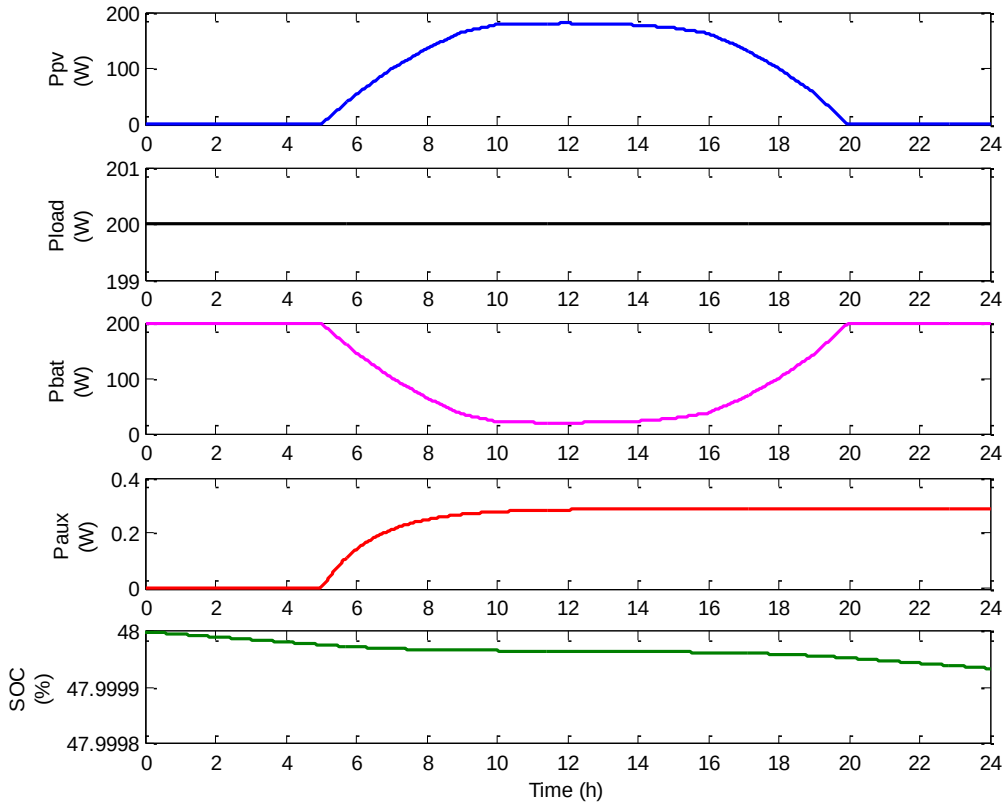

Figure 6.10: PV without shading-Part2: (a) PV power (b) load (c) battery power (d) auxiliary power (e) SOC

Case 2: Simulation results when PV is working with shading:

Shading occurs between t=9h to t=13h in this case and solar irradiation is shown in Figure 6.11(a). The irradiation drops from around 1225W/m^2 at t=9h to around 240W/m^2 at t=10h (representing diffuse irradiation) and continues with this value up to t=12h before the irradiation starts rising and reaching the normal value without shading which is 1320W/m^2 at t=13h. Hence, the PV power drops during the shading period. Power from individual PV cell, module power and module losses are all follow the shape of the irradiation including the shading as shown in Figure 6.11(b) where the PV generation outside the shading period is the same as the case in Figure 6.9(b) with similar maximum values of generation and losses. Frequency and frequency deviations are shown in Figure 6.11(c) and (d), respectively with very minor increase in the negative deviation in comparison to the case in Figure 6.9(d).

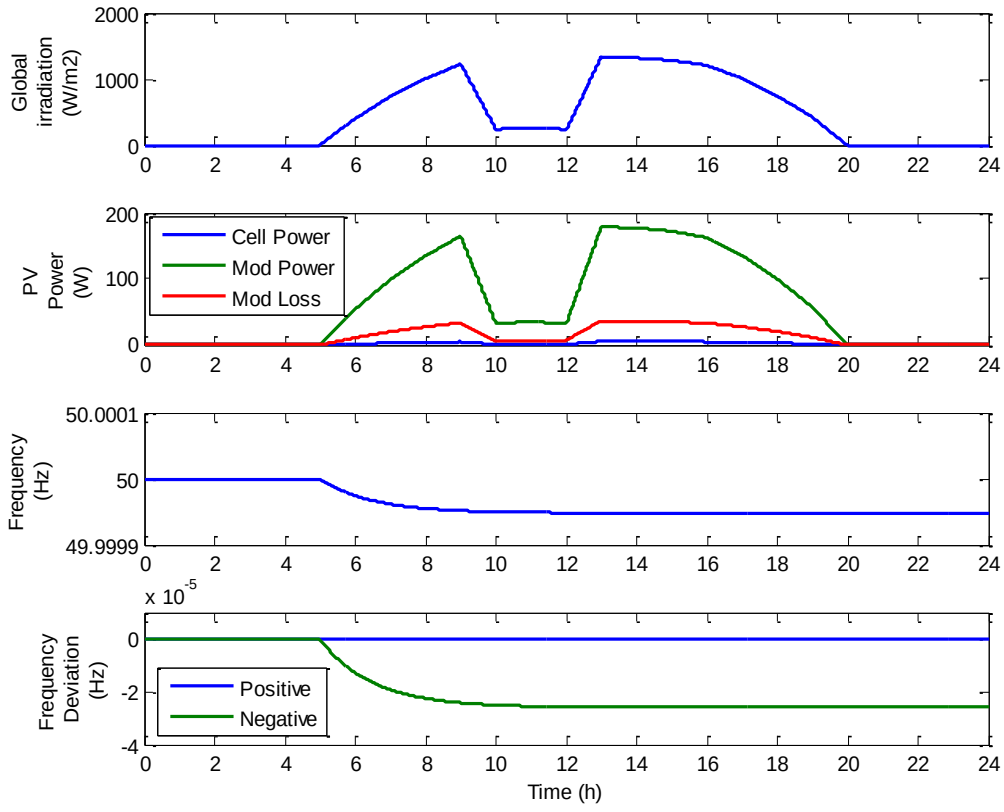

Figure 6.11: PV with shading-Part1: (a) global irradiation (b) PV power (c) frequency (d) frequency deviation

Figure 6.12 shows similar responses like the ones in Figure 6.10 apart from the period of shading that is between t=9h to t=13h. The PV power as shown in

Figure 6.12(a) drops from around 164W at t=9h to around 35W between t=10h and t=12h before the irradiation starts rising and the PV power reaches the normal value without shading which is 178W at t=13h in line with the changes in irradiation as a result of shading during this period. The same 200W fixed load is used as shown in Figure 6.12(b). The battery is in discharging mode as shown in Figure 6.12(c) and provides required power with a maximum power of 200W when there is no PV generation. The auxiliary unit provides very little power from t=5h onwards as shown in Figure 6.12(d). Similar to the case in Figure 6.10(e), the SOC is declining as shown in Figure 6.12(e).

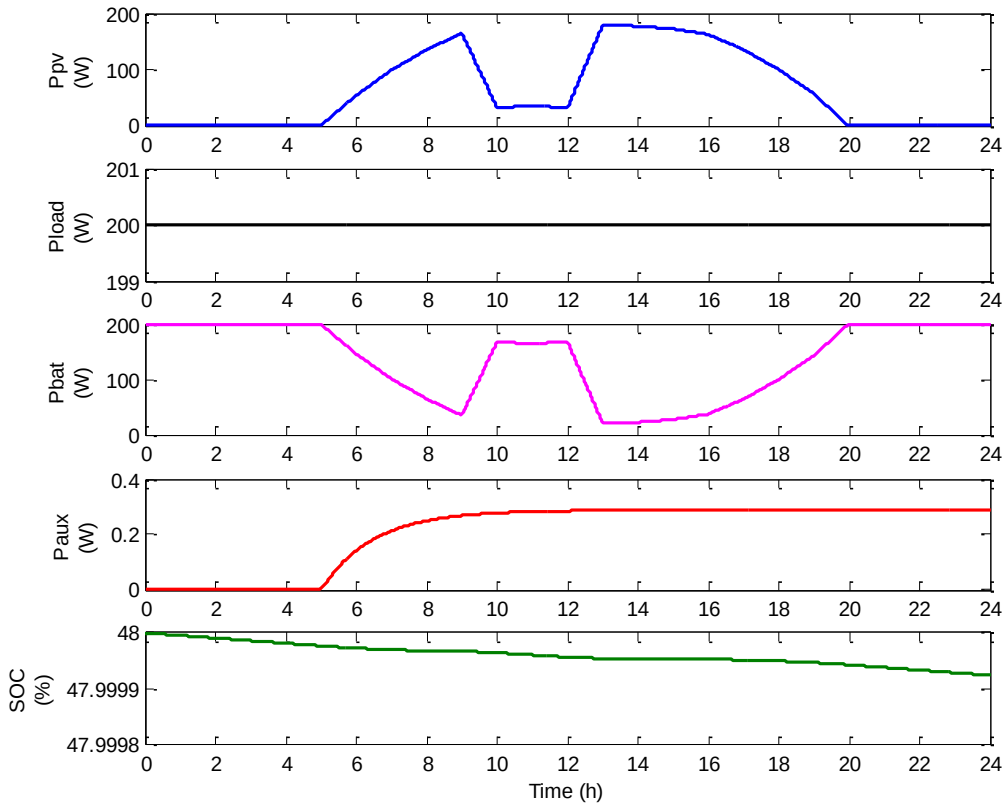

Figure 6.12: PV with shading-Part2: (a) PV power (b) load (c) battery power (d) auxiliary power (e) SOC

Case 3: Simulation results when CPV is working without shading:

Direct solar irradiation is shown in Figure 6.13(a) with a maximum value of around 1118W/m^2 where CPV generates power from t=5h until t=20h. The rest of the duration has zero CPV generation. Figure 6.13(b) shows power from individual CPV cell, module power and module losses where all of them are following the same shape of the irradiation. The maximum power of individual

CPV cell is around 13W while the maximum actual electrical power from the CPV module is around 240W with peak module losses of around 32W. Frequency is shown in Figure 6.13(c) whereas frequency deviations are shown in Figure 6.13(d). Unlike the case with the PV shown in Figure 6.9, the positive deviation in this case prevails and the frequency is increased by the positive deviation amount. This can be easily noticed from the shape of the frequency after t=9h which follows the shape of the positive deviation.

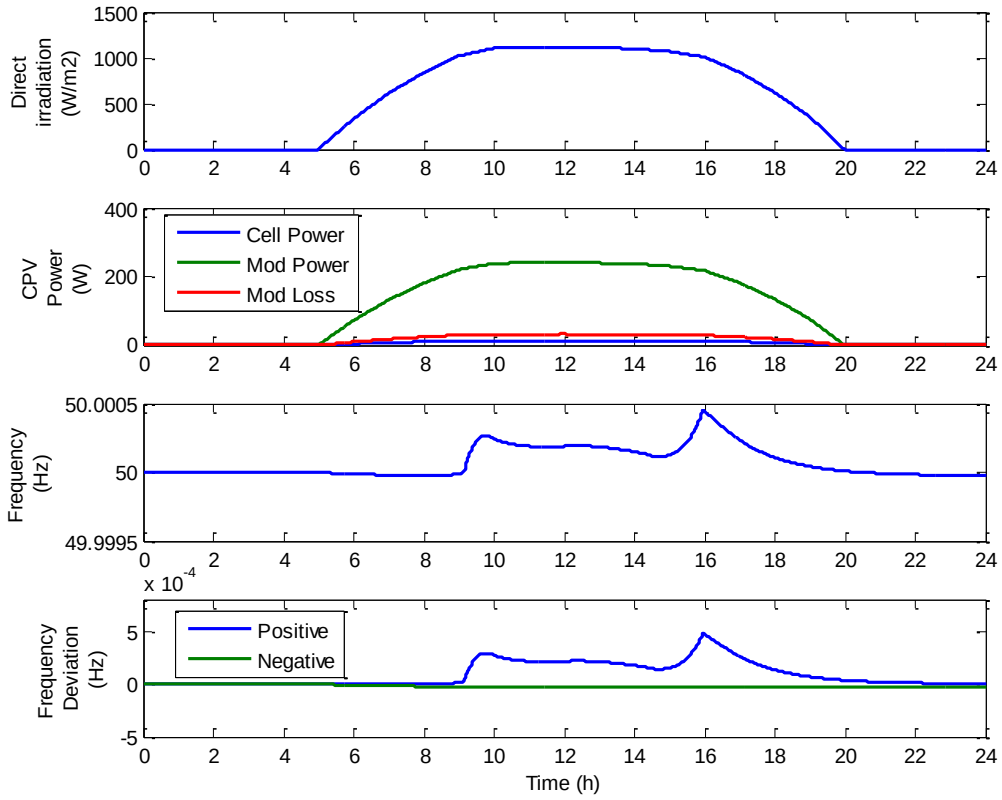

Figure 6.13: CPV without shading-Part1: (a) direct irradiation (b) CPV power (c) frequency (d) frequency deviation

Figure 6.14(a) shows the CPV power (P_{cpv}) with a fixed load of 200W as shown in Figure 6.14(b). The battery provides the required power (P_{bat}) to meet the load's demand that cannot be met by the CPV as shown in Figure 6.14(c). The whole power is initially coming from the battery until t=5h where the CPV starts producing power. The battery is in discharging mode until around t=8h where the CPV provides almost the full power required by the load and the battery changes slowly to the charging mode. The maximum charging power for the battery reaches around 40W. At about t=16h, the contribution from the battery

starts rising because the CPV power starts declining due to reduction in the irradiation. The CPV generates power until t=20h where the solar irradiation goes back to zero and the battery provides the whole power again. The auxiliary power (P_{aux}) is almost zero with two discrete power supplies of around 0.26W as shown in Figure 6.14(d). The SOC is declining as shown in Figure 6.14(e).

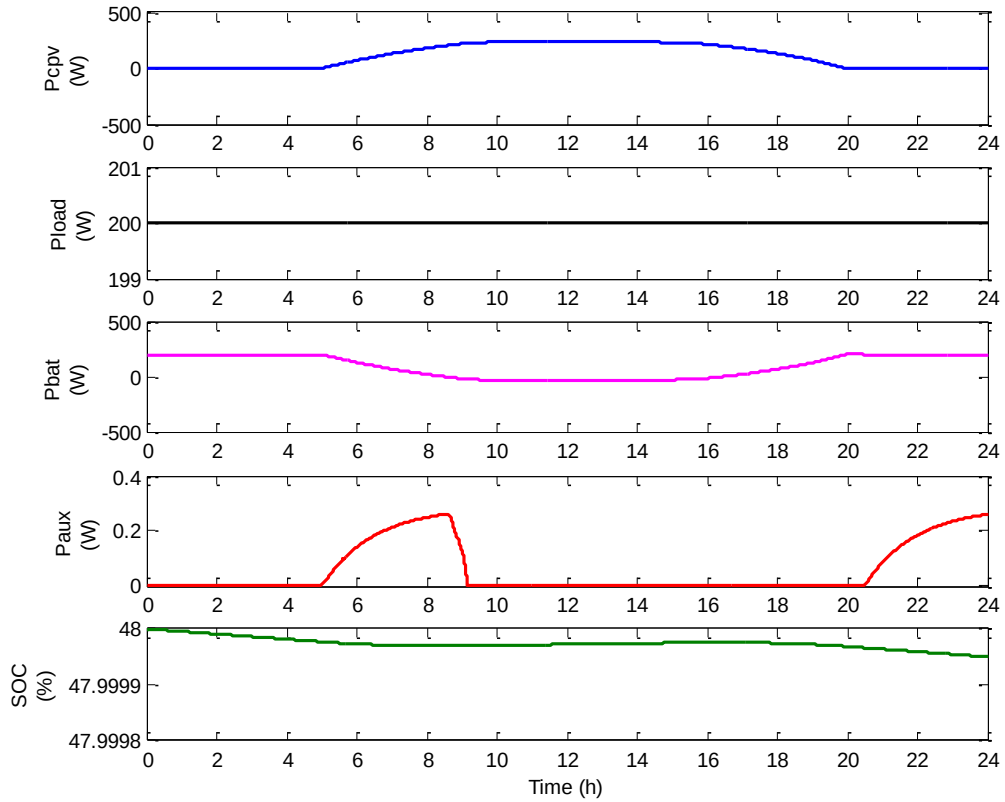

Figure 6.14: CPV without shading-Part2: (a) CPV power (b) load (c) battery power (d) auxiliary power (e) SOC

Case 4: Simulation results when CPV is working with shading:

Figure 6.15(a) shows direct solar irradiation where the shading takes place between t=9h and t=13h, but this time the irradiation goes to zero from t=10h to t=12h unlike the case of Figure 6.11(a) because CPV uses only direct irradiation without diffused irradiation. Figure 6.15(b) shows power from individual CPV cell, module power and module losses that are similar in shape to the irradiation. Frequency and frequency deviations are shown in Figure 6.15 (c) and (d) respectively. The positive deviation in this case has more influence on the frequency. Therefore, the frequency mainly takes the shape of the

positive frequency shape unlike the case with PV shading where the frequency is changed based on the negative deviation as shown in Figure 6.11(c).

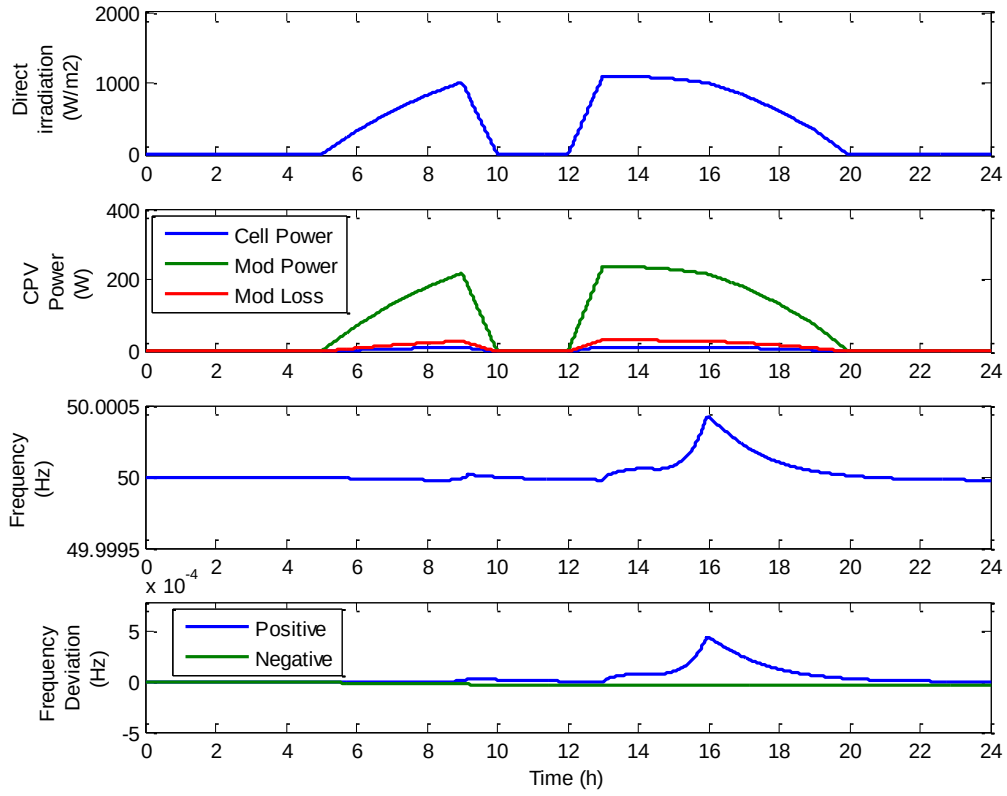

Figure 6.15: CPV with shading-Part1: (a) direct irradiation (b) CPV power (c) frequency (d) frequency deviation

Figure 6.16 shows similar responses as in Figure 6.14 apart from the shading interval between t=9h to t=13h. Figure 6.16(a) shows the CPV power which drops from around 220W at t=9h to zero between t=10h and t=12h before the CPV power reaches the normal value without shading which is around 240W at t=13h in line with the changes in irradiation. The load of 200W is shown in Figure 6.16(b). The battery power is shown in Figure 6.16(c) where the maximum charging power for the battery reaches around 20W which is half of the amount for the case in Figure 6.14(c). The auxiliary power has almost zero contribution with three discrete power supplies of around 0.26W as shown in Figure 6.16(d) in comparison to two in the case of Figure 6.14(d) due to less overall power supply from the CPV as a result of the shading. The SOC is declining as shown in Figure 6.16(e).

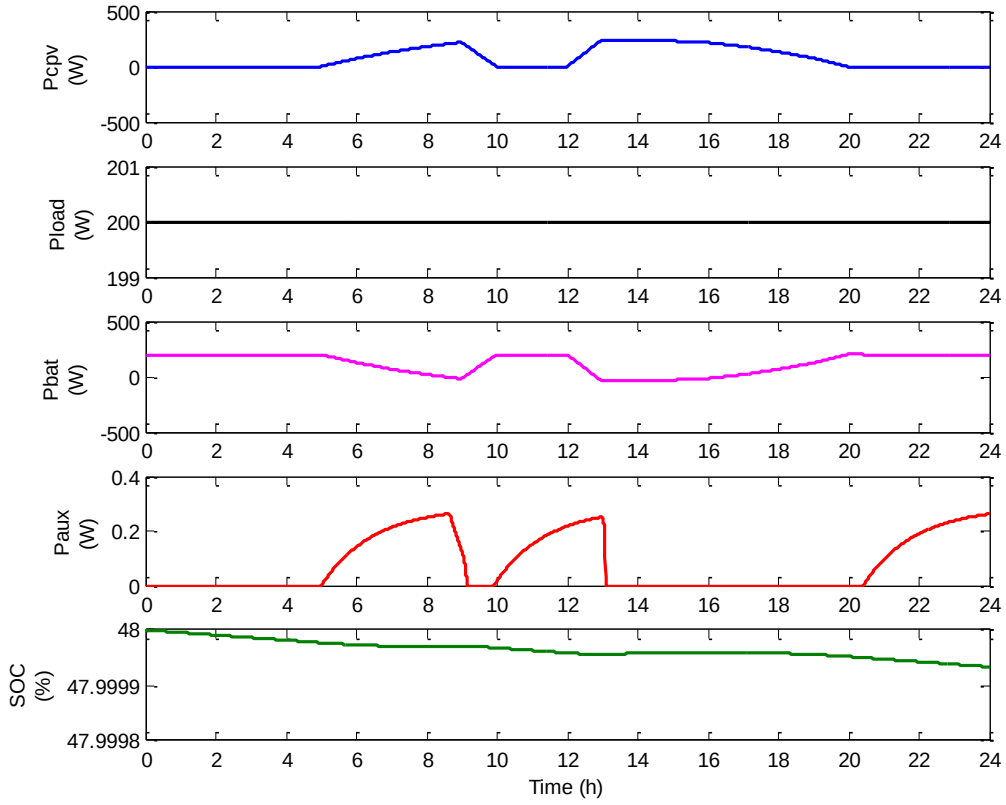

Figure 6.16: CPV with shading-Part2: (a) CPV power (b) load (c) battery power (d) auxiliary power (e) SOC

Further to the individual details provided earlier for each case, Figure 6.17 shows the output responses for PV and CPV in terms of power, frequency and frequency deviations from the cases 2 and 4 above. This is done to aid the comparison in a simple method. Figure 6.17(a) shows the responses for PV while Figure 6.17(b) shows the responses for CPV. As can be seen from Figure 6.17(a), the PV power drops to around 35W between t=10h and t=12h while the CPV power drops to zero in the same period because PV can generate power even with diffused irradiation unlike the CPV which works only with direct irradiation. The frequency is influenced and changed based on the negative deviation for the case of the PV as shown in Figure 6.17(a). Unlike the PV case, the positive deviation has more influence on the frequency in the CPV case as shown in Figure 6.17(b). Therefore, the frequency mainly takes the shape of the positive frequency deviation.

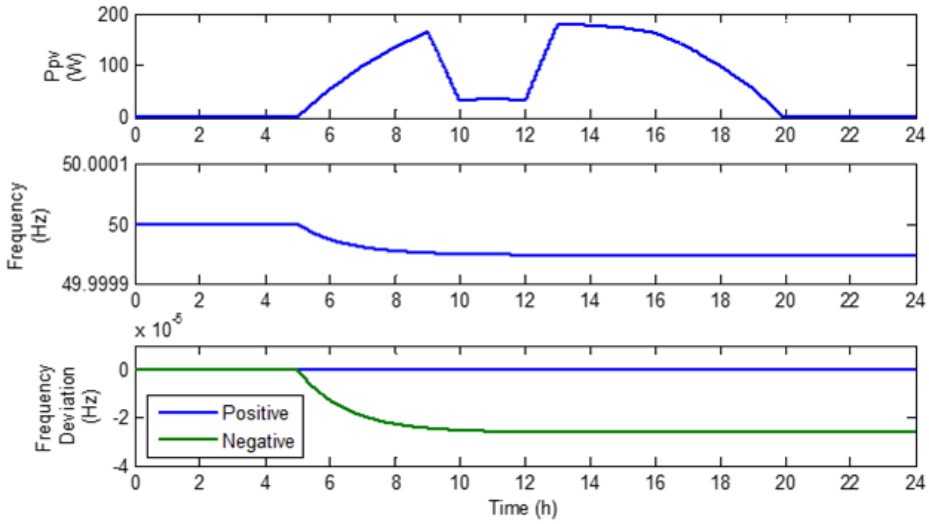

(a)

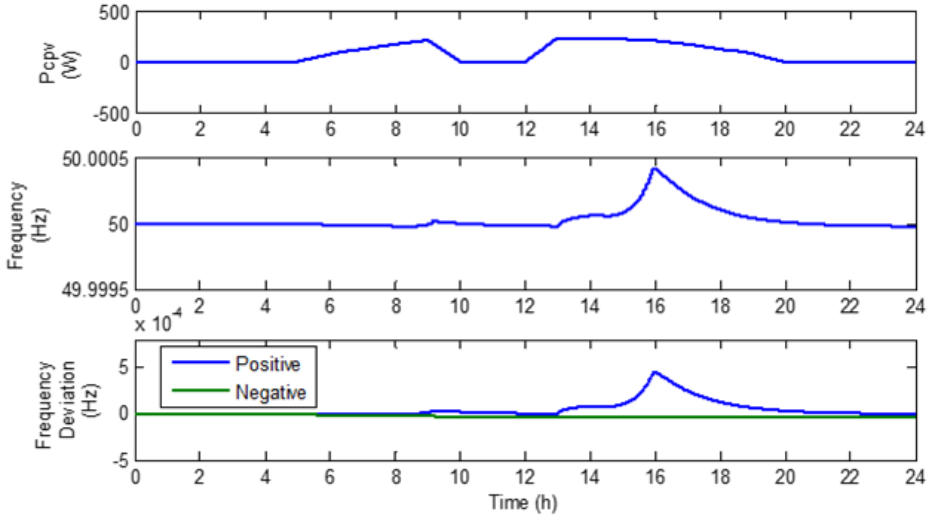

(b)

Figure 6.17: Output responses with shading: (a) PV (b) CPV

6.3 Summary

This chapter has provided details on a PV and a CPV modelling including single-diode and two-diode models that are used for modelling a PV cell. It also provided details on I-V curve and how to obtain important parameters from it. The chapter showed the impact of changing solar irradiation or shading of a PV and a CPV on the microgrid AC bus frequency. Sample simulation results of 1m^2 area of 135Wp PV, and 500X CPV modules both with and without shading have been shown for assessing the impact on the frequency. It is found that the shading of CPV has a more noticeable effect on the bus frequency in comparison to the PV.

CHAPTER 7: CONCLUSIONS & FUTURE WORK

This final chapter of the thesis presents the conclusions of the study and suggests future work that can be carried out as a continuation from this work.

7.1 Conclusions

The thesis examined the development of a supervisory controller for the power management of a stand-alone AC microgrid. The power management system has been developed for the stand-alone AC microgrid consisting of a PV based RES, BESS, auxiliary unit and a load connected in a common AC bus. The thesis presented a wireless supervisory controller to limit the charging and discharging power of the BESS and the state of charge from exceeding their maximum limits and control the operation of the auxiliary unit. The conclusions of the thesis can be summarized as follows:

- The main research works reported in the literature with regard to optimal sizing design, power electronics topologies and control including the supervisory control of both grid-connected and stand-alone microgrids have been reviewed. Different control techniques used for power managements of both standalone and grid-connected microgrids have been reviewed. This review should provide insights to aid the improvement of supervisory control of the microgrids including a fuzzy logic controller. The literature revealed that the supervisory control and power management for conventional energy sources along with RES including controllers based on Fuzzy Logic are not fully resolved yet and research into obtaining optimal operational modes continues to increase as concluded in Chapter 2. Therefore, more research work is required on the supervisory control and energy management of hybrid RES along with non-conventional type of control.
- The effect of intermittency and varying load on the operation of the battery has been studied.
- Analysis has been carried out to study the different possible control strategies for controlling two-stage converters. It clarified the method that a specific power unit is required to operate and identified the droop

control strategies for the different power units. The local controllers for the RES, BESS and auxiliary units have been designed where the BESS is forming the AC bus of the AC microgrid. The concept of a floating auxiliary unit on the common bus has been developed to provide power automatically whenever required as a result of the reduction in the bus frequency below its nominal value.

- A fuzzy logic supervisory controller has been designed to protect the battery and prevent its SOC and charging/discharging power from exceeding their maximum limits regardless of the variation in the load and RES intermittent power. The controller was implemented within the battery unit that varies the bus frequency of the AC microgrid according to the battery unit power and state of charge. The supervisory controller was designed to decide whether to curtail the power generated by the PV or to supplement power from the auxiliary unit. If the frequency is increased above the nominal value, the PV unit curtails its power. On the other hand, if the frequency is decreased, the auxiliary unit generates power. The amount of deviation of the frequency determines the amount of power to be curtailed or supplied by the auxiliary unit. The FLC deals with the management of the real power only. The reactive power is not covered under this thesis. Furthermore, the economics of the power units have not been considered in the thesis. These can form additional inputs to the FLC.
- A Matlab/Simulink AC microgrid model has been developed to assess the performance of the FLC. The microgrid was composed of a PV based RES, BESS, auxiliary unit and a load connected in a common AC bus. The model was based on ideal voltage and current sources and it included all the required control loops. With its limited capacity and power rating, the BESS maintained the bus voltage and frequency in the AC stand-alone microgrid. The BESS balanced the difference between the intermittent RES power and that consumed by load. By varying the AC bus frequency and making use of the local droop controllers, the power management controller was implemented wirelessly to increase the reliability of the system as shown in Chapter 3. Furthermore, no dump load was used. The simulation showed that the battery's SOC and charging/discharging power were maintained within their allowable limits.

- A simplified microgrid model, which considers only droop control level and battery model, has been developed to speed up the simulation time in order to assess the performance of the FLC especially over long periods of time. Non-real-time and real-time simulations for different cases were presented in Chapter 4 using the simplified model. The real-time simulation was used to speed up the simulation time. Results from both simulations validated the functionality and performance of the proposed controller. Both simulations showed that the proposed FLC uses the full available PV power whenever required and curtails it, only when needed, to prevent the battery from over-charging. In addition, it activates the auxiliary unit to support the battery and protect it from over-discharging. The FLC was compared with a proportional controller and the results showed that the FLC performs better than the proportional controller in achieving the required results within the given constraints. The FLC managed to provide a suitable power management of the microgrid in full compliance with the design limits of the SOC and charging/discharging power of the battery irrespective of changes in generation from the RES or changes in the load.
- The effectiveness of the proposed controller has been evaluated using real solar radiation data and different load profiles.
- A laboratory scale AC microgrid, consisting of a PV based RES, BESS, auxiliary unit, and load, has been built and the supervisory controller has been implemented experimentally as shown in Chapter 5. The rated power of the generation units were lower than those presented in Chapter 4 due to the limitations of the laboratory facilities. The design and practical implementation of the prototype AC microgrid including the DC/AC inverters and DC/DC converters have been carried out along with the design of the different controller loops for the DC/DC converters using linearized method. Practical realisation of the controller using OPAL real-time controller has been conducted. The proposed FLC / power management strategy was verified experimentally. The FLC was compared with a proportional controller. The results showed that the FLC was far superior in achieving the required goals within the given constraints as the proportional controller was not always able to maintain the SOC and charging/discharging power within their design limits.

- The effect of a sudden shading of a PV and CPV on the AC bus frequency was studied in Chapter 6. Sample simulation results of 1m^2 area of 135Wp PV, and 500X CPV modules both with and without shading were shown for assessing the impact on the frequency. It is found that the shading of the CPV has a more noticeable effect on the bus frequency.

7.2 Future Work

Further to the outcomes of this thesis, the following promising aspects could be investigated in the future as an extension to the work:

- Modelling of other intermittent renewable energy sources such as wind power could be included to understand the concurrent effect of the power distribution to the microgrid. This might be achieved by developing a droop control equation for the wind power and then modifying the FLC rules to include the wind power in the first input of each FLC subsystem. The expectation is that there would be less usage of the battery and the auxiliary units since there would be extra power coming from the wind power system and it might be at the time when there is a shortage in the PV power, which would be a clear advantage.
- Further experimental investigation could be carried out in a combination of wind, PV, CPV, and CSP powers supplied to the microgrid and its stability, reliability and the effect on the load could be tested. An auxiliary unit could be included as well as a back-up source. Small scale units of a wind turbine, CPV, and CSP could be purchased and installed as part of the microgrid. Control systems including the droop control equations and FLC rules need to be modified to include the new units. The additional units would provide more power from the RES to the microgrid which could support bigger loads and add extra reliability and stability to the overall microgrid power system. There would be less usage of the battery and the auxiliary units since there would be extra power coming from the new units.
- Design a supervisory controller wirelessly using the DC bus voltage for a DC microgrid similar to the bus frequency for the AC microgrid. Therefore, changes on the DC bus voltage could either trigger the

curtailment of the RES power or supplement of power by the auxiliary unit. Hence, the DC bus voltage would be used as a communication means instead of the AC bus frequency in the AC microgrid. A similar method of the power management that has been used in the AC microgrid could be adopted for the DC microgrid. This would provide equivalent outcomes to those achieved in the AC microgrid.

- Include the reactive power as part of the power management system probably by creating another FLC which would be responsible for the management of the reactive power and adding some capacitor banks that would support the voltage whenever required. This would enhance the reactive power requirements. The DC bus voltage could be used as a trigger or communication means for supplying the reactive power or not. The outcome of this work would provide a management system for the reactive power.
- Add an estimated operating cost for each power unit to the power management system which could be another input to the FLC. This could be used as one of the deciding factors for running a particular unit at a particular time and for giving the unit a priority in comparison to the other ones. This provides an economic element to the decision of the FLC.
- Microgrid with multiple PV and/or battery units could be studied instead of only single PV unit and single battery unit that are considered in this thesis. In addition, other energy generator devices such as a fuel cell could also be investigated to identify its stability on the microgrid environment. The effect of different storage technologies in respect to their sudden changes of SOC could be fully investigated. Furthermore, the effect of alternative energy storage mechanism such as thermal energy storage or liquid air could be explored for a better understanding of its effect to the microgrid. This would provide more options in terms of selection of the energy storage system.
- Use different capacities of generation, for example from 1kW up to 10kW to 100kW or even MW level generation system that could supply much higher loads than the one considered in this thesis. The installation of very high RES capacities is not easy to achieve for research purposes due to the limitation in the site and funding. Hence, limiting this scope to simulation is more feasible compared to actual installations. However,

simulation's result could support the feasibility and encourage investors to build a microgrid with high RES capacities and control them using FLC. This would provide a wider scope to assess the FLC capabilities in managing the microgrid.

- Use one of the optimization methods such as Artificial Neural Network (ANN) or Genetic Algorithm (GA) or even Particle Swarm Optimization (PSO) to further optimize the membership functions of the fuzzy logic controller. This might provide a great benefit by using the advantage of another intelligent optimization method along with the FLC. It could improve the decision making process of the FLC.

APPENDIX

Appendix A: Detailed Matlab/Simulink files

Appendix B: Copies of published papers

Appendix C: Bode plot program for DC/DC Converter

Appendix A: Detailed Matlab/Simulink files

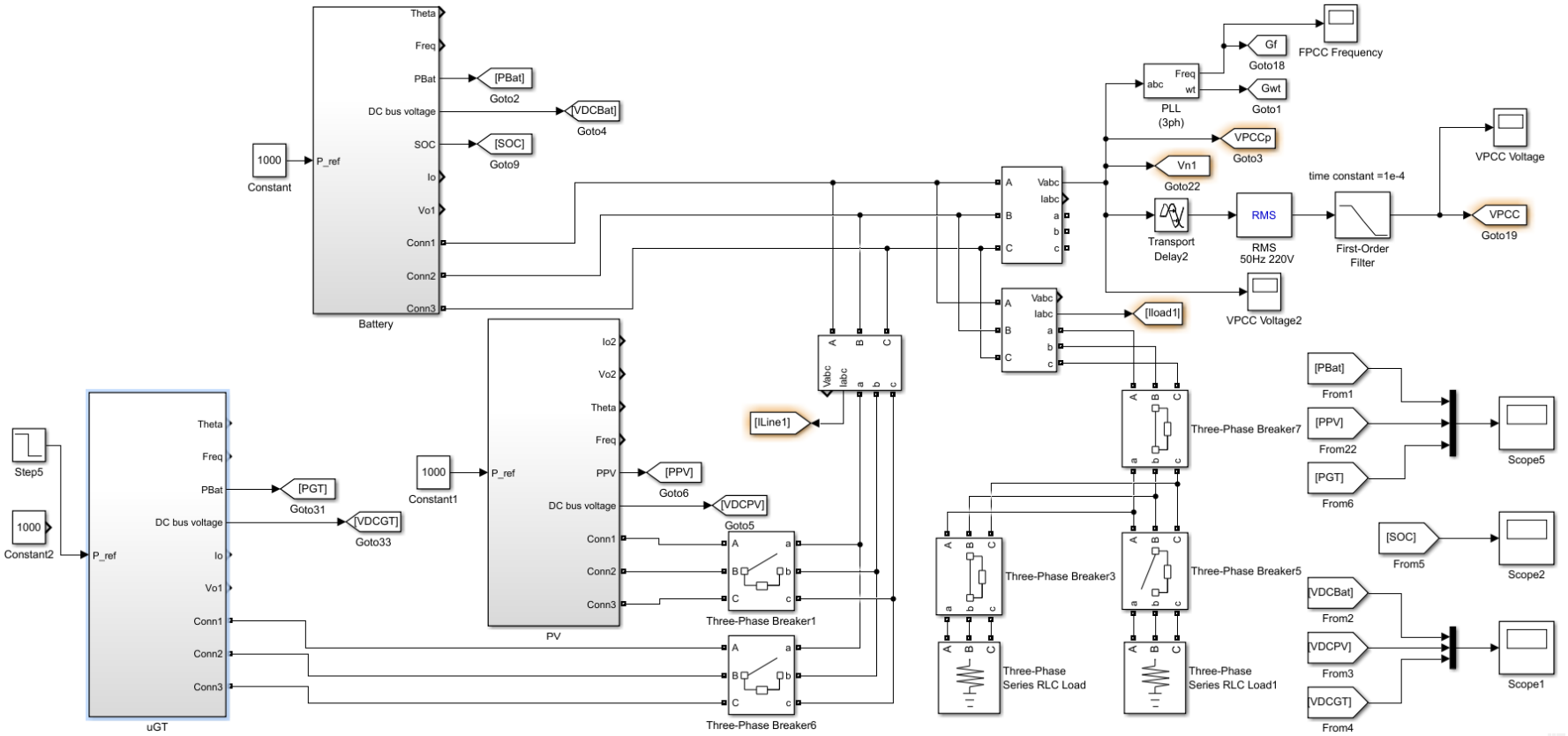

Figure A.1: Matlab/Simulink model of the microgrid

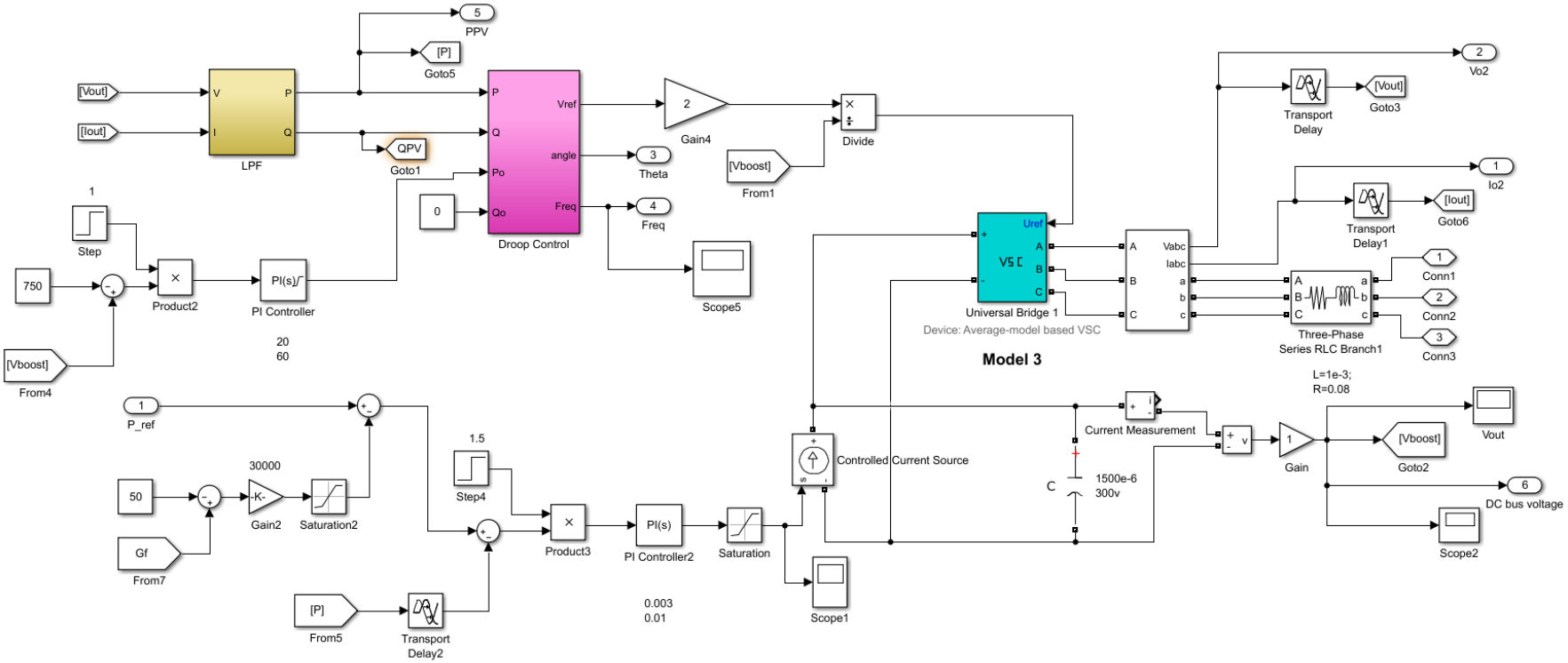

Figure A.2: Matlab/Simulink model for PV unit

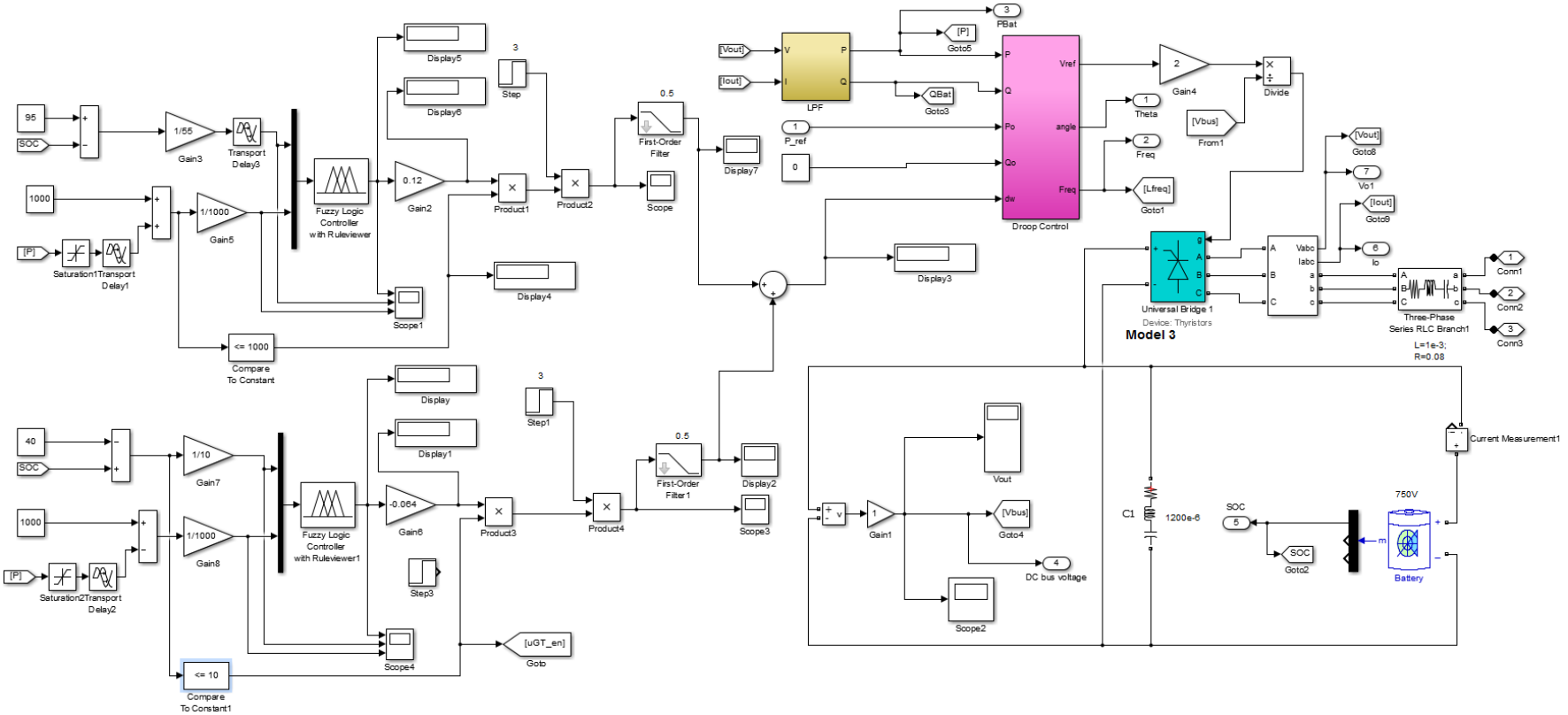

Figure A.3: Matlab/Simulink model for battery unit

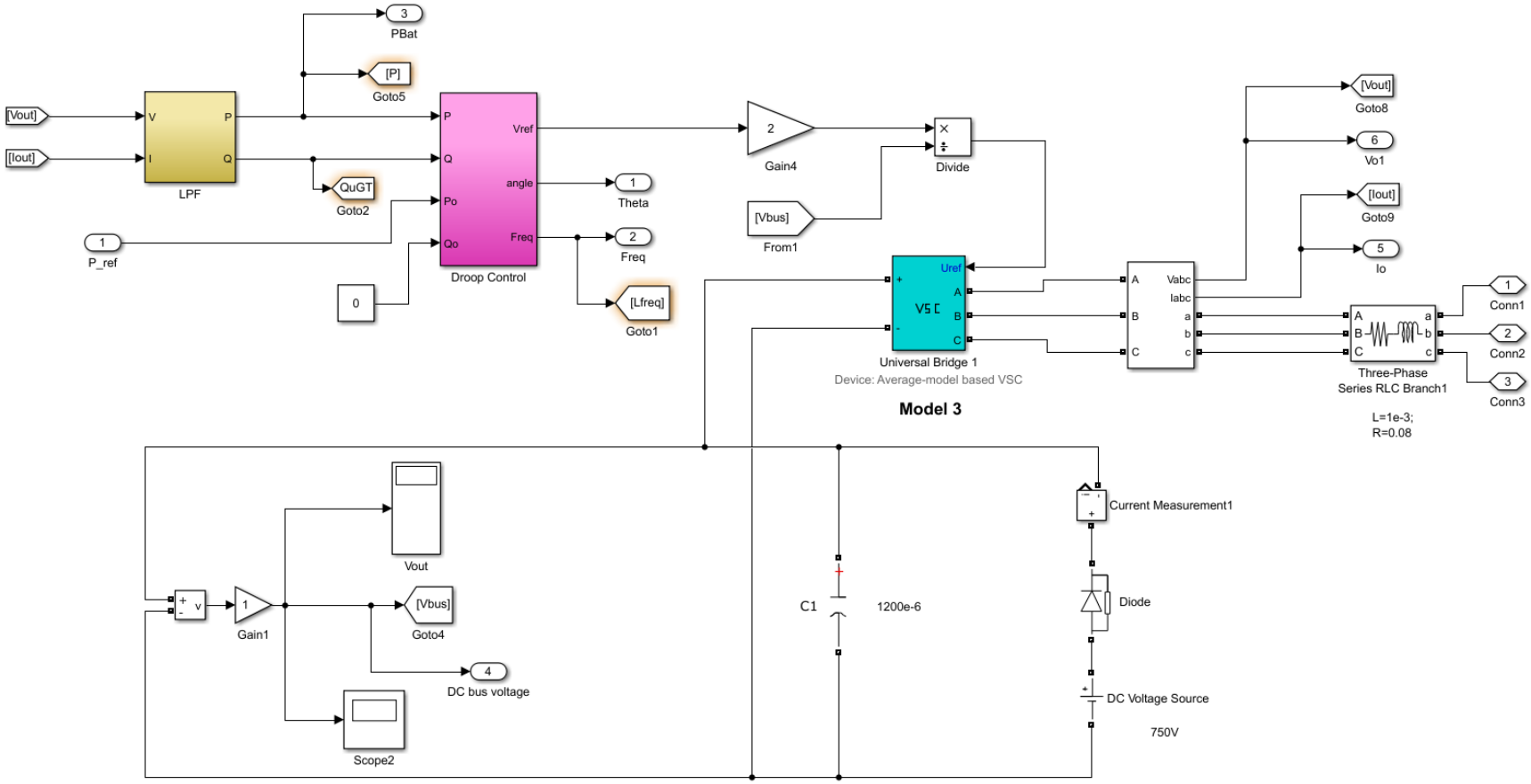

Figure A.4: Matlab/Simulink model for auxiliary unit

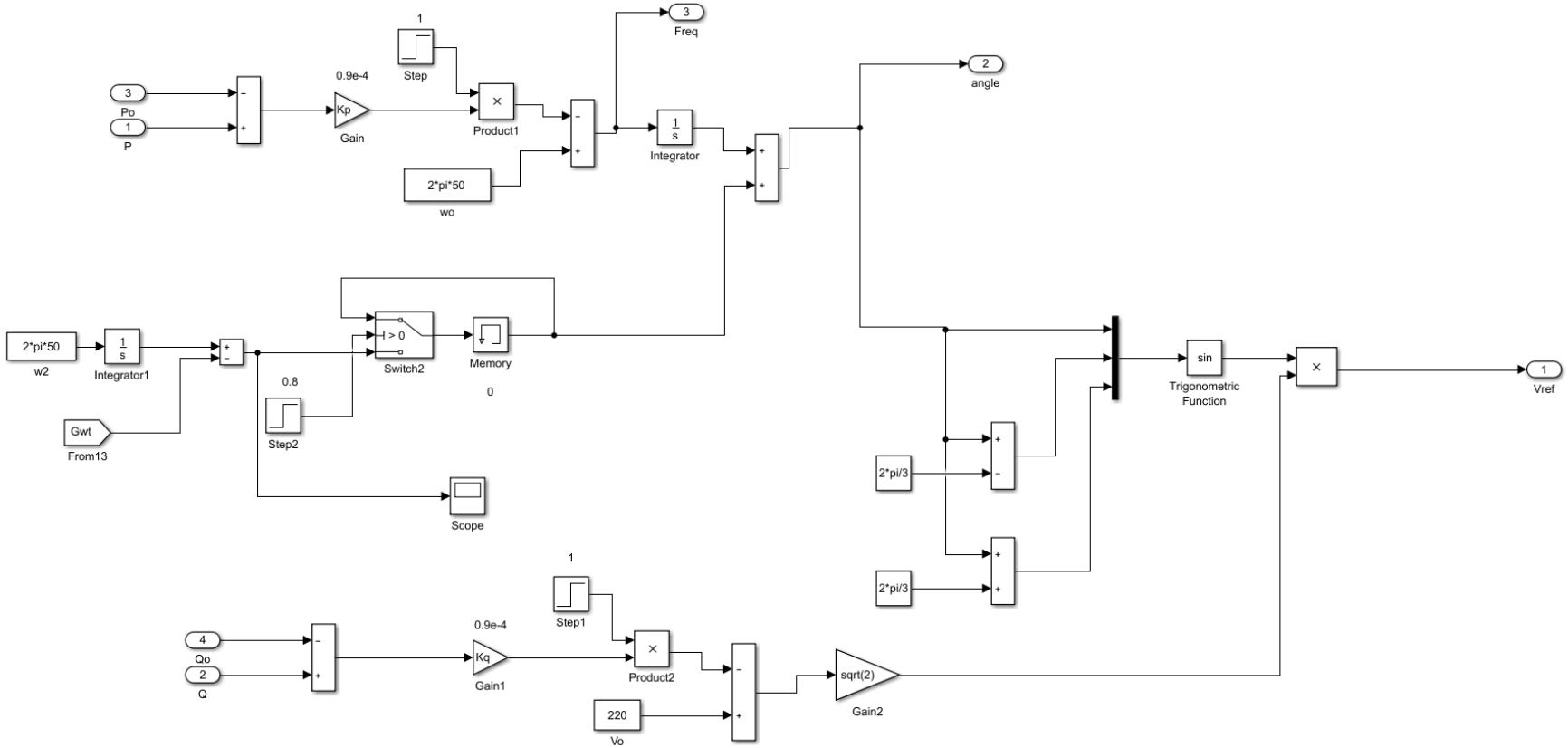

Figure A.5: Matlab/Simulink model for PV unit droop control

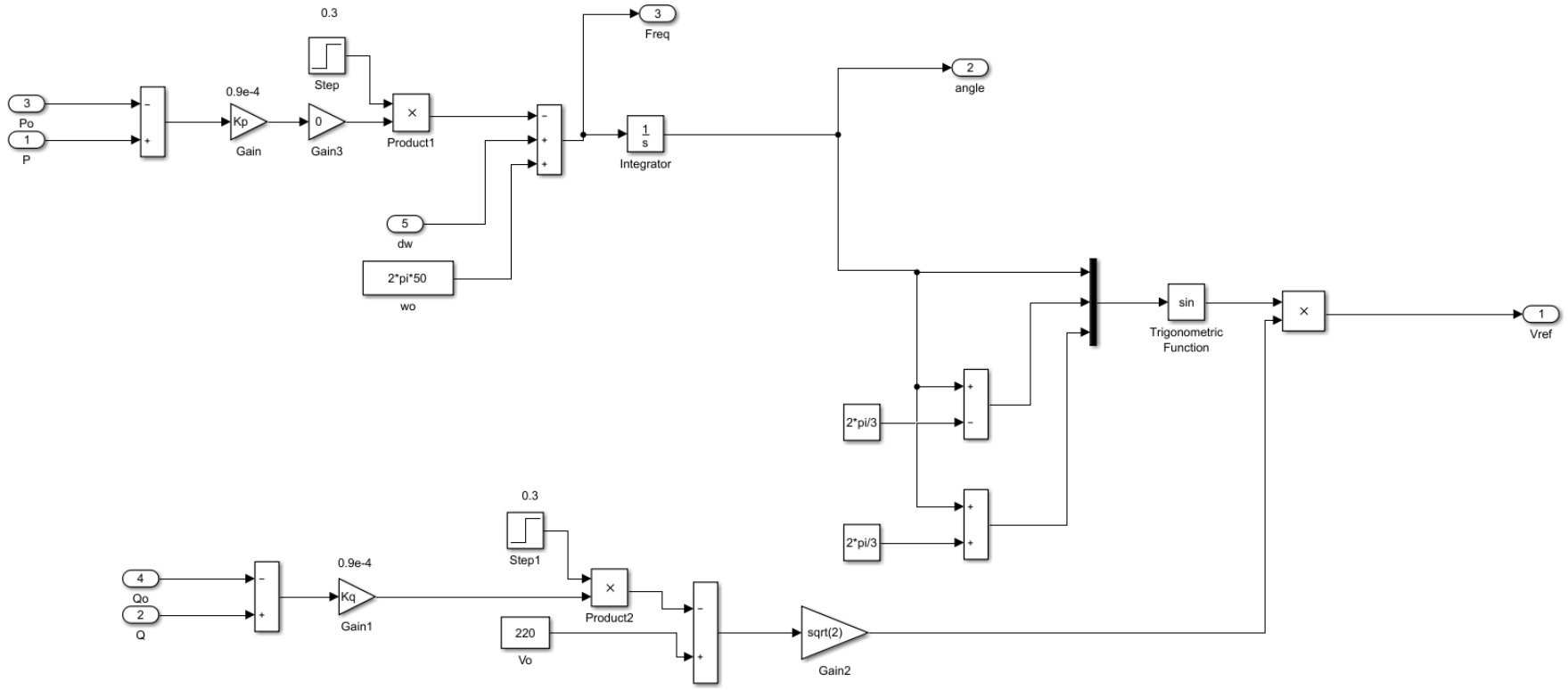

Figure A.6: Matlab/Simulink model for battery unit droop control

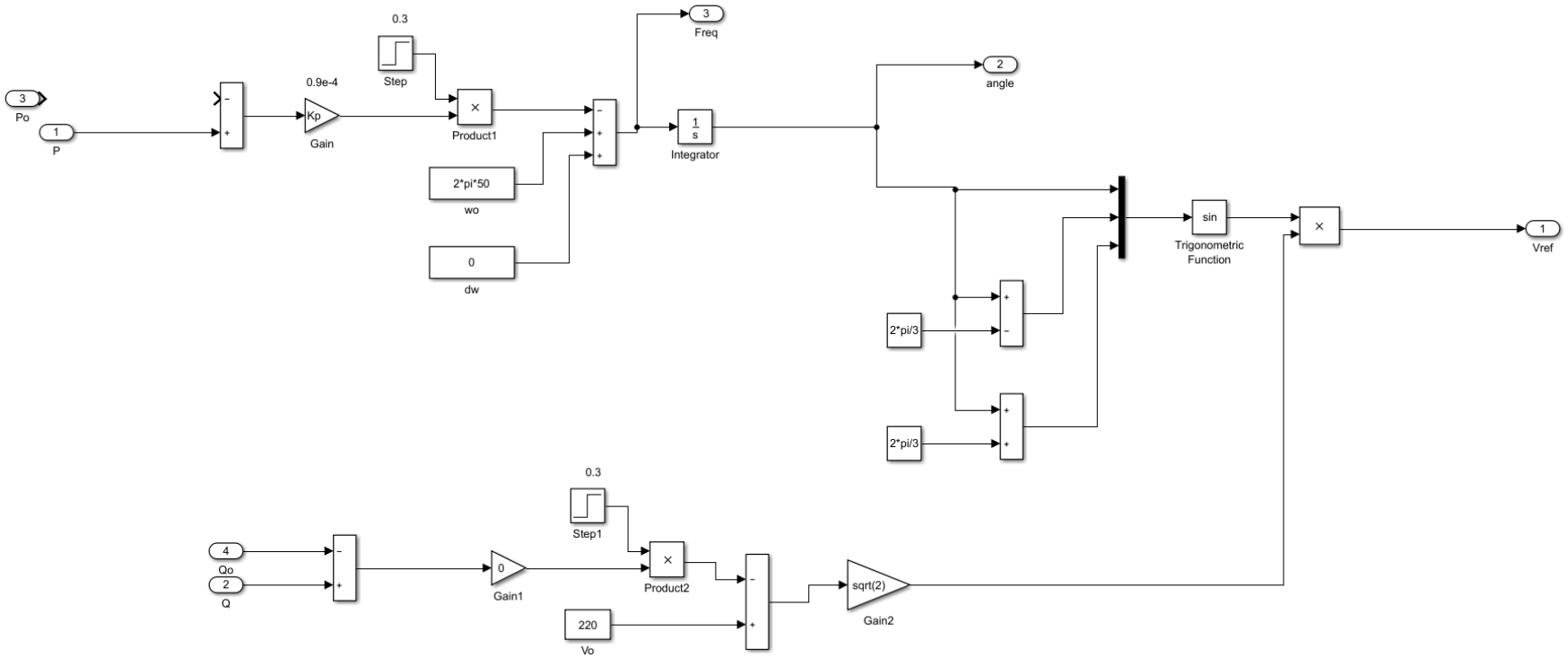

Figure A.7: Matlab/Simulink model for auxiliary unit droop control

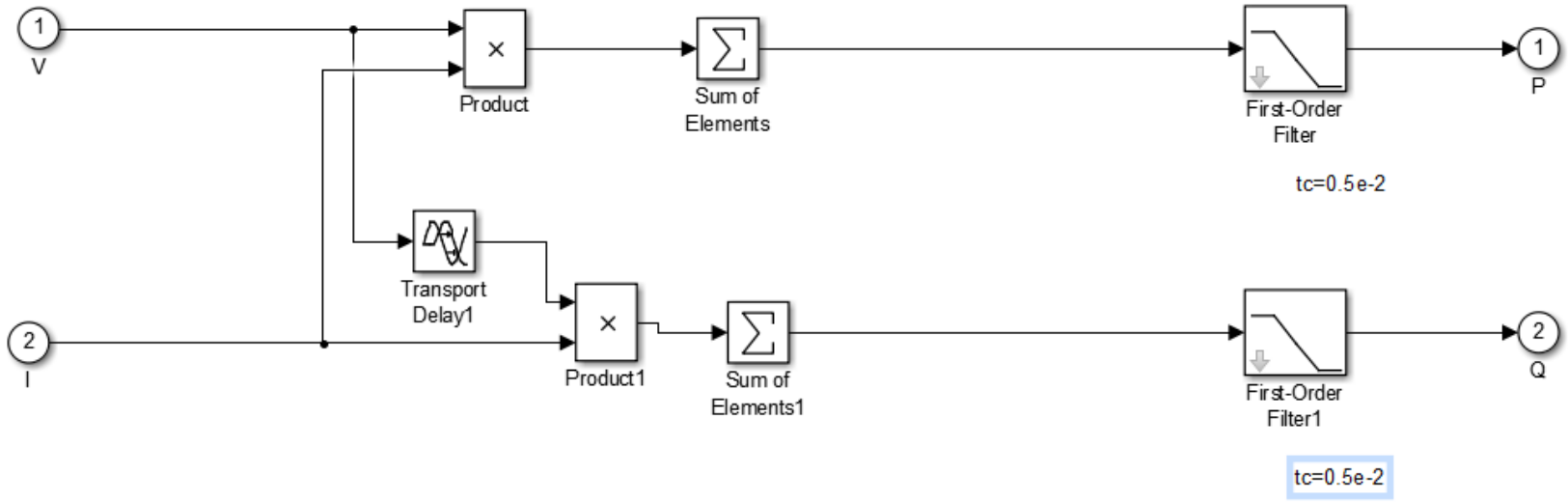

Figure A.8: Matlab/Simulink for power calculation block for power units

Appendix B: Copies of published papers

Smart Science Vol. 3, No. 3, pp. 127-138(2015)

http://dx.doi.org/10.6493/SmartSci.2015.324

A Review of Hybrid Solar PV and Wind Energy System

Rashid Al Badwawi[1,*], Mohammad Abusara[1] and Tapas Mallick[1]

[1]College of Engineering, Mathematics and Physical Sciences, University of Exeter, Penryn Campus, Cornwall, TR109EZ, United Kingdom
* Corresponding Author / E-mail: rsma202@exeter.ac.uk, TEL: +44(0)1326-259478

KEYWORDS : Hybrid renewable energy, Photovoltaic, Wind energy, Grid-connected, Stand-alone

Due to the fact that solar and wind power is intermittent and unpredictable in nature, higher penetration of their types in existing power system could cause and create high technical challenges especially to weak grids or stand-alone systems without proper and enough storage capacity. By integrating the two renewable resources into an optimum combination, the impact of the variable nature of solar and wind resources can be partially resolved and the overall system becomes more reliable and economical to run. This paper provides a review of challenges and opportunities / solutions of hybrid solar PV and wind energy integration systems. Voltage and frequency fluctuation, and harmonics are major power quality issues for both grid-connected and stand-alone systems with bigger impact in case of weak grid. This can be resolved to a large extent by having proper design, advanced fast response control facilities, and good optimization of the hybrid systems. The paper gives a review of the main research work reported in the literature with regard to optimal sizing design, power electronics topologies and control. The paper presents a review of the state of the art of both grid-connected and stand-alone hybrid solar and wind systems.

Manuscript received: January 15, 2015 / Accepted: April 29, 2015

NOMENCLATURE

PV = photovoltaic
WT = wind turbine
DC = direct current
AC = alternating current
MPPT = maximum power point tracking
FC = fuel cell
RES = renewable energy system
UPS = uninterruptable power supply
PWM = pulse width modulation
LPSP = loss of power supply probability
TNPC = total net present cost
TAC = total annualized cost
BEDA = break-even distance analysis

1. Introduction

The global penetration of renewable energy in power systems is increasing rapidly especially for solar photovoltaic (PV) and wind systems. The renewable energy counted for around 19% of the final energy consumption worldwide in 2012 and continued to rise during the year 2013 as per 2014 renewables global status report [1]. The report highlighted that for the first time the PV installation capacity was more than the wind power capacity worldwide. Table 1 below summarizes some important selected indicators from that report and the previous year report which shows the global rapid increase of renewable energy. Although Europe has dominated the PV market worldwide, the rest of the world starts picking-up with the lead from China and India [2-3].

Table 1 Important global indicators for renewable energy

		2010	2011	2012	2013
Renewable power installed capacity (with hydro)	GW	1,250	1,355	1,470	1,560
Renewable power installed capacity (without hydro)	GW	315	395	480	560
Solar PV installed capacity	GW	40	71	100	139
Wind power installed capacity	GW	198	238	283	318
Concentrating solar thermal power installed capacity	GW	1.1	1.6	2.5	3.4

Solar and wind power is naturally intermittent and can create technical challenges to the grid power supply especially when the amount of solar and wind power integration increases or the grid is not strong enough to handle rapid changes in generation levels. In addition, if solar or wind are used to supply power to a stand-alone

system, energy storage system becomes essential to guarantee continuous supply of power. The size of the energy storage depends on the intermittency level of the solar or wind.

This paper provides a review of challenges and opportunities for hybrid system of solar PV and wind. The paper reviews the main research works related to optimal sizing design, power electronics topologies and control for both grid-connected, stand-alone hybrid solar and wind systems.

2. Hybrid solar PV-wind systems

Hybrid solar PV and wind generation system become very attractive solution in particular for stand-alone applications. Combining the two sources of solar and wind can provide better reliability and their hybrid system becomes more economical to run since the weakness of one system can be complemented by the strength of the other one. The integration of hybrid solar and wind power systems into the grid can further help in improving the overall economy and reliability of renewable power generation to supply its load. Similarly, the integration of hybrid solar and wind power in a stand-alone system can reduce the size of energy storage needed to supply continuous power.

Solar electricity generation systems use either photovoltaics or concentrated solar power. The focus in this paper will be on the photovoltaics type. Detailed descriptions of the different technologies, physics and basics of PV can be found in many textbooks and papers such as [4-7]. Kurtz [8] pointed out that ten years ago the concentrator cell was only ~30% efficient compared with more than 40% today with the potential to approach 50% in the coming years. Si cells have efficiencies of 26% and multi-junction III-V-compound cells have efficiencies above 45% (48% in the laboratory) as pointed out in reference [9]. PV modules produce outputs that are determined mainly by the level of incident radiation. As the light intensity increases, photocurrent will be increased and the open-circuit voltage will be reduced [10]. The efficiency of any photovoltaic cell decreases with the increasing temperature which is non-uniformly distributed across the cell [11]. The solar output power can be smoothed by the distribution of solar power in different geographical areas [12]. Electricity from solar PV and concentrated solar power plants is significantly expensive and requires significant drop in cost or change in policies by either subsidizing or forcing the use of these technologies to be able to achieve significant market penetration [13].

Global wind report (2012) indicated that the annual market grew by around 10% to reach around 45 GW and the cumulative market growth was almost 19% [14]. Detailed descriptions of the wind energy can be found in references [4] and [15]. Wind turbines (WTs) are classified into two types: horizontal-axis WT (HAWT) and vertical-axis WT (VAWT). The highest achievable extraction of power by a WT is 59% of the total theoretical wind power [15].

Hybrid solar-wind systems can be classified into two types: grid-connected and stand-alone. Literature reviews for hybrid grid-connected and stand-alone solar PV and wind energies were conducted worldwide by many researchers who have presented various challenges and proposed several possible solutions. Due to the nature of hybrid solar PV and wind energies, optimization techniques can play a good role in utilizing them efficiently. Graphic construction methods [16], linear programming [17-18], and probabilistic approach [19] are few examples of optimization techniques that have been developed for techno-economically optimum hybrid renewable energy system for both types. Luna-Rubio et al. [20] conducted a review of existing research of optimal sizing of renewable hybrids energy systems with energy storage components for both stand-alone and grid-connected systems. The authors gave brief descriptions about those indicators and the different sizing methods. A review of control strategies for a hybrid renewable energy system was carried out in [21] and another review was done in [22] for optimization of hybrid renewable energy system with more focus on wind and solar PV systems. The reviews in [21] and [22] are applicable for both types; grid-connected and stand-alone systems.

2.1 Grid-connected system

The integration of combined solar and wind power systems into the grid can help in reducing the overall cost and improving reliability of renewable power generation to supply its load. The grid takes excess renewable power from renewable energy site and supplies power to the site' loads when required. Fig. 1 and Fig. 2 show the common DC and common AC bus grid-connected to solar PV and wind hybrid system, respectively.

2.1.1 Optimization

A solar PV and wind systems can't provide a continuous supply due to the fact that those systems will generate electricity only during sunny and windy days. Hence, a combination of these two sources improves overall energy output especially if they are connected to grid. A proper optimization is required to ensure having optimal number and size of PV and WT. The traditional sizing method for hybrid solar PV and wind systems was based on availability of long-term weather data, such as solar radiation and wind speed [23]. Since long-term weather data is not always available, artificial intelligence techniques such as fuzzy logic [24], genetic algorithms and artificial neural network are used. Furthermore, optimization performance indicators such as Net Present Value [25], Energy Index Reliability and Energy Expected Not Supplied [26], Cost of Energy [27], etc. have been used and reported. Those indicators are used to decide whether to proceed with a particular project or not and how reliable is a project will be.

With the aim of maximizing the Net Present Value of a hybrid PV-wind systems connected to electrical grid, Dufo-López et al. [25] concluded that only with high wind speed rate and current prices of components, intermittent hydrogen could be economically viable for external selling if the selling price is at a minimum of 10 €/kg. Tina and Gagliano [26] presented and analyzed a probabilistic model of a PV/WT system using a fixed tilt angle, a one-axis, and a two-axis

tracking system. They found out that the two-axis tracking system has a better performance in terms of monthly power generation in comparison with single-axis tracker which reached a maximum of 7% in particular at summer. Another probabilistic method was proposed by Niknam et al. [28]. It was for energy and operation management of micro-grids that cover uncertainties in load demand, market price and available output powers from WT and PV units. Essalaimeh et al. [29] conducted a feasibility study using payback period for hybrid PV-wind system to utilize its energy for heating and cooling purposes for Amman city in Jordan. They pointed out that clean PV panels could produce extra power, with 31% to 35% on the maximum solar intensity, compared to panels with dust. Ahmed et al. [30] simulated and controlled a hybrid PV-wind generation system connected to a grid. They highlighted that as a result of constant rotational speed, the DC voltage at high wind speed is almost constant. Kolhe et al. [31] described a hybrid PV, wind and battery storage energy system that can be interfaced with different remote monitoring and control components. An energy dispatching of a wind/PV/hydrogen/battery hybrid power system in Algeciras (Spain) was presented and carried out through a predictive controller in [32].

2.1.2 Power electronics topologies and control

There are two topologies for grid-connected solar PV and wind hybrid system as can be seen from Fig. 1 and Fig. 2. Fig. 1 shows that the DC outputs' voltages from individual solar PV, wind and battery bank stream, through individual DC/DC and AC/DC units, are integrated on the DC side and go through one common DC/AC inverter which acts as an interface between the power sources and the grid to provide the desired power even with only one source available. Hence, the renewable energy sources act as current sources and can exchange power with the grid and the common DC/AC inverter controls the DC bus voltage. The individual units can be employed for maximum power point tracking (MPPT) systems to have the maximum power from the solar PV and wind systems and the common DC/AC inverter will control the DC bus voltage. The battery bank is charged when there is an extra power and discharged (by supplying power) when there is shortage of power from the renewable energy sources. On the other hand, Fig. 2 shows that renewable energy sources are injecting power directly to the grid through individual DC/AC and AC/DC-DC/AC units.

Many researches have proposed and presented experimental results of PV-wind-battery hybrid systems along with power management schemes and control systems [33-35]. Their proposed systems were capable to operate in different modes of operation and able to transfer from one mode to another easily. Ahmed et al. [36] presented a utility hybrid PV/wind/fuel cell power system with MPPT. With the DC bus line output voltage from each converter is set to be fixed and controlled independently in that system, the controller of wind and PV has MPPT functionality whereas the controller of the fuel cell (FC) takes care of compensations of the system for the load power fluctuation. The voltage converters play an important role in controlling the amount and the type of voltage whether AC or DC and the duty cycle of those converters can be used to improve the quality of power. Huang et al. [37] highlighted that the response of the duty cycle of a DC/DC converter is relatively fast in MPPT control process. They added that the charging current of a battery is changing with the automatic adjustment of duty cycle. Liu et al. [38] proposed a hybrid AC-DC microgrid in order to reduce multiple DC/AC/DC or AC/DC/AC conversions in an individual AC or DC grid. The authors concluded that although the hybrid grid could reduce the processes of DC/AC and AC/DC conversions in an individual grid, there were many practical problems for applying the hybrid grid based on current AC dominated infrastructure. A controller was designed by Hossain et al. [39] to ensure both dynamic voltage and transient stability for a specific PV integration level that can lead to a higher potential penetration of PV units without requiring network reinforcements or violating system operating constraints. A fuzzy control was used for grid-connected hybrid PV/FC/battery power system in [40] to control flow of power via DC/DC and DC/AC converters.

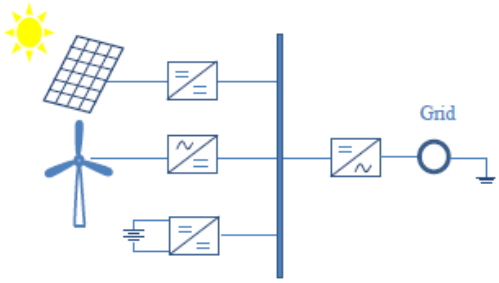

Fig. 1 Grid-connected hybrid system at common DC bus

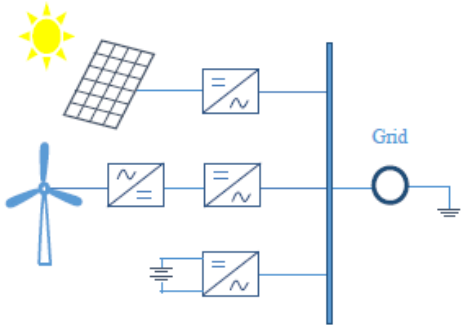

Fig. 2 Grid-connected hybrid system at common AC bus

2.1.3 Power quality

The increased penetration of grid-connected renewable energy sources has an impact on the grid power quality in particular weak grids. Voltage fluctuation, frequency fluctuation and harmonics are major power quality issues. Furthermore, intermittent energy from solar PV and wind has a huge impact on network reliability. However, accurate forecasting and scheduling systems can minimize the impacts. Various statistical forecasting and regression analysis

approaches and algorithms are used to forecast weather pattern, solar radiation and wind speed [41-44]. System operator can adjust other dispatchable generation elsewhere in a system to deal with any deficit or surplus power from renewable power generation [45]. This will reduce the impact of the fluctuations from the generation of the renewable energy sources. In addition, the distribution of RES to larger geographical area in small units instead of large unit concentrating in one area can control the intermittence effect of power generation from RES [46]. Energy storage devices like batteries or Uninterruptable Power Supply (UPS) can work as a balancing devises that provide power when there is an energy deficiency in renewable generation and store excess energy when there is surplus power from renewable generation [47-48].

Variations in solar radiation and wind speed with time can cause voltage fluctuation. The characteristics of voltage fluctuation depend mostly on the load type and size in addition to the strength of the connected electrical grid and its size. Active power filters such as dynamic voltage regulators, static synchronous compensators and unified power quality conditioners can be used to resolve voltage fluctuation [41], [49]. Similarly, power compensators such as fixed or switched capacitor can be used to resolve reactive power issue [41], [50]. They are the latest interfacing devices between grids and consumer appliances. Sudden changes in active power drawn by a load could cause system frequency fluctuation in AC grids. These changes represent unbalance situations between load and generation. In view of the above, it is important to design control loops for power and frequency control to mitigate quality issues [51]. Bae and Kwasinski [35] highlighted that a primary goal of a pulse width modulation (PWM) inverter controller was to regulate three-phase local AC bus voltage and frequency in a microgrid. Harmonics are normally caused by power electronics devices and non-linear appliances. Appropriate filters and PWM switching converter can be used to mitigate harmonic's distortion [49-50].

2.2 Stand-alone (autonomous) system

The stand-alone or autonomous power system is an excellent solution for remote areas where utilities facilities, in particular transmission lines, are not economical to run or difficult to install due to their high cost and/or difficulties of terrain, etc. The stand-alone systems can be sub-classified into common DC bus or common AC bus. Variable nature of solar and wind resources can be partially overcome by integration of the two resources into an optimum combination and hence the system becomes more reliable. The strength of one source could overcome the weakness of the other during a certain period of time [52-54]. For stand-alone applications, storage cost still represents the major economic issue. Combining both PV solar and wind powers can minimize the storage requirements and ultimately the overall cost of the system [55]. Increasing PV panels and capacity of wind turbines could be a better choice compared to the increasing of batteries since batteries are much more expensive with a shorter lifespan compared to the life time of a PV or WT. However, for high reliability systems, too few batteries can't meet the reliability requirements, which will incur more cost since too many PV modules or too large WTs will be required [56]. For a small islanded electricity system in New Zealand, with winter peaking demand, I. G. Mason [57] found that the average storage ratio for solar PV to wind was 1.768:1 in comparison to 0.613:1 (residential) and 0.455:1 (farm dairy) with summer peaking demand. Huang et al. [58] highlighted that when a single 400w wind turbine of a hybrid solar PV-wind power system was replaced by 8 smaller wind turbines with a capacity of 50w each at three different locations in China, the power output of the overall system increased by 18.69% (at Shenyang), 31.24% (at Shanghai) and 53.79% at Guangzhou) due to the fact that small wind turbines can capture wind at a lower speed in comparison to larger ones.

Integration of renewable energy generation with battery storage and diesel generator back-up systems is becoming cost-effective solution for resolving less usable renewable energy during the year. [59-62]. However, if storage runs out, there is no way of importing energy. Therefore, integrating PV and wind energy sources with fuel cells is a promising alternative back up energy source for hybrid generation systems [63-64]. Distributed generators can help fluctuations in power supply since generations' units will be close to the loads. However, introducing distributed generators will require an up gradation in the existing protection schemes [65].

2.2.1 Optimization

As mentioned earlier, a combination of solar PV and wind sources improves overall energy output. However, energy storage system is required to have a continuous power supply and cover any deficiency in power generation from the renewable energy sources. The storage system can be battery banks, fuel cells, etc. with a more focus here on battery banks. Various optimization techniques have been reported which could be applied to reach a techno-economically optimum hybrid renewable energy system [16-19], [66-67]. A comparison was made for many optimization techniques of hybrid systems in [68]. For remote areas which represent most of the stand-alone application for hybrid solar PV and wind systems, it is not always easy to find long-term weather data, such as solar radiation and wind speed that are used for sizing purposes. Hence, more artificial intelligence techniques such as fuzzy logic, genetic algorithms and artificial neural network are used for sizing stand-alone systems in comparison with traditional sizing method based on long-term weather data.

Habib et al. [69] achieved minimum capital cost with an optimal solar/wind ratio of 70% in terms of size of a hybrid PV-wind energy system for a constant load in Dhahran area, Saudi Arabia. For a Loss of Power Supply Probability (LPSP) of 0, Diaf et al. [70] found that in order to obtain a total renewable contribution of an autonomous hybrid PV/wind system, more than 30% of the energy production was unused unless the battery capacity was very large. Koutroulis et al. [71] proposed a methodology for optimal sizing of stand-alone PV and wind generator systems to minimize the 20-year total system cost. This was including the number of battery chargers, PV modules, tilt

angle and wind generator installation height that highly affect the resulting energy production and the installation and maintenance costs. Ekren and Ekren [72] optimized the size of a PV/wind hybrid energy conversion system with battery storage using OptQuest tool in ARENA 12.0 software based on an hourly operating cost.

Many researches such as [73-81] have presented experimental results of PV-wind-battery hybrid systems. They proposed optimized models with the aim to reduce the life cycle cost and increase reliability of the proposed system. Various significant hybrid RES aspects and techniques such as unit sizing and optimization, modelling of system components and optimal energy flow management strategies were reviewed by Bajpai and Dash [82]. Kaabeche et al. [83] recommended an integrated PV/wind hybrid system optimization model that utilizes iterative optimization technique following deficiency of power supply probability, relative excess power generated, total net present cost (TNPC), total annualized cost (TAC) and break-even distance analysis (BEDA) for power reliability and system costs. They found that the configuration with the lowest TNPC, TAC and BEDA gave the optimal one. The lowest Levelized Cost of Energy for stand-alone hybrid PV/wind power generating systems which meet the desired LPSP depends largely on the renewable energy potential quality [84]. An energy management strategy for a hybrid solar PV and wind system was presented in [85]. It gave a reduction up to 88% in LPSP as a result of using prediction of future generation.

Rajkumar et al. [86] used an adaptive neuro-fuzzy inference system to model and optimize the sizing of a hybrid stand-alone power system. The optimized configuration was produced with the lowest cost and excess energy for the desired LPSP. Kaldellis et al. [87] developed a methodology for stand-alone PV-battery configuration with minimum life-cycle energy requirements. They highlighted that, in all cases examined, the contribution of the battery component exceeded 27% of the system life-cycle energy requirements. Hiendro et al. [88] carried out a techno-economic feasibility study of a PV/wind hybrid system using Hybrid Optimization Model for Electric Renewable (HOMER) software and highlighted that WT and battery were essentially required to meet demand loads at night hours although they represent the highest cost to the system. Notton et al. [89] found that for windy sites, more than 40% of the total production is provided by the WT, whereas the WT contribution represents only 20% of total production energy for non-windy regions. Further sizing, optimization and review of hybrid PV-wind system can be found in references [90-115].

2.2. 2 Power electronics topologies and control

There are two main topologies for stand-alone solar PV and wind hybrid system as mentioned before; DC-common bus and AC-Common bus. Fig. 3 below shows a stand-alone solar PV and wind hybrid system with DC common bus. One of its main advantages is to include DC interface bus for coupling different generation sources, which do not have to operate at a constant frequency and in synchronism [17]. The DC bus line output voltage from all streams is set to be fixed and the output current from each source is controlled independently. The DC outputs' voltages from individual solar PV, wind and battery bank stream, through individual DC/DC and AC/DC units, are integrated on the DC side, combined in parallel and go through one common DC/AC inverter which acts as an interface between the power sources and the loads to provide the required power to the load by regulating the AC output voltage. The battery bank is interfaced by a DC/DC converter which regulates the DC-link bus voltage by charging (in case of extra power) or discharging the battery (in case of shortage of power). The renewable energy sources act as current sources and supply directly the loads. The interface common unit regulates the magnitude of the load's voltage. The individual AC/DC and DC/DC units can be employed for MPPT systems to have the maximum power from the solar PV and wind systems and the common DC/AC inverter will control magnitude of the load's voltage. The battery bank acts as a voltage source to control the common DC bus voltage by charging or discharging.

In the conventional way for controlling the complete hybrid system, power electronics converters are used for maximum energy extract from solar and wind energy resources. In addition, advanced controlling techniques can remove the power fluctuations caused by the variability of the renewable energy sources [116-119]. Fig. 4 below shows stand-alone solar PV and wind hybrid system with AC common bus. The form of pure AC bus bar system is widely used worldwide with lot of advantages, such as simple operation, plug and play scenario, low cost and easy extension according to the load's requirement. On the other hand, controlling AC voltage and frequency and energy management are some of the challenges for this type of topology. In this topology, the AC outputs' voltages from individual solar PV, wind and battery bank stream, through individual DC/AC and AC/DC-DC/AC units, are feeding the loads directly. The renewable energy sources can act as current sources provided that the battery bank exists as a voltage source to control the common AC bus voltage by charging or discharging. Hence, the individual units can be employed for MPPT systems to have the maximum power from the solar PV and wind systems provided that the battery bank exists as a voltage source to control the common AC bus voltage by charging or discharging. The battery bank is charged when there is an extra power and discharged and can supply power in case of shortage of power from the renewable energy sources.

Droop control is normally applied to generators for frequency control and sometimes voltage control in order to have load sharing of parallel generators. It can also be used to perform proper current sharing in a microgrid. With droop control, decentralized control for each interfacing converter is achieved. At the same time, no communication or only low bandwidth communication, such as power line communication, can be used in AC systems [120]. A line interactive UPS and its control system were presented by Abusara et al. [121]. Power flow was controlled using frequency and voltage drooping technique in order to ensure seamless transfer between grid-connected and stand-alone parallel modes of operation. A supervisory control strategy was designed in [122] for a DC distributed solar

microgrid to have MPPT and decide on power flow direction.

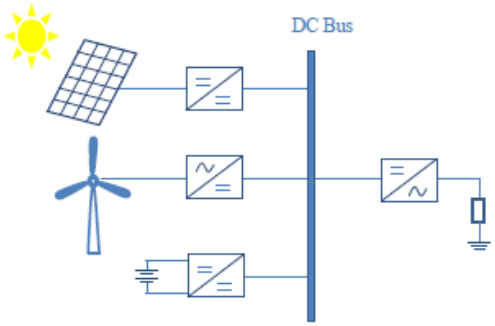

Fig. 3 Stand-alone hybrid system at common DC bus

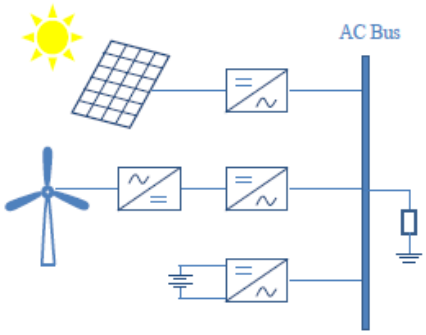

Fig. 4 Stand-alone hybrid system at common AC bus

2.2.3 Power quality

Intermittent energy from solar and wind has a huge impact on loads security since those loads have no connection with grid. So, any shortfall in power generation from those sources may leave the connected loads without power supply. Voltage fluctuation, frequency fluctuation and harmonics are major power quality issues. The voltage fluctuation as a result of irradiation changes could make the PV system unstable which will have an impact on the overall reliability of the hybrid stand-alone solar PV and wind system. The same thing is applicable with respects to variations in wind speed which affects the performance of the wind system and ultimately the overall hybrid system. Accurate forecasting and scheduling systems can minimize the impacts. The frequency stability of a generator should be taken into account based on load requirements and whether the generator is connected to AC loads with critical power frequency requirements or not. High frequency fluctuations can be suppressed by using storage devices such as electrolytic double layer capacitor [64]. An experimental investigation was carried out in [123] to assess the wind impacts on PV module. The mean pressure magnitude on the PV module was measured for both cases; under smooth wind exposure and open terrain wind exposure where the magnitude was smaller in the latter case.

2.3 AC Microgrid

Fig. 5 below shows a hybrid solar PV and wind system along with battery bank which is connected to an AC Microgrid. The system can work in grid-connected mode or stand-alone mode. The DC outputs' voltages from individual solar PV and wind stream, through individual DC/AC and AC/DC-DC/AC units, are integrated and combined in parallel on the AC side to provide the power to the grid/loads even with only one source available. Hence, in the grid-connected mode of operation, the renewable energy sources act as current sources and inject power directly into the AC bus. The battery system interfaced by a bi-directional converter and can be charged or discharged depending on the situation of the generation, load and its state of charge. However, in the stand-alone mode, the renewable energy sources act as current sources feeding directly the loads and the battery bank acts as a voltage source controlling the AC bus voltage by charging or discharging. The battery converter regulates the magnitude and frequency of the load voltage. The individual RES units can be employed for MPPT systems to have the maximum power from the solar PV and wind systems in the grid-connected mode. The same thing can be applicable in the stand-alone mode provided that the battery bank exists as a voltage source to control the AC bus voltage by charging or discharging.

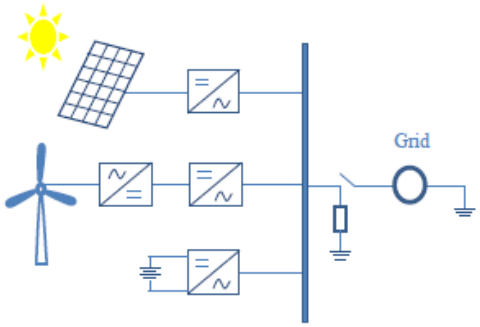

Fig. 5 Hybrid system with AC Microgrid

3. Summary and findings

Table 2 summarizes main challenges for grid-connected hybrid solar PV and wind systems with possible solutions or mitigations. Similarly, main challenges and solutions / mitigations for stand-alone systems are summarized in Table 3.

4. Conclusion

This paper has provided a review of challenges and opportunities on integrating solar PV and wind energy sources for electricity generation. The main challenge for grid-connected system as well as the stand-alone system is the intermittent nature of solar PV and wind sources. By integrating the two resources into an optimum

combination, the impact of the variable nature of solar and wind resources can be partially resolved and the overall system becomes more reliable and economical to run. This definitely has bigger impact on the stand-alone generation. Integration of renewable energy generation with battery storage and diesel generator back-up systems is becoming a cost-effective solution for stand-alone type. The wind-battery-diesel hybrid configuration can meet the system load including peak times. Energy management strategies should ensure high system efficiency along with high reliability and least cost. Good planning with accurate forecasting of weather pattern, solar radiation and wind speed can help in reducing the impact of intermittent energy.

Voltage and frequency fluctuation, and harmonics are major power quality issues for both grid-connected and stand-alone systems with bigger impact in case of weak grid. This can be resolved to a large extent by having proper design, advanced fast response control facilities, and good optimization of the hybrid systems. The paper gave an overview of different research works related to optimal sizing design, power electronics topologies and control for grid-connected and stand-alone hybrid solar PV and wind systems. Solar PV and wind hybrid system can be connected in a common DC or common AC bus whether they are working in a grid-connected mode or a stand-alone mode.

Table 2 Main challenges and possible solutions for grid-connected system

No.	Challenges	Solutions	References
1	Voltage fluctuation due to variations in wind speed and irregular solar radiation	Series and shunt active power filters. Power compensators such as fixed/switched capacitor or static compensator. Less sensitive customer's equipment to power disturbance/voltage distortions and utilities line conditioning systems	41& 49 41 & 50 49
2	Frequency fluctuation for sudden changes in active power by loads	PWM inverter controller for regulating three-phase local AC bus voltage and frequency in a microgrid.	51
3	Harmonics by power electronics devices and non-linear appliances.	PWM switching converter and appropriate filters.	41, 49 & 50
4	Intermittent energy's impacts on network security	Accurate statistical forecasting and scheduling systems. Regression analysis approaches and algorithms for forecasting weather pattern, solar radiation and wind speed. Increase or decrease dispatchable generation by system operator to deal with any deficit/surplus in renewable power generation. Advanced fast response control facilities such as Automatic Generation Control and Flexible AC Transmission System.	41 & 42 45 43 & 44
5	Synchronization	The most popular grid synchronization technique is based on phase-locked loop. Other techniques for synchronization include detecting the zero crossing of the grid voltages or using combinations of filters coupled with a non-linear transformation.	41

Table 3 Main challenges and possible solutions for stand-alone system

No.	Challenges	Solutions	References
1	High storage cost	Combining both PV solar and wind powers will minimize the storage requirements and ultimately the overall cost of the system.	16 & 55
2	Less usable energy during the year.	Integration of renewable energy generation with battery storage and diesel generator back-up systems.	18 & 59-61
3	Intermittent energy / power quality	Integration of renewable energy generation with battery storage or fuel cell and in some cases with diesel generator back-up systems.	18, 52-54, 59-65 & 116
4	Protection	Suitable protection devices need to be installed for safety reasons including up gradation of existing protection schemes in particular when distributed generators are introduced.	65
5	Storage runs out	Integrate PV and wind energy sources with fuel cells.	63 & 64
6	Environmental and safety concerns of batteries and hydrogen tanks.	Integrating PV and wind energy sources with fuel cells instead of large lead-acid batteries or super storage capacitors, leads to a non-polluting reliable energy source and reduces the total maintenance costs.	63, 64 & 74

ACKNOWLEDGEMENT

The work is financially supported by the Government of Sultanate of Oman which provides a PhD grant for Rashid Al Badwawi.

REFERENCES

[1] M. Brower, E. M. Galán, J. F. Li, D. Green, R. Hinrichs-rahlwes, S. Sawyer, M. Sander, R. Taylor, H. Kopetz, and S.

Gsänger, "Renewables 2014 global status report," REN21 2014 (2014)

[2] EPIA, "Global market outlook for photovoltaics until 2016," EPIA Report, May (2012)

[3] J. H. R. Enslin, "The role of power electronics and storage to increase penetration levels of renewable power," Power and Energy Society General Meeting - Conversion and Delivery of Electrical Energy in the 21st Century, IEEE Press, pp. 1-2, July (2008) DOI: 10.1109/PES.2008.4596958

[4] O. Edenhofer, R. Pichs-Madruga and Y. Sokona, Eds., "Renewable energy sources and climate change mitigation," SRREN_FD_SPN_Final Report, http://www.ipcc.ch/report/srren/, (2012)

[5] A. Luque and S. Hegedus, Ed., Handbook of photovoltaic science and engineering (Wiley, Chichester, 2003)

[6] L. Freris, D. Infield, Renewable energy in power systems (Wiley, Chichester, 2008) [first edition]

[7] B. Parida, S. Iniyan, and R. Goic, "A review of solar photovoltaic technologies" *Renewable and Sustainable Energy Review*, **15**, 1625-1636 (2011) DOI: 10.1016/j.rser.2010.11.032

[8] S. Kurtz, "Opportunities and challenges for development of a mature concentrating photovoltaic power industry," Technical Report NREL/TP-520-43208, Revised November (2009)

[9] EPTP, "A strategic research agenda for photovoltaic solar energy technology," September (2011) [second edition]

[10] J. Karp, "Concentrating solar power: progress and trends," Jacobs School of Engineering, University of California San Diego, Triton SPIE/OSA, February 12 (2009) http://psilab.ucsd.edu/research/Multiband%20Solar%20Concentration/files/UCSD_CPV.pdf

[11] L. Micheli, N. Sarmah, X. Luo, K. S. Reddy, and T. K. Mallick, "Opportunities and challenges in micro- and nano-technologies for concentrating photovoltaic cooling: A review" *Renewable and Sustainable Energy Reviews*, **20**, 595-610 (2013) DOI: 10.1016/j.rser.2012.11.051

[12] H. Zhang and L. L. Lai, "Research on wind and solar penetration in a 9- bus network" Proc. IEEE Power and Energy Society General Meeting, IEEE Press, pp. 1-6, July (2012) DOI: 10.1109/PESGM.2012.6345218

[13] P. Komor, "Wind and solar electricity: challenges and opportunities," University of Colorado at Boulder, Pew Center on Global Climate Change, June (2009)

[14] GWEC, "Global wind report annual market update 2012," http://www.gwec.net/wp-content/uploads/2012/06/Annual_report_2012_LowRes.pdf, GWEC Report, April (2013)

[15] K. Grogg, "Harvesting the wind: the physics of wind turbines," Carleton College, Physics and Astronomy Comps Papers 2005, http://digitalcommons.carleton.edu/pacp/7, April 13 (2005)

[16] B. S. Borowy and Z. M. Salameh, "Methodology for optimally sizing the combination of a battery bank and PV array in a Wind/PV hybrid system" *IEEE Transactions on Energy Conversion*, **11**, 367-375 (1996) DOI: 10.1109/60.507648

[17] W. Kellogg, G. Venkataramanan, and V. Gerez, "Optimal unit sizing for a hybrid wind-photovoltaic generating system" *Electric Power Systems Research*, **39**, 35-38 (1996) DOI: 10.1016/S0378-7796(96)01096-6

[18] R. Chedid and Y. Saliba, "Optimization and control of autonomous renewable energy systems" *International Journal Of Energy Research*, **20**, 609-624 (1996) DOI: 10.1002/(SICI)1099-114X(199607)20:7<609::AID-ER176>3.0.CO;2-O

[19] S. H. Karaki, I. R. B. Chedid, and R. Ramadan, "Probabilistic performance assessment of autonomous solar-wind energy conversion systems" *IEEE Transactions on Energy Conversion*, **14**, 766-772 (1999) DOI: 10.1109/60.790949

[20] R. Luna-Rubio, M. Trejo-Perea, D. Vargas-Vázquez, and G. J. Ríos-Moreno, "Optimal sizing of renewable hybrids energy systems: A review of methodologies" *Solar Energy*, **86**, 1077-1088 (2012) DOI: 10.1016/j.solener.2011.10.016

[21] P. G. Arul, V. K. Ramachandaramurthy, and R. K. Rajkumar, "Control strategies for a hybrid renewable energy system: A review" *Renewable and Sustainable Energy Reviews*, **42**, 597-608 (2015) DOI: 10.1016/j.rser.2014.10.062

[22] B. Bhandari, K. T. Lee, G. Y. Lee, Y. M. Cho, and S. H. Ahn, "Optimization of hybrid renewable energy power systems: A review" *International Journal of Precison Engineering and Manufacturing - Green Technology*, **2**, 99-112 (2015) DOI: 10.1007/s40684-015-0013-z

[23] M. Esteban, Q. Zhang, A. Utama, T. Tezuka, and K. N. Ishihara, "Methodology to estimate the output of a dual solar-wind renewable energy system in Japan" *Energy Policy*, **38**, 7793-7802 (2010) DOI: 10.1016/j.enpol.2010.08.039

[24] H. H. Chen, H. Y. Kang, and A. H. I. Lee, "Strategic selection of suitable projects for hybrid solar-wind power generation systems" *Renewable and Sustainable Energy Reviews*, **14**, 413-421 (2010) DOI: 10.1016/j.rser.2009.08.004

[25] R. Dufo-López, J. L. Bernal-Agustín, and F. Mendoza, "Design and economical analysis of hybrid PV-wind systems connected to the grid for the intermittent production of hydrogen" *Energy Policy*, **37**, 3082-3095 (2009) DOI: 10.1016/j.enpol.2009.03.059

[26] G. M. Tina and S. Gagliano, "Probabilistic modelling of hybrid solar/wind power system with solar tracking system" *Renewable Energy*, **36**, 1719-1727 (2011) DOI: 10.1016/j.renene.2010.12.001

[27] S. Bhattacharjee and S. Acharya, "PV-wind hybrid power option for a low wind topography" *Energy Conversion and Management*, **89**, 942-954 (2015) DOI: 10.1016/j.enconman.2014.10.065

[28] T. Niknam, F. Golestaneh, and A. Malekpour, "Probabilistic energy and operation management of a microgrid containing wind/photovoltaic/fuel cell generation and energy storage devices based on point estimate method and self-adaptive gravitational search algorithm" *Energy*, **43**, 427-437 (2012) DOI: 10.1016/j.energy.2012.03.064

[29] S. Essalaimeh, A. Al-Salaymeh, and Y. Abdullat, "Electrical production for domestic and industrial applications using hybrid PV-wind system" *Energy Conversion and Management*, **65**, 736-743 (2013) DOI: 10.1016/j.enconman.2012.01.044

[30] A. A. Ahmed, L. Ran, and J. Bumby, "Simulation and control of a hybrid PV-wind system," Proc. 4th IET International Conference on Power Electronics, Machines and Drives (PEMD 08), pp. 421-425, April (2008) DOI: 10.1049/cp:20080556

[31] P. Kolhe, B. Bitzer, S. P. Chowdhury, and S. Chowdhury, "Hybrid power system model and TELELAB," Proc. 47th International Universities Power Engineering Conference (UPEC 12), IEEE Press, pp. 1-5, September (2012) DOI: 10.1109/UPEC.2012.6398630

[32] J. P. Torreglosa, P. García, L. M. Fernández, and F. Jurado, "Energy dispatching based on predictive controller of an off-grid wind turbine/photovoltaic/hydrogen/battery hybrid system" *Renewable Energy*, **74**, 326-396 (2015) DOI: 10.1016/j.renene.2014.08.010

[33] M. Dali, J. Belhadj, and X. Roboam, "Hybrid solar-wind system with battery storage operating in grid-connected and standalone mode: Control and energy management - Experimental investigation" *Energy*, **35**, 2587-2595 (2010) DOI: 10.1016/j.energy.2010.03.005

[34] H. Ghoddami, M. B. Delghavi, and A. Yazdani, "An integrated wind-photovoltaic-battery system with reduced power-electronic interface and fast control for grid-tied and off-grid applications" *Renewable Energy*, **45**, 128-137 (2012) DOI: 10.1016/j.renene.2012.02.016

[35] S. Bae and A. Kwasinski, "Dynamic modeling and operation strategy for a microgrid with wind and photovoltaic resources," *IEEE Transactions on Smart Grid*, **3**, 1867-1876 (2012) DOI: 10.1109/TSG.2012.2198498

[36] N. A. Ahmed, A. K. Al-Othman, and M. R. AlRashidi, "Development of an efficient utility interactive combined wind/photovoltaic/fuel cell power system with MPPT and DC bus voltage regulation" *Electric Power Systems Research*, **81**, 1096-1106 (2011) DOI: 10.1016/j.epsr.2010.12.015

[37] Y. Huang, Y. Xu, and X. Zhou, "Study on wind-solar hybrid generating system control strategy," International Conference on Multimedia Technology (ICMT 11), IEEE Press, pp. 773-776, July (2011) DOI: 10.1109/ICMT.2011.6002600

[38] X. Liu, P. Wang, and P. C. Loh, "A hybrid AC/DC microgrid and its coordination control" *IEEE Transactions on Smart Grid*, **2**, 278-286 (2011) DOI: 10.1109/TSG.2011.2116162

[39] M. J. Hossain, T. K. Saha, N. Mithulananthan, and H. R. Pota "Robust control strategy for PV system integration in distribution systems" *Applied Energy*, **99**, 355-362, (2012) DOI: 10.1016/j.apenergy.2012.05.027

[40] T. P. Kumar, Y. Chandrashekar, N. Subrahmanyam, and M. Sydulu, "Control strategies of a fuzzy controlled grid connected hybrid PV/PEMFC/Battery distributed generation system," 2015 IEEE Power and Energy Conference at Illinois (PECI), IEEE Press, pp. 1-6, February (2015) DOI: 10.1109/PECI.2015.7064932

[41] G. M. Shafiullah, A. M. T. Oo, D. Jarvis, A. B. M. S. Ali, and P. Wolfs, "Potential challenges : Integrating renewable energy with the smart grid," Proc. 20th Australasian Universities Power Engineering Conference (AUPEC 10), IEEE Press, pp. 1-6 (2010)

[42] B. Ernst, F. Reyer, and J. Vanzetta, "Wind power and photovoltaic prediction tools for balancing and grid operation," Proc. Integration of Wide-Scale Renewable Resources Into the Power Delivery System, CIGRE/IEEE PES Joint Symposium, IEEE Press, pp. 1-9, July (2009)

[43] Y. J. Liu and C. W. Jiang, "A review on technologies and methods of mitigating impacts of large-scale intermittent renewable generations on power system" *Research Journal of Applied Sciences, Engineering and Technology*, **5**, 2765-2770 (2013)

[44] E.F. Camacho, T. Samad, M. Garcia-sanz, and I. Hiskens, "Control for renewable energy and smart grids," http://web.eecs.umich.edu/~hiskens/publications/IoCT-Part1-06RESG.pdf, (2011)

[45] D. A. Halamay, T. K. A. Brekken, A. Simmons, and S. Mcarthur, "Reserve requirement impacts of large-scale integration of wind, solar and ocean wave power generation" *IEEE Transactions on Sustainable Energy*, **2**, 321-328 (2011) DOI: 10.1109/TSTE.2011.2114902

[46] A. S. Anees, "Grid integration of renewable energy sources: Challenges, issues and possible solutions," Proc. IEEE 5th India International Conference on Power Electronics (IICPE 12), pp. 1-6, December (2012) DOI: 10.1109/IICPE.2012.6450514

[47] M. F. Almi, M. Arrouf, H. Belmili, S. Boulouma, and B. Bendib, "Energy management of wind/PV and battery hybrid system" *International Journal of New Computer Architectures and their Applications (IJNCAA)*, **4**, 30-38 (2014) DOI: 10.17781/P003

[48] S. Jahdi, L. L. Lai, and D. Nankoo, "Grid integration of wind-solar hybrid renewables using AC/DC converters as DG power sources," Proc. IEEE World Congress on Sustainable Technologies (WCST 11), IEEE Press, pp. 171-177, November (2011)

[49] S. K. Khadem, M. Basu, and M. F. Conlon, "Power quality in grid connected renewable energy systems : Role of custom power devices," Electric Power Research Group, School of Electrical Engineering Systems, Dublin Institute of Technology (2010)

[50] N. T. Linh, "Power quality investigation of grid connected wind turbines," Proc. 4th IEEE Conference on Industrial Electronics and Applications (ICIEA 09), IEEE Press, pp. 2218-2222, May (2009) DOI: 10.1109/ICIEA.2009.5138593

[51] F. O. Resende and J. A. P. Lopes, "Management and control systems for large scale integration of renewable energy sources into the electrical networks," Proc. IEEE International Conference

on Computer as a Tool (EUROCON 11), IEEE Press, pp. 1-6, April (2011) DOI: 10.1109/EUROCON.2011.5929423

[52] M. R. Patel, "Wind and Solar Power Systems," (Taylor and Francis, New York, ed. 2, 2006) [second edition]

[53] M. Engin, "Sizing and simulation of PV-Wind hybrid power system," *International Journal of Photoenergy*, **2013**, 1-10 (2013) DOI: 10.1155/2013/217526

[54] P. Dalwadi, V. Shrinet, C. R. Mehta, and P. Shah, "Optimization of solar-wind hybrid system for distributed generation," Proc. Nirma University International Conference on Engineering (NUiCONE 11), IEEE Press, pp. 1-4, December (2011) DOI: 10.1109/NUiConE.2011.6153300

[55] Z. M. Salameh and B. S. Borowy, "Optimum photovoltaic array size for a hybrid wind/PV system" *IEEE Transactions on Energy Conversion*, **9**, 482-488 (1994) DOI: 10.1109/60.326466

[56] H. Yang, L. Lu, and W. Zhou, "A novel optimization sizing model for hybrid solar-wind power generation system" *Solar Energy*, **81**, 76-84 (2007) DOI: 10.1016/j.solener.2006.06.010

[57] I.G. Mason, "Comparative impacts of wind and photovoltaic generation on energy storage for small islanded electricity systems" *Renewable Energy*, **80**, 793-805 (2015) DOI: 10.1016/j.renene.2015.02.040

[58] Q. Huang, Y. Shi, Y. Wang, L. Lu, and Y. Cui, "Multi-turbine wind-solar hybrid system" *Renewable Energy*, **76**, 401-407 (2015) DOI: 10.1016/j.renene.2014.11.060

[59] R. Belfkira, L. Zhang, and G. Barakat, "Optimal sizing study of hybrid wind/PV/diesel power generation unit" *Solar Energy*, **85**, 100-110 (2011) DOI: 10.1016/j.solener.2010.10.018

[60] M. A. Elhadidy and S. M. Shaahid, "Optimal sizing of battery storage for hybrid (wind-diesel) power systems" *Renewable Energy*, **18**, 77-86 (1999) DOI: 10.1016/S0960-1481(98)00796-4

[61] R. Kumar, R. A. Gupta, and A. K. "Bansal Economic analysis and power management of a stand-alone wind/photovoltaic hybrid energy system using biogeography based optimization algorithm" *Swarm and Evolutionary Computation*, **8**, 33-43 (2013) DOI: 10.1016/j.swevo.2012.08.002

[62] C. Jian, C. Yanbo, and Z. Lihua, "Design and research of off-grid wind-solar hybrid power generation systems," Proc. 4th International Conference on Power Electronics Systems and Applications (PESA 11), IEEE Press, pp. 1-5, June (2011) DOI: 10.1109/PESA.2011.5982922

[63] D. B. Nelson, M. H. Nehrir, and C. Wang, "Unit sizing and cost analysis of stand-alone hybrid wind/PV/fuel cell power generation systems" *Renewable Energy*, **31**, 1641-1656 (2006) DOI: 10.1016/j.renene.2005.08.031

[64] N. A. Ahmed, M. Miyatake, and A. K. Al-Othman, "Power fluctuations suppression of stand-alone hybrid generation combining solar photovoltaic/wind turbine and fuel cell systems" *Energy Conversion and Management*, **49**, 2711-2719, (2008) DOI: 10.1016/j.enconman.2008.04.005

[65] A. N. Celik, "Optimisation and techno-economic analysis of autonomous photovoltaic-wind hybrid energy systems in comparison to single photovoltaic and wind systems" *Energy Conversion and Management*, **43**, 2453-2468 (2002) DOI: 10.1016/S0196-8904(01)00198-4

[66] W. D. Kellogg, M. H. Nehrir, G. Venkataramanan, and V. Gerez, "Generation unit sizing and cost analysis for stand-alone wind, photovoltaic, and hybrid wind-PV systems," *IEEE Transactions on Energy Conversion*, **13**, 70-75 (1998) DOI: 10.1109/60.658206

[67] R. A. Gupta, R. Kumar, and A. K. Bansal, "BBO-based small autonomous hybrid power system optimization incorporating wind speed and solar radiation forecasting" *Renewable and Sustainable Energy Reviews*, **41**, 1366-1375 (2015) DOI: 10.1016/j.rser.2014.09.017

[68] N. Bigdeli, "Optimal management of hybrid PV/fuel cell/battery power system: A comparison of optimal hybrid approaches" *Renewable and Sustainable Energy Reviews*, **42**, 377-393 (2015) DOI: 10.1016/j.rser.2014.10.032

[69] M. A. Habib and S. A. M. Said, "Optimization procedure of a hybrid photovoltaic wind energy system" *Energy*, **24**, 919-929 (1999) DOI: 10.1016/S0360-5442(99)00042-0

[70] S. Diaf, D. Diaf, M. Belhamel, M. Haddadi, and A. Louche, "A methodology for optimal sizing of autonomous hybrid PV/wind system" *Energy Policy*, **35**, 5708-5718 (2007) DOI: 10.1016/j.enpol.2007.06.020

[71] E. Koutroulis, D. Kolokotsa, A. Potirakis, and K. Kalaitzakis, "Methodology for optimal sizing of stand-alone photovoltaic/wind-generator systems using genetic algorithms" *Solar Energy*, **80**, 1072-1088 (2006) DOI: 10.1016/j.solener.2005.11.002

[72] B. Y. Ekren and O. Ekren, "Simulation based size optimization of a PV/wind hybrid energy conversion system with battery storage under various load and auxiliary energy conditions" *Applied Energy*, **86**, 1387-1394 (2009) DOI: 10.1016/j.apenergy.2008.12.015

[73] S. Ashok, "Optimised model for community-based hybrid energy system" *Renewable Energy*, **32**, 1155-1164 (2007) DOI: 10.1016/j.renene.2006.04.008

[74] H. X. Yang, L. Lu, and J. Burnett, "Weather data and probability analysis of hybrid photovoltaic-wind power generation systems in Hong Kong" *Renewable Energy*, **28**, 1813-1824 (2003) DOI: 10.1016/S0960-1481(03)00015-6

[75] Z. W. Geem, "Size optimization for a hybrid photovoltaic-wind energy system" *Electrical Power and Energy Systems*, **42**, 448-451 (2012) DOI: 10.1016/j.ijepes.2012.04.051

[76] J. K. Kaldellis, D. Zafirakis, and E. Kondili, "Optimum sizing of photovoltaic-energy storage systems for autonomous small islands" *Electrical Power & Energy Systems*, **32**, 24-36 (2010) DOI: 10.1016/j.ijepes.2009.06.013

[77] S. Georges and F. H. Slaoui, "Case study of hybrid wind-solar power systems for street lighting," Proc. 21st International Conference on Systems Engineering (ICSEng 11), IEEE Press, pp. 82-85, August (2011) DOI: 10.1109/ICSEng.2011.22

[78] A. Kaabeche, M. Belhamel, and R. Ibtiouen, "Sizing

optimization of grid-independent hybrid photovoltaic/wind power generation system" *Energy*, **36**, 1214-1222 (2011) DOI: 10.1016/j.energy.2010.11.024

[79] A. T. D. Perera, R. A. Attalage, K. K. C. K. Perera, and V. P. C. Dassanayake, "Designing standalone hybrid energy systems minimizing initial investment, life cycle cost and pollutant emission" *Energy*, **54**, 220-230 (2013) DOI: 10.1016/j.energy.2013.03.028

[80] R. Dufo-López, J. L. Bernal-Agustín, J. M. Yusta-Loyo, J. A. Domínguez-Navarro, I. J. Ramírez-Rosado, J. Lujano, and I. Aso, "Multi-objective optimization minimizing cost and life cycle emissions of stand-alone PV-wind-diesel systems with batteries storage" *Applied Energy*, **88**, 4033-4041 (2011) DOI: 10.1016/j.apenergy.2011.04.019

[81] S. K. Nandi and H. R. Ghosh, "A wind-PV-battery hybrid power system at Sitakunda in Bangladesh" *Energy Policy*, **37**, 3659-3664 (2009) DOI: 10.1016/j.enpol.2009.04.039

[82] P. Bajpai and V. Dash, "Hybrid renewable energy systems for power generation in stand-alone applications: A review" *Renewable and Sustainable Energy Reviews*, **16**, 2926-2939, (2012) DOI: 10.1016/j.rser.2012.02.009

[83] A. Kaabeche, M. Belhamel, and R. Ibtiouen, "Techno-economic valuation and optimization of integrated photovoltaic/wind energy conversion system" *Solar Energy*, **85**, 2407-2420 (2011) DOI: 10.1016/j.solener.2011.06.032

[84] S. Diaf, G. Notton, M. Belhamel, M. Haddadi, and A. Louche, "Design and techno-economical optimization for hybrid PV/wind system under various meteorological conditions" *Applied Energy*, **85**, 968-987 (2008) DOI: 10.1016/j.apenergy.2008.02.012

[85] D. Feroldi, P. Rullo, and D. Zumoffen, "Energy management strategy based on receding horizon for a power hybrid system" *Renewable Energy*, **75**, 550-559 (2015) DOI: 10.1016/j.renene.2014.09.056

[86] R. K. Rajkumar, V. K. Ramachandaramurthy, B. L. Yong, and D. B. Chia, "Techno-economical optimization of hybrid pv/wind/battery system using Neuro-Fuzzy" *Energy*, **36**, 5148-5153 (2011) DOI: 10.1016/j.energy.2011.06.017

[87] J. K. Kaldellis, D. Zafirakis, and E. Kondili, "Optimum autonomous stand-alone photovoltaic system design on the basis of energy pay-back analysis" *Energy*, **34**, 1187-1198, (2009) DOI: 10.1016/j.energy.2009.05.003

[88] A. Hiendro, R. Kurnianto, M. Rajagukguk, and Y. M. Simanjuntak, "Techno-economic analysis of photovoltaic/wind hybrid system for onshore/remote area in Indonesia" *Energy*, **59**, 652-657 (2013) DOI: 10.1016/j.energy.2013.06.005

[89] G. Notton, S. Diaf, and L. Stoyanov, "Hybrid Photovoltaic/Wind Energy Systems For Remote Locations" *Energy Procedia*, **6**, 666-677 (2011) DOI: 10.1016/j.egypro.2011.05.076

[90] H. Cherif and J. Belhadj, "Large-scale time evaluation for energy estimation of stand-alone hybrid photovoltaic-wind system feeding a reverse osmosis desalination unit" *Energy*, **36**, 6058-6067 (2011) DOI: 10.1016/j.energy.2011.08.010

[91] E. Cetin, A. Yilanci, H. K. Ozturk, M. Colak, I. Kasikci, and S. Iplikci, "A micro-DC power distribution system for a residential application energized by photovoltaic-wind/fuel cell hybrid energy systems" *Energy and Buildings*, **42**, 1344-1352 (2010) DOI: 10.1016/j.enbuild.2010.03.003

[92] E. Kabalci, "Design and analysis of a hybrid renewable energy plant with solar and wind power" *Energy Conversion and Management*, **72**, 51-59 (2013) DOI: 10.1016/j.enconman.2012.08.027

[93] M. S. Ngan and C. W. Tan, "Assessment of economic viability for PV/wind/diesel hybrid energy system in southern Peninsular Malaysia" *Renewable and Sustainable Energy Reviews*, **16**, 634-647 (2012) DOI: 10.1016/j.rser.2011.08.028

[94] A. Higier, A. Arbide, A. Awaad, J. Eiroa, J. Miller, N. Munroe, A. Ravineta, and B. Redding, "Design, development and deployment of a hybrid renewable energy powered mobile medical clinic with automated modular control system" *Renewable Energy*, **50**, 847-857 (2013) DOI: 10.1016/j.renene.2012.07.036

[95] P. Nema, R. K. Nema, and S. Rangnekar, "A current and future state of art development of hybrid energy system using wind and PV-solar: A review" *Renewable and Sustainable Energy Reviews*, **13**, 2096-2103 (2009) DOI: 10.1016/j.rser.2008.10.006

[96] O. C. Onar, M. Uzunoglu, and M. S. Alam, "Modeling, control and simulation of an autonomous wind turbine/photovoltaic/ fuel cell/ultra-capacitor hybrid power system" *Journal of Power Sources*, **185**, 1273-1283 (2008) DOI: 10.1016/j.jpowsour.2008.08.083

[97] J. L. Bernal-Agustín and R. Dufo-López, "Multi-objective design and control of hybrid systems minimizing costs and unmet load" *Electric Power Systems Research*, **79**, 170-180 (2009) DOI: 10.1016/j.epsr.2008.05.011

[98] M. Uzunoglu, O. C. Onar, and M. S. Alam, "Modeling, control and simulation of a PV/FC/UC based hybrid power generation system for stand-alone applications" *Renewable Energy*, **34**, 509-520 (2009) DOI: 10.1016/j.renene.2008.06.009

[99] C. S. Chiu, Y. L. Ouyang, C. Y. Ku, "Terminal sliding mode control for maximum power point tracking of photovoltaic power generation systems" *Solar Energy*, **86**, 2986-2995 (2012) DOI: 10.1016/j.solener.2012.07.008

[100] M. A. Elhadidy, "Performance evaluation of hybrid (wind/solar/diesel) power systems" *Renewable Energy*, **26**, 401-143 (2002) DOI: 10.1016/S0960-1481(01)00139-2

[101] J. Li, W. Wei, and J. Xiang, "A simple sizing algorithm for stand-alone PV/wind/battery hybrid microgrids" *Energies*, **5**, 5307-5323 (2012) DOI: 10.3390/en5125307

[102] G. C. Bakos and N. F. Tsagas, "Technoeconomic assessment of a hybrid solar/wind installation for electrical energy saving" *Energy and Buildings*, **35**, 139-145 (2003) DOI: 10.1016/S0378-7788(02)00023-3

[103] M. Fadaee and M. A. M. Radzi, "Multi-objective optimization of a stand-alone hybrid renewable energy system by using evolutionary algorithms: A review" *Renewable and Sustainable Energy Reviews*, **16**, 3364-3369 (2012) DOI: 10.1016/j.rser.2012.02.071

[104] S. Abedi, A. Alimardani, G. B. Gharehpetian, G. H. Riahy, and S. H. Hosseinian, "A comprehensive method for optimal power management and design of hybrid RES-based autonomous energy systems" *Renewable and Sustainable Energy Reviews*, **16**, 1577-1587 (2012) DOI: 10.1016/j.rser.2011.11.030

[105] G. Bekele and G. Boneya, "Design of a photovoltaic-wind hybrid power generation system for ethiopian remote area" *Energy Procedia*, **14**, 1760-1765 (2012) DOI: 10.1016/j.egypro.2011.12.1164

[106] R. Baños, F. Manzano-Agugliaro, F. G. Montoya, C. Gil, A. Alcayde, and J. Gómez, "Optimization methods applied to renewable and sustainable energy: A review" *Renewable and Sustainable Energy Reviews*, **15**, 1753-1766 (2011) DOI: 10.1016/j.rser.2010.12.008

[107] G. Panayiotou, S. Kalogirou, and S. Tassou, "Design and simulation of a PV and a PV-Wind standalone energy system to power a household application" *Renewable Energy*, **37**, 355-363 (2012) DOI: 10.1016/j.renene.2011.06.038

[108] I. P. Panapakidis, D. N. Sarafianos, and M. C. Alexiadis, "Comparative analysis of different grid-independent hybrid power generation systems for a residential load" *Renewable and Sustainable Energy Reviews*, **16**, 551-563 (2012) DOI: 10.1016/j.rser.2011.08.021

[109] H. Belmili, M. F. Almi, and S. Bolouma, "A Computer program development for sizing stand-alone photovoltaic-wind hybrid systems" *Energy Procedia*, **36**, 546-557 (2013) DOI: 10.1016/j.egypro.2013.07.063

[110] M. K. Deshmukh and S. S. Deshmukh, "Modeling of hybrid renewable energy systems" *Renewable and Sustainable Energy Reviews*, **12**, 235-249 (2008) DOI: 10.1016/j.rser.2006.07.011

[111] O. Erdinc and M. Uzunoglu, "Optimum design of hybrid renewable energy systems: Overview of different approaches" *Renewable and Sustainable Energy Reviews*, **16**, 1412-1425 (2012) DOI: 10.1016/j.rser.2011.11.011

[112] D. Connolly, H. Lund, B. V. Mathiesen, and M. Leahy, "A review of computer tools for analysing the integration of renewable energy into various energy systems" *Applied Energy*, **87**, 1059-1082 (2010) DOI: 10.1016/j.apenergy.2009.09.026

[113] J. L. Bernal-Agustín and R. Dufo-López, "Simulation and optimization of stand-alone hybrid renewable energy systems" *Renewable and Sustainable Energy Reviews*, **13**, 2111-2118 (2009) DOI: 10.1016/j.rser.2009.01.010

[114] S. Rehman, M. Mahbub Alam, J. P. Meyer, and L. M. Al-Hadhrami, "Feasibility study of a wind-pv-diesel hybrid power system for a village" *Renewable Energy*, **38**, 258-268 (2012) DOI: 10.1016/j.renene.2011.06.028

[115] D. C. Das, A. K. Roy, and N. Sinha, "GA based frequency controller for solar thermal-diesel-wind hybrid energy generation/energy storage system" *Electrical Power and Energy Systems*, **43**, 262-279 (2012) DOI: 10.1016/j.ijepes.2012.05.025

[116] W. Zhou, C. Lou, Z. Li, L. Lu, and H. Yang, "Current status of research on optimum sizing of stand-alone hybrid solar-wind power generation systems" *Applied Energy*, **87**, 380-389 (2010) DOI: 10.1016/j.apenergy.2009.08.012

[117] F. Zhang, Y. Wang, and E. Shang, "Design and realization controller in wind solar hybrid generating system," Proc. Joint International Conference on Power System Technology and IEEE Power India Conference (POWERCON 08), IEEE Press, pp. 1-6, October (2008) DOI: 10.1109/ICPST.2008.4745372

[118] P. Kong, J. Zhao, and Y. Xing, "Series-parallel resonant high frequency inverter for standalone hybrid PV/wind power system" *Energy Procedia*, **12**, 1090-1097 (2011) DOI: 10.1016/j.egypro.2011.10.142

[119] N. J. Mhusa, G. N. Nyakoe, and E. V. Mgaya, "Power management in photovoltaic-wind hybrid system based on artificial intelligence" *Journal of Multidisciplinary Engineering Science and Technology*, **2**, 140-148 (2015)

[120] X. Lu, J. M. Guerrero, K. Sun, J. C. Vasquez, R. Teodorescu, and L. Huang, "Hierarchical control of parallel AC-DC converter interfaces for hybrid microgrids" *IEEE Transaction on Smart Grid*, **5**, 683-692 (2014) DOI: 10.1109/TSG.2013.2272327

[121] M. A. Abusara, J. M. Guerrero, and S. M.Sharkh, "Line-Interactive UPS for Microgrids" *IEEE Transactions on Industrial Electronics*, **61**, 1292-1300 (2014) DOI: 10.1109/TIE.2013.2262763

[122] D. Shen and A. Izadian, "Sliding mode control of a DC distributed solar microgrid," Power and Energy Conference at Illinois (PECI), IEEE Press, pp. 1-6, February (2015) DOI: 10.1109/PECI.2015.7064929

[123] A. Abiola-Ogedengbe, H. Hangan, and K. Siddiqui, "Experimental investigation of wind effects on a standalone photovoltaic (PV) module" *Renewable Energy*, **78**, 657-665 (2015) DOI: 10.1016/j.renene.2015.01.037

AIMS Energy, 3(4): 728-739.
DOI: 10.3934/energy.2015.4.728
Received date 11 May 2015,
Accepted date 01 November 2015,
Published date 05 November 2015

http://www.aimspress.com/

Research article

Speed control of synchronous machine by changing duty cycle of DC/DC buck converter

Rashid Al Badwawi [1,*], Mohammad Abusara [2], and Tapas Mallick [1]

[1] Environment and Sustainability Institute, University of Exeter, Penryn Campus, TR10 9FE, United Kingdom
[2] College of Engineering, Mathematics and Physical Sciences, University of Exeter, Penryn Campus, Penryn, Cornwall, TR10 9EZ, United Kingdom

* **Correspondence:** Email: rsma202@exeter.ac.uk; Tel: +44(0)1326259478.

Abstract: Renewable energies such as wind or solar energy are naturally intermittent and can create technical challenges to interconnected grid in particular with high integration amounts. In addition, if wind or solar is used to supply power to a stand-alone system, continuous power supply will be met only if sufficient energy storage system is available. The global penetration of renewable energy in power systems is increasing rapidly especially wind and solar photovoltaic (PV) systems. Hybrid wind and solar PV generation system becomes very attractive solution in particular for stand-alone applications. It can provide better reliability since the weakness of one system could be complemented by the strength of the other one. When wind energy is integrated into grid, maximum power point tracking control could be used to optimize the output of wind turbine. In variable speed wind turbine, the turbine speed is varied according to the wind speed. This paper presents a comparison between two methods of controlling the speed of a wind turbine in a microgrid namely; Proportional-Integral (PI) control of the tip speed ratio and stored power curve. The PI method provides more controllability, but it requires an anemometer to measure the wind speed. The stored power curve method, however, is easier to implement, but the amount of energy extracted can be less. The system has been modelled using Matlab/Simulink.

Keywords: wind energy; wind turbine; tip speed ratio; stored power curve; buck converter

1. Introduction

Solar Photovoltaic (PV) and wind energies are intermittent and unpredictable in nature. Therefore, proper scheduling and forecasting tools are required to improve system reliability. Furthermore, combining the two technologies together can improve the availability of the overall system because one energy source can complement the other. During sunny and windy days/hours, power is generated from solar PV and wind turbines. Energy storage systems such as batteries can play a great role in supporting power supply as they can act as balancing devices that provide power (discharging) when there is an energy deficiency and store excess energy (charging) when there is surplus power from renewable energy sources. Hence, hybrid solar PV and wind power system along with batteries can minimize the effect of intermittency and provide continuous power to the load and/or grid. This hybrid system becomes a good solution for power when the infrastructure facilities such as overhead lines, gas lines, etc. are far away from loads or they are expensive and/or difficult to construct. This also has become a very attractive solution for stand-alone systems.

Figure 1 shows a hybrid solar PV and wind system along with battery bank. The common DC bus is connected to the grid via a DC/AC converter. The system can work in either grid-connected mode or stand-alone mode. The DC output voltages from individual solar PV and wind stream, through individual DC/DC and AC/DC-DC/DC units, are integrated and combined in parallel to provide power to the grid/load even with only one source available without the need to work with constant frequency. The different generating sources are not required to be synchronized with the grid which will simplify the operation of the overall system in particular when changing from one mode of operation to the other. The common DC bus voltage is set to be fixed and the output current from each source is controlled independently through individual converters.

In grid-connected mode of operation, the renewable energy sources act as current sources that inject power directly into the DC bus. The battery bank interfaced by a bi-directional converter and can be charged or discharged depending on the situation of the generation, load and its state of charge. The common DC/AC inverter regulates the DC voltage by injecting/absorbing power to/from the grid. In stand-alone mode of operation, the renewable energy sources still act as current sources feeding directly the load while the battery converter regulates the DC bus by charging (in case of extra power) or discharging the battery (in case of shortage of power). Hence, the battery system acts as a voltage source. In grid-connected mode, the output power from individual renewable energy sources is extracted using a maximum power point tracking (MPPT) technique. The same thing is applicable in the stand-alone mode provided that the battery bank exists as a voltage source to control the DC bus voltage by charging or discharging depending on the status of generation and load requirement.

Various papers have been reported and published for control of wind power system or hybrid wind and solar photovoltaic (PV) power systems [1–8]. This paper focuses on the modelling and control design of the wind energy systems. The paper presents a comparison between two methods of controlling a wind turbine in a microgrid namely, PI control of the tip speed ratio and stored power curve. The paper will provide brief information about the wind energy system along with modelling and the two methods of speed control. Simulation results from simplified and detailed models will be presented.

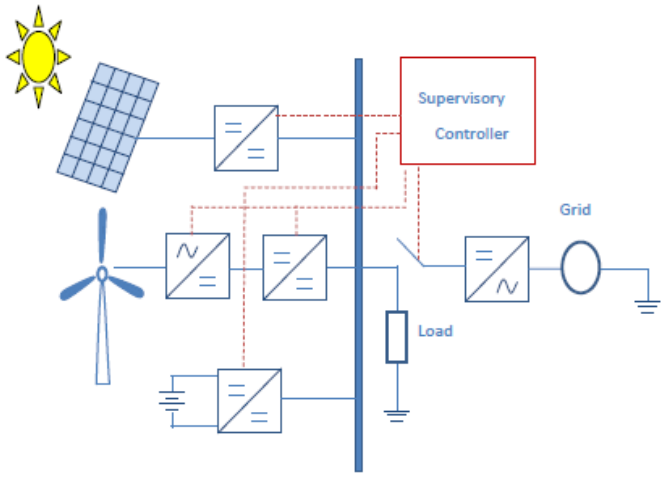

Figure 1. Hybrid system with AC microgrid.

2. Materials and Method

The wind energy system that is considered in this paper is shown in Figure 2. It consists of a wind turbine, a permanent magnet synchronous machine (PMSM), a rectifier and a DC/DC buck converter. The power output is controlled by regulating the buck output current I_L injected into the common DC bus. The controller system consists of two loops. The inner loop controls the buck inductor control by varying the duty ratio of the buck power switch. The outer loop controls the speed of the wind turbine by varying the current demand I_L* of the inner loop.

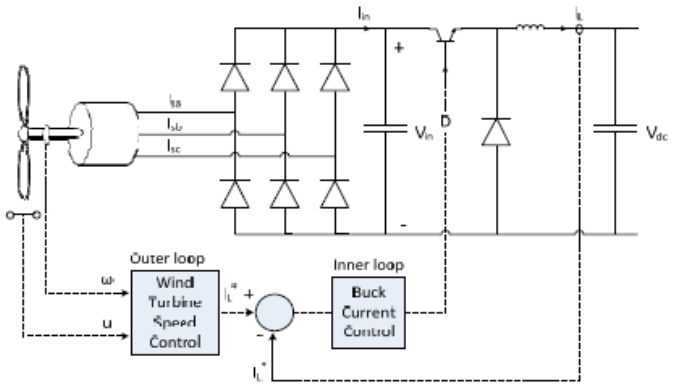

Figure 2. Wind energy system.

2.1. Wind turbine modelling

The wind turbine output mechanical power can be expressed by the following equation:

$$P_m = \frac{1}{2}\rho\pi R^2 u^3 C_P \tag{1}$$

where

P_m : turbine mechanical power

ρ : air density

R : turbine rotor radius

u : wind speed

C_P : turbine performance coefficient (rotor efficiency)

The performance coefficient C_p is a function of the tip speed ratio λ and the pitch angle β in a pitch controlled system. The wind turbine considered in this paper has a fixed blade pitch angle. The tip speed ratio (TSR) is given by the following equation:

$$\lambda = \frac{R\omega}{u} \tag{2}$$

where ω is the turbine rotational speed. The relationship between C_p and λ is non-linear. For the turbine considered in this paper, this relationship is shown in Figure 3. This curve has been produced experimentally by testing the wind turbine under variable wind speed. It can be noticed that the maximum output power for the considered turbine is obtained when λ = 1.3. The turbine rotational speed is given by:

$$\omega = \frac{1}{J}\int (T_m - T_e)\, dt \tag{3}$$

where

T_m: turbine mechanical torque

T_e: turbine electrical torque

J: rotational inertia

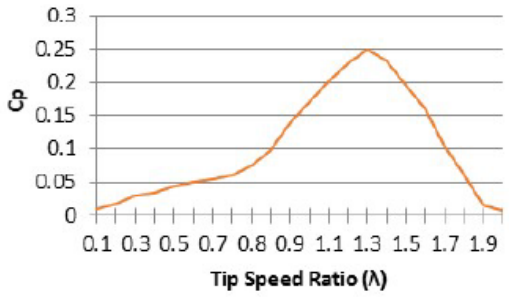

Figure 3. Power coefficient curve.

The mechanical output torque depends on the turbine output mechanical power and turbine rotational speed. It can be calculated as follows:

$$T_m = \frac{P_m}{\omega} \tag{4}$$

where P_m is the turbine mechanical power and ω is the turbine rotational speed. The electrical torque is related to the PMSM stator current I_s by

$$T_e = K_I I_s \tag{5}$$

where K_I is the machine torque constant. In this system, the electrical torque is controlled by controlling the buck output current I_L rather than the machine stator current I_s. Hence, the electrical torque can be related to the buck current via a new defined constant K_T

$$T_e = K_T I_L \tag{6}$$

Equations (1) to (6) represent the model for the wind turbine system and combined together to form the block diagram model shown in Figure 4.

2.2. Speed control of wind turbine

Two methods for controlling the speed of the wind turbine have been considered namely; stored power curve and PI control of the λ. Both methods are described below:

a) Stored Power curve

The relationship between C_p and λ is a non-linear curve shown in Figure 3. The maximum output power of the wind turbine considered in this paper is obtained when λ = 1.3 which corresponds to C_p = 0.25. In order to extract maximum possible power at a given wind speed condition, the wind turbine speed needs to vary so the tip speed ratio λ is always 1.3. Substituting (2) in (1) and using the above values for C_p and λ gives the maximum power

$$P_{max} = \frac{1}{2}\rho\pi R^2 \left(\frac{R * \omega}{1.3}\right)^3 0.25 \tag{7}$$

Equation (7) defines the relationship between maximum power that can be extracted versus turbine speed. The optimised stored power curve has been plotted for turbine speed varying from 0 to 200 RPM as shown in Figure 5. This curve can be used to control the speed of the wind turbine without the need to measure the wind speed. That can be done by creating a lookup table that produces a particular power demand for a particular turbine speed. This controller is as shown in Figure 6.

b) PI Control of the λ

The second control method considered in this paper is PI method. This method is shown in Figure 7. The turbine speed and the wind speed are measured and λ is calculated using (2). The calculated λ is then compared with the optimal λ* which is 1.3 in this case. The error signal is fed into a PI controller that sets the current demand for the inner loop controller of the buck current.

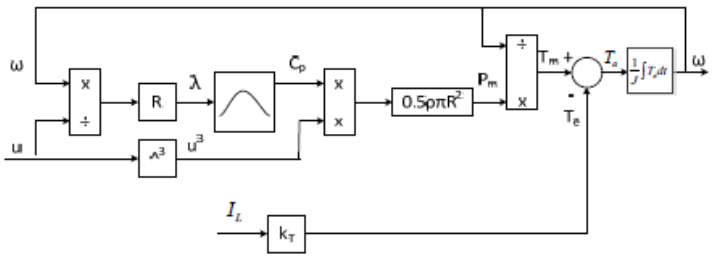

Figure 4. Block diagram of the system model.

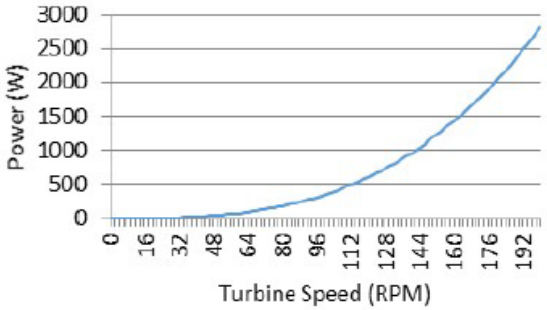

Figure 5. Stored power curve.

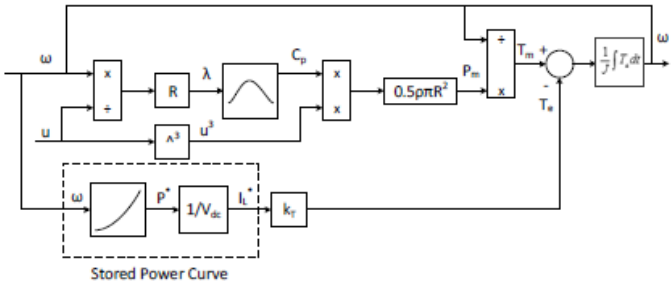

Figure 6. Stored power curve control.

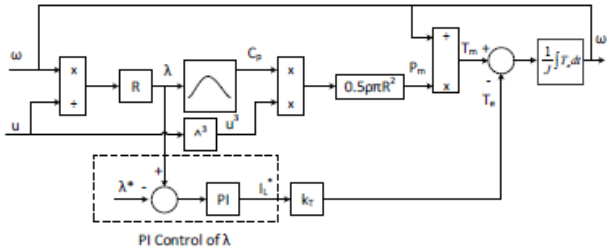

Figure 7. PI control of λ.

3. Results and Discussion

3.1. Simulation results of the simplified model

Figures 6 and 7 use a simplified model of the system in which the buck demand current I_L^* (the output from the stored power curve and PI controllers) is directly proportional to the electrical torque T_e. In this simplified model, the electric system including the PMSM, the rectifier, the DC/DC buck converter are all linearized and represented by the torque coefficient K_I. The two models represented in Figures 6 and 7 were built in Matlab/Simulink. Weather data were measured on the roof of the Environmental Sustainable Institute (ESI) in the University of Exeter-Penryn Campus. The measurements were taken using MetPak Pro (Gill Instruments). It is a multi-sensor instrument that can be used to measure essential weather data such as wind speed, wind direction, temperature, pressure, humidity, etc. Wind speed is measured every second at ESI and a sample of measurement for 07/04/2014 is shown in Figure 8. It was used as an input to the wind turbine model. Table 1 below shows the system parameters used in the simulation.

Table 1. Values used in the simplified model simulations.

Symbol	Description	Value
J	Rotational inertia	38 kg.m^2
R	Turbine rotor radius	1m
V_{dc}	DC voltage source in buck converter	50V
P_{c1}	Wind speed controller - Proportional Parameter (for results in Figure 10 below)	15
I_{c1}	Wind speed controller - Integral Parameter (for results in Figure 10 below)	2.5
P_{c2}	Wind speed controller - Proportional Parameter (for results in Figure 11 below)	130
I_{c2}	Wind speed controller - Integral Parameter (for results in Figure 11 below)	0

Figure 9 shows the electrical and mechanical powers along with wind turbine speed for the stored power curve control method. As can been seen, the electrical power curve is having a smooth

follow up of the mechanical power curve in corresponding to changes in wind speed. The generated electrical energy was 28.81 kJ. The stored power curve control method is very simple and straightforward way of control of power with no complication at all.

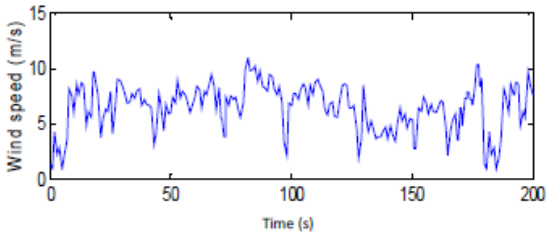

Figure 8. Measured wind speed at ESI.

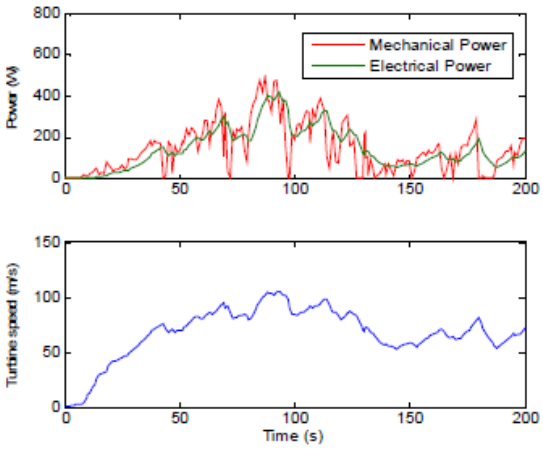

Figure 9. Power & speed for stored power curve case.

For the PI control method, the Simulink PI control block was used and the values of the controller parameters; Proportional (P) and Integral (I) were changed to have different electrical power and torque responses. In other words, by changing those parameters, different values of electrical power and torque can be obtained. The PI method provides more controllability in comparison to the stored power curve control method, but it requires an anemometer to measure the wind speed. Figure 10 shows the electrical and mechanical powers along with wind turbine speed for the PI control method with PI parameters values of P_{c1} and I_{c1} as shown in Table 1. By changing the parameters to the values of P_{c2} and I_{c2} of Table 1, the maximum generated electrical energy was obtained. It was equal to 30.39 kJ for the PI control method against 28.81 kJ for the stored power curve control. However, the maximum generated electrical energy in the case of PI control of λ was obtained at the expenses of

more fluctuations in the generated power and turbine speed as can be seen in Figure 11. The turbine speed is changing a lot which is not good for the machine.

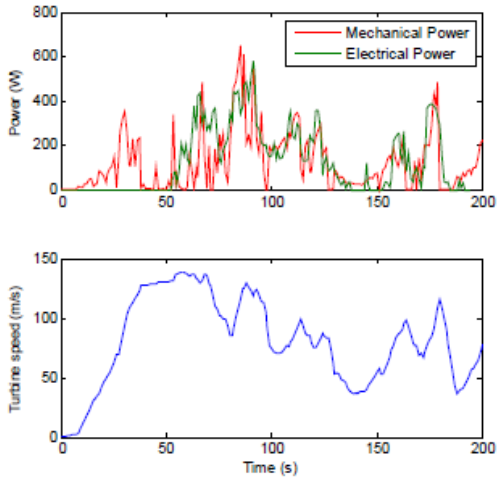

Figure 10. Power & speed for PI control of λ case.

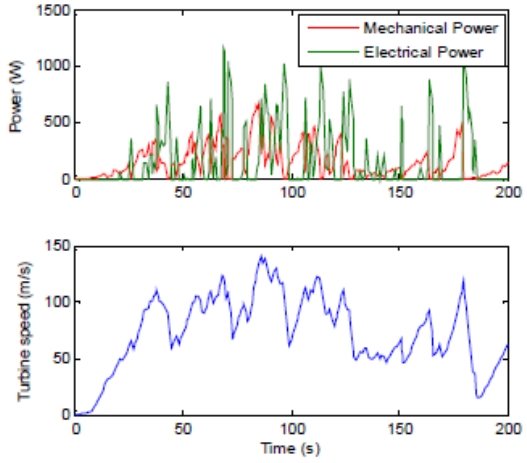

Figure 11. Maximum power & speed for PI control of λ case.

3.2. Simulation results of the detailed model

A detailed model of the system was built in Matlab/Simulink using SimPowerSystem toolbox as shown in Figure 12. The wind turbine block includes equations (1) and (2). The mechanical torque is fed into the PMSM. The three-phase output of the PMSM is connected to a passive rectifier. The PI control method is used. The rectified voltage is connected to a DC/DC buck converter. The measured

λ *(TSR)* value by equation (2) in the wind turbine block is fed to the wind speed control block and then compared with the optimal λ^* (TSR*), which is 1.3 in this case. The error signal is fed into a PI controller, with P_{c3} and I_{c3} values as shown in Table 2, which sets the current demand for the buck current of the buck converter. The simulation parameters used are shown in Table 2. The same wind speed data shown in Figure 8 is used.

Table 2. Values used in the detailed model simulations.

Symbol	Description	Value
J	Rotational inertia	38 kg.m^2
R	Turbine rotor radius	1m
R_s	Machine stator phase resistance	0.425Ω
L_a	Machine armature inductance	0.000835 H
K_I	Machine torque constant	5.308
P	Machine pole pairs	5
V_{dc}	DC voltage source in buck converter	50V
L	Inductor in buck converter	500μH
C	Capacitor in buck converter	300 μF
P_{c3}	Wind speed controller - Proportional Parameter	15
I_{c3}	Wind speed controller - Integral Parameter	2.5

Electrical power, mechanical power and turbine speed results are shown in Figure 13. The generated electrical energy is 32.05 kJ. It is slightly higher than the obtained values with simplified models in both speed control types (stored power curve and PI control of the λ) and the result looks better where the electrical power curve is almost following the mechanical power curve. The turbine's speed has very little fluctuations and almost constant once it reached its peak value.

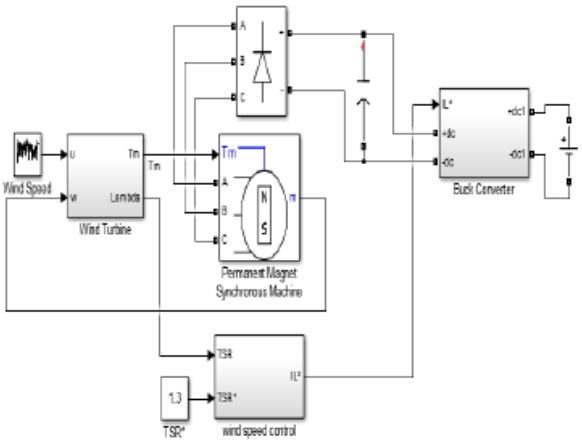

Figure 12. Detailed model.

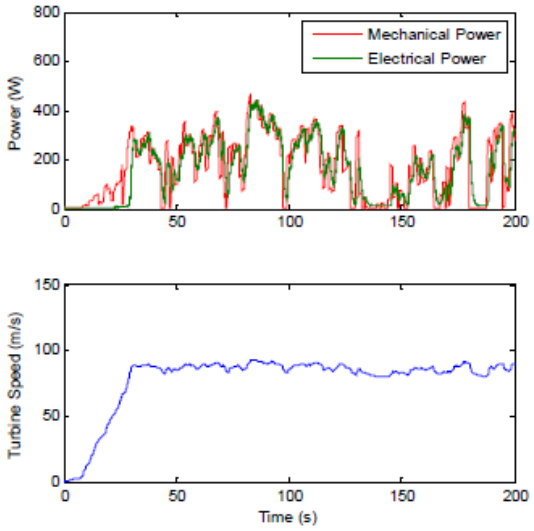

Figure 13. Power & speed for detailed model.

4. Conclusion

The paper presents a comparison between two methods of controlling the speed of a wind turbine in a microgird namely; PI control of the tip speed ratio and stored power curve. The PI method provides more controllability, but it requires an anemometer to measure the wind speed. The stored energy method, however, is easier to implement, but the amount of energy extracted can be less.

Acknowledgments

The work is financially supported by the Government of Oman, which provides a PhD grant for Rashid Al Badwawi. Also, financial support from EPSRC-DST funded RESCUES project (EP/K03619X/1).

Conflict of Interest

All authors declare no conflicts of interest in this paper.

References

1. Chen Z, Guerrero JM, Blaabjerg F (2009) A review of the state of the art of power electronics for wind turbines. *IEEE T Power Electr* 24: 1859–1875.
2. Valenciaga F, Puleston PF (2008) High-order sliding control for a wind energy conversion system based on a permanent magnet synchronous generator. *IEEE T Energy Conver* 23: 860–867.

3. Kenji A, Yukichi T, Takahisa O, et al. (2002) A maximum power control of wind generator system using a permanent magnet synchronous generator and a boost chopper circuit. *IEEE Power Conversion Conference* 3: 1447–1452.
4. Dali M, Belhadj J, Roboam X (2010) Hybrid solar-wind system with battery storage operating in grid-connected and standalone mode. Control and energy management—Experimental investigation. *Energy* 35: 2587–2595.
5. Ahmed AA, Ran L, Bumby J (2008) Simulation and control of a hybrid PV-wind system. *4th IET International Conference on Power Electronics, Machines and Drives PEMD* 3: 421–425.
6. Sechilariu M, Wang BC, Locment F (2014) Supervision control for optimal energy cost management in DC microgrid. Design and simulation. *Int J Electr Power Energy Syst* 58: 140–149.
7. Resende FO, Lopes JAP (2011) Management and control systems for large scale integration of renewable energy sources into the electrical networks. *IEEE International Conference on Computer as a Tool (EUROCON)*: 27–29.
8. AlBadwawi R, Abusara M, Mallick T (2015) A Review of Hybrid Solar PV and Wind Energy System. *J Smart Sci* 3: 127–138.

AIMS Press

Power Management of AC Islanded Microgrids using Fuzzy Logic

R Al Badwawi, W Issa, T Mallick, and M Abusara

Environment and Sustainability Institute, University of Exeter, Penryn Campus, Penryn, TR10 9FE, United Kingdom,
*Correspondence: Email: rsma202@exeter.ac.uk Tel: +44(0)1326259478.

Keywords: Fuzzy logic controller, power management, microgrid, energy storage system, renewable energy sources.

Abstract

In an islanded AC microgrid consisting of renewable energy sources, battery, and load, the battery balances the difference between power generated by renewable sources and that consumed by the load. However, battery charging capacity is limited and its state of charge needs to be maintained within the safety limits. Furthermore, battery has limited maximum charging and discharging power. This paper proposes a controller based on fuzzy logic to prevent the battery state of charge and charging/discharging power from exceeding their limits regardless of variations in load and intermittent power of renewable sources. The microgrid considered in this paper consists of PV, battery, load and auxiliary supplementary unit. The fuzzy logic controller alters the AC bus frequency which is used by the local controllers of the parallel units to curtail the power generated by PV or to supplement power from the auxiliary unit. The main merits of the proposed controller are simplicity and easiness of implementation without the need for any communication links between the parallel units. Matlab/Simulink results are presented to validate the performance of the proposed controller.

1 Introduction

AC microgrid can provide an elegant and efficient solution for integrating Renewable Energy Sources (RES). A microgrid is basically an aggregation of RES, Energy Storage Systems (ESS), and local loads. It can operate in grid-connected mode as well as in autonomous island mode. In grid-connected mode, the bus voltage and frequency are maintained by the grid and any difference between the power generated by RES and that required by the load is balanced by the gird. The ESS in this case can be used to control the amount of power exchanged between the grid and the microgrid. In island mode, however, ESS has to play a much more important role; it has to maintain the bus voltage and frequency and it needs to balance the difference between the RES power and load. Due to the limited charging capacity of ESS, power generated from RES might need to be curtailed to prevent the ESS from overcharging. Similarly, the load might need to be shed or an auxiliary power unit might need to supplement power in order to prevent the ESS from undercharging. In addition, battery ESS (BESS) has limited maximum charging and discharging power and exceeding this will reduce the lifetime of the battery. Therefore, the energy management controller has to fulfil two main tasks; firstly, the State of Charge (SOC) of the battery has to be maintained between the maximum and minimum limits and secondly, the battery power needs to be kept below the maximum charging/discharging limits.

Fuzzy Logic Control (FLC) is a flexible tool with rules based on human knowledge and experience that can deal with unpredictable variables or uncertainties. FLC can deal with complex systems such as microgrids with different types of imprecise inputs, variables and disturbances in particular if the power is supplied by intermittent RES and consumed by varying and unpredictable load. FLC has been used for both DC and AC microgrids (grid-connected and island mode of operations) in the literature for several purposes due to its good performance and simplicity. FLC has been used for Maximum Power Point Tracking (MPPT) of solar PV [1–5], frequency regulation [6,7], controlling batteries' output charger current [8] and improvement in wind power prediction accuracy [9].

Review of hybrid RES (PV and wind) and BESS including the applications of FLC for energy management of microgrid can be found in [10,11]. In [12, 13], FLC has been used to provide a split in power between solar PV, wind and BESS according to a pre-defined rules based on the operator's experience. A FLC was used to manage the SOC of a Li-ion battery in a DC microgrid with solar PV, wind and fuel cell system [14]. There were two inputs to the FLC; power difference between generation and load and difference between measured SOC and required SOC. The output of the FLC was the charging/discharging current demand for the battery.

In grid-connected mode, a FLC was proposed in [15] to minimize energy storage range of the battery and power variation range exchanged between the grid and the microgrid. A smart FLC was also proposed in [16] in order to minimize the number of times required to switch between island and grid-connected modes. This in turn maximized the usage of renewable energy and reduced the dependency on the main grid. The SOC of a BESS in a hybrid microgrid was controlled by a FLC in [17] to improve the performance of the hybrid generation system with smaller energy capacity of BESS. A decentralized fuzzy logic gain-scheduling controller was proposed in [18] to balance the stored energy between different battery systems in a DC microgrid by adjusting the droop coefficients of the primary controllers. A controller was proposed for an autonomous active power control of islanded AC microgrids with PV and ESS along with load in [19]. The controller was based on frequency bus-signalling such that the

ESS controls the PV power using local controllers and without the need for external communication.

In this paper, a FLC is proposed to control BESS in an islanded microgrid. It prevents the battery SOC and power from exceeding their maximum and minimum limits regardless of variation in load and intermittent power generated by renewable sources. The microgrid considered in this paper consists of PV, battery, load and auxiliary unit which can be a fuel cell, micro gas turbine or another battery. The fuzzy logic controller (located in BESS) alters the AC bus frequency which is used by the local controllers of the parallel units to curtail the power generated by PV or to supplement power from the auxiliary unit. The FLC is divided into two subsystems to simplify the design. The main merits of the proposed controller are simplicity and easiness of implementation without the need for any communication links between the parallel units. Matlab/Simulink results are presented to validate the performance of the proposed controller.

The paper is organized as follows. Section 2 gives system overview and droop control strategy. In Section 3, the proposed fuzzy logic controller is described. Section 4 provides simulation results. Finally, Section 5 gives the conclusion.

2 System Overview and Droop Control Strategy

The microgrid considered in this paper is shown in Fig.1. It contains three power generation units:

1) PV-based RES unit which consists of a unidirectional DC/DC converter and a DC/AC inverter. The DC/DC converter controls the PV output voltage to achieve MPPT while the DC/AC inverter regulates the DC link voltage.
2) BESS unit which has a bidirectional DC/DC converter to regulate the DC link voltage while the DC/AC inverter represents the master unit that maintains and controls the AC bus frequency and voltage of the islanded microgrid. It also alters the bus frequency according to FLC command.
3) Auxiliary supplementary unit which can be a fuel cell, micro-gas turbine, or another battery. It operates in case of low battery SOC and/or low PV generation. It has a unidirectional DC/DC converter that regulates the DC link voltage while the DC/AC inverter controls the output power according to the AC bus frequency as will be explained later.

All the three DC/AC inverters use droop control [20] to stay in parallel and share load. If the power generated by the PV unit is more than the load, the battery unit will absorb the surplus power. Similarly, if the PV power is less than the load, the battery will supply the shortage. However, the battery capacity is limited so if the SOC is approaching its maximum limit, PV power needs to be curtailed and if the SOC is reaching its lower limit, the auxiliary unit will need to supply power.

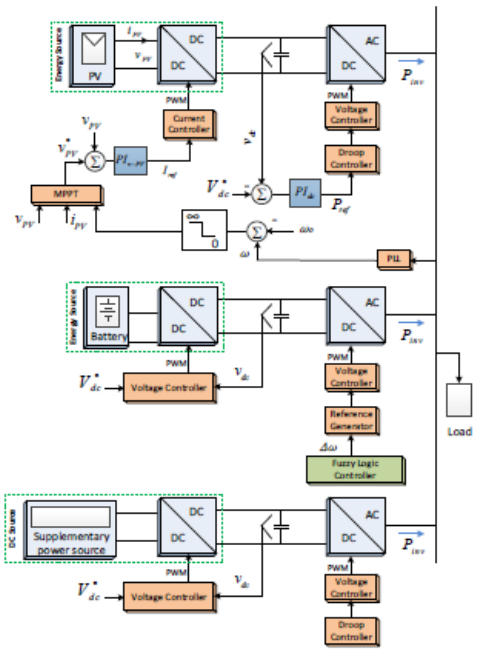

Fig.1: Microgrid Structure.

In a traditional droop control, the output frequency ω and voltage amplitude V of any DC/AC inverter are given by Equations (1) and (2), respectively,

$$\omega = \omega_o - m(P - P^*) \qquad (1)$$

$$V = V_o - n(Q - Q^*) \qquad (2)$$

where ω_o, V_o , m, and n are the nominal frequency, nominal voltage, frequency drooping coefficient, and voltage drooping coefficient, respectively. P and Q are the measured active and reactive powers and $P^*$and Q^* are active and reactive power demands, respectively.

The three DC/AC inverters in Fig. 1 have the same droop equation for reactive power as in (2). However, for active power, each unit has a different droop coefficient and power demand depending on its role. The battery unit forms the AC bus and it has to control the output voltage and frequency. The power delivered/absorbed by the battery depends on the PV power and load. To achieve this functionality, the droop coefficient m needs to be set to zero. In addition, in order to be able to curtail the PV power or to supplement power from the auxiliary unit, the bus frequency will vary by $\Delta\omega$ which is the output from the FLC. Thus, the output frequency of the battery unit is given by Equation (3).

$$\omega = \omega_o + \Delta\omega \qquad (3)$$

The DC/AC inverter of the PV unit controls the DC link voltage by injecting more or less power into the AC bus. The droop control of the PV unit is given by Equation (4).

$$\omega = \omega_o - m_{pv}(P - P^*_{pv}) \qquad (4)$$

where the power demand P^*_{pv} is the output of the proportional-integral (PI) controller that regulates the DC link voltage (see Fig. 1). In the steady state, the power demand P^*_{pv} equals the power generated by the DC/DC converter according to its MPPT algorithm. The PV unit acts as a power source injecting maximum power available from PV to the AC bus. The auxiliary unit needs to provide power only when needed according to the bus frequency and its droop control is given by Equation (5).

$$\omega = \omega_o - m_{aux}P \qquad (5)$$

Fig. 2 shows the frequency/power droop control for the three units based on (3) to (5). The zero droop coefficient of the battery unit makes it the master controller for the AC bus frequency. The bus frequency can be shifted up to curtail the PV power or shifted down to produce power from the auxiliary unit. For the PV unit, the output power P equals the demanded power P^*_{pv} when the bus frequency ω equals the nominal frequency ω_o. If the bus frequency is shifted down, the DC/AC inverter of the PV unit will deliver more power than that produced by the DC/DC converter which will cause the DC link voltage to drop. This drop will cause the PI controller of DC link voltage to reduce the power demand P^*_{pv} so that the DC/AC inverter delivers the same power produced by the DC/DC converter. However, if the bus frequency is shifted up, this will act as a message to the MPPT controller that the PV power needs to be curtailed. The MPPT controller measured the bus frequency using Phase Looked Loop (PLL) (see Fig. 1) and it will shift the maximum power point to a lower value by increasing the PV output voltage as illustrated in Fig. 3. The more rise in frequency the more curtailment in PV power. When the bus frequency is equal or higher than the nominal frequency ω_o, the auxiliary unit will produce no power according to (5) and as shown in Fig. 2. If the bus frequency is shifted down, however, the auxiliary unit will start producing power and the more drop in frequency the more power produced. This way, power curtailment and supplement is controlled wirelessly through the bus frequency without any extra communication.

3 Proposed Fuzzy Logic Controller

The proposed FLC is responsible for varying the bus frequency and is shown in Fig. 4. It consists of two subsystems. The top subsystem is responsible for preventing the battery from overcharging i.e. keeping the SOC below its maximum limit. It also prevents the battery charging power from exceeding its limit. The inputs are ΔSOC (the difference between the current SOC and its maximum value SOC^*_{max}) and ΔP_{charge} (the difference between the charging power and its maximum charging power value $P^*_{charge\_max}$). The output is a positive shift in the frequency $\Delta\omega_+$ to curtail the PV power. On the other hand, the bottom FLC subsystem is responsible for preventing the battery from over discharging i.e. keeping the SOC above its minimum limit. It also prevents the battery discharging power from exceeding its limit. The inputs are ΔSOC (the difference between the current SOC and its minimum limit SOC^*_{min}) and $\Delta P_{discharge}$ (the difference between the discharging power and its maximum discharging power value $P^*_{discharge\_max}$). The output of the bottom FLC subsystem is a negative shift in the frequency $\Delta\omega_-$ to cause the auxiliary unit to supplement power.

The rules for the FLC are shown in Table 2 (top subsystem and Table 3 (bottom subsystem). The terms L, M and H denote low, medium and high membership functions, respectively. The frequency scaling values for top and bottom FLC subsystems shown in Fig. 4 are 0.12 and 0.064 respectively. They have been chosen to change the PV power from 0% to 100% in such a way that $\Delta\omega_+ = 0$ means that PV will generate 100% of the MPPT value, while $\Delta\omega_+ = 0.12$ curtails PV power to zero. Similarly, $\Delta\omega_- = 0$ will not generate any power by the auxiliary unit, while $\Delta\omega_- = 0.064$ will generate maximum power from the auxiliary unit.

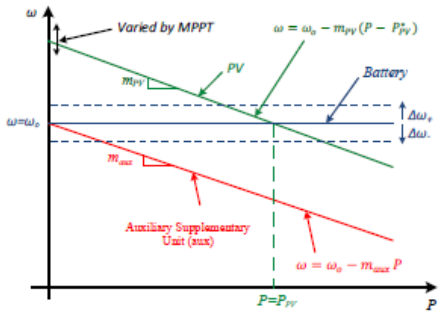

Fig. 2: Power – frequency droop control curves.

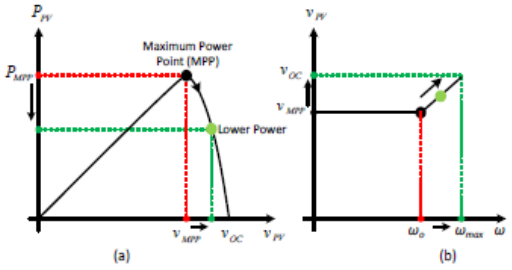

Fig. 3: PV MPP shifting operation: (a) PV power versus output voltage, (b) output voltage versus frequency.

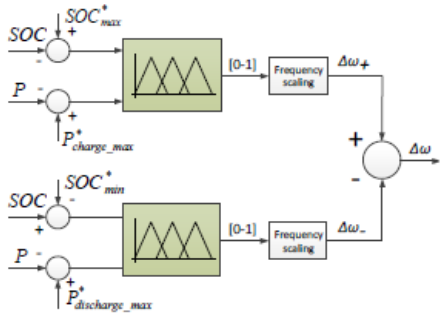

Fig. 4: Proposed fuzzy controller.

$\Delta\omega_+$		ΔP_{charge}		
		L	M	H
ΔSOC	L	H	H	H
	M	M	M	M
	H	L	L	L

Table 2: Rules of top FLC.

$\Delta\omega_-$		$\Delta P_{discharge}$		
		L	M	H
ΔSOC	L	H	H	H
	M	H	M	M
	H	M	M	L

Table 3: Rules of bottom FLC.

Parameter	Symbol	Value
Maximum state of charge	SOC^*_{max}	95%
Minimum state of charge	SOC^*_{min}	40%
Maximum charging power	$P^*_{Charge\_max}$	1000W
Maximum discharging power	$P^*_{Discharge\_max}$	1000W
Nominal bus frequency	ω_o	314rad/s
Nominal bus voltage	V_o	220V
Battery nominal voltage	V^*_{DC}	750V
Active power droop coefficients	m_{pv}, m_{mux}	0.9e-4 rad/s/W
Reactive power droop coefficients	n	0.9e-4 V/Var

Table 4: System parameters.

4 Simulation Results

A microgrid including the three power units and the proposed controllers has been built in Matlab/Simulink SimPowerSystem and Fuzzy Logic tool boxes. The system parameters used in the simulation are shown in Table 4.

For a high SOC case with initial value approaching the maximum limit of 95%, Fig. 5 shows the power output of PV, battery and auxiliary units along with load power. The auxiliary unit was not running as the battery SOC was high with moderate load (500W). The FLC was deactivated before t = 3s. The battery charging power (500W) could cause overcharging. However, after activating the proposed FLC at t = 3s, the PV power was curtailed from 1000W to around 500W. The frequency was increased to reduce the PV's power generation. SOC was increasing although it was high prior to the FLC activation. However, it was stopped from increasing, kept constant and limited from exceeding its maximum limit after FLC activation. At t = 5s, the load became 1000W and the generation from the PV unit was proportional to the change in the frequency commanded by the FLC until the PV restored its full generation. The frequency was decreased to increase the PV's power production. The SOC was prevented from increasing beyond the maximum limit by curtailing the PV power but when the load increases the curtailment stopped so to make use of all available PV power.

Fig. 6 shows the power output of PV, battery and auxiliary units and load when the battery SOC was approaching its minimum limit of 40%. The FLC was deactivated before t = 3s. The battery was discharging and providing 600W since the load was 1600W and higher than the power generated from the PV which was 1000W. SOC was declining prior to the activation of the FLC (under-charging). The auxiliary unit was not running. However, at t = 3s, the FLC was activated and it decreased the bus frequency so the auxiliary unit reacted by generating 600W. The generated power was proportional to the frequency drop. The SOC was stopped from declining, kept constant and hence protected from undercharging. At t = 5s, the load dropped from 1600W to 100W, the available generation to be absorbed by the battery is now 1500W which exceeds the maximum charging power of 1000W. Thanks to FLC, the auxiliary unit stopped generating and the PV power supplied the load and the surplus power was absorbed by the battery to heal the low SOC. The charging power was limited to 900W instead of 1500W (if the auxiliary unit was left to generate). The FLC increased the bus frequency in order to stop the auxiliary unit from generating. The SOC started to increase making use of the available surplus power. As can be seen, the FLC prevented the battery SOC and power from exceeding their limits. During transient, however, the battery power exceeded the 1000W limit but only for a short period of time of 1 second.

In view of the above, the FLC controller used the full available PV power when required and curtailed it to prevent the battery from overcharging. In addition, it activated the auxiliary unit to support the battery and protect it from undercharging.

5 Conclusion

A controller based on fuzzy logic has been proposed for power management of islanded microgrids. The controller prevents the battery state of charge and charging/discharging power from exceeding their limits regardless of variations in

load and intermittent power of renewable energy sources. By varying the AC bus frequency and making use of local droop controllers, the power management controller was implemented without the need for any communication links between the microgrid units. Simulation results have been presented to validate the functionality of the proposed controller.

Acknowledgements

The work is financially supported by the Government of Oman, which provides a PhD grant for Rashid Al Badwawi. Also, the work is supported by EPSRC-DST funded project: Reliable and Efficient System for Community Energy Solutions (RESCUES- EP/K03619X/1).

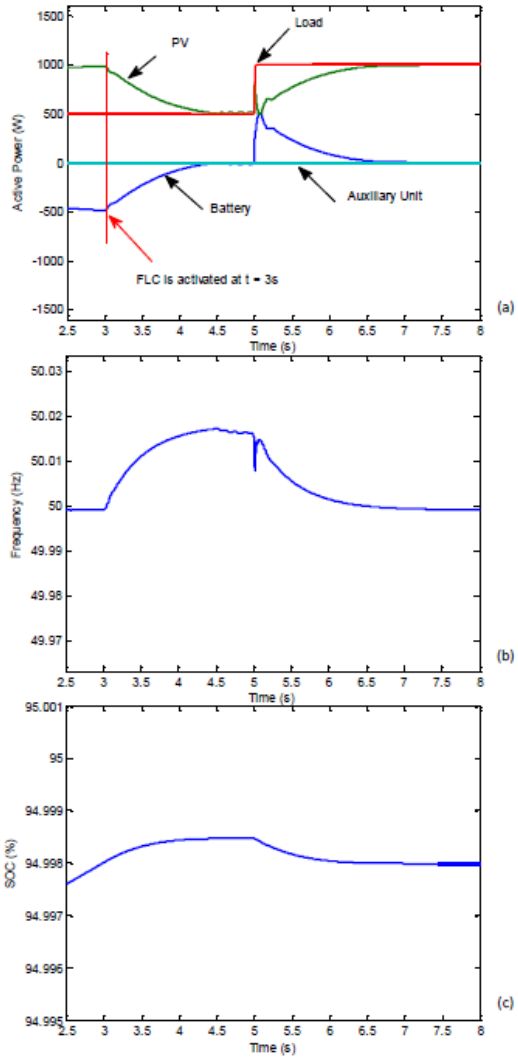

Fig. 5: Output response for 95% SOC case: (a) output power, (b) frequency (c) SOC.

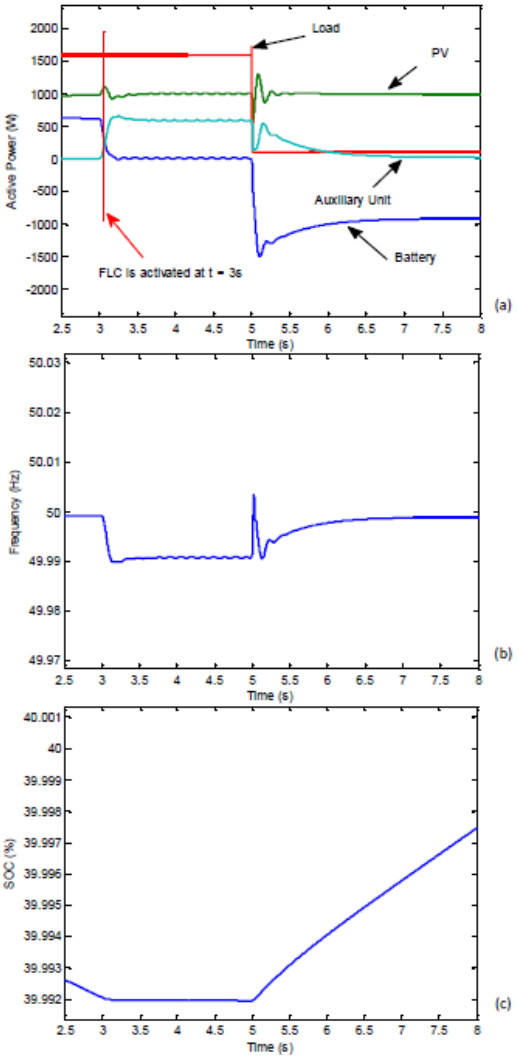

Fig. 6: Output responses for 40% SOC case: (a) output power. (b) Frequency, (c) SOC.

References

[1] N. Bigdeli, "Optimal management of hybrid PV / fuel cell / battery power system: A comparison of optimal hybrid approaches", *Renew. Sustain. Energy Rev.*, vol. 42, pp. 377–393, (2015).

[2] M. Cheikh, C. Larbes, G. Tchoketch, A. Zerguerras. "Maximum power point tracking using a fuzzy logic control scheme", *Rev. des energies ...*, **vol. 10**, pp. 387–395, (2007).

[3] T. Esram, P. L. Chapman, "Comparison of photovoltaic array maximum power point tracking techniques", *IEEE Trans. Energy Convers.*, **vol. 22, no. 2**, pp. 439–449, (2007).

[4] B. Hamed, M. El-Moghany. "Fuzzy controller design using FPGA for photovoltaic maximum power point tracking", *J. Adv. Res. Artif. Intell.*, **vol. 1, no. 3**, pp. 14–21, (2012).

[5] G. Balasubramanian, S. Singaravelu. "Fuzzy logic based controller for a stand-alone hybrid generation system using wind and photovoltaic energy", *Int. J. Adv. Eng. Technol. (IJAET)*, **vol. 3, no. 2**, pp. 668–679, (2012).

[6] M. S. Bisht, Sathans. "Fuzzy based intelligent frequency control strategy in standalone hybrid AC microgrid", *2014 IEEE Conference on Control Applications (CCA)*, pp. 873–878, (2014).

[7] M. Marzband, A. Sumper, O. Gomis-Bellmunt, P. Pezzini, M. Chindris. "Frequency control of isolated wind and diesel hybrid microgrid power system by using fuzzy logic controllers and PID controllers", *Proceeding of the 11th International Conference on Electrical Power Quality and Utilisation, EPQU*, pp. 114–119, (2011).

[8] M.-W. Cheng, S.-M. Wang, Y.-S. Lee, S.-H. Hsiao. "Fuzzy controlled fast charging system for lithium-ion batteries", *International Conference on Power Electronics and Drive Systems (PEDS)*, pp. 1498–1503, (2009).

[9] A. L. A Mu-ti, C. Qin, T. E. Y Bu-la-yin, L. Jian-chun. "Application of fuzzy control for the energy storage system in improving wind power prediction accuracy", *Am. J. Energy Res.*, **vol. 1, no. 3**, pp. 54–58, (2013).

[10] R. AlBadwawi, M. Abusara, T. Mallick. "A review of hybrid solar PV and wind energy system", *Smart Sci.*, **vol. 3, no. 3**, pp. 127–138, (2015).

[11] L. Suganthi, S. Iniyan, A. A. Samuel. "Applications of fuzzy logic in renewable energy systems – A review", *Renew. Sustain. Energy Rev.*, **vol. 48**, pp. 585–607, (2015).

[12] C. Ben Salah, M. Ouali. "Energy management of a hybrid photovoltaic system", *Int. J. Energy Res.*, **vol. 36**, pp. 130–138, (2012).

[13] T. P. Kumar, Y. Chandrashekar, N. Subrahmanyam, M. Sydulu. "Control strategies of a fuzzy controlled grid connected hybrid PV / PEMFC / battery distributed generation system", *2015 IEEE Power and Energy Conference at Illinois (PECI)*, pp. 1–6, (2015).

[14] Y. Chen, Y. Wu, C. Song. "Design and implementation of energy management system with fuzzy control for DC micro-grid systems", *IEEE Trans. Power Electron.*, **vol. 28, no. 4**, pp. 1563–1570, (2012).

[15] D. Arcos-Aviles, F. Guinjoan, J. Barricarte, L. Marroyo, P. Sanchis, H. Valderrama. "Battery management fuzzy control for a grid-tied microgrid with renewable generation", *IECON 2012 - 38th Annu. Conf. IEEE Ind. Electron. Soc.*, pp. 5607–5612, (2012).

[16] A. Lal, R. Kumar, U. Mehta. "Energy dispatch fuzzy model in hybrid power system", *Int. Energy J.*, **vol. 14**, pp. 133–142, (2014).

[17] X. Li, D. Hui, L. Wu, X. Lai. "Control strategy of battery state of charge for wind / battery hybrid power system", *IEEE Int. Symp. Ind. Electron.*, pp. 2723–2726, (2010).

[18] N. L. Diaz, T. Dragi, J. C. Vasquez, J. M. Guerrero, "Fuzzy-logic-based gain-scheduling control for state-of-charge balance of distributed energy storage systems for DC microgrids", *Appl. Power Electron. Conf. Expo. (APEC), 2014 Twenty-Ninth Annu. IEEE*, pp. 2171–2176, (2014).

[19] D. Wu, F. Tang, T. Dragicevic, J. C. Vasquez, J. M. Guerrero, "Autonomous active power control for islanded AC microgrids with photovoltaic generation and energy storage system", *IEEE Trans. Energy Convers.*, **vol. 29, no. 4**, pp. 882–892, (2014).

[20] W. R. Issa, M. A. Abusara, S. M. Sharkh. "Control of transient power during unintentional islanding of microgrids", *IEEE Trans. Power Electron.*, **vol. 30, no. 8**, pp. 4573–4584, (2015).

DC Microgrid Power Coordination Based on Fuzzy Logic Control

Rashid Al Badwawi*, Walid Issa, Tapas Mallick, and Mohammad Abusara
Environment and Sustainability Institute, University of Exeter
Penryn Campus, TR10 9FE
Penryn, UK
Tel.: +44 / (01326) – 259.478.
*E-Mail: rsma202@exeter.ac.uk
URL: http://www.exeter.ac.uk/esi/

Acknowledgements

The work is financially supported by the Government of Oman, which provides a PhD grant for Rashid Al Badwawi. Also, the work is supported by EPSRC-DST funded project: Reliable and Efficient System for Community Energy Solutions (RESCUES- EP/K03619X/1).

Keywords

«Microgrid», «Power management», «Fuzzy control», «Energy storage», «Renewable energy systems».

Abstract

The power coordination in DC microgrids has a vital role in enhancing the performance and management of multi generation units. Renewable Energy Sources (RES) are limited to their available power with intermittent nature. Battery-based energy storage sources have limitations in the charging and discharging capabilities to avoid depleting the battery and preserve the State of Charge (SOC) within its satisfactory limits. The battery balances the power difference between RES and loads. However, in severe cases where the SOC is very low, load shedding is crucial. In this paper, a Fuzzy Logic Controller (FLC) has been proposed to coordinate the power flow of PV unit and battery to satisfy the load by full use of the available PV power. It controls the PV's output power and keeps the SOC and charging / discharging power of the battery within their required margins regardless of the variations in load. Furthermore, load shedding of low priority load has been implemented when the battery couldn't balance the microgrid power flow. Simplicity in managing multi input-multi output system by FLC is the main merit. Matlab/Simulink results are presented to validate the performance of the proposed controller.

Introduction

Renewable energy sources become preferable option for powering areas that are not connected to main grid. Energy Storage System (ESS) such as battery is essential to balance the power flow between the microgrid elements (generations and loads). Furthermore, it provides more reliability to the microgrid especially for working in different modes of operation; grid-connected or island modes. Although AC microgrid [1] is more dominant in terms of research and existence compared to DC microgrid; DC microgrid starts getting more attention and consideration due to its higher efficiency. In addition, some of the issues that are faced in AC microgrids like reactive power flow, power quality, and frequency control are not issues in DC microgrids. This in turn makes the corresponding primary control notably less complex than its equivalent AC version [2]. Energy management and control design is one of the challenges for microgrids with RES systems along with Battery Energy Storage System (BESS) [3], [4]. However, in the last couple of years, the interest on designing rule-based microgrid' supervisory controller increased to provide a proper power management of different power generation units, including renewable energy sources. In line with this direction, researchers worldwide adopted Fuzzy Logic Controller (FLC) for energy management in both standalone and grid-connected hybrid

renewable energy systems. As per the literature, FLC has been used in both DC and AC microgrids, whether in standalone or grid-connected mode of operations, for several purposes such as maximum power point tracking (MPPT) of solar PV and/or wind power systems [5]–[7], controlling batteries' output charge current [8], etc. FLC was used to manage the state of charge (SOC) of a Li-ion battery connected to a DC microgrid with solar photovoltaic (PV), wind and fuel cell system [9]. The FLC provides the output current for charging or discharging the battery. By adjusting the droop coefficient of primary controllers in a DC microgrid, a decentralized fuzzy logic gain-scheduling controller was proposed in [10] in order to balance the stored energy between different batteries' systems. To improve the performance of a hybrid microgrid generation system with smaller energy capacity of BESS, the SOC of the BESS was controlled by FLC in [11]. FLC has been also used in [12] to provide powers' split between solar PV and BESS based on operator's experience through a pre-defined rules in order to supply DC load. The PV power, SOC of the battery and power required by the load are the inputs to the FLC. The output of the FLC decides the operation of the different switches to have one of the possible connections; PVP-battery, battery-load and PVP-load.

In this paper, PV system has been used along with battery system to form a DC microgrid. Unlike most of designed FLCs in the literature, the proposed FLC in this paper is divided into two subsystems to simplify the design. One subsystem is responsible for preventing the battery SOC and charging power from exceeding their maximum design limits or overcharging. The output of the FLC decides whether to use the maximum power from PV or curtail it according to the SOC, the charging / discharging power and the load. On the other hand, the second subsystem is responsible for preventing the battery SOC from exceeding its minimum design limit and the discharging power from its maximum value. At the same time, the output of the FLC decides the load shedding switches operation to decide to supply the whole loads or go for load shedding whenever required. The FLC is designed for efficient use of the PV and battery powers to keep the SOC and charging/ discharging power of the battery within their required margins regardless of variation in load and intermittent power. Matlab/Simulink results validated the performance of the proposed FLC.

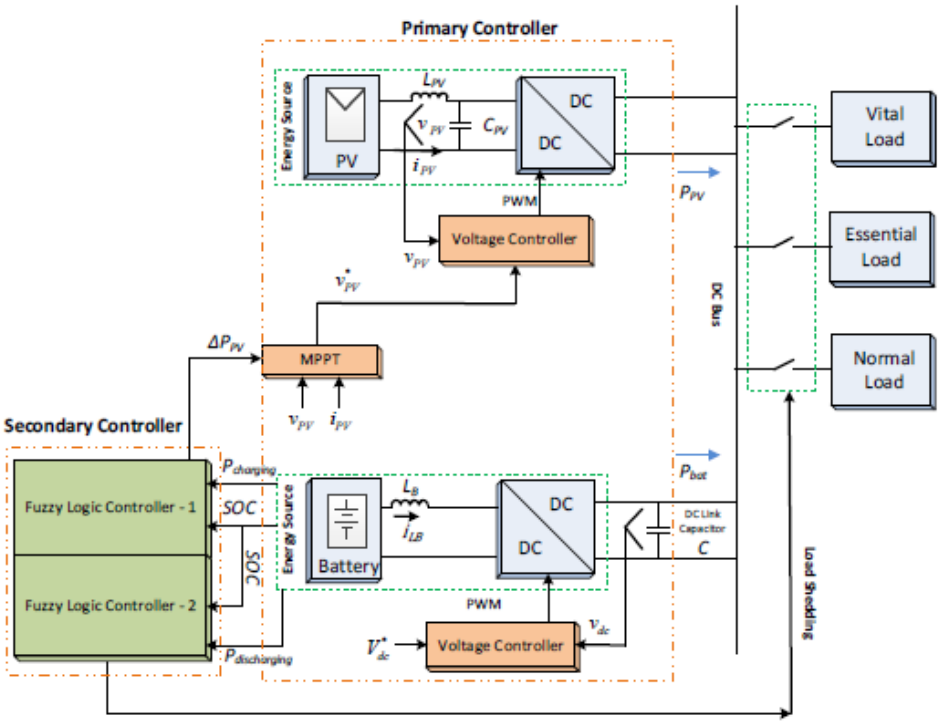

Fig. 1: Microgrid structure

Microgrid structure

The main microgrid structure under consideration in this paper is shown in Fig.1 in islanded mode. It consists of a renewable energy source represented by PV unit and an energy storage system represented by a battery bank. The operation of both generation units is as follows.

1. PV unit exports power to the common DC bus according to MPPT command via a unidirectional DC/DC converter. The latter controls the PV's output voltage to achieve MPPT.
2. BESS unit which has a bidirectional DC/DC converter to regulate the DC bus voltage. The BESS is working as a master voltage source to maintain the DC bus stability of the islanded microgrid. A PI controller is embedded in battery system to control the DC bus voltage at 380V.

The control system is divided into two levels separated by control bandwidth. The primary level contains the voltage and current controllers for the DC/DC converters. The latter is designed to have fast disturbance rejection with high bandwidth control loop (i.e. > 500 rad/s) to track the commanded references values. The secondary level is represented by the FLC which is designed to have lower bandwidth. This criterion is a rule of thumb for nested control loops to preserve system stability. The FLC maintains the power flow in the microgrid according to pre-defined rules. The output of it manipulates the references values (voltage or current) of the primary control level.

Primary control loops design

The primary level control loop design of the BESS bidirectional boost converter and PV uni-directional DC/DC converter are as described below. The key parameters of the BESS and PV systems are as shown in Table I.

BESS DC/DC converter

The linearized averaged state-space model for bidirectional boost BESS DC/DC converter are as follows [13], [14].

$$\begin{bmatrix} \dot{i_{LB}} \\ \dot{v_{dc}} \end{bmatrix} = \begin{bmatrix} 0 & \frac{-(1-D)}{L_B} \\ \frac{1-D}{C} & \frac{-1}{RC} \end{bmatrix} \begin{bmatrix} i_{LB} \\ v_{dc} \end{bmatrix} + \begin{bmatrix} \frac{V_{dc}}{L_B} \\ \frac{-I_{LB}}{C} \end{bmatrix} d \tag{1}$$

$$y = \begin{bmatrix} 1 & 0 \\ 0 & 1 \end{bmatrix} \begin{bmatrix} i_{LB} \\ v_{dc} \end{bmatrix} \tag{2}$$

where L_B, V_{dc}, C and R are the converter inductor, nominal DC-link voltage, DC-link capacitor and equivalent load resistor. I_{LB}, D are the inductor current and averaged duty cycle considered in steady state of the operating point. d is the averaged control input. From (1) and (2), the transfer functions G_{iLB-d} and $G_{vdc-iLB}$ are calculated [14].

$$G_{iLB-d} = \frac{i_{LB}(s)}{d(s)} = \frac{RCV_{dc}s + [(1-D)RI_{LB} + V_{dc}]}{RCL_Bs^2 + L_Bs + R(1-D)^2} \tag{3}$$

$$G_{vdc-iLB} = \frac{v_{dc}(s)}{i_{LB}(s)} = \frac{-I_{LB}RL_Bs + V_{dc}R(1-D)}{V_{dc}RCs + [V_{dc} + (1-D)I_{LB}R]} \tag{4}$$

The PI controllers of the current loop and voltage loop are as follows:

$$G_{PI-B1(s)} = \frac{0.005s + 1}{s} \tag{5}$$

$$G_{PI-B2(s)} = \frac{s + 50}{s} \tag{6}$$

Based on above, the open-loop and closed-loop bode diagram for the bidirectional boost DC/DC converter is as shown in Fig. 2 where the controller has a gain margin of 46.6 dB and a phase margin of 69.4 deg. The PI controller is also designed to provide a bandwidth of 1580 rad/s. The control system structure for the battery bidirectional boost converter is as shown in Fig. 3.

PV DC/DC converter

The linearized averaged state-space model for unidirectional boost PV DC/DC converter are as follows [13]–[15]:

$$\begin{bmatrix} \dot{i_{Lpv}} \\ \dot{v_{pv}} \end{bmatrix} = \begin{bmatrix} 0 & \frac{1}{L_{PV}} \\ \frac{-1}{C_{pv}} & \frac{1}{r_{pv}C_{pv}} \end{bmatrix} \begin{bmatrix} i_{Lpv} \\ v_{pv} \end{bmatrix} + \begin{bmatrix} V_{dc} \\ 0 \end{bmatrix} d \tag{7}$$

$$y = \begin{bmatrix} 1 & 0 \\ 0 & 1 \end{bmatrix} \begin{bmatrix} i_{Lpv} \\ v_{pv} \end{bmatrix} \tag{8}$$

where L_{pv}, V_{dc} , C_{pv} and r_{pv} are the converter inductor, nominal DC-link voltage, PV input capacitor and dynamic resistor of the PV at the considered operating point. d is the averaged control input. From (7) and (8), the transfer functions G_{iLpv-d} and $G_{vpv-iLpv}$ are defined [14].

$$G_{iLpv-d} = \frac{i_{Lpv}(s)}{d(s)} = \frac{(C_{pv}r_{pv}s-1)V_{dc}}{L_{pv}C_{pv}r_{pv}s^2 - L_{pv}s+r_{pv}} \tag{9}$$

$$G_{vpv-iLpv} = \frac{v_{pv}(s)}{i_{Lpv}(s)} = \frac{-r_{pv}}{C_{pv}r_{pv}s-1} \tag{10}$$

The PI controllers of the current loop and voltage loop are designed as follows:

$$G_{PI-pv1(s)} = \frac{10s + 250}{s} \tag{11}$$

$$G_{PI-pv2(s)} = \frac{0.05s + 1}{s} \tag{12}$$

Based on above, the open-loop and closed-loop bode diagram for the unidirectional boost PV DC/DC converter is as shown in Fig. 4 where the controller has a very high gain margin and a phase margin of 66.6 deg. The bandwidth of the control loop is 745 rad/s. The control system structure for the PV unidirectional boost converter is as shown in Fig. 5.

Table I: Key system parameters

Parameter	Symbol	Value
Equivalent load resistor for BESS DC/DC converter	R	440 Ω
DC output capacitor	C	1100 µF
Nominal DC-link voltage	V_{dc}	380 V
Duty cycle	D	0.25
Inductor current	I_{LB}	0.7 A
BESS and PV converter inductor	L_B, L_{pv}	0.8 mH
PV Dynamic resistor	r_{pv}	-6Ω
PV Input capacitor	C_{pv}	1100 µF

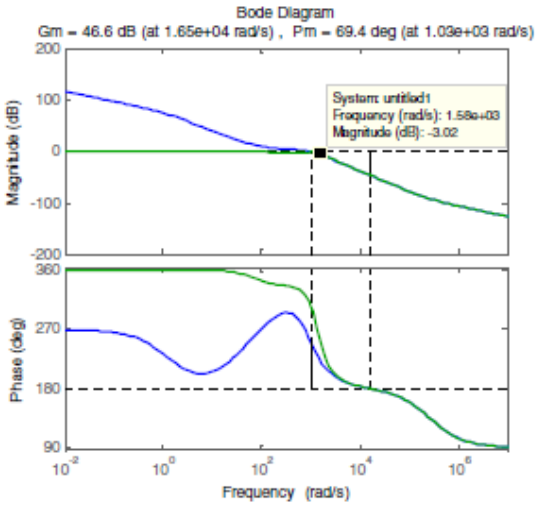

Fig. 2: Open-loop and closed-loop bode diagram for the bidirectional boost BESS DC/DC converter

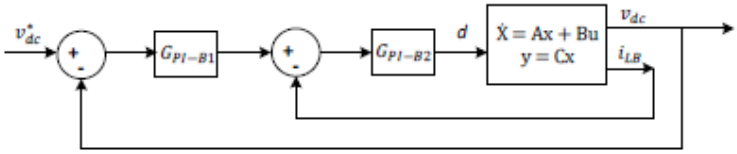

Fig. 3: Control system structure for the battery bidirectional boost BESS DC/DC converter

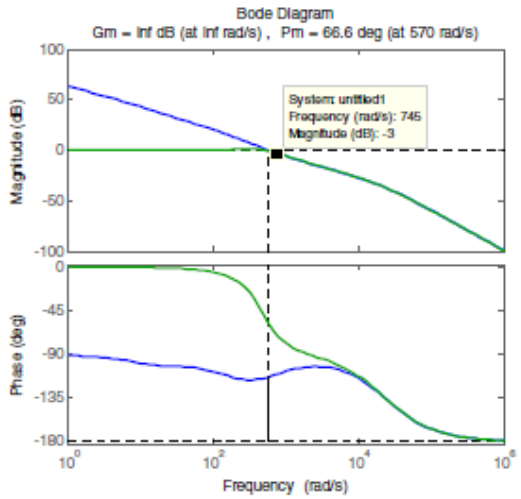

Fig. 4: Open-loop and closed-loop bode diagram for the unidirectional boost PV DC/DC converter

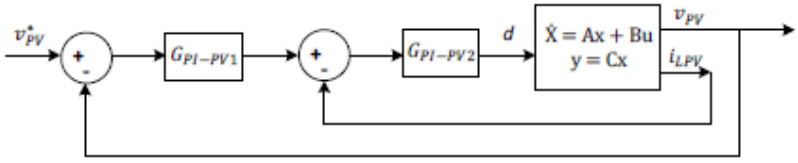

Fig. 5: Control system structure for the unidirectional boost PV DC/DC converter

PV Power shifter

If the power generation from PV is higher than the load, the battery normally absorbs the excess power. However, if the SOC of the BESS is very high, the PV power should be curtailed to prevent overcharging the battery. For the latter objective, a PV power shifter is implemented. Normally, the MPPT controller regulates the voltage across the PV to supply the maximum power. When a curtailment is needed, the power shifter shifts the PV voltage to deviate it from the maximum power point to a lower point as illustrated in Fig. 6(a). The more rise in the PV output voltage; the more curtailment in PV power and vice versa.

Proposed fuzzy logic controller

The proposed FLC is designed to work as a supervisory controller and divided into two subsystems to simplify the design in order to achieve the required objectives. One general objective of the FLC is to control the generated power distribution efficiently between the PV and battery to meet the required load power. The main objective is to protect the battery from overcharging or over discharging with full use of the PV power. The basic FLC is as shown in Fig. 7 and it consists of two subsystems;

1. The top subsystem is designed to limit the battery from overcharging (i.e. keeping the SOC below its maximum limit SOC^*_{max}) and also to prevent the maximum charging power from exceeding its limit by curtailing the PV power if needed. The inputs are ΔSOC (difference between current SOC and its maximum value SOC^*_{max}) and ΔP_{charge} (difference between charging power and its maximum charging power value $P^*_{charge\_max}$). The output is an increase or decrease in the PV power ΔP_{PV} which will be translated by the power shifter as illustrated in Fig. 6(b).
2. The bottom FLC subsystem is designed to limit the battery from over discharging (i.e. keeping the SOC above its minimum limit SOC^*_{min}) by shedding some loads whenever required. The inputs are ΔSOC (difference between current SOC and its minimum limit SOC^*_{min}) and $\Delta P_{discharge}$ (difference between discharging power and its maximum discharging power value $P^*_{discharge\_max}$). The output is a change in load power ΔP_{Load} realized by logic signals that control the state of the loads switches in Fig 1. It is worth mentioning here that the load has been classified to three groups according to its priory: vital (170W), essential (400W) and normal (570W) loads. The normal load shedding will be done first when required. Then if necessary, the essential load shedding will be done next and the last resort in terms of load shedding will be for vital load. The SOC and power limits are shown in Table II.

The rules for the FLC are shown in Table III (top subsystem) and Table IV (bottom subsystem). The terms L, M and H denote low, medium and high membership functions, respectively. The membership functions of top and bottom FLC subsystems are shown in Fig. 8 and Fig. 9 respectively. To satisfy the nested control loop operation, a low pass filer (LPF) is used on the FLC outputs; which provides a slower bandwidth than the primary controllers. Its cut-off frequency is equal to 150 rad/s which is chosen to be 5 times less than the lowest primary control bandwidth.

Simulation results

A DC microgrid as shown in Fig. 1 has been built in Matlab/Simulink with the proposed controllers. For the sake of validating the performance of the proposed FLC in the secondary control level. The bandwidth separation securely supports the assumption of considering ideal current and voltage sources instead of the DC/DC converters. Therefore, in the simulation, ideal current and voltage sources are implemented in the primary level and the reference values obtained from FLC in the secondary level. The FLC is designed in Matlab/Simulink using Fuzzy Logic tool box.

Several cases of battery SOC, PV power and load have been carried out to validate the performance of the proposed FLC. The load and PV power profiles have been defined to cover comprehensive scenarios. Fig. 10(a) shows the power output of the battery and PV systems in addition to the loads' power and SOC curve for initial SOC value of 95%. During each load value, the PV power changes from zero to medium to high generation. The aim is to keep the SOC and charging power within the

maximum limits; otherwise PV generation should be curtailed. At t = 0s, the PV generation was zero and the whole power was supplied by the battery. When the PV power dropped to around 380W at t = 1s, the battery provided the remaining power since the load was higher than PV power until the generated power from the PV increased to 1000W at t = 2s. After that, the PV generation dropped to zero at t = 3s. Hence, the battery supplied the whole power by discharging. The above profile of the PV was repeated again for the period from t = 3s to 6s, but with a lower load. At t = 4s, the PV produced 380W and the battery provided the remaining power by discharging. At t = 5s, the PV could have produced 1000W. However, there was no need for the whole PV generation since the load was less than the generation and the SOC was high and around 95%, so the PV generation was curtailed accordingly as per the FLC command. At the same time, there was no power provided by the battery. To assess the performance of the FLC with even lower load than previously considered, the same PV's profile was repeated again for the period from t = 6s to 9s. Again, when there was no power generation from the PV at t = 6s, the whole power was supplied by the battery. Then, the generated PV power became sufficient for the load at t = 7s, so the battery didn't provide any further power. With a higher available power from the PV in comparison to the load, the PV generation was curtailed at t = 8s. At the same time, there was no power provided by the battery and the surplus generated power by the PV was used for charging the battery. When the load was dropped to zero for the period from t = 9 to 12s, the PV generation was further curtailed as per the FLC command and became around 100W only. At the same time, there was no power provided by the battery. As can be seen from Fig. 10(a), the curtailed PV power and original/available PV power are shown in dotted line and solid line respectively. Fig. 10(b) shows the battery and PV power outputs along with the loads' power and SOC curve for SOC = 80%. At t = 0 to 2s, the PV generation was 1140W (maximum generation) that equal to the total load. The battery didn't provide any power. However, when the PV generation dropped to a very low value at t = 2s, load shedding was done for the normal load as per the FLC command. So, the load became 570W (essential and vital) instead of total load (1140W).

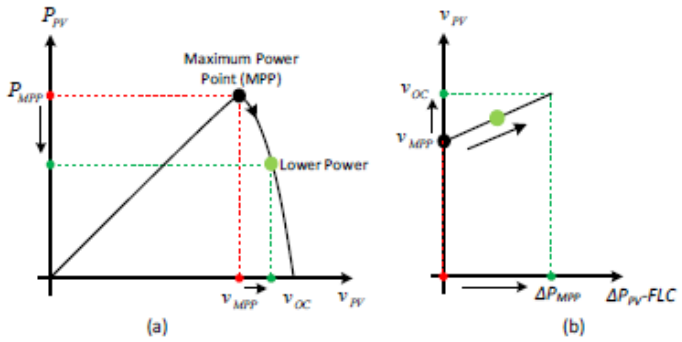

Fig. 6: PV MPP shifting operation: (a) PV power versus output voltage (b) Change of P_{PV} by FLC.

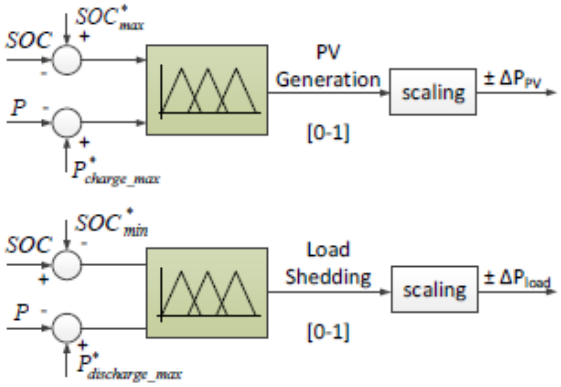

Fig. 7: Proposed fuzzy controller

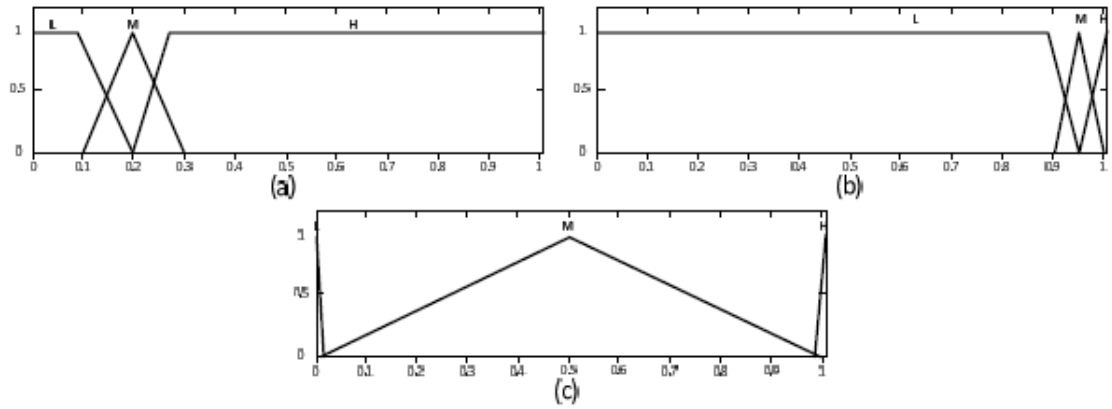

Fig. 8: Membership functions of top FLC: (a) Input-ΔSOC (b) Input-ΔP_{charge} (c) Output-ΔP_{PV}

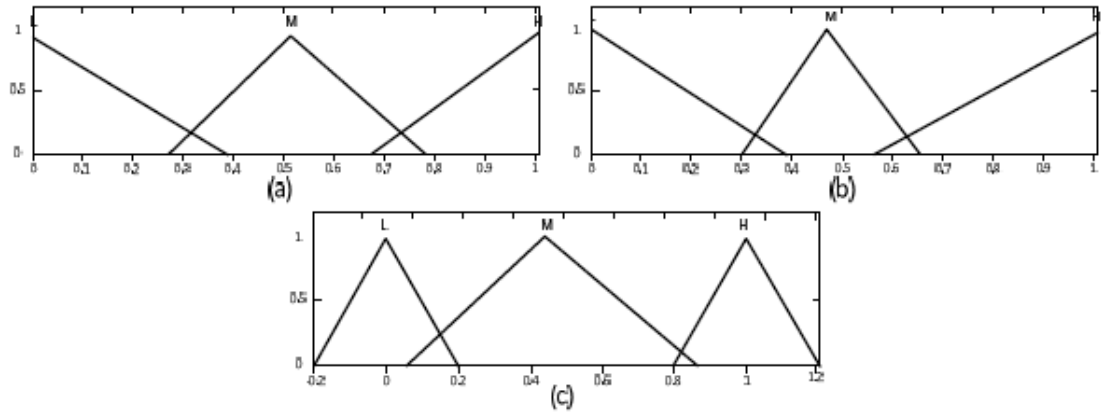

Fig. 9: Membership functions of top FLC: (a) Input-ΔSOC (b) Input-$\Delta P_{discharge}$ (c) Output-ΔP_{Load}

Table II: State of charge and power limits

Parameter	Symbol	Value
Maximum state of charge	SOC^{*}_{max}	95%
Minimum state of charge	SOC^{*}_{min}	40%
Maximum charging power	$P^{*}_{Charge\_max}$	1000W
Maximum discharging power	$P^{*}_{Discharge\_max}$	1000W

Table III: Rules of top FLC

ΔP_{PV}		ΔP_{charge}		
		L	M	H
ΔSOC	L	L	M	H
	M	M	H	H
	H	M	H	H

Table IV: Rules of bottom FLC

ΔP_{Load}		$\Delta P_{discharge}$		
		L	M	H
ΔSOC	L	L	L	L
	M	M	M	M
	H	H	H	H

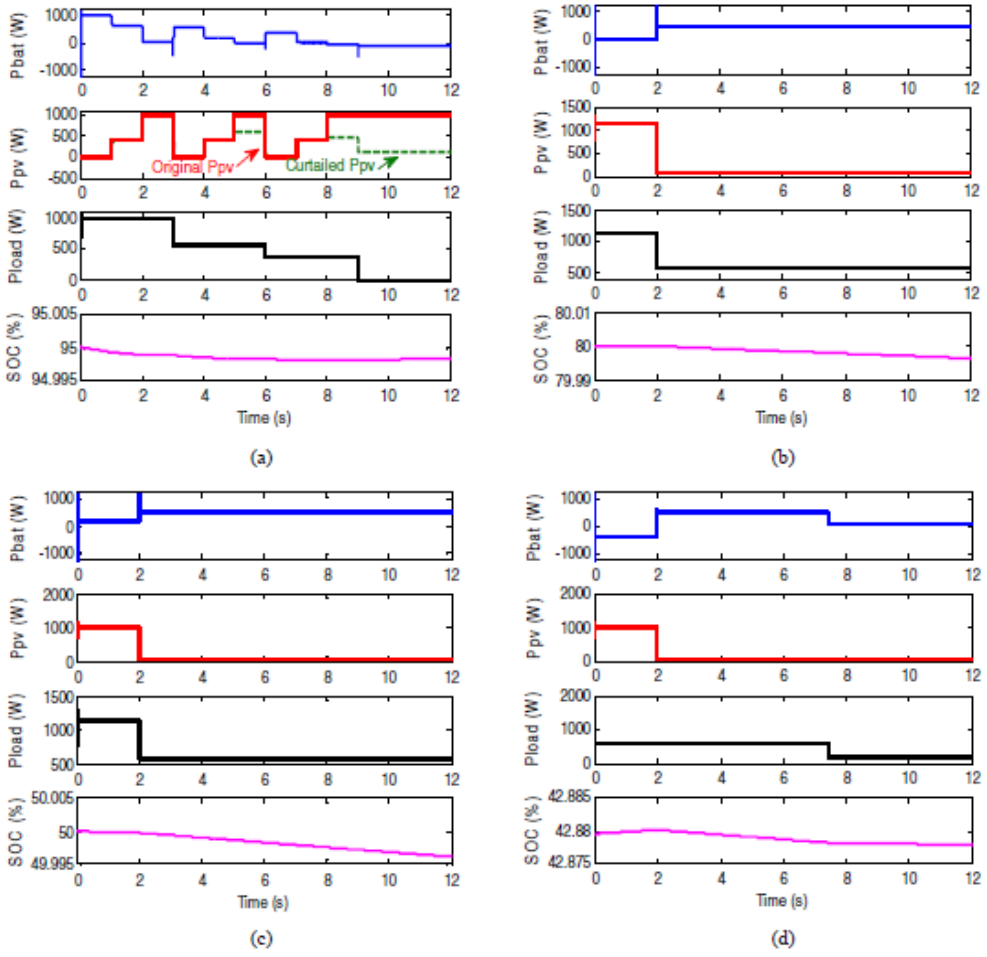

Fig. 10: Battery, PV and load Powers (a) SOC=95% (b) SOC=80% (c) SOC=50% (d) SOC=42.88%

Fig. 10(c) shows the battery and PV power outputs along with the loads' power and SOC curve for SOC = 50%. At t = 0 to 2s, the PV generation was 1000W while the load was 1140W. So, the battery provided 140W. At t = 2s, the PV generation dropped to a very low value. Hence, shedding was done for the normal load as per the FLC command and the load became 570W (essential and vital loads only) instead of total load (1140W). Fig. 10(d) shows the battery and PV power outputs along with the loads' power and SOC curve for SOC = 42.88%. At t = 0 to 2s, the PV generation was 1000W while the load was 570W (essential and vital). There was no power from the battery. At t = 2s, the PV generation dropped to a very low value. The battery managed to provide the required extra power for the load up to around 7.4s since the SOC was still above the minimum allowable limit. However, at

around 7.4s, load shedding was carried out for the essential load as per the FLC command and the load became 170W (vital load only) instead of 570W to keep the SOC of the battery within its design margin. As can be seen from the above results, the SOC and charging / discharging power of the battery were maintained within their design margins for all cases.

Conclusion

A fuzzy logic controller has been proposed for DC microgrid to coordinate the power flow between PV-based RES and Battery-based ESS in island mode. The proposed controller provides an efficient use of the PV's and battery's powers in order to keep the SOC and charging / discharging power of the battery within their required margins regardless of variations in load and intermittent power of renewable energy sources. If necessary, loads' shedding is done whenever required to prevent SOC from exceeding the lower limit and PV curtailment is carried out to realize over charging protection. The power management controller was implemented in a secondary control level to maintain the stability in transients and to provide efficient reference values for steady state operation. Matlab/Simulink results validated the performance of the proposed FLC.

References

[1] Issa W. R., Abusara M. A., and Sharkh S. M.: Control of transient power during unintentional islanding of microgrids, IEEE Trans. Power Electron., Vol. 30 no 8, pp. 4573–4584, 2015

[2] Dragicevic T., Guerrero J. M., Vasquez J. C., and Skrlec D.: Supervisory control of an adaptive-droop regulated DC microgrid with battery management capability, IEEE Trans. Power Electron. Vol. 29 no 2, pp. 695–706, 2014

[3] AlBadwawi R., Abusara M., and Mallick T.: A review of hybrid solar PV and wind energy system, Smart Sci. Vol. 3 no 3, pp. 127–138, 2015

[4] Suganthi L., Iniyan S., and Samuel A. A.: Applications of fuzzy logic in renewable energy systems – A review, Renew. Sustain. Energy Rev. Vol. 48, pp. 585–607, 2015

[5] Cheikh M., Larbes C., Tchoketch G., and Zerguerras A.: Maximum power point tracking using a fuzzy logic control scheme, Rev. des energies, Vol. 10, pp. 387–395, 2007

[6] Bigdeli N.: Optimal management of hybrid PV/fuel cell/battery power system: A comparison of optimal hybrid approaches, Renew. Sustain. Energy Rev., Vol. 42, pp. 377–393, 2015

[7] Esram T. and Chapman P. L.: Comparison of photovoltaic array maximum power point tracking techniques, IEEE Trans. Energy Convers., Vol. 22, no 2, pp. 439–449, 2007

[8] Cheng M.-W., Wang S.-M., Lee Y.-S., and Hsiao S.-H.: Fuzzy controlled fast charging system for lithium-ion batteries, International Conference on Power Electronics and Drive Systems (PEDS), pp. 1498–1503, 2009

[9] Chen Y., Wu Y., and Song C.: Design and implementation of energy management system with fuzzy control for DC micro-grid systems, IEEE Trans. Power Electron., Vol. 28, no 4, pp. 1563–1570, 2012

[10] Diaz N. L., Dragicevic T., Vasquez J. C., and Guerrero J. M.: Fuzzy-logic-based gain-scheduling control for state-of-charge balance of distributed energy storage systems for DC microgrids, Appl. Power Electron. Conf. Expo. (APEC), Twenty-Ninth Annu. IEEE, pp. 2171–2176, 2014

[11] Li X., Hui D., Wu L., and Lai X.: Control strategy of battery state of charge for wind/battery hybrid power system, IEEE Int. Symp. Ind. Electron., no 1, pp. 2723–2726, 2010

[12] Ben Salah C. and Ouali M.: Energy management of a hybrid photovoltaic system, Int. J. Energy Res., Vol. 36, pp. 130–138, 2012

[13] Hassanzadeh A., Monfared M., Golestan S., and Dowlatabadi R.: Small signal averaged model of DC choppers for control studies, Proc. 2011 Int. Conf. Electr. Eng. Informatics, ICEEI, pp. 17–20, 2011

[14] Mahmood H., Michaelson D., and Jiang J.: Control strategy for a standalone PV/battery hybrid system, 38th Annu. Conf. IECON 2012 Proc. (Industrial Electron. Conf.), pp. 3412–3418, 2012

[15] Weidong X., Dunford W. G., Palmer P. R., Capel A., Xiao W.: "Regulation of Photovoltaic Voltage," Ind. Electron. IEEE Trans., vol. 54, no 3, pp. 1365–1374, 2007

Appendix C: Bode plot program for DC/DC Converter

Bode plot program for DC/DC Converter for BESS (See section 5.4)

```
Gpib2=tf([1.5 50],[1 0])
Gpib1=tf([5e-3 1],[1 0])

R=440
C=1100e-6
Vdc=200
D=0.25
Ilb=0.7
Lb=0.8e-3
Gidb=tf([R*C*Vdc ((1-D)*R*Ilb+Vdc)],[R*C*Lb Lb R*(1-D)^2])
A=Gpib1*Gidb
B=feedback(A,1)

Gvib=tf([-Ilb*R*Lb (Vdc*R*(1-D))],[Vdc*R*C Vdc+(1-D)*Ilb*R])
C1=B*Gpib2*Gvib
margin(C1)
hold
bode(feedback(C1,1))
```

Bode plot program for DC/DC Converter for PV (See section 5.5)

```
Gpipvi=tf([0.05 1],[1 0])
Gpipvv=-1*tf([10 250],[1 0])

rpv=-6
Cpv=1100e-6
Vdc=380
Lpv=0.8e-3
Gidpv=tf([Cpv*rpv*Vdc -Vdc],[Lpv*Cpv*rpv -Lpv rpv])
A=Gpipvi*Gidpv
%fi=tf(1,[5e-5 1])
B=feedback(A,1)

Gvipv=tf(-rpv,[Cpv*rpv -1])
C1=B*Gpipvv*Gvipv
%fv=tf(1,[1e-4 1])
margin(C1)
hold
bode(feedback(C1,1))
```

BIBLIOGRAPHY

[1] M. Asif and T. Muneer, “Energy supply, its demand and security issues for developed and emerging economies,” *Renew. Sustain. Energy Rev.*, vol. 11, no. 7, pp. 1388–1413, 2007.

[2] H. H. Chen, H.-Y. Kang, and A. H. I. Lee, “Strategic selection of suitable projects for hybrid solar-wind power generation systems,” *Renew. Sustain. Energy Rev.*, vol. 14, no. 1, pp. 413–421, Jan. 2010.

[3] REN21. 2016 Renewable 2016 Global Status Report, *Renewables 2016: global status report*. 2016.

[4] Y. Chen, Y. Wu, and C. Song, “Design and Implementation of Energy Management System with Fuzzy Control for DC Micro-Grid Systems,” *IEEE Trans. Power Electron.*, vol. 28, no. 4, pp. 1563–1570, 2012.

[5] IEA: Directorate of Global Energy Economics, “World Energy Outlook 2015,” *Int. Energy Agency IEA*, p. 726, 2015.

[6] M. A. Abusara, J. M. Guerrero, and S. M. Sharkh, “Line-Interactive UPS for Microgrids,” *IEEE Trans. Ind. Electron.*, vol. 61, no. 3, pp. 1292–1300, Mar. 2014.

[7] R. AlBadwawi, M. Abusara, and T. Mallick, “A Review of Hybrid Solar PV and Wind Energy System,” *Smart Sci.*, vol. 3, no. 3, pp. 127–138, 2015.

[8] D. Wu, F. Tang, T. Dragicevic, J. C. Vasquez, and J. M. Guerrero, “Autonomous Active Power Control for Islanded AC Microgrids With Photovoltaic Generation and Energy Storage System,” *IEEE Trans. Energy Convers.*, vol. 29, no. 4, pp. 882–892, 2014.

[9] T. Dragicevic, J. M. Guerrero, J. C. Vasquez, and D. Skrlec, “Supervisory control of an adaptive-droop regulated DC microgrid with battery management capability,” *IEEE Trans. Power Electron.*, vol. 29, no. 2, pp. 695–706, 2014.

[10] G. Hug-Glanzmann, “Coordination of intermittent generation with storage, demand control and conventional energy sources,” *2010 IREP Symp. - Bulk Power Syst. Dyn. Control - VIII, IREP2010*, 2010.

[11] R. Luna-Rubio, M. Trejo-Perea, D. Vargas-Vázquez, and G. J. Ríos-Moreno, “Optimal sizing of renewable hybrids energy systems: A review of methodologies,” *Sol. Energy*, vol. 86, no. 4, pp. 1077–1088, Apr. 2012.

[12] B. Bhandari, K.-T. Lee, Y.-M. Cho, and S.-H. Ahn, “Optimization of Hybrid Renewable Energy Power systems: A review,” *Int. J. Precison Eng. Manuf. - Green Technol.*, vol. 2, no. 1, pp. 99–112, 2015.

[13] B. Parida, S. Iniyan, and R. Goic, “A review of solar photovoltaic technologies,” *Renew. Sustain. Energy Rev.*, vol. 15, no. 3, pp. 1625–1636, Apr. 2011.

[14] A. Luque and S. Hegedus, *Handbook of Photovoltaic Science*. .

[15] L. Freris and D. Infield, *Renewable Energy in Power Systems*. .

[16] E. O. Edenhofer, R. Pichs-Madruga and Y. Sokona, *Renewable Energy Sources and Climate Change Mitigation*. 2012.

[17] J. Karp, “Concentrating Solar Power : Progress and Trends,” 2009.

[18] X. Weidong, W. G. Dunford, P. R. Palmer, and A. Capel, “Regulation of Photovoltaic Voltage,” *Ind. Electron. IEEE Trans.*, vol. 54, no. 3, pp. 1365–1374, 2007.

[19] L. Micheli, N. Sarmah, X. Luo, K. S. Reddy, and T. K. Mallick, “Opportunities and challenges in micro- and nano-technologies for concentrating photovoltaic cooling : A review,” *Renew. Sustain. Energy Rev.*, vol. 20, pp. 595–610, 2013.

[20] S. Kurtz, “Opportunities and Challenges for Development of a Mature Concentrating Photovoltaic Power Industry Opportunities and Challenges for Development of a Mature Concentrating Photovoltaic Power Industry,” no. November, 2009.

[21] R. Al Badwawi, M. Abusara, and T. Mallick, “Speed control of synchronous machine by changing duty cycle of DC/DC buck converter,” *AIMS Energy*, vol. 3, no. 4, pp. 728–739, 2015.

[22] K. Grogg, “Harvesting the Wind : The Physics of Wind Turbines,” *Carleton College, Physics and Astronomy Comps Papers 2005, http://digitalcommons.carleton.edu/pacp/7*, 2005. .

[23] E. M. Natsheh, “Hybrid Power Systems Energy Management Based on Artificial Intelligence,” Manchester Metropolitan University, 2013.

[24] H. Mahmood, “Power Management Strategies for Islanded Microgrids,” University of Western Ontario, 2015.

[25] B. S. Borowy and Z. M. Salameh, “Methodology for optimally sizing the combination of a battery bank and PV array in a Wind/PV hybrid system,” *IEEE Trans. Energy Convers.*, vol. 11, no. 2, pp. 367–375, 1996.

[26] W. Kellogg, G. Venkataramanan, and V. Gerez, “Optimal unit sizing for a hybrid wind-photovoltaic generating system,” vol. 39, pp. 35–38, 1996.

[27] A. Kaabeche, M. Belhamel, and R. Ibtiouen, “Sizing optimization of grid-independent hybrid photovoltaic/wind power generation system,” *Energy*, vol. 36, no. 2, pp. 1214–1222, Feb. 2011.

[28] M. Esteban, Q. Zhang, A. Utama, T. Tezuka, and K. N. Ishihara, “Methodology to estimate the output of a dual solar–wind renewable energy system in Japan,” *Energy Policy*, vol. 38, no. 12, pp. 7793–7802, Dec. 2010.

[29] R. Dufo-López, J. L. Bernal-Agustín, and F. Mendoza, “Design and economical analysis of hybrid PV–wind systems connected to the grid for the intermittent production of hydrogen,” *Energy Policy*, vol. 37, no. 8, pp. 3082–3095, Aug. 2009.

[30] G. M. Tina and S. Gagliano, “Probabilistic modelling of hybrid solar/wind power system with solar tracking system,” *Renew. Energy*, vol. 36, no. 6, pp. 1719–1727, Jun. 2011.

[31] S. Bhattacharjee and S. Acharya, “PV–wind hybrid power option for a low wind topography,” *Energy Convers. Manag.*, vol. 89, pp. 942–954, 2015.

[32] S. Essalaimeh, a. Al-Salaymeh, and Y. Abdullat, “Electrical production for domestic and industrial applications using hybrid PV-wind system,” *Energy Convers. Manag.*, vol. 65, pp. 736–743, Jan. 2013.

[33] N. A. Ahmed, A. K. Al-Othman, and M. R. AlRashidi, “Development of an efficient utility interactive combined wind/photovoltaic/fuel cell power system with MPPT and DC bus voltage regulation,” *Electr. Power Syst. Res.*, vol. 81, no. 5, pp. 1096–1106, May 2011.

[34] G. M. Shafiullah, A. M. T. Oo, D. Jarvis, A. B. M. S. Ali, and P. Wolfs, “Potential Challenges : Integrating Renewable Energy with the Smart Grid,” in *20th Australasian Universities Power Engineering Conference (AUPEC)*, 2010, pp. 1–6.

[35] B. Ernst, F. Reyer, and J. Vanzetta, “Wind power and photovoltaic prediction tools for balancing and grid operation,” *CIGRE/IEEE PES Jt. Symp.*, vol. CALGARY 20, pp. 1–9, 2009.

[36] Y. Liu and C. Jiang, “A Review on Technologies and Methods of Mitigating Impacts of Large - Scale Intermittent Renewable Generations on Power System,” *Res. J. Appl. Sci. Eng. Technol.*, vol. 5, no. 9, pp.

2765–2770, 2013.

[37] D. A. Halamay, S. Member, T. K. A. Brekken, A. Simmons, and S. Mcarthur, “Reserve Requirement Impacts of Large-Scale Integration of Wind , Solar , and Ocean Wave Power Generation,” *IEEE Trans. Sustain. Energy*, vol. 2, no. 3, pp. 321–328, 2011.

[38] A. S. Anees, “Grid integration of renewable energy sources: Challenges, issues and possible solutions,” *2012 IEEE 5th India Int. Conf. Power Electron.*, pp. 1–6, Dec. 2012.

[39] F. O. Resende and J. A. P. Lopes, “Management and Control Systems for Large Scale Integration of Renewable Energy Sources into the Electrical Networks,” *IEEE Int. Conf. Comput. as a Tool*, vol. Lisbone, no. 27–29 April 2011, pp. 1–6, 2011.

[40] S. K. Khadem, M. Basu, and M. F. Conlon, “Power Quality in Grid connected Renewable Energy Systems : Role of Custom Power Devices 3 . Grid integration of Renewable Energy,” 2010.

[41] N. T. Linh, “Power quality investigation of grid connected wind turbines,” *2009 4th IEEE Conf. Ind. Electron. Appl.*, pp. 2218–2222, May 2009.

[42] J. C. Vasquez, J. M. Guerrero, J. Miret, M. Castilla, and L. G. De Vicuña, “Hierarchical Control of Intelligent Microgrids,” *IEEE Ind. Electron. Mag.*, no. December 2010, pp. 23–29, 2010.

[43] M. R. Patel, *Wind and Solar Power Systems*, Second Edi. Taylor and Francis, New York, 2006.

[44] Z. M. Salameh and B. S. Borowy, “Optimum photovoltaic array size for a hybrid wind/PV system - Energy Conversion, IEEE Transactions on,” *IEEE Trans. Energy Convers.*, vol. 9, no. 3, pp. 482–488, 1994.

[45] H. Yang, L. Lu, and W. Zhou, “A novel optimization sizing model for hybrid solar-wind power generation system,” *Sol. Energy*, vol. 81, no. 1, pp. 76–84, Jan. 2007.

[46] R. Belfkira, L. Zhang, and G. Barakat, “Optimal sizing study of hybrid wind/PV/diesel power generation unit,” *Sol. Energy*, vol. 85, no. 1, pp. 100–110, Jan. 2011.

[47] M. A. Elhadidy and S. M. Shaahid, “Optimal sizing of battery storage for hybrid (wind+diesel) power systems,” *Renew. Energy*, vol. 18, pp. 77–86, 1999.

[48] R. Chedid and Y. Saliba, “Optimization and control of autonomous

renewable energy systems," *Int. J. Energy Res.*, vol. 20, no. October 1994, pp. 609–624, 1996.

[49] S. H. Karaki and I. R. B. Chedid, "Probabilistic Performance Assessment of Autonomous Solar-Wind Energy Conversion Systems," *IEEE Trans. Energy Convers.*, vol. 14, no. 3, 1999.

[50] N. Bigdeli, "Optimal management of hybrid PV/fuel cell/battery power system: A comparison of optimal hybrid approaches," *Renew. Sustain. Energy Rev.*, vol. 42, pp. 377–393, 2015.

[51] J. K. Kaldellis, D. Zafirakis, and E. Kondili, "Optimum sizing of photovoltaic-energy storage systems for autonomous small islands," *Int. J. Electr. Power Energy Syst.*, vol. 32, no. 1, pp. 24–36, Jan. 2010.

[52] A. Kaabeche, M. Belhamel, and R. Ibtiouen, "Techno-economic valuation and optimization of integrated photovoltaic/wind energy conversion system," *Sol. Energy*, vol. 85, no. 10, pp. 2407–2420, Oct. 2011.

[53] E. Koutroulis, D. Kolokotsa, A. Potirakis, and K. Kalaitzakis, "Methodology for optimal sizing of stand-alone photovoltaic/wind-generator systems using genetic algorithms," *Sol. Energy*, vol. 80, no. 9, pp. 1072–1088, Sep. 2006.

[54] M. A. Habib and S. A. M. Said, "Optimization procedure of a hybrid photovoltaic wind energy system," *Energy*, vol. 24, pp. 919–929, 1999.

[55] S. Diaf, D. Diaf, M. Belhamel, M. Haddadi, and a. Louche, "A methodology for optimal sizing of autonomous hybrid PV/wind system," *Energy Policy*, vol. 35, no. 11, pp. 5708–5718, Nov. 2007.

[56] J. K. Kaldellis, D. Zafirakis, and E. Kondili, "Optimum autonomous stand-alone photovoltaic system design on the basis of energy pay-back analysis," *Energy*, vol. 34, no. 9, pp. 1187–1198, Sep. 2009.

[57] G. Notton, S. Diaf, and L. Stoyanov, "Hybrid Photovoltaic/Wind Energy Systems For Remote Locations," *Energy Procedia*, vol. 6, pp. 666–677, Jan. 2011.

[58] Q. Huang, Y. Shi, Y. Wang, L. Lu, and Y. Cui, "Multi-turbine wind-solar hybrid system," *Renew. Energy*, vol. 76, pp. 401–407, 2015.

[59] W. Zhou, C. Lou, Z. Li, L. Lu, and H. Yang, "Current status of research on optimum sizing of stand-alone hybrid solar–wind power generation systems," *Appl. Energy*, vol. 87, no. 2, pp. 380–389, Feb. 2010.

[60] P. Kong, J. Zhao, and Y. Xing, "Series-parallel Resonant High Frequency

Inverter for Standalone Hybrid PV/Wind Power System," *Energy Procedia*, vol. 12, pp. 1090–1097, Jan. 2011.

[61] X. Lu, J. M. Guerrero, K. Sun, J. C. Vasquez, R. Teodorescu, and L. Huang, "Hierarchical Control of Parallel AC-DC Converter Interfaces for Hybrid Microgrids," *IEEE Trans. Smart Grid*, pp. 683–692, 2013.

[62] N. A. Ahmed, M. Miyatake, and A. K. Al-Othman, "Power fluctuations suppression of stand-alone hybrid generation combining solar photovoltaic/wind turbine and fuel cell systems," *Energy Convers. Manag.*, vol. 49, no. 10, pp. 2711–2719, Oct. 2008.

[63] E. Dursun and O. Kilic, "Comparative evaluation of different power management strategies of a stand-alone PV/Wind/PEMFC hybrid power system," *Int. J. Electr. Power Energy Syst.*, vol. 34, no. 1, pp. 81–89, 2012.

[64] W. Qi, J. Liu, X. Chen, and P. D. Christofides, "Supervisory Predictive Control of Standalone Wind/Solar Energy Generation Systems," *IEEE Trans. Control Syst. Technol.*, vol. 19, no. 1, pp. 199–207, Jan. 2011.

[65] J. M. Guerrero, J. C. Vasquez, J. Matas, L. G. De Vicuña, and M. Castilla, "Hierarchical Control of Droop-Controlled AC and DC Microgrids — A General Approach Toward Standardization," *IEEE Trans. Ind. Electron.*, vol. 58, no. 1, pp. 158–172, 2011.

[66] L. Meng, E. R. Sanseverino, A. Luna, T. Dragicevic, J. C. Vasquez, and J. M. Guerrero, "Microgrid supervisory controllers and energy management systems: A literature review," *Renew. Sustain. Energy Rev.*, vol. 60, no. July, pp. 1263–1273, 2016.

[67] A. Chauhan and R. P. Saini, "A review on Integrated Renewable Energy System based power generation for stand-alone applications: Configurations, storage options, sizing methodologies and control," *Renew. Sustain. Energy Rev.*, vol. 38, pp. 99–120, 2014.

[68] J. Y. Kim, J. H. Jeon, S. K. Kim, C. Cho, J. H. Park, H. M. Kim, and K. Y. Nam, "Cooperative control strategy of energy storage system and microsources for stabilizing the microgrid during islanded operation," *IEEE Trans. Power Electron.*, vol. 25, no. 12, pp. 3037–3048, 2010.

[69] B. Belvedere, M. Bianchi, A. Borghetti, C. a. Nucci, M. Paolone, and A. Peretto, "A Microcontroller-Based Power Management System for Standalone Microgrids With Hybrid Power Supply," *IEEE Trans. Sustain.*

Energy, vol. 3, no. 3, pp. 422–431, 2012.

[70] C. Wang and M. H. Nehrir, “Power Management of a Stand-Alone Wind / Photovoltaic / Fuel Cell Energy System,” *IEEE Trans. ENERGY Convers.*, vol. 23, no. 3, pp. 957–967, 2008.

[71] H. Mahmood and D. Michaelson, “A Power Management Strategy for PV/Battery Hybrid Systems in Islanded Microgrids,” *IEEE J. Emerg. Sel. Top. Power Electron.*, vol. 2, no. 4, pp. 1–14, 2014.

[72] P. G. Arul, V. K. Ramachandaramurthy, and R. K. Rajkumar, “Control strategies for a hybrid renewable energy system : A review,” *Renew. Sustain. Energy Rev.*, vol. 42, pp. 597–608, 2015.

[73] M. S. Ismail, M. Moghavvemi, T. M. I. Mahlia, K. M. Muttaqi, and S. Moghavvemi, “Effective utilization of excess energy in standalone hybrid renewable energy systems for improving comfort ability and reducing cost of energy: A review and analysis,” *Renew. Sustain. Energy Rev.*, vol. 42, pp. 726–734, 2015.

[74] L. Olatomiwa, S. Mekhilef, M. S. Ismail, and M. Moghavvemi, “Energy management strategies in hybrid renewable energy systems : A review,” *Renew. Sustain. Energy Rev.*, vol. 62, no. May, pp. 821–835, 2016.

[75] A. M. Dizqah, “Non-Linear Model Predictive Eenergy Management Strategies For Stand-alone DC Microgrids,” University of Northumbria, 2014.

[76] J. de Matos, F. e Silva, and L. Ribeiro, “Power Control in AC Isolated Microgrids with Renewable Energy Sources and Energy Storage Systems,” *IEEE Trans. Ind. Electron.*, vol. 62, no. 6, pp. 3490–3498, 2014.

[77] D. Wu, J. M. Guerrero, J. C. Vasquez, T. Dragicevic, and F. Tang, “Coordinated power control strategy based on primary-frequency-signaling for islanded microgrids,” *2013 IEEE Energy Convers. Congr. Expo. ECCE 2013*, pp. 1033–1038, 2013.

[78] A. Urtasun, E. L. Barrios, P. Sanchis, and L. Marroyo, “Frequency-Based Energy-Management Strategy for Stand-Alone Systems With Distributed Battery Storage,” *IEEE Trans. Power Electron.*, vol. 30, no. 9, pp. 4794–4808, 2015.

[79] A. Mahesh and K. S. Sandhu, “Hybrid wind/photovoltaic energy system developments: Critical review and findings,” *Renew. Sustain. Energy*

Rev., vol. 52, pp. 1135–1147, 2015.

[80] L. Suganthi, S. Iniyan, and A. A. Samuel, “Applications of fuzzy logic in renewable energy systems – A review,” *Renew. Sustain. Energy Rev.*, vol. 48, pp. 585–607, 2015.

[81] B. Robyns, A. Davigny, and C. Saudemont, “Methodologies for supervision of Hybrid Energy Sources based on Storage Systems - A survey,” *Math. Comput. Simul.*, vol. 91, pp. 52–71, 2013.

[82] M. Cheikh, C. Larbes, G. Tchoketch, and A. Zerguerras, “Maximum power point tracking using a fuzzy logic control scheme,” *Rev. des energies …*, vol. 10, pp. 387–395, 2007.

[83] T. Esram and P. L. Chapman, “Comparison of Photovoltaic Array Maximum Power Point Tracking Techniques,” *IEEE Trans. Energy Convers.*, vol. 22, no. 2, pp. 439–449, 2007.

[84] B. Hamed and M. El-Moghany, “Fuzzy controller design using FPGA for photovoltaic maximum power point tracking,” *J. Adv. Res. Artif. Intell.*, vol. 1, no. 3, pp. 14–21, 2012.

[85] M. S. Bisht and Sathans, “Fuzzy based Intelligent Frequency Control Strategy in Standalone Hybrid AC MicroGrid,” in *2014 IEEE Conference on Control Applications (CCA)*, 2014, pp. 873–878.

[86] M. Marzband, A. Sumper, O. Gomis-Bellmunt, P. Pezzini, and M. Chindris, “Frequency Control of Isolated Wind and Diesel Hybrid Microgrid Power System by Using Fuzzy Logic Controllers and PID Controllers,” in *Proceeding of the 11th International Conference on Electrical Power Quality and Utilisation, EPQU*, 2011, pp. 114–119.

[87] M.-W. Cheng, S.-M. Wang, Y.-S. Lee, and S.-H. Hsiao, “Fuzzy controlled fast charging system for lithium-ion batteries,” in *International Conference on Power Electronics and Drive Systems (PEDS)*, 2009, pp. 1498–1503.

[88] A. Li-nu-er A Mu-ti, C. Qin, T. Er-xun Yi Bu-la-yin, and L. Jian-chun, “Application of Fuzzy Control for the Energy Storage System in Improving Wind Power Prediction Accuracy,” *Am. J. Energy Res.*, vol. 1, no. 3, pp. 54–58, 2013.

[89] C. Ben Salah and M. Ouali, “Energy management of a hybrid photovoltaic system,” *Int. J. Energy Res.*, vol. 36, pp. 130–138, 2012.

[90] D. Arcos-Aviles, F. Guinjoan, J. Barricarte, L. Marroyo, P. Sanchis, and H. Valderrama, “Battery management fuzzy control for a grid- tied microgrid

with renewable generation," *IECON 2012 - 38th Annu. Conf. IEEE Ind. Electron. Soc.*, no. 1, pp. 5607–5612, 2012.

[91] A. Lal, R. Kumar, and U. Mehta, "Energy Dispatch Fuzzy Model in Hybrid Power System," *Int. Energy J.*, vol. 14, pp. 133–142, 2014.

[92] X. Li, D. Hui, L. Wu, and X. Lai, "Control strategy of battery state of charge for wind/battery hybrid power system," *IEEE Int. Symp. Ind. Electron.*, no. 1, pp. 2723–2726, 2010.

[93] N. L. Diaz, T. Dragicevic, J. C. Vasquez, and J. M. Guerrero, "Fuzzy-Logic-Based Gain-Scheduling Control for State-of-Charge Balance of Distributed Energy Storage Systems for DC Microgrids," *Appl. Power Electron. Conf. Expo. (APEC), 2014 Twenty-Ninth Annu. IEEE*, pp. 2171–2176, 2014.

[94] W. R. Issa, M. A. Abusara, and S. M. Sharkh, "Control of Transient Power During Unintentional Islanding of Microgrids," *IEEE Trans. Power Electron.*, vol. 30, no. 8, pp. 4573–4584, 2015.

[95] W. Issa, M. Abusara, S. Sharkh, and T. Mallick, "A small signal model of an inverter-based microgrid including DC link voltages," *2015 17th Eur. Conf. Power Electron. Appl. EPE-ECCE Eur. 2015*, 2015.

[96] R. Al Badwawi, W. Issa, T. Mallick, and M. Abusara, "Power Management of AC Islanded Microgrids using Fuzzy Logic," in *8th IET International Conference on Power Electronics, Machines and Drives (PEMD 2016)*, 2016, pp. 1–6.

[97] Walid R M Issa, "Improved Control Strategies for Droop - Controlled Inverter - Based Microgrid," 2015.

[98] W. Issa, S. Sharkh, T. Mallick, and M. Abusara, "Improved Reactive Power Sharing for Parallel-operated Inverters in Islanded Microgrids," *J. Power Electron.*, vol. 16, no. 3, pp. 1152–1162, 2016.

[99] L. A. Zadeh, "Fuzzy sets," *Inf. Control*, vol. 8, no. 3, pp. 338–353, 1965.

[100] L. A. Zadeh, "Outline of a new approach to the analysis of complex systems and decision processes," *Syst. Man Cybern. IEEE Trans.*, no. 1, pp. 28–44, 1973.

[101] E. H. Mamdani, "Application of fuzzy algorithms for control of simple dynamic plant," *Proc. Inst. Electr. Eng.*, vol. 121, no. 12, pp. 1585–1588, 1974.

[102] M. G. Simoes, "Introduction to Fuzzy Control ∗," *Color. Sch. Mines, Eng.*

Div. Golden, Color., pp. 1–5, 2003.

[103] Y. Yin, X. Luo, S. Guo, Z. Zhou, and J. Wang, “A Battery Charging Control Strategy for Renewable Energy Generation Systems,” in *Proceedings of the World Congress on Engineering (WCE 2008)*, 2008, vol. I, pp. 356–361.

[104] K. M. Passino and S. Yurkovich, *Fuzzy control*. ADDISON-WESLEY, 1998.

[105] M. G. Simoes, “Introduction to Fuzzy Control,” *Color. Sch. Mines, Eng. Div. Golden, Color.*, pp. 1–5, 2003.

[106] J. Zhao and B. K. Bose, “Evaluation of Membership Functions for Fuzzy Logic Controlled Induction Motor Drive,” *IEEE 2002 28th Annu. Conf. Ind. Electron. Soc.*, pp. 229–234, 2002.

[107] “Generating Fuzzy Rules By Learnign From Examples,” *IEEE Trans. Syst. Man. Cybern.*, vol. 22, no. 6, pp. 1414–1426, 1992.

[108] J. Casillas, O. Cordon, and F. Herrera, “Improving the Wang and Mendel ’ s Fuzzy Rule Learning Method by Inducing Cooperation Among Rules,” *Proc. 8th Inf. Process. Manag. Uncertain. Knowledge-Based Syst. Conf.*, pp. 1682–1688, 2000.

[109] J. M. Guerrero, L. G. de Vicuna, J. Matas, M. Castilla, and J. Miret, “A wireless controller to enhance dynamic performance of parallel inverters in distributed generation systems,” *IEEE Trans. Power Electron.*, vol. 19, no. 5, pp. 1205–1213, 2004.

[110] P. Venne, J.-N. Paquin, and J. Belanger, “The What, Where and Why of Real-Time Simulation,” *Power Energy Soc.*, vol. 1, pp. 37–49, 2010.

[111] S. K. Khadem, M. Basu, and M. F. Conlon, “Intelligent islanding and seamless reconnection technique for microgrid with UPQC,” *IEEE J. Emerg. Sel. Top. Power Electron.*, vol. 3, no. 2, pp. 483–492, 2015.

[112] Semikron, “IGBT Power electronics teaching system principle for sizing power converters,” 2008.

[113] W. R. Issa, M. A. Abusara, and S. M. Sharkh, “Impedance Interaction between Islanded Parallel Voltage Source Inverters and the Distribution Network,” in *7th IET International Conference on Power Electronics, Machines and Drives (PEMD 2014)*, 2014, pp. 1–6.

[114] A. Hassanzadeh, M. Monfared, S. Golestan, and R. Dowlatabadi, “Small signal averaged model of DC choppers for control studies,” *Proc. 2011*

Int. Conf. Electr. Eng. Informatics, ICEEI 2011, no. July, pp. 17–20, 2011.

[115] H. Mahmood, D. Michaelson, and J. Jiang, “Control strategy for a standalone PV/battery hybrid system,” *38th Annu. Conf. IECON 2012 Proc. (Industrial Electron. Conf.*, pp. 3412–3418, 2012.

[116] R. Al Badwawi, W. Issa, T. Mallick, and M. Abusara, “DC Microgrid Power Coordination Based on Fuzzy Logic Control,” in *18th European Conference on Power Electronics and Applications*, 2016, pp. 1–10.

[117] Technical Support OPAL-RT, “OPAL-RT: IT Network Setup Procedure,” 2012.

[118] N. Sellami, “Design and characterisation of a novel translucent solar concentrator,” Heriot-Watt University, 2013.

[119] N. Karami, N. Moubayed, and R. Outbib, “Energy management for a PEMFC-PV hybrid system,” *Energy Convers. Manag.*, vol. 82, pp. 154–168, 2014.

[120] E. Kabalci, “Design and analysis of a hybrid renewable energy plant with solar and wind power,” *Energy Convers. Manag.*, vol. 72, pp. 51–59, Aug. 2013.

[121] A. A. Ahmed, R. L., and J. Bumby, “Simulation and control of a hybrid PV-wind system,” in *4th IET International Conference on Power Electronics, Machines and Drives (PEMD 2008)*, 2008, no. 3, pp. 421–425.

[122] P. Bajpai and V. Dash, “Hybrid renewable energy systems for power generation in stand-alone applications: A review,” *Renew. Sustain. Energy Rev.*, vol. 16, no. 5, pp. 2926–2939, Jun. 2012.

[123] C. Renno and F. Petito, “Design and modeling of a concentrating photovoltaic thermal (CPV/T) system for a domestic application,” *Energy Build.*, vol. 62, no. July 2013, pp. 392–402, 2013.

[124] K. Nishioka, T. Takamoto, T. Agui, M. Kaneiwa, Y. Uraoka, and T. Fuyuki, “Annual output estimation of concentrator photovoltaic systems using high-efficiency InGaP/InGaAs/Ge triple-junction solar cells based on experimental solar cell’s characteristics and field-test meteorological data,” *Sol. Energy Mater. Sol. Cells*, vol. 90, no. 1, pp. 57–67, 2006.

[125] H. Baig, K. C. Heasman, and T. K. Mallick, “Non-uniform illumination in concentrating solar cells,” *Renew. Sustain. Energy Rev.*, vol. 16, no. 8, pp. 5890–5909, 2012.